UAB
Universitat Autònoma de Barcelona

Multi-dimensional Multipath Mitigation for GNSS Signals

Ning Chang

ADVERTIMENT. L'accés als continguts d'aquesta tesi queda condicionat a l'acceptació de les condicions d'ús establertes per la següent llicència Creative Commons: https://creativecommons.org/licenses/?lang=ca

ADVERTENCIA. El acceso a los contenidos de esta tesis queda condicionado a la aceptación de las condiciones de uso establecidas por la siguiente licencia Creative Commons: https://creativecommons.org/licenses/?lang=es

WARNING. The access to the contents of this doctoral thesis it is limited to the acceptance of the use conditions set by the following Creative Commons license: https://creativecommons.org/licenses/?lang=en



西安交通大學
XI'AN JIAOTONG UNIVERSITY

UAB
Universitat Autònoma de Barcelona

Double Doctoral Degree Programme

Doctoral Program in Electronic and Telecommunication Engineering

Ph.D. Dissertation

Multi-dimensional Multipath Mitigation for GNSS Signals

Ning Chang

Supervisor

Prof. Wenjie Wang,

Prof. Gonzalo Seco-Granados

Any

2023

ACADEMIC DISSERTATION

Xi’an Jiaotong University, Faculty of Electronic and Information Engineering
China
Universitat Autònoma de Barcelona, Department of Telecommunications and Systems Engineering
Spain

Supervisors	Professor Wenjie Wang Xi’an Jiaotong University China	Professor Gonzalo Seco-Granados Universitat Autònoma de Barcelona Spain
Pre-examiners	Professor Elena Simona Lohan Tampere University Finland	Professor Jie Chen Northwestern Polytechnical University China
Opponents	Dr. David Gómez Casco European Space Agency Spain	Professor Huiming Wang Xi’an Jiaotong University China
	Dr. Francisco José Fabra Cervellera Institut d’Estudis Espacials de Catalunya Spain	Professor Adrià Rovira García Universitat Politècnica de Catalunya Spain
	Professor Kai Xie Xidian University China	

Preface

The research presented in this thesis was conducted from 2016 to 2023 in two departments: the Department of Information and Communication Engineering at Xi'an Jiaotong University (XJTU) and the Department of Telecommunications and Systems Engineering at Universitat Autònoma de Barcelona (UAB), specifically within the Ministry of Education Key Lab for Intelligent Networks and Network Security and the Signal Processing for Communications and Navigation (SPCOMNAV) group, respectively. This work was carried out under a cooperation agreement for a double Ph.D. degree between XJTU and UAB. I would like to express my special appreciation to the individuals who contributed to the success of this research.

In the first place, this work would not have been possible without the guidance and support of my supervisors, Prof. Gonzalo Seco-Granados and Prof. Wenjie Wang. I am extremely grateful for their constant encouragement, insightful comments and suggestions, and unwavering support throughout my research. Their expertise in the field of GNSS array signal processing has been invaluable to me and will undoubtedly continue to influence my future academic pursuits.

I am also deeply thankful to Prof. José A. López-Salcedo, Dr. Xi Hong, and Dr. Daniel Egea-Roca for their significant contributions to my research. Their valuable feedback and suggestions have greatly enhanced the quality of my work.

Special thanks are due to all my colleagues at the SPCOMNAV group and the Ministry of Education Key Lab for Intelligent Networks and Network Security for their support, encouragement, and friendship. In particular, I would like to thank Dr. Sergi Locubiche, Alda Xhafa, Dr. Rubén Morales-Ferré, Dr. Jose A. del Peral-Rosado, Dr. Olivier Renaudin and Menghan Lin, Dr. Cahowen Liu, Chenhao Zhang, Jianwei Zhou, Dr. Weile Zhang, Dr. Pengcheng Mu.

I would like to express my heartfelt appreciation to my family for their love, support, and encouragement throughout my academic journey.

Finally, I would like to extend my sincere appreciation to the experts, professors, and teachers who took part in reviewing this doctoral thesis and provided invaluable insights.

Abstract

Global Navigation Satellite Systems (GNSSs) have undergone significant development and widespread adoption to meet the increasing demands for positioning, timing, and navigation. GNSS has not only revolutionized civilian fields such as wireless communications and autonomous driving but also advanced military applications in aerospace and weaponry. However, the accuracy of GNSS has been severely affected by multipath signals, which are reflected by high-rise buildings and complex terrains. This degradation in accuracy has particularly impacted high-precision and high-dynamic GNSS applications. Consequently, multipath mitigation has remained a long-standing challenge in academic research.

The main objective of this thesis is to address the issues related to multipath mitigation and parameter estimation in GNSS multipath environments. By utilizing GNSS multipath signals and channel characteristics, this thesis investigates the critical technology of joint multi-dimensional processing, such as spatial, temporal, polarization, and frequential domains in GNSS multipath mitigation. The main contributions of this thesis can be summarized as follows:

1. Establishment of GNSS multi-dimensional receiving architecture and system model. To address the issue of insufficient utilization of space and time information in cascaded spatial and temporal GNSS receivers, this thesis explores the GNSS signal and channel features in spatial, temporal, polarization, and frequential domains. Based on the short-term quasi-static characteristics at the discriminator, a generalized multi-dimensional GNSS multipath mitigating signal model is proposed. This architecture fully integrates the characteristics of GNSS multipath signals in various dimensions and lays the foundation for enriching and enhancing the multipath mitigation of GNSS receivers in urban environments.

2. Spatial and temporal GNSS multipath mitigation. This thesis primarily focuses on the advantages of joint space and time multipath mitigation in GNSS and proposes two categories of algorithms: subspace-based and multiple sparse Bayesian learning (MSBL)-based joint spatial and temporal GNSS multipath mitigation algorithms. To achieve a balance between complexity and multipath mitigation enhancement, the thesis presents a subspace-based joint angle and time delay estimation architecture that considers rotation invariance in space and time. By leveraging the Vandermonde phase relationship between the spatial steering vectors and the frequential

code phase vectors, a joint spatial and frequential smoothing approach is proposed to address the rank-deficiency issue of the covariance matrix in spatially correlated signals. Moreover, in scenarios where both spatial and temporal domains exhibit correlation, the thesis proposes the use of the MSBL method in conjunction with joint angle and delay estimation techniques to exploit the sparsity present in both domains. To overcome the limitations of sparse representations, two different algorithms based on on-grid and off-grid estimators are introduced, aiming to reduce complexity or enhance resolution. These algorithms allow the proposed multipath mitigation approach to be adaptable to various practical GNSS scenarios. Furthermore, an improved resolution algorithm is obtained by applying the space alternating generalized expectation–maximization (SAGE) algorithm to refine the MSBL-based joint angle and delay estimates. These three MSBL-based methods effectively resolve GNSS multipath signals and outperform existing methods, even in challenging situations such as low carrier-to-noise ratio and spatially or temporally correlated multipath scenarios.

3. Spatial, polarization, and temporal GNSS multipath mitigation. In severe multipath environments, tracking performance can be significantly degraded, resulting in meter-level pseudorange errors. To address the challenges of parameter estimation in such environments, particularly when the line-of-sight (LOS) signal and multipath signals are highly spatially and temporally correlated, we explore polarization diversity in addition to the joint spatial and temporal sparsity. An off-grid MSBL-based joint estimator for the angle, polarization, and time delay of each multipath signal is then derived to reduce complexity and improve resolution. The proposed MSBL-based method has excellent robustness and effectiveness in combating multipath, which achieves close-to-optimal performance compared to the Cramér-Rao bound and outperforms other methods, particularly under highly spatially or temporally correlated signals.

4. Spatial and frequential GNSS multipath mitigation. Growing evidence suggests that wide-bandwidth signals and multi-antenna technology are set to become two vital factors in improving GNSS multipath mitigation, leading to the concept of meta-GNSS signal and multi-dimensional processing. To estimate the time delay of LOS signal in multipath environments, we propose a meta-signal SAGE-based locked loop (SAGELL) design, which exploits the high-resolution meta-signal together with the characteristics from spatial and temporal domains. The SAGELL design comprises two main setups: the SAGE-based discriminator and combinational loops. Benefiting from the multi-dimensional processing and meta-signal bandwidth, the SAGE-based discriminator first estimates the LOS and multipath signals in single side-band components and coherently achieves global estimates of the dual side-band components. Aiming to track meta-signal accurately, we further close the SAGELL via angle, code phase, and carrier phase locked loops to filter and predict the estimates. The proposed GNSS meta-signal multipath mitigating loop design allows for GNSS high-precision mitigation and tracking in

multipath scenarios, even in the presence of extremely highly correlated signals, as confirmed by the numerical results.

5. Furthermore, this thesis aims to validate the proposed joint spatial and temporal methods through the collection of GNSS signals using a multi-antenna GNSS data collection platform. The collected data also serve to showcase the viability of online GNSS data received by multi-antenna for scientific research, thereby facilitating data uploading and sharing.

Glossary

ACF	Auto-Correlation Function
ADC	Analog-to-Digital Converter
ALL	Angle Locked Loop
AR	Axial Ratio
ARD	Automatic Correlation Determinism
BOC	Binary Offset Carrier
CDMA	Code Division Multiple Access
CRLB	Cramér-Rao Lower Bound
DC	Direct Current
DFO	Doppler Frequency Offset
DLL	Delay Locked Loop
DOA	Direction-Of-Arrival
DOAMatrix	DOA Matrix
DPA	Dual-Polarization Antennas
DSB	Double Side-Band
EM	Expectation-Maximization
ESPRIT	Estimating Signal Parameter via Rotational Invariance Techniques
FOCUSS	FOCal Underdetermined System Solution
GLONASS	GLObal NAvigation Satellite System
GNSS	Global Satellite Navigation Systems
GPS	Global Positioning System
IAA	Iterative Adaptive Approach

JADE	Joint Angle and Delay Estimation
JADE-FSF-DOAMatrix	Joint Angle and Delay Estimation based on Spatial and Frequential Smoothing DOAMatrix
JADE-SS-DOAMatrix	Joint Angle and Delay Estimation based on Spatial Smoothing DOAMatrix
JAODE-MSBL	Joint off-grid Angle and On-grid Delay Estimation based on MSBL
JAPDE-MSBL	Joint off-grid Angle, Polarization, and time Delay Estimation based on MSBL
JOADE-MSBL	Joint On-grid Angle and off-grid Delay Estimation based on MSBL
JOAODE-MSBL&SAGE	Joint On-grid Angle and On-grid Delay Estimation based on MSBL and SAGE
LHCP	Left-Hand Circular Polarization
LOS(S)	Line-Of-Sight (Signal)
MEDLL	Multipath Estimating Delay Locked Loop
ML	Maximum Likelihood
(M)SBL	(Multiple) Sparse Bayesian Learning
MUSIC	MUltiple SIgnal Classification
NCO	Numerically Controlled Oscillator
PDF	Probability Density Function
PLL	carrier Phase Locked Loop
PSD	Power Spectrum Density
RFFE	Radio Frequency Front-End
RHCP	Right-Hand Circular Polarization
SAGE	Space Alternating Generalized Expectation-Maximization
SAGELL	SAGE based Locked Loop
SMR	Signal-to-Multipath Ratio
SS	Spatial Smoothing
UDP	User Datagram Protocol
ULA	Uniform Linear Antenna

Contents

Preface i

Abstract ii

Glossary v

Contents viii

1 Introduction 1

1.1 Research Background 1

1.2 Review of GNSS Multipath Mitigation 3

1.2.1 GNSS Single-dimensional or Multi-dimensional Multipath Mitigation . . 3

1.2.2 GNSS Traditional or Sparse Representation Multipath Mitigation 7

1.3 Objectives and Organization of the Thesis 10

1.4 Novelty and Author Contributions 13

2 GNSS Signal Model and Multipath Mitigation Foundation 16

2.1 Introduction 16

2.2 GNSS Signal Model 17

2.2.1 Generalized GNSS Signal Model 17

2.2.2 Sparse GNSS Signal Model 22

2.3 Analysis of Channel Characteristics in Multipath Environments 26

2.3.1 Analysis of Spatial and Temporal Characteristics in Multipath Environments 26

2.3.2 Analysis of Polarization Characteristics in Multipath Environments . . . 29

2.3.3 Analysis of Frequential Characteristics in Multipath Environments 31

2.4 Introduction to Classical Multipath Mitigation 32

2.4.1 Introduction to Maximization Likelihood Methods 32

2.4.2 Introduction to Subspace-based Methods 33

2.4.3 Introduction to Sparse Representation Methods 35

2.4.4 Merits and Flaws 38

2.5 Conclusions . . . 39

3 Joint Spatial and Temporal GNSS Multipath Mitigation 41

3.1 Introduction . . . 41
3.2 Feasibility Analysis of GNSS Joint Spatial and Temporal Multipath Mitigation . 42
3.3 Joint Spatial and Temporal Multipath Mitigation based on Subspace Method . . . 44
3.3.1 Coherent Incidence Effects on Signal Subspace . . . 44
3.3.2 Joint Spatial and Frequential Smoothing . . . 45
3.3.3 Joint Spatial and Temporal Estimation based on Subspace Method . . . 48
3.4 Joint Spatial and Temporal Multipath Mitigation based on off-grid MSBL . . . 49
3.4.1 Joint On-grid Angle and Off-grid Delay Estimation based on MSBL . . . 50
3.4.2 Joint Off-grid Angle and On-grid Delay Estimation based on MSBL . . . 53
3.4.3 Joint Angle and Delay Estimation based on MSBL and SAGE . . . 54
3.5 Complexity and Convergence Analysis . . . 56
3.5.1 Complexity Analysis . . . 56
3.5.2 Convergence Analysis . . . 57
3.6 Simulation Results and Performance Analysis . . . 60
3.6.1 RMSEs as a Function of C/N_0 . . . 60
3.6.2 RMSEs as a Function of Angle Difference or Delay Difference . . . 65
3.7 Conclusions . . . 66
3.8 Derivation of (3.32) . . . 67

4 Joint Spatial, Polarization, and Temporal GNSS Multipath Mitigation 69

4.1 Introduction . . . 69
4.2 Feasibility Analysis of GNSS Joint Spatial, Polarization, and Temporal Multipath Mitigation . . . 70
4.3 Joint Spatial, Polarization, and Temporal Multipath Mitigation based on MSBL . 71
4.3.1 Joint On-grid Angle, Polarization and Delay Estimation based on MSBL 71
4.3.2 Joint Off-grid Angle and Delay Estimation based on MSBL . . . 74
4.4 CRLB Derivation and Convergence Analysis . . . 75
4.4.1 Derivation of CRLB with Dual-polarization Antenna . . . 75
4.4.2 Convergence Analysis . . . 75
4.5 Simulation Results and Performance Analysis . . . 78
4.5.1 Multi-dimensional Spectra . . . 79
4.5.2 RMSEs as a Function of Angle Difference . . . 80
4.5.3 RMSEs as a Function of Delay Difference . . . 81
4.5.4 RMSEs as a Function of the Number of Antenna Elements . . . 82

4.5.5 RMSEs as a function of DPG . . . 83
4.6 Conclusions . . . 83
4.7 Derivation of CRLB with Dual-polarization Antenna . . . 84

5 Joint Spatial and Frequential GNSS Multipath Mitigation 87
5.1 Introduction . . . 87
5.2 Feasibility Analysis of Joint Spatial and Frequential GNSS Multipath Mitigation 88
5.2.1 Brief Introduction to Meta-signal . . . 88
5.2.2 Characteristic Analysis of Meta-signal in Multipath Case . . . 90
5.2.3 Feasibility Analysis of Spatial and Frequential Multipath Mitigation . . . 90
5.3 GNSS Meta-signal SAGE-based Multipath-Mitigating Loop Design . . . 92
5.3.1 SAGE-based Estimator for Side-band Component . . . 92
5.3.2 SAGELL for Meta-signal . . . 93
5.4 Simulation Results and Performance Analysis . . . 97
5.4.1 MEEs via Multipath Delay . . . 98
5.4.2 RMSEs via C/N_0 . . . 99
5.5 Conclusions . . . 102

6 Multi-antenna GNSS Signal Collection Platform and Verification 103
6.1 Introduction . . . 103
6.2 Introduction to Multi-antenna GNSS Signal Collection Platform . . . 103
6.3 Introduction to GNSS Signal Collecting Environment . . . 106
6.4 Channel Calibration and Attitude Estimation . . . 107
6.4.1 Amplitude and Phase Calibration . . . 108
6.4.2 Attitude Estimation for Array . . . 108
6.5 Verifications . . . 111
6.5.1 Short Period Estimation Verification . . . 111
6.5.2 Tracking Performance Verification . . . 112
6.6 Conclusions . . . 114

7 Summary and Topics for Future Research 116
7.1 Summary . . . 116
7.2 Topics for Future Research . . . 118

8 References 121

Introduction

1.1 Research Background

Global Satellite Navigation System (GNSS) is a crucial component of modern navigation technology that employs unique signals transmitted by navigation satellites to provide real-time positioning information with high accuracy for ground, sea, air, and space users. GNSS has numerous advantages, including giving precise position, velocity, and time information for any location and at any time, and it is widely used in various civilian fields such as industrial production, wireless communication, autonomous driving, and precision agriculture, as well as in military areas such as aerospace and weapons equipment.

The GNSS acronym generally refers to diverse systems such as the Global Positioning System (GPS) of America, Galileo of Europe, the Global Navigation Satellite System (GLONASS) of Russia, Beidou of China, and their augmentation systems. In addition to the established navigation systems mentioned above, critical regional economic powers such as Japan, South Korea, and India are also dedicated to developing regional enhanced satellite positioning systems that focus on improving positioning accuracy in essential areas.

GNSS signals are weak and challenging to detect when they reach the ground due to the long distance, up to 20-30 thousand kilometers away from ground or airborne receivers, and their low transmission power of typically only a few tens of watts. For instance, the GPS L1 signal reaching the earth's surface has a signal power of approximately -160 dBw, about 20 dB lower than the noise level of the receiver [1]. This makes GNSS highly susceptible to various types of external interference, and effective anti-interference algorithms are needed to enhance their performance in complex electromagnetic environments. Among the different types of interference, multipath interference is the primary source of errors for GNSS. Multipath signals occur when GNSS signals reflect off objects surrounding the receiver antenna and arrive at the receiver, leading to significant degradation in tracking performance and large increases in positioning errors [2]. In traditional GNSS receivers, multipath interference can cause pseudo-range errors of several meters or even

hundreds of meters, which imposes strict requirements on system accuracy and reliability. Therefore, there is a need to improve the ability to mitigate multipath effects through signal processing. The formation of multipath signals depends on various factors, including the receiver's environment, motion state, and the directional characteristics of the receiving antenna. However, due to the differences among these factors, there currently needs to be a universal and accurate mathematical model for correcting multipath errors. Moreover, there is a high correlation between the reflected path and the direct path of the GNSS signal in time domain, making it challenging to use traditional techniques for multipath mitigation. Therefore, multipath mitigation remains a hot research topic in the field of GNSS receiver design [2–5].

Current technologies for mitigating multipath mainly involve receiver antenna design and signal processing. Antenna enhancement technologies include constructing a multipath environment diagram, employing specialized antenna types, and selecting suitable sites for antenna deployment [6–8]. Mitigating multipath signals can be achieved through two main signal processing approaches. The first approach leverages the inherent characteristics of GNSS signals to distinguish or suppress signals. The second approach focuses on principles that can identify and mitigate multipath signals. Identifying multipath based on inherent GNSS signal characteristics involves analyzing temporal, frequency, spatial, and polarization domain features. By observing different features in various domains or combining multiple domains, the receiver can differentiate between signals from different paths. Early GNSS receivers were mainly restricted to temporal processing methods due to antenna limitations, such as narrow correlation techniques [9] and delay-locked loop methods [10, 11]. With the development of multi-antenna technology, multi-antenna GNSS receivers have emerged, which utilize the spatial domain features of multipath signals for adaptive array signal processing [12–14]. Polarization processing is another method for mitigating multipath using the polarization characteristics of the signal [15–17]. As industries such as autonomous driving and precision agriculture continue to advance, the need for high-precision positioning of vehicles and equipment in various environments becomes increasingly urgent. Observations in time, space, and polarization alone may not meet the demands for high-precision positioning. Therefore, the bandwidth expansion brought by frequency domain processing has become a hot research topic [18–20], providing new hope for multipath mitigation. In addition to utilizing observations and combining different domains, the criteria on which different principles are based also have varying effects on mitigating multipath signals. There are three main classes of methods today: maximum likelihood-based (ML) algorithms [21–25], subspace-based algorithms [26, 27], and sparse representation algorithms [13, 28]. Each category has unique features, such as good performance, low complexity, or direct processing of correlation signals with fewer snapshots, and can meet the demands of different multipath scenarios.

In addition to the traditional observation of GNSS multipath signals in time domain, the characteristics of space, polarization, and frequency of the signals can improve the ability of multipath

mitigation to varying degrees. At the same time, the principles on which multipath mitigation are based also greatly affect the performance. Therefore, this thesis focuses on the analysis of GNSS signal and channel characteristics in multipath environments and explores how to combine multi-dimensional multipath-mitigating processing methods such as temporal, spatial, polarization, and frequency domains to obtain good multipath mitigation performances and provide robustness to multipath signals with different correlations.

1.2 Review of GNSS Multipath Mitigation

Significant research and development efforts have been devoted to mitigating the multipath effects. They may be classified according to a variety of criteria, e.g., single-dimensional versus multi-dimensional processing and traditional versus sparse representation methods, as it will be described in detail below.

1.2.1 GNSS Single-dimensional or Multi-dimensional Multipath Mitigation

Research on temporal domain multipath mitigation

Traditionally, multipath mitigation methods are applied in a single time domain, making the time delay difference between the line-of-sight (LOS) and multipath signals crucial in combating multipath. Typically, temporal domain receivers rely on the sharp and conventional auto-correlation function (ACF) to determine the time delay. However, due to the presence of multipath signals, the main lobe of the signal's ACF no longer takes the shape of a triangle, especially with noise, potentially leading to the discriminator of the receiver identifying a wrong estimate. With respect to single-antenna GNSS receiver, the narrow correlator delay locked loop (DLL) [9] and multipath estimating DLL (MEDLL) [10] are some of the most popular methods. The narrow correlator DLL searches only near the acquisition time delay to effectively suppress multipath signals, while MEDLL is based on the expectation-maximization (EM) principle and iteratively separates the multipath from the temporal domain. Both algorithms have been widely used in multipath mitigation for GNSS receivers. The former improves the settings of the discriminator, while the latter completely abandons the existing discriminator structure. Unfortunately, the narrow correlator DLL and MEDLL come with limited multipath discrimination capabilities, as only the signal feature from the temporal domain is exploited.

Research on spatial domain multipath mitigation

Thanks to a significant leap forward in multi-antenna technology, the spatial domain provides additional degrees of freedom for direction-of-arrival (DOA) resolving multipath. In terms of multi-antenna technology, it mainly consists of multipath mitigation and multipath identification

(the former is referred to as parameterized beamforming). The data-independent delay-and-sum beamforming [29] is widely used but suffers from low-resolution and high sidelobes. Another commonly used beamforming algorithm is the standard Capon beamformer [12], which forms the optimal spatial filter that maximizes the output signal-to-noise ratio based on the real covariance matrix and steering vector under the mitigation of interference. However, its performance may be poor due to limited data. Reference [30] utilized the interference null space projection and the angle estimation results of input signals to perform multipath cancellation using the least-squares beamforming in the spatial domain. Subspace-based methods also belong to this kind, such as multiple signal classification (MUSIC) [26], estimating signal parameter via rotational invariance techniques (ESPRIT) [27], and DOA matrix algorithm (DOAMatrix) [31]. These methods are susceptible to the presence of multipath signals, and the existence of correlated sources can lead to a rank-deficiency covariance matrix. In general, spatial smoothing (SS) techniques [32] are used to alleviate the rank deficiency issue. The rapid growth of sparse representation can also be applied to beamforming. The prominent methods in this field mainly rely on convex optimization, such as orthogonal matching pursuit [33], ℓ_1-singular value matrix decomposition [34], sparse Bayesian learning (SBL) [13], multi-snapshot SBL (MSBL) [35], and iterative adaptive approach (IAA) [14]. MSBL uses the Bayesian criterion and the EM algorithm to eliminate and identify multipath signals. IAA iteratively updates the spatial power estimate and weight vector based on the weighted least squares method. They can handle signals received with low carrier-to-noise ratio in few snapshots. These sparse representation algorithms model signals directly in the signal domain, so they do not suffer from rank-deficiency issues caused by coherent sources like the subspace-based methods.

Research on polarization domain multipath mitigation

Multipath mitigation can also be performed based on the polarization domain. The fact that the GNSS transmits a right-hand circular polarization (RHCP) signal that partially turns into a left-hand circular polarization (LHCP) signal upon reflection [15, 16] supports the idea of polarization domain processing. Most GNSS antennas are designed to be sensitive to RHCP signals [17], which naturally rejects multipath. Standard receiving antennas only output RHCP signals while suppressing LHCP signals [36]. However, considering the output of LHCP signals can provide an additional approach to detect and suppress multipath. With the development of dual-polarization antennas (DPA), research on multipath mitigation in the polarization domain has further explored the potential advantages of RHCP and LHCP signals. Reference [37] attempted to estimate the parameters of LOS and multipath signals separately using independent correlation processing of RHCP and LHCP signals for reconstruction and interference cancellation methods for multipath mitigation. Reference [38] jointly considered RHCP and LHCP signals and estimated the time delay parameters of the LOS signal based on the ML principle.

Research on frequential domain multipath mitigation

The narrow bandwidth, in general, can only cope with the multipath mitigation under a large time delay difference between the LOS signal and the multipath signals and is therefore restricted to the meter-level ranging accuracy. To handle the multipath mitigation of GNSS that has highly correlated signals, a direct but efficient solution is to break the bandwidth limitation of narrow-band signal (The large bandwidth signal allows the narrower main peak of ACF, hence a better temporal resolution). Therefore, meta-signal, a paradigm of multi-signal combination based on two different GNSS signals transmitted at different carrier frequencies, has recently received significant academic interest. It is expected that the typical meta-signal reaches bandwidths of tens or hundreds of megahertz and hence can fundamentally support a superior tracking accuracy and promising multipath mitigation [39].

Several approaches and estimators are available to perform time delay estimation for meta-signals, categorized into direct meta-signal processing and double side-band (DSB) processing. The former involves considering the meta-signal as a whole using a meta-signal local replica at the receiver, thus following the matched filter principle [40]. The researchers in [41–43] directly adopt an ML-based solution to the whole meta-signal and analyze the corresponding CRLBs. Since the spectra of the constituent side-band signals may result in a large bandwidth, the sampling rate can even reach hundreds of megahertz, which seriously aggravates the complexity burden [44]. In order to reduce the complexity, the matched filter can be equivalently implemented by splitting it into two different matched filters in DSB processing, one corresponding to each side-band signal, which are then coherently combined. This approach was adopted, for instance, in the pioneering work [20] via two ML-based estimators, laying a solid foundation for DSB processing of the meta-signal. Later on, the classical double estimator technique was proposed for binary offset carrier (BOC) signals in [45], with extensions to combat the multipath in [46, 47]. Due to the similar frequency separation characteristic to meta-signal, this method was ingeniously applied to meta-signal processing in [47–49]. As a consequence of the double loops for code and subcarrier, ambiguities are diminished to some extent. Although the existing meta-signal processing methods have decimeter- or centimeter-level ranging accuracy, all these discussions were carried out under the ideal precondition of single signal. While for the meta-signal paradigm in a more practical multipath condition, several relevant investigations, including the detailed working mechanism and the fundamental capability in terms of multipath mitigation, have yet to be explored.

To improve multipath mitigation performance, multi-dimensional processing techniques, such as spatial, temporal, polarization, and frequential domains, have been widely explored. Current research has focused on joint spatial and temporal processing, joint spatial and polarization processing, and joint spatial and frequential processing, which will be discussed in detail in the following sections.

Research on joint spatial and temporal domains multipath mitigation

Founded on the establishment of joint angle and delay estimation (JADE) structure, the reference [50] was the first to estimate angle and delay by observing both spatial and temporal channel characteristics. One of the advantages of JADE over cascaded spatial and temporal processing is its ability to fully integrate available space and time information, which in turn enhances multipath mitigation capability and increases the number of estimable signals. References [50] and [51] proposed JADE-MUSIC or JADE-ESPRIT for joint estimation of angle and delay, which laid the foundation for joint spatial and temporal processing. Reference [52] extended the DOAMatrix algorithm, initially developed for a dual parallel-line array, to estimate the angle and delay in both spatial and temporal domains. Reference [53] introduced joint spatial and temporal processing for code division multiple access (CDMA) systems, which entirely takes advantage of CDMA and smart antenna technology, effectively suppresses multi-access interference, and increases system capacity. The code spreading of CDMA is similar to that of GNSS signals, which also inspired us to introduce and verify the effectiveness of joint spatial and temporal processing. Although the above algorithms [50–53] are universal and have motivated our thinking, they lack detailed discussion on the unique features of GNSS signals and the improvement of tracking accuracy, which limits their practicality in GNSS.

References [54, 55] proposed a combined approach that integrates subspace-based spatial and temporal multipath mitigation with GNSS tracking loops. This approach aims to mitigate the bias in time delay estimation caused by code phase drift during long-period accumulation and achieve a good balance between computational complexity and performance. However, subspace-based algorithms exhibit sub-optimal performance under scenarios with few snapshots, fractional Doppler frequency offsets (DFOs), and high spatial and temporal correlations. Reference [22] proposed the space alternating generalized expectation-maximization (SAGE) algorithm, which employs parallel interference cancellation and EM algorithm iterations to transform the multi-dimensional searching problem into multiple one-dimensional optimization problems, achieving the CRLB in multipath environments. Subsequently, Professor Antreich et al. applied SAGE to address multipath issues in GNSS receivers, providing reasonable spatial and temporal parameter estimates. Furthermore, reference [25] combined SAGE with the principle of extended invariance to simultaneously suppress interference and multipath signals within uncalibrated antenna arrays. Similarly, the reference [24] proposed a spatial and temporal WRELAXation parameter estimation based on nonlinear least squares criteria for GNSS multipath mitigation, transforming the two-dimensional linear optimization problem into a series of one-dimensional optimizations. However, ML search-type algorithms have complex complexity, and the SAGE algorithm [22] is highly sensitive to initial values, requiring accurate initial values to ensure tracking accuracy in practice.

Research on joint spatial and polarization domains multipath mitigation

In view of the high spatial and temporal correlations of multipath signals, joint space and polarization processing is another promising solution, which is generally fulfilled by deploying an array of polarized antennas. By exploiting the polarization diversity in addition to the spatial diversity, the reference [56] used LHCP signals to estimate the DOA of multipath and suppressed the multipath component in RHCP signals based on null-steering techniques. In the presence of radio frequency interference, the reference [57] proposed the use of dual-polarized null-steering techniques to combat interference. The results of reference [58] showed that joint estimation in the spatial and polarization domains could significantly improve the estimation performance of DOA under RF interference conditions. Further considering the urgent need for the accurate time delay of LOSS in practical GNSS applications, various beamformers based on angle and polarization estimates of multipath signals, such as spatial null-steering [59], and joint spatial and polarization linear constraint minimum variance [60] or Capon beamformers [61], have been ingeniously designed to mitigate the multipath signals. While joint spatial and polarization processing offers increased degrees of freedom for identifying highly spatially correlated signals, it does not fully consider temporal separations, limiting its ability to enhance robustness. Additionally, this processing is constrained by the antenna size and may need to improve in rich multipath environments.

Research on joint spatial and frequential domains multipath mitigation

The multi-antenna technique can provide considerable spatial degrees of freedom. If they can be processed with large bandwidth signals such as meta-signal, specific spatial processing capacity can be improved. At present, only a few researchers have introduced multi-antenna technology into the field of meta-GNSS signal processing. In [62], multi-antenna is used to receive meta-signals in the environment of LOS signal only. By simulation, the multi-antenna is aligned with the direction of the received LOS signal so as to improve the receiving gain of meta-GNSS signals. However, the above literature does not discuss the improvement advantages of joint spatial and frequential domain processing for multipath mitigation. This field is still blank and needs to be explored urgently.

1.2.2 GNSS Traditional or Sparse Representation Multipath Mitigation

The previous section discussed the advantages and shortcomings of one-dimensional and multi-dimensional processing for mitigating multipath signals, both of which rely on the physical characteristics of GNSS signals. However, different methods for multipath mitigation are based on various criteria, resulting in differing abilities. In the subsequent sections, we will delve into the current research status of traditional methods and emerging sparse representation multipath-mitigating methods, which enable us to gain insights and perspectives for developing effective

multipath mitigation methods.

Research on traditional multipath mitigation

Traditional multipath mitigation methods, including ML-based and subspace-based methods, have been extensively studied. The ML-based methods [22–25, 63] fully exploit the statistical properties of the signals and generally require a simultaneous search over all unknown parameters. Therefore, their performances are achieved at the expense of an increased complexity [21]. Stemming from the ML method, the SAGE algorithm [22, 23] was proposed for the classical multipath estimation problem. It is a sequential approximation of the ML-based estimator, which can attain a higher accuracy close to the Cramér-Rao lower bound (CRLB) and with improvements regarding the trade-off between convergence rate and complexity. In addition to the successful application of parameter estimation in mobile radio environments, it has been shown that SAGE is also a promising candidate to combat multipath for GNSS due to its multi-dimensional processing. However, the SAGE requires a high computational complexity and is sensitive to initial values, which can result in erroneous estimates due to local extrema. To simplify the received signal in GNSS multipath environments, reference [63] represented it as a set of LOS signals and all other interference. Using the ML principle, they derived a novel estimator for the code and carrier phase that utilized the DOA of the LOS signal. This estimator is much simpler than other estimators derived under more detailed signal models and forms the basis for effectively handling multipath and interference using the extended invariance principle, as demonstrated in reference [25].

Subspace-based methods represent the other class of signal processing for multipath mitigation. These methods can decompose the signal into signal and noise subspaces, striking a favorable balance between multipath separation and computational complexity. Examples of subspace-based methods include the MUSIC algorithm [26, 64], the ESPRIT algorithm [27], and the DOAMatrix algorithm [31]. Although they are generally suboptimal compared to ML-based algorithms, subspace-based methods are less computationally intensive and widely used for signal parameter estimation. To tackle the limitations of the covariance matrix within coherent signals, forward-backward averaging and SS methods have been proposed [32]. In GNSS receivers, researchers have applied the combination of spatial and temporal subspace-based methods and SS methods for multipath mitigation [54, 65]. While subspace-based methods are computationally efficient and do not require iterative searches, their ability to provide reliable parameter estimates in highly correlated multipath environments warrants further investigation.

Research on sparse representation multipath mitigation

Besides the traditional methods above, sparse representation, an alternative obtained by formulating the problem using sparsity, has attracted noticeable interest. The estimation problem

recasts a sparse linear problem in the sparse representation by defining an over-complete matrix of steering vectors evaluated over a certain domain. The prerequisite is that the received signal should show sparsity in its corresponding spatial or other domains. This means the signal only appears at a few values in the corresponding domain while the other values remain zero. The application of sparse representation in GNSS has been centered on angle estimation: see, for example, the basis pursuit method [33], the orthogonal basis pursuit method [66], ℓ_1-singular value decomposition obeying minimization optimization [28], iterative methods such as focal under-determined system solution (FOCUSS) [67], IAA based on weighted least squares [14], and MSBL following the Bayesian method together with EM method [13]. Sparse representation methods possess a natural capability to handle multipath scenarios, as they perform linear reconstruction of the signal without incorporating its covariance matrix.

The distinction between sparse representation and traditional methods lies in the fact that the former is based on the sparsity of a particular domain (such as spatial sparsity). Sparse representation estimates the angle of a signal by using a reconstructed sparse dictionary. This method maintains a spatial sparsity that remains unchanged, regardless of signal correlations. The resolution of sparse representation depends on the separation between the two spectral peaks formed in the spatial spectrum. If the vectors in the dictionary are sparse enough, i.e., the amplitudes outside of the true angle are close to zero, even if two signals are correlated in the spatial domain, theoretically, the super-resolution can be achieved by reducing the spatial discretization interval. However, the subspace-based methods rely on the covariance matrix for subspace decomposition and utilize the orthogonality between the noise subspace and signal subspace to estimate signals. If the signals are correlated, the covariance matrix will become rank-deficient, and the correlation between signals will weaken the orthogonality between the noise subspace and signal subspace. The array aperture influences the resolution of subspace methods, and their resolution remains fixed.

Compared with other sparse representation methods, SBL-type algorithms are based on probabilistic modeling. They do not require any user parameters, including regularization parameters and signal sparsity. This allows SBL to maintain multipath-mitigating capability even with few snapshots in severe multipath environments [68]. These methods are built upon the framework of SBL, which first proposes a prior hypothesis for the sparse vector based on the probability model. A cost function containing the sparse vector is then derived to optimize the posterior information of the sparse vector. The critical factor of this method lies in the incorporation of empirical priors, which depend on a set of hyperparameters. Importantly, these hyperparameters must be estimated through observing data. One attraction of SBL is that, different from the ℓ_1 minimization-based algorithms mentioned above, whose global minimum is generally not the sparsest solution [69, 70], the global minima of SBL are always the sparsest one. Also, SBL has much fewer local minima than some classic algorithms, such as the FOCUSS family [67, 71]. All these advantages make SBL excel in multipath mitigation with few snapshots and the presence of severe multipath signals

[68]. In addition, the sparse representation performance can be improved by the dense sampling grids. However, the complexity and the mutual coherence between the steering vectors in the over-complete matrix are increased [72]. Considering the requirement of low complexity and the reduction of off-grid effects * [73], the off-grid SBL estimators are proposed and have been tested effectively [74]. This method provides a solid foundation for the subsequent application of MSBL in GNSS receivers.

From the summary of various multipath mitigation methods, it is clear that relying solely on signal characteristics from a single domain in GNSS is not robust enough to handle different types of multipath signals. Therefore, combining different domains, such as joint spatial and temporal domains, joint spatial, polarization, and temporal domains, or joint spatial and frequency domains, can provide more effective ways to combat multipath. Additionally, algorithms that are better suited for GNSS multipath mitigation should be developed to meet the requirements of different GNSS receivers to achieve accurate estimation. This thesis will primarily focus on combining multi-dimensional methods with multipath mitigation to achieve high-precision LOS time delay estimation in multipath environments.

1.3 Objectives and Organization of the Thesis

The thesis consists of seven chapters, and this chapter is the introduction. The rest of the thesis is organized as follows:

Chapter 2 analyzes the signal model and characteristics of GNSS channels from both a motivation and systems perspective. To explore the idea of multi-dimensional processing, a generalized GNSS multi-dimensional multipath signal model is further refined and derived to guide subsequent discussions. Accordingly, we also propose a generalized off-grid sparse GNSS multi-dimensional signal model. The subsequent discussions at the motivation level are all based on this generalized multi-dimensional signal model and its off-grid sparse model. Three types of joint GNSS spatial and temporal signal models and their off-grid sparse models, joint GNSS spatial, polarization, and temporal signal model and its off-grid sparse model, and joint GNSS spatial and frequential signal model needed in the subsequent chapters are further refined. Chapter 2 explores various channel characteristics of GNSS in spatial, temporal, polarization, and frequency domains, providing attention and guidance for subsequent multipath mitigation methods that jointly consider multiple dimensions of GNSS. It is noted that there are sparsity characteristics in both space and time, which provide relevant theoretical foundations for the sparse representation applied in the following chapters. Additionally, Chapter 2 introduces three effective multipath-mitigating methods: ML-, subspace-, and sparse representation-based methods. The following chapters analyze

*Off-grid effects refer to the phenomenon that the true estimates are not on the discretized sampling grid yielding the on-grid operation a critical factor in intrinsically introducing a residual bias.

Their advantages and disadvantages to provide targeted multipath-mitigating measures for different scenarios.

Chapter 3 begins by comparing the joint spatial and temporal processing structure with a general GNSS receiver to explore the feasibility of this structure in GNSS multipath environments. Using the concept of two-dimensional processing in space and time and the short-time quasi-static characteristics of the signal, the chapter proposes two joint GNSS spatial and temporal multipath mitigation algorithms based on subspace and off-grid MSBL. The subspace-based GNSS spatial and temporal multipath mitigation maintains a perfect balance between effective multipath mitigation and low complexity. For the purpose of multipath identification and suppression improvement in situations with high spatial correlation, the chapter explores the Vandermonde structure of GNSS signals in space and frequency, and then applies spatial and frequential smoothing to alleviate the rank-deficiency effect of the covariance matrix. To fully exploit the sparsity in both space and time, we propose utilizing the MSBL method along with the joint angle and delay estimation technique in GNSS multipath environments. Additionally, we extend the techniques to include the fractional Doppler frequency offset estimation in addition to angle and delay. To counteract the inherent drawbacks of sparse representations, we propose two different algorithms based on on-grid and off-grid estimators to reduce complexity or enhance resolution, thus allowing the proposed multipath mitigation approach to be adapted to various GNSS practical situations. Furthermore, we obtain a third algorithm with an improved resolution by applying the SAGE algorithm to refine the MSBL-based joint angle and delay estimates. Simulation results indicate that the three proposed MSBL-based algorithms can effectively resolve GNSS multipath signals and perform better than existing methods, even in severe situations such as those with signals with low carrier-to-noise ratio and spatially and temporally correlated multipath.

Chapter 4 analyzes the advantages and limitations of using only the spatial and temporal dimensions to mitigate multipath in Chapter 3. It is clear that in some scenarios with abundant multipath signals, especially when either the space or time domain is highly correlated, relying solely on joint spatial and temporal processing for multipath mitigation is insufficient. Therefore, this chapter combines the diversity characteristics of the polarization domain and deploys a DPA to distinguish between the LOS and multipath signals in the polarization domain. Furthermore, considering the advantages of joint spatial and temporal waveform features, this chapter investigates multipath-mitigating methods using a joint spatial-polarization-temporal structure to achieve better multipath mitigation capability in highly correlated environments. This chapter also considers the MSBL algorithm, which has the ability to find global extremum, and extends the joint spatial and temporal MSBL algorithm proposed in Chapter 3 to the joint spatial, polarization, and temporal MSBL-based one. The relative theoretical lower bound received by DPA is derived in a closed-form expression of CRLB for the time delay. The chapter also conducts simulations and compares the proposed joint spatial, polarization, and temporal MSBL algorithm with other algo-

rithms, such as joint spatial and temporal processing and pure spatial processing, under different multipath environments.

Chapter 5 further discusses the development of GNSS multipath mitigation for high-precision applications. Generally, GNSS signals are limited by the narrow bandwidth of the signal and can only cope with situations where there is a significant delay between the LOS signal and multipath signals, which limits the ranging accuracy to the meter level. To improve the resolution capability in a multipath environment, this chapter combines two GNSS signals transmitted on different carrier frequencies, whose bandwidth is much larger than that of a conventional GNSS signal, to achieve sub-decimeter or even centimeter-level estimation accuracy while promoting multipath mitigation capabilities. Based on the concept of meta-GNSS signals, this chapter first explores the characteristics of this signal in a multipath environment and synergistically employs the spatial degrees of freedom brought by multi-antenna technology and the temporal domain advantages of meta-GNSS signals, as discussed in earlier chapters. Furthermore, this chapter proposes the concept of joint spatial and frequency processing, designs a meta-GNSS signal tracking loop based on multi-dimensional processing using the SAGE algorithm, and aims to solve the problem of mitigating highly correlated multipath signals in both space and time domains, providing higher estimation accuracy to meet the high-precision requirements of different GNSS applications. Finally, this chapter validates the effectiveness of the proposed meta-GNSS signal tracking loop design under different multipath environments.

Chapter 6 implemented the collection of real satellite signals using an existing multi-antenna GNSS data collection platform. By implementing a series of amplitude and phase calibration and array attitude estimation methods on the collected multi-antenna GNSS signals, this chapter validated the joint spatial and frequential smoothing subspace-based algorithm and the joint spatial and temporal off-grid MSBL algorithm proposed in Chapter 3, respectively. The comparison focused on their ability to use spatial and temporal spectra as discriminators in short integration time and their code phase tracking performances when embedded in a tracking loop.

Chapter 7 provides a summary and outlook of the entire thesis. This chapter concludes the work presented in this thesis, discusses the potential for extension of the proposed methods in complex electromagnetic environments, and further optimization of off-grid sparse representation. Future research directions are also discussed, such as applying the proposed plans to anti-spoofing interference and localization of unmanned aerial vehicles.

To facilitate the understanding of the relationship between the proposed algorithms, the summary structure is displayed in Figure 1.1 (see the following chapters for abbreviations).

Notations: Matrices are denoted by capital letters in boldface (e.g.,$\boldsymbol{A}$), and vectors are denoted by lowercase letters in boldface (e.g.,$\boldsymbol{a}$). $\mathbb{C}^{M\times N}$ denotes the set of $M\times N$ matrices with the entries being complex numbers. $I_N \in \mathbb{C}^{N\times N}$ denotes an identity matrix. $E\{\cdot\}$ denotes the expectation operation. $\mathcal{CN}(\mu, \boldsymbol{\Sigma})$ denotes the complex Gaussian distribution with the mean being $\boldsymbol{\mu}$ and the

variance matrix being $\mathbf{\Sigma}$. $\|\cdot\|_F^2$, $\|\cdot\|_2^2$, $\diamondsuit$, $\otimes$, $\odot$, $\mathrm{tr}\{\cdot\}$, $vec\{\cdot\}$, $\mathrm{diag}\{\cdot\}$, $(\cdot)^{-1}$, $(\cdot)^T$, $(\cdot)^H$ denote the Frobenius norm, the ℓ_2-norm, the Khatri-Rao product, the Kronecker product, the Hadamard product, the trace of a matrix, the vectorization of a matrix, the diagonalization of a matrix, the inversion, the matrix transpose and the Hermitian transpose, respectively.

1.4 Novelty and Author Contributions

In this section we describe the novel contributions provided in this thesis along with the main author's contributions:

1. Based on the short-time quasi-static characteristics of GNSS transmitted signals, the classical cascaded space-time receiver is abandoned in favor of a generalized multi-dimensional GNSS multipath-mitigating reception model that fully exploits the characteristics of GNSS signals in spatial, temporal, polarization, and frequency domains. The author has also published the contributions related to this point in [65, 75].

2. Spatial and temporal GNSS multipath mitigation. The thesis proposes two methods for spatial and temporal GNSS multipath mitigation. The first method utilizes subspace-based techniques to analyze the phase relationship between GNSS signals and establish a structure based on space-time rotation invariance, effectively improving real-time performance and pseudo-range estimation. The second method combines MSBL with joint angle and delay estimation and addresses the limitations of sparse representations using on-grid and off-grid estimators. Simulation results demonstrate the effectiveness of both methods in dealing with multipath signals with low complexity and high correlation. Four papers [65, 75–77] have been published on this theme by the author. Papers [65, 76] mainly focus on joint angle and time delay estimation based on subspace methods, while papers [75, 77] focus on joint angle and time delay estimation based on MSBL methods.

3. Spatial, polarization, and temporal GNSS multipath mitigation. A severe multipath environment hampers tracking, but the thesis proposes an MSBL-based method for parameter estimation in the presence of spatial and temporal correlation. It establishes and solves a joint GNSS signal model using multi-dimensional processing, such as spatial, polarization, and temporal domains. The method shows robustness and outperforms other approaches in combating multipath, especially in highly correlated signals. Contribution related to this topic has been submitted to the journal and is under review.

4. Spatial and frequential GNSS multipath mitigation. Wide-bandwidth signals and multi-antenna technology are crucial for GNSS multipath mitigation. We propose a meta-signal SAGELL design that utilizes meta-signals and multi-dimensional processing to estimate time delays in

multipath environments. The design includes a SAGE-based discriminator and combinational loops to accurately track each signal. Our approach enables high-precision discrimination and tracking in multipath scenarios, even with highly correlated signals. Contributions related to this point are addressed in [78].

5. In addition, we build up a multi-antenna GNSS data collection platform and verify the proposed joint angle and time delay estimation methods in the thesis using collecting signals.

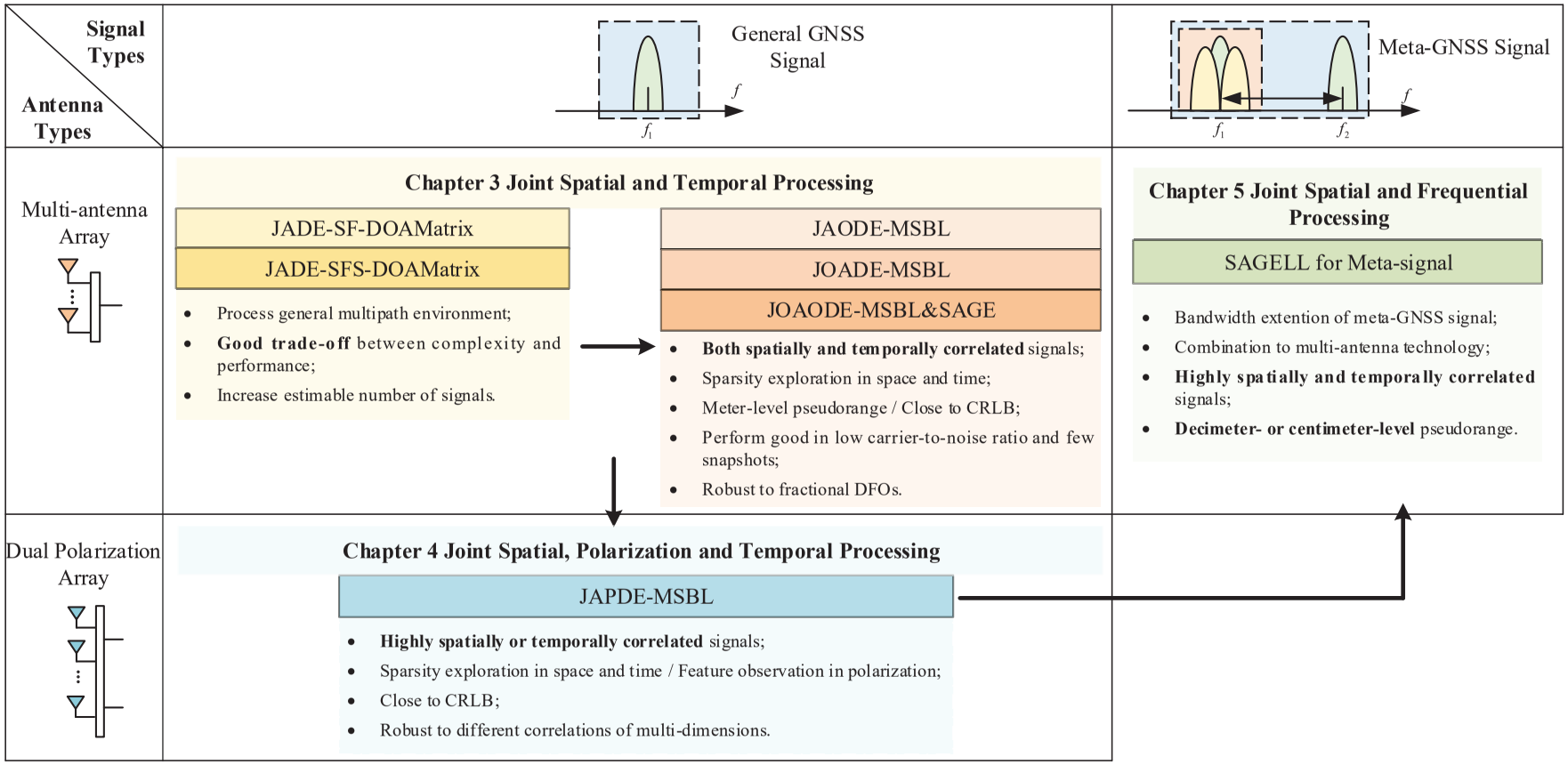


Figure 1.1: Overview of the relationships between the algorithms proposed in the thesis

GNSS Signal Model and Multipath Mitigation Foundation

2.1 Introduction

The characteristics of GNSS signals in multipath environments can be analyzed from two perspectives: Firstly, the LOS and multipath signals exhibit distinct properties in spatial, temporal, polarization, and frequency domains. Combining these multi-dimensional characteristics can improve the accuracy of multipath mitigation. Secondly, understanding the characteristics of GNSS signals transmitted through the channel is essential for making reasonable assumptions and appropriate selections in subsequent processing steps. These insights enable more effective and efficient processing of GNSS signals in challenging environments. Therefore, a comprehensive analysis of GNSS signals in multipath environments can enhance the performance of GNSS and improve user experience in various applications.

In this chapter, we first establish a generalized multi-dimensional GNSS signal model, from which we derive the simplified or evolved signal models required for the joint space and time (Chapter 3), joint space, time, and polarization (Chapter 4), and joint space and frequency (Chapter 5), respectively. Additionally, to apply sparse representation methods, this chapter also constructs the multi-dimensional sparse GNSS signal model and thus derives the joint space and time sparse model and joint space, time, and polarization sparse model. Furthermore, this chapter discusses the GNSS multipath channel characteristics in spatial, temporal, polarization, and frequential domains. These discussions are intended to guide the establishment of GNSS signal models and the use of multipath mitigation. Finally, a brief introduction and analysis of the advantages and disadvantages of typical methods, such as maximum likelihood, subspace decomposition, and sparse representation, are provided to guide the selection of algorithms for different GNSS receiver requirements.

2.2 GNSS Signal Model

This section utilizes the generalized GNSS signal model in a multipath environment to develop specific models based on antenna array types and signal characteristics. Specifically, we subdivide the generalized spatial and temporal signal model into three models: the joint spatial and temporal GNSS signal model, the joint spatial, polarization, and temporal GNSS signal model, and the joint spatial and frequential GNSS signal model. In addition, this section also presents the corresponding sparse signal models for these improved signal models, which serve as a foundation for applying sparse representation techniques in subsequent processing steps.

2.2.1 Generalized GNSS Signal Model

The signals received by a GNSS receiver can be divided into two types: LOS signals transmitted directly from satellites and multipath signals generated by reflections from nearby objects. These two signal types exhibit differences in multiple dimensions, enabling us to distinguish between them. In the temporal domain, the transmission paths of the LOS and multipath signals result in different delays, while the delay difference is relatively small compared to the long transmission distance from the satellite to the ground. In the spatial domain, the DOAs of the two signal types are distinct, which makes it possible to separate easily. In the polarization domain, the LHCP and RHCP signals show polarization differences that allow for further differentiation between the two signal types. These differences in the temporal, spatial, and polarization domains provide significant advantages for mitigating multipath effects on GNSS signals.

Consider the wavefield generated by one LOS signal and $K-1$ multipath signals arriving from DOAs $\boldsymbol{\theta} \doteq [\theta_1, \ldots, \theta_K]^T$ with corresponding time delays $\boldsymbol{\tau} \doteq [\tau_1, \ldots, \tau_K]^T$ and DFOs $\boldsymbol{f}_d \doteq [f_{d1}, \ldots, f_{dK}]^T$. Under the narrowband approximation, the vector $\boldsymbol{y}(t)$ at the output of an M_θ-element array for one specific satellite signal can be expressed as

$$\boldsymbol{y}(t) = \sum_{k=1}^{K} \gamma_k \boldsymbol{a}(\theta_k)\, c(t-\tau_k)\, e^{j(2\pi f_{dk} t + \phi_k)} + \boldsymbol{n}(t) \tag{2.1}$$

where $\boldsymbol{a}(\theta_k)$ is the steering vector and γ_k is the amplitude of the k th signal. The term $c(t-\tau_k)$ denotes the code waveform of the k th signal with delay τ_k, and its corresponding DFO is f_{dk} and the initial phase ϕ_k.

The Gaussian noise contribution $\boldsymbol{n}(t)$ are assumed spatially and temporally uncorrelated. Meanwhile, we assume that the number of signals K is already known, and some specific criteria can be applied to determine the number of signals, e.g., classical criteria [79, 80] and burgeoning techniques [81, 82]. Note that the DFO is mainly caused by the relative movement between the satellites and receiver, and it can be as large as nearly ± 10 KHz when the GPS signals are impinging the

antenna. However, the Doppler differences of the multipath components among themselves and the LOS are usually small and within several hertz, as verified in several practical measurements [83, 84]. Without loss of generality, we can reasonably assume that the LOS and multipath signals have similar DFOs, and most of the DFOs will be compensated in the acquisition stage. Thanks to the carrier phase-locked loop (PLL) in the tracking stage of the GNSS receiver, the residue DFOs and phases can also be accurately [85, 86]. Therefore, on the premise that the carrier phase of the received signal has been stably tracked, the signal model (2.1) can be expressed as

$$\boldsymbol{y}(t) \approx \sum_{k=1}^{K} \gamma_k \boldsymbol{a}(\theta_k)\, c(t-\tau_k) + \boldsymbol{n}(t) \tag{2.2}$$

Collecting L samples in each code period, the observed signal during the n th period can be expressed as

$$\dot{\boldsymbol{Y}}(n) \doteq [\boldsymbol{y}(((n-1)L+1)T_s), \ldots, \boldsymbol{y}(((n-1)L+L)T_s)] \tag{2.3}$$

where T_s is the sample interval and $l = 1, \ldots, L$, $n = 1, \ldots N$. Likewise, the sampled shifted waveform is

$$\boldsymbol{c}(\tau_k) \doteq [c(T_s - \tau_k), \ldots, c(LT_s - \tau_k)]^T \tag{2.4}$$

In this way, the signal of the n th code period in matrix format is denoted as

$$\dot{\boldsymbol{Y}}(n) = \boldsymbol{A}(\boldsymbol{\theta})\, \mathrm{diag}(\boldsymbol{\gamma})\, \boldsymbol{C}^T(\boldsymbol{\tau}) + \dot{\boldsymbol{N}}(n) \tag{2.5}$$

where the steering vector matrix denotes as $\boldsymbol{A}(\theta) \doteq [\boldsymbol{a}(\theta_1), \ldots, \boldsymbol{a}(\theta_K)]$, the complex amplitude vector $\boldsymbol{\gamma} \doteq [\gamma_1, \ldots, \gamma_K]^T$, and code waveform matrix $\boldsymbol{C}(\boldsymbol{\tau}) \doteq [\boldsymbol{c}(\tau_1), \ldots, \boldsymbol{c}(\tau_K)]$. $\dot{\boldsymbol{N}}(n)$ represents the set of Gaussian noise in n th code period.

It is commonly understood that GNSS signals employ spread spectrum modulation to provide spreading gain, enabling demodulation even when signal power is lower than noise. However, this modulation technique typically involves a large number of sampling points per code period, leading to increased computational complexity. To obtain the spreading gain and reduce the computational complexity, a transformation matrix to the codespace $\boldsymbol{B} \doteq [\boldsymbol{c}(\bar{\tau}_1), \ldots, \boldsymbol{c}(\bar{\tau}_{M_\tau})]^T$ can be applied on each code period. According to the information obtained from the acquisition phase, the set of the uniformly distributed delays $\bar{\boldsymbol{\tau}} \doteq [\bar{\tau}_1, \ldots, \bar{\tau}_{M_\tau}]$ is centered on the correlation peak and span both sides, and the number of codebeams satisfies $M_\tau \ll L$

$$\begin{aligned} \boldsymbol{Y}_b(n) &= \dot{\boldsymbol{Y}}(n)\, \boldsymbol{B}^H \\ &= \boldsymbol{A}(\boldsymbol{\theta})\, \mathrm{diag}(\boldsymbol{\gamma})\, \boldsymbol{R}^T(\bar{\boldsymbol{\tau}}, \boldsymbol{\tau}) + \dot{\boldsymbol{N}}_b(n) \end{aligned} \tag{2.6}$$

with the temporal matrix $\boldsymbol{R}(\bar{\boldsymbol{\tau}}, \boldsymbol{\tau}) \in \mathbb{C}^{M_\tau \times K}$, the element in the temporal matrix are defined as the conjugate between the waveform of delay set centered on the correlation peak and the waveform of true delay $r(\bar{\tau}_{m_\tau}, \tau_k) \doteq \boldsymbol{c}^H(\bar{\tau}_{m_\tau})\boldsymbol{c}(\tau_k)$ and $m_\tau = 1, \ldots, M_\tau, k = 1, \ldots, K$. $\dot{\boldsymbol{N}}_b(n)$ represents the noise matrix obeying Gaussian distribution.

To observe both the spatial and temporal domains so as to obtain the estimation of the angles and time delays simultaneously, the vectorization operator spreading in the column is carried out to the temporally filtered data, and we get

$$\begin{aligned} \boldsymbol{y}_b(n) &= vec\left(\dot{\boldsymbol{Y}}_b(n)\right) \\ &= \left(\boldsymbol{A}(\boldsymbol{\theta}) \otimes \boldsymbol{R}(\bar{\boldsymbol{\tau}}, \boldsymbol{\tau})\right)\boldsymbol{\gamma}_b + \boldsymbol{n}_b(n) \end{aligned} \tag{2.7}$$

where we define $\boldsymbol{\gamma}_b \doteq vec(\mathrm{diag}(\boldsymbol{\gamma}))$ and $\boldsymbol{n}_b(n) \doteq vec\left(\dot{\boldsymbol{N}}_b(n)\right)$. Equation (2.7) represents the fundamental expression of multi-dimensional processing. This thesis proposes three types of multi-dimensional processing structures: the joint spatial and temporal, the joint spatial, polarization, and temporal, and the joint spatial and frequential multipath-mitigating structure. When different antenna types or signal modes are adopted, such as uniform linear antenna (ULA), DPA, or meta-signal, formula (2.7) can be easily transformed into the specific signal model.

In the following subsections, we will specifically introduce the three signal models derived by (2.7): the spatial and temporal, the spatial, polarization, and temporal, and the spatial and frequential GNSS signal models.

Spatial and Temporal GNSS Signal Model

In multipath environments, the GNSS receiver is equipped with a M_θ-element ULA to provide the multipath mitigation in spatial domain, as shown in Figure 2.1. Based on the GNSS receiver

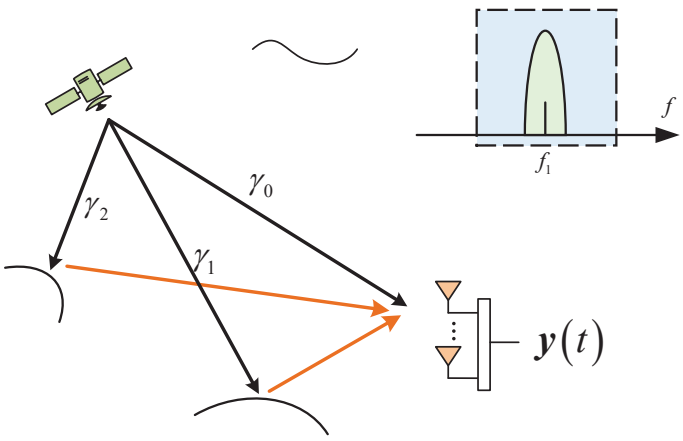


Figure 2.1: Diagram of GNSS multi-antenna receiver

with ULA, the spatial and temporal signal model established using a ULA is consistent with the

model (2.7). However, the steering vector $\boldsymbol{A}(\boldsymbol{\theta})$ in GNSS receiver with ULA can be concretized into

$$\boldsymbol{a}(\theta_k) = \left[1, e^{j\frac{2\pi d}{\lambda_{ant}}\sin(\theta_k)}, \ldots, e^{j\frac{2\pi d}{\lambda_{ant}}(M_\theta - 1)\sin(\theta_k)}\right]^T \tag{2.8}$$

where d and λ_{ant} respectively represents the element spacing and signal wavelength. The equations (2.7) and (2.8) are the foundations of signal model for joint spatial and temporal multipath mitigation in Chapter 3.

Spatial, Polarization, and Temporal GNSS Signal Model

When GNSS signals propagate through the air and reach the ground, multipath signals are generated by reflections from nearby objects. Current GNSSs typically employ RHCP transmit and receive antennas. However, the polarization of reflected signals can reverse for reflection angles greater than the Brewster angle, resulting in LHCP signals. In general, multipath signals exhibit elliptical polarization, a superposition of both RHCP and LHCP polarization. The powers of two polarization may differ due to differences in the reflecting object and its polarization properties. Equipping GNSS receivers with DPAs, as shown in Figure 2.2 makes it possible to discriminate between multipath signals in the polarization domain.

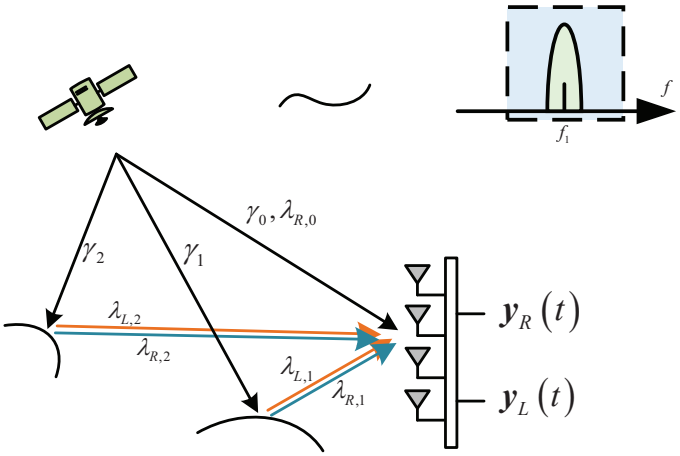


Figure 2.2: Diagram of GNSS multi-antenna receiver with DPA

In the case of M_θ-element DPA, the steering vector matrix $\boldsymbol{A}(\boldsymbol{\theta})$ in model (2.7) is denoted as

$$\boldsymbol{A}(\boldsymbol{\theta}) = [\boldsymbol{A}_M(\theta_1), \ldots, \boldsymbol{A}_{M,K}(\theta_K)] \tag{2.9}$$

and

$$\boldsymbol{A}(\boldsymbol{\theta}) = \begin{bmatrix} \boldsymbol{a}_{Rc}(\theta_k) & \boldsymbol{a}_{Rx}(\theta_k) \\ \boldsymbol{a}_{Lx}(\theta_k) & \boldsymbol{a}_{Lc}(\theta_k) \end{bmatrix} \tag{2.10}$$

where the steering vectors $\boldsymbol{a}_{Lc}(\theta_k), \boldsymbol{a}_{Rc}(\theta_k) \in \mathbb{C}^{M_\theta \times 1}$ represent the k th co-polar LHCP and

RHCP signal,respectively. Accordingly, the steering vectors $\boldsymbol{a}_{Lx}(\theta_k)$,$\boldsymbol{a}_{Rx}(\theta_k) \in \mathbb{C}^{M_\theta \times 1}$ represent the k th cross-talk from RHCP and LHCP waves to LHCP and RHCP antenna output, respectively.

In this way, the complex amplitude vector $\boldsymbol{\gamma}_b$ is no longer constituted by each signal's amplitude but replaced by the polarization coefficient vector $\boldsymbol{\lambda} = [\lambda_{R,1}, \lambda_{L,1}, \ldots, \lambda_{R,K}, \lambda_{L,K}]^T$ and amplitude vector $\boldsymbol{\gamma}$. Define the left and right polarization coefficient $\lambda_{L,k}$ and $\lambda_{R,k}$ of the k th signal as the complex amplitude of LHCP and RHCP signals, we have

$$\boldsymbol{\gamma}_b \doteq vec\left(\text{diag}\left(\boldsymbol{\lambda}\right)\boldsymbol{I}_d \text{diag}\left(\boldsymbol{\gamma}\right)\right) \tag{2.11}$$

with the transition matrix $\boldsymbol{I}_d \in \mathbb{C}^{2K \times K}$. It is a connection between the polarization coefficient vector and the amplitude vector, composed of zeros and K vectors $[1, 1]^T$ on the left diagonal. The equations (2.7), (2.9), (2.10), and (2.10) are the foundation for joint spatial, polarization, and temporal multipath mitigation in Chapter 4.

Spatial and Frequential GNSS Meta-signal Model

It is widely recognized that breaking the bandwidth limitation is a crucial approach to mitigating multipath signals in GNSS systems with highly correlated signals, increasing the signal bandwidth results in a narrower main peak of the ACF and improving temporal resolution and enhancing multipath mitigation, as illustrated in Figure 2.3. To achieve this, multi-frequency GNSS receivers are used to receive signals from the same satellite at two different frequencies. By exploiting the bandwidth difference between these two signals, along with spatial diversity, a GNSS multi-antenna multi-frequency receiver can be constructed. We can develop more effective techniques for mitigating multipath in GNSS signals by utilizing multi-antenna multi-frequency receiver architectures to increase signal bandwidth. These approaches enhance accuracy and reliability under challenging operating conditions, supporting a wide range of applications.

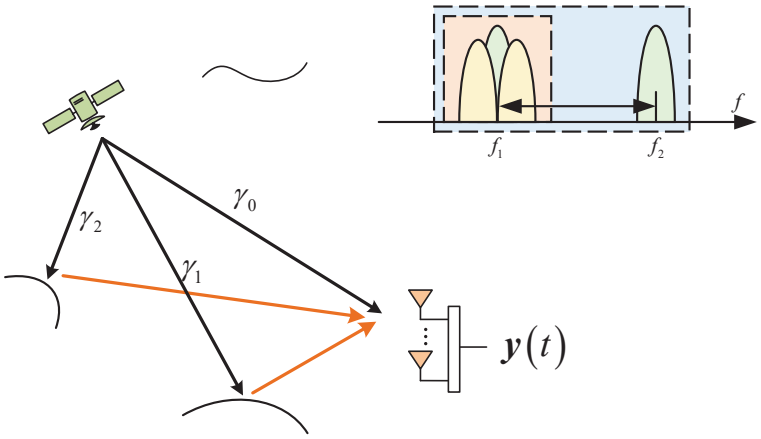


Figure 2.3: Diagram of GNSS multi-antenna multi-frequency receiver

A multi-antenna multi-frequency GNSS receiver receives a signal comprised of two signals of different frequencies transmitted by the same satellite simultaneously. This signal is referred to as a meta-GNSS signal. The two different frequency signals $\boldsymbol{y}^L(t)$ and $\boldsymbol{y}^R(t)$, taking the center position of the two signals as the center frequency, are $-f_s$ and $f_s$distance from the center frequency respectively. Referring to Equation (2.1), there is

$$\begin{aligned}\boldsymbol{y}(t) &= \boldsymbol{y}^L(t) + \boldsymbol{y}^R(t) \\ &= \sum_{k=1}^{K} \boldsymbol{a}^L(\theta_k)\gamma_k^L c^L(t-\tau_k)\, e^{-j2\pi f_s(t-\tau_k)} e^{j(2\pi f_{dk}t+\phi_k)} + \boldsymbol{n}^L(t) \\ &+ \sum_{k=1}^{K} \boldsymbol{a}^R(\theta_k)\gamma_k^R c^R(t-\tau_k)\, e^{j2\pi f_s(t-\tau_k)} e^{j(2\pi f_{dk}t+\phi_k)} + \boldsymbol{n}^R(t)\end{aligned} \tag{2.12}$$

where the superscripts L and R respectively represent the left and right components of the meta-GNSS signal, so the corresponding steering vectors, code waveforms, complex amplitudes, and noises are different. The subcarrier phases $-2\pi f_s\tau_k$ and $2\pi f_s\tau_k$ of the k th signal of each component is the key to obtaining high temporal resolution. For the ULA case, the steering vectors of the left and right components can be expressed as

$$\boldsymbol{a}^L(\theta_k) = \left[1, e^{j\frac{2\pi d}{\lambda_{ant}^L}\sin(\theta_k)}, \ldots, e^{j\frac{2\pi d}{\lambda_{ant}^L}(M_\theta-1)\sin(\theta_k)}\right]^T \tag{2.13a}$$

$$\boldsymbol{a}^R(\theta_k) = \left[1, e^{j\frac{2\pi d}{\lambda_{ant}^R}\sin(\theta_k)}, \ldots, e^{j\frac{2\pi d}{\lambda_{ant}^R}(M_\theta-1)\sin(\theta_k)}\right]^T \tag{2.13b}$$

The λ_{ant}^L and λ_{ant}^R corresponds to the left and right component's wavelengths. Equation (2.12) is the foundation for joint spatial and frequential multipath mitigation in Chapter 5.

2.2.2 Sparse GNSS Signal Model

The concept of sparse representation involves describing signals using optimization techniques combined with a minimal number of vectors from an overcomplete dictionary. To leverage the sparsity properties of spatial and temporal domains in GNSS signals, we extend the received signal $\boldsymbol{y}_b$ in Equation (2.7) into a sparse representation across both spatial and temporal domains [73, 74].

The spatially uniformly sampling grid points set is $\tilde{\boldsymbol{\theta}} \doteq \left[\tilde{\theta}_1, \ldots, \tilde{\theta}_{N_\theta}\right]$ with fixed angle interval r_θ. Similarly, the temporally uniformly fixed sampling grid points set is $\tilde{\boldsymbol{\tau}} \doteq [\tilde{\tau}_1, \ldots, \tilde{\tau}_{N_\tau}]$ with fixed delay interval r_τ and covering the range of $\bar{\boldsymbol{\tau}}$. T_c is defined as the duration of each code. Based on the above definitions, the on-grid over-complete basis matrix of the joint spatial and temporal processing can be obtained

$$\boldsymbol{\Phi} = \boldsymbol{A} \otimes \boldsymbol{C} \tag{2.14}$$

where $\boldsymbol{A}$ denotes the sparse spatial over-complete basis matrix with the definition $\boldsymbol{A}\left(\tilde{\boldsymbol{\theta}}\right) \doteq$

$\left[\boldsymbol{a}\left(\tilde{\theta}_1\right),\ldots,\boldsymbol{a}\left(\tilde{\theta}_K\right)\right]$. Likewise, $\boldsymbol{C}$ denotes the sparse temporal over-complete basis matrix with the element $c_\tau\left(\bar{\tau}_{m_\tau},\tilde{\tau}_{n_\tau}\right)$ defined as $c_\tau\left(\bar{\tau}_{m_\tau},\tilde{\tau}_{n_\tau}\right)=\boldsymbol{c}^H\left(\tilde{\tau}_{n_\tau}\right)\boldsymbol{c}\left(\bar{\tau}_{m_\tau}\right)$ with $m_\tau=1,\ldots,M_\tau$ and $n_\tau=1,\ldots,N_\tau$.

The traditional sparse representation method is proposed based on the sparse on-grid model. However, the on-grid sparse model (2.14) to the off-grid effects that most of the true parameters do not strictly fall onto the grid point [73]. The bias between the real value and the nearest grid tends to zero only as the number of the grid points tends to infinity and vice versa. Still, the number of grid points cannot be arbitrarily increased for computational cost. To significantly improve the angle estimation performance without dense sampling grids, the off-grid sparse model for angle estimation is proposed in [74, 87].

In this thesis, the off-grid sparse model is modeled in both spatial and temporal domains so that two kinds of off-grid over-complete basis matrices are assumed. The off-grid angle vector $\boldsymbol{\beta}_\theta\doteq[\beta_1,\ldots,\beta_{N_\theta}]^T$ contains the components $\beta_{n_\theta}=\theta_k-\tilde{\theta}_{n_\theta k}$, which are assumed to be uniformly distributed in the interval $\left[-\frac{1}{2}r_\theta,\frac{1}{2}r_\theta\right]$ with θ_k being the true angle value and $\tilde{\theta}_{n_\theta k}$ being the nearest grid point to the k th signal. Similarly, for off-grid delay vector $\boldsymbol{\beta}_\tau\doteq[\beta_1,\ldots,\beta_{N_\theta}]^T$, it is formed by $\beta_{n_\tau}=\tau_k-\tilde{\tau}_{n_\tau k}$, which are assumed to be uniformly distributed in the range $\left[-\frac{1}{2}r_\tau,\frac{1}{2}r_\tau\right]$, with τ_k being the true delay value and each $\tilde{\tau}_{n_\tau k}$ being the nearest point to the k th signal. Thus, we can construct an over-complete off-grid spatial and temporal matrix based on the first-order Taylor series expansion

$$\begin{aligned}\boldsymbol{\Phi}_\beta&=\boldsymbol{\Phi}_{\boldsymbol{\beta}_\theta}\otimes\boldsymbol{\Phi}_{\boldsymbol{\beta}_\tau}\\&=\left(\boldsymbol{A}+\boldsymbol{B}_\theta\text{diag}\left(\boldsymbol{\beta}_\theta\right)\right)\otimes\left(\boldsymbol{C}+\boldsymbol{B}_\tau\text{diag}\left(\boldsymbol{\beta}_\tau\right)\right)\end{aligned}\tag{2.15}$$

where $\boldsymbol{B}_\theta$ is the first order derivative of $\boldsymbol{A}$ with respect to $\tilde{\tau}_{n_\tau}$, which is composed of $b_\theta\left(m_\theta,\tilde{\theta}_{n_\theta}\right)$ with $b_\theta\left(m_\theta,\tilde{\theta}_{n_\theta}\right)=\frac{\partial a\left(m_\theta,\tilde{\theta}_{n_\theta}\right)}{\partial\tilde{\theta}_{n_\theta}}$ and $m_\theta=1,\ldots,M_\theta$ and $n_\theta=1,\ldots,N_\theta$. Similarly, $\boldsymbol{B}_\tau$ is the first order derivative of $\boldsymbol{C}$ with respect to $\tilde{\tau}_{n_\tau}$, which is composed of $b_\tau\left(\bar{\tau}_{m_\tau},\tilde{\tau}_{n_\tau}\right)\doteq\frac{\partial r\left(\bar{\tau}_{m_\tau},\tilde{\tau}_{n_\tau}\right)}{\partial\tilde{\tau}_{n_\tau}}$ and $m_\tau=1,\ldots,M_\tau$ and $n_\tau=1,\ldots,N_\tau$.

So far, the over-complete off-grid spatial and temporal matrix has been established. To further improve the performance, we extend the above single measurement vector to multiple, specifically N, measurement vectors as $\boldsymbol{Y}\doteq[\boldsymbol{y}_b(1),\ldots,\boldsymbol{y}_b(N)]$ and $\boldsymbol{N}\doteq[\boldsymbol{n}_b(1),\ldots,\boldsymbol{n}_b(N)]$. Then, the joint on-grid angle and on-grid delay estimation sparse model is given by

$$\boldsymbol{Y}=\boldsymbol{\Phi}_{\boldsymbol{\beta}}\boldsymbol{X}+\boldsymbol{N}\tag{2.16}$$

with complex source amplitudes matrix $\boldsymbol{X}\doteq[\boldsymbol{x}_b(1),\ldots,\boldsymbol{x}_b(N)]$ where $\boldsymbol{X}$ is row sparse since only a few entries of $\boldsymbol{X}$ are nonzero, and they tend to appear in the same positions in each column. Equation (2.16) is the basic spatial and temporal model for adopting sparse representation.

In the following two subsections, we will specifically introduce the sparse model concretely

introduced by the spatial and temporal sparse model (2.15): on-grid sparse spatial and temporal GNSS signal model, sparse on-grid spatial and off-grid temporal GNSS signal model, sparse off-grid spatial and on-grid temporal GNSS signal model, off-grid sparse spatial, polarization, and temporal GNSS signal model for Chapter 3 and 4.

Sparse Spatial and Temporal GNSS Signal Model

In real-world environments, it is essential to balance the complexity of GNSS receiver systems while meeting practical requirements. In addition to the on-grid sparse spatial and temporal GNSS signal model presented in Equation (2.14), two additional sparse models have been proposed to address different needs. The first model prioritizes the accuracy of delay estimation over angle estimation. This approach recognizes that delay accuracy directly impacts the precision of GNSS pseudo-range observable, making it critical for achieving accurate positioning results.

$$\begin{aligned} \boldsymbol{\Phi}_{\boldsymbol{\beta}} &= \boldsymbol{A} \otimes \boldsymbol{\Phi}_{\boldsymbol{\beta}_\tau} \\ &= \boldsymbol{A} \otimes \left(\boldsymbol{C} + \boldsymbol{B}_\tau \text{diag}\left(\boldsymbol{\beta}_\tau\right)\right) \end{aligned} \tag{2.17}$$

The second approach relies on the assumption that the accuracy of the angle estimates is prioritized because the angle is needed to create a beamformer that can mitigate spoofing or multipath.

$$\begin{aligned} \boldsymbol{\Phi}_{\beta} &= \boldsymbol{\Phi}_{\boldsymbol{\beta}_\theta} \otimes \boldsymbol{C} \\ &= \left(\boldsymbol{A} + \boldsymbol{B}_\theta \text{diag}\left(\boldsymbol{\beta}_\theta\right)\right) \otimes \boldsymbol{C} \end{aligned} \tag{2.18}$$

Sparse Spatial, Polarization, and Temporal GNSS Signal Model

In the combination of spatial, polarization, and temporal sparse representation, an on-grid sparse spatial, polarization, and temporal GNSS signal model is established according to (2.14) where the angle over-complete basis matrix $\boldsymbol{A} \in \mathbb{C}^{2M_\theta \times 2N_\theta}$ is denoted as a sparse spatial and polarization basis matrix $\boldsymbol{A}\left(\boldsymbol{\theta}\right) \doteq \left[\boldsymbol{A}_M\left(\tilde{\theta}_1\right), \ldots, \boldsymbol{A}_{M,K}\left(\tilde{\theta}_K\right)\right]$. Note that $\boldsymbol{\Phi} \in \mathbb{C}^{2M_\theta M_\tau \times 2N_\theta N_\tau}$ represents an on-grid sparse spatial, polarization, and temporal over-complete basis matrix. For better clarity, we present the specific diagram of $\boldsymbol{\Phi}$ in Figure 2.4. This joint sparse spatial, polarization, and temporal basis matrix is denoted by $\boldsymbol{\Phi} \in \mathbb{C}^{2M_\theta M_\tau \times 2N_\theta N_\tau}$ and is composed of N_τ blocks, such as b_1, each with a size of $2M_\theta M_\tau \times 2N_\theta$. Each block is formed by taking the Kronecker product of matrix $\boldsymbol{A}$ and the n_τ th column of matrix $\boldsymbol{C}$, as illustrated in the leftmost figure of Figure 2.4. For instance, the n_τ th block b_1 (shown in the middle of Figure 2.4) is comprised of two parts that respectively represent the RHCP and LHCP antenna receive signals. Each part comprises N_θ blocks with dimensions $M_\theta M_\tau \times 2$, referred to as b_2. These blocks are created by taking the Kronecker product of matrix $\boldsymbol{A}_M\left(\tilde{\theta}_{n_\theta}\right)$ and the n_τ th column of matrix $\boldsymbol{C}$. To illustrate

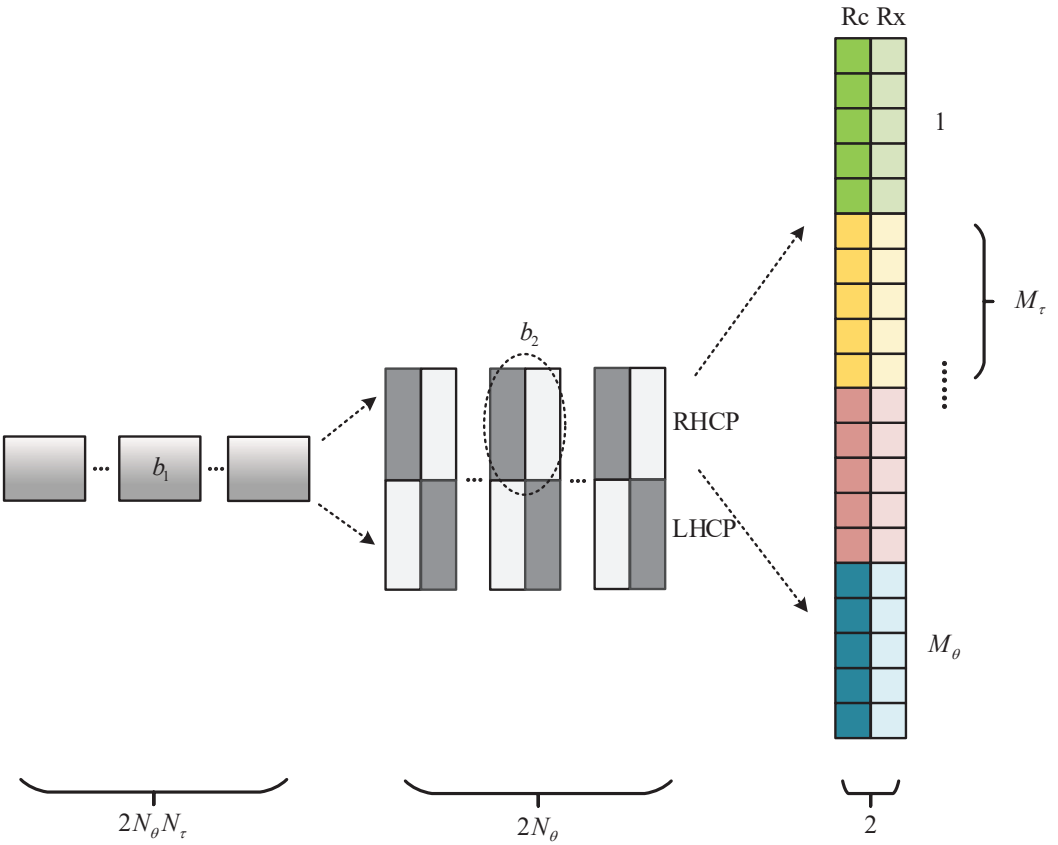


Figure 2.4: Diagram of a joint sparse spatial, polarization, and temporal over-complete basis matrix

further, the n_θ th block b_2 (depicted in the rightmost of Figure 2.4) can be divided into two parts: the left side with a darker color represents the co-polar component of the RHCP signal, which is the Kronecker product of $\boldsymbol{a}_{Rc}\left(\tilde{\theta}_{n_\theta}\right)$ and the n_τ th column of matrix $\boldsymbol{C}$, while the right side with a lighter color represents the cross-polar component of the LHCP signal, which is the Kronecker product of $\boldsymbol{a}_{Rx}\left(\tilde{\theta}_{n_\theta}\right)$ and the n_τ th column of matrix $\boldsymbol{C}$.

When establishing the off-grid spatial and polarization over-complete basis matrix, this off-grid vector $\boldsymbol{\beta}_\theta$ can be redefined as $\boldsymbol{\beta}_\theta \doteq \boldsymbol{\beta}_{\theta_s} \otimes [1,1]^T$. The off-grid spatial vector $\boldsymbol{\beta}_{\theta_s} \doteq [\beta_1, \ldots, \beta_{N_\theta}]^T$, where $\beta_{n_\theta} = \theta_k - \tilde{\theta}_{n_\theta}$ for $n_\theta = 1, \ldots, N_\theta$, with $\tilde{\theta_{n_\theta}}$ being the nearest grid point to the kth signal. Thus, an off-grid spatial, polarization, and temporal over-complete basis matrix can be constructed as (2.14), but with $\boldsymbol{B}_\theta \in \mathbb{C}^{2M_\theta \times 2N_\theta}$ being the first order Taylor series expansion derivation of $\boldsymbol{A}$ with respect to $\tilde{\tau}_{n_\tau}$, which is composed of $b_\theta\left(m_\theta, \tilde{\theta}_{n_\theta}\right)$ with $b_\theta\left(m_\theta, \tilde{\theta}_{n_\theta}\right) = \frac{\partial A_{M,k}\left(m_\theta, \tilde{\theta}_{n_\theta}\right)}{\partial \tilde{\theta}_{n_\theta}}$ and $k = 1, \ldots, K$, $n_\theta = 1, \ldots, N_\theta$. The amplitude vector $\boldsymbol{X} \in \mathbb{C}^{2M_\theta N_\theta \times 2N}$ correspondingly upgrades, which displays spatial-right-polarization-temporal spectrum in its odd columns but also spatial-left-polarization-temporal spectrum in its even columns.

2.3 Analysis of Channel Characteristics in Multipath Environments

Section 2.2 focuses on analyzing the channel characteristics of GNSS in multipath environments. These characteristics are crucial for estimating satellite signals that pass through wireless transmission channels. Furthermore, the channel characteristics impact the choice of estimation algorithms for GNSS in complex environments. Hence, it is essential to analyze and explain the wireless channel characteristics of GNSS before exploring the application of the multi-dimensional signal model for mitigating multipath effects.

2.3.1 Analysis of Spatial and Temporal Characteristics in Multipath Environments

This subsection aims to analyze the spatial and temporal distribution of features in a multipath environment through an examination of the measured spatial characteristics distribution of GNSS signals in urban areas, the impact of the Doppler effect on code phase, and the phenomenon of code phase drift. These analyses provide valuable guidance for making assumptions about quasi-static channels and exploring the possibility of mitigating multipath in the spatial domain.

Spatial Characteristics Distribution

The number of antenna elements plays a critical role in the ability to identify between signals in the spatial domain. Additionally, the extent of DOA expansion for each signal influences the required array aperture size. In a study of [84], a synthetic aperture technique was used to measure the spatial angle distribution characteristics in urban environments by moving the receiver at a constant velocity. The measurement of azimuth and elevation angles for different satellites in various urban environments are partially presented in Figure 2.5 of [84].

These findings provide valuable insights into the sparsity of GNSS signals in the spatial domain with the limited number of signals in urban environments. Each signal corresponds to a specific angle range within the receiver's reception range, with no multipath signals present in other angle ranges. Additionally, the measured data includes both azimuth and elevation angles, and there is a minimum angular separation of approximately 5° between different signals.

Based on these findings, we can draw some guiding principles for modeling various signal models and channel assumptions. In particular, they suggest that multipath signals in the GNSS environment exhibit sparsity in the spatial domain, and a large number of antenna elements are not necessary when using spatial domain multiple antennas for multipath mitigation. However, the distance between antenna elements in a multi-antenna array should be a manageable size to ensure sufficient spatial resolution.

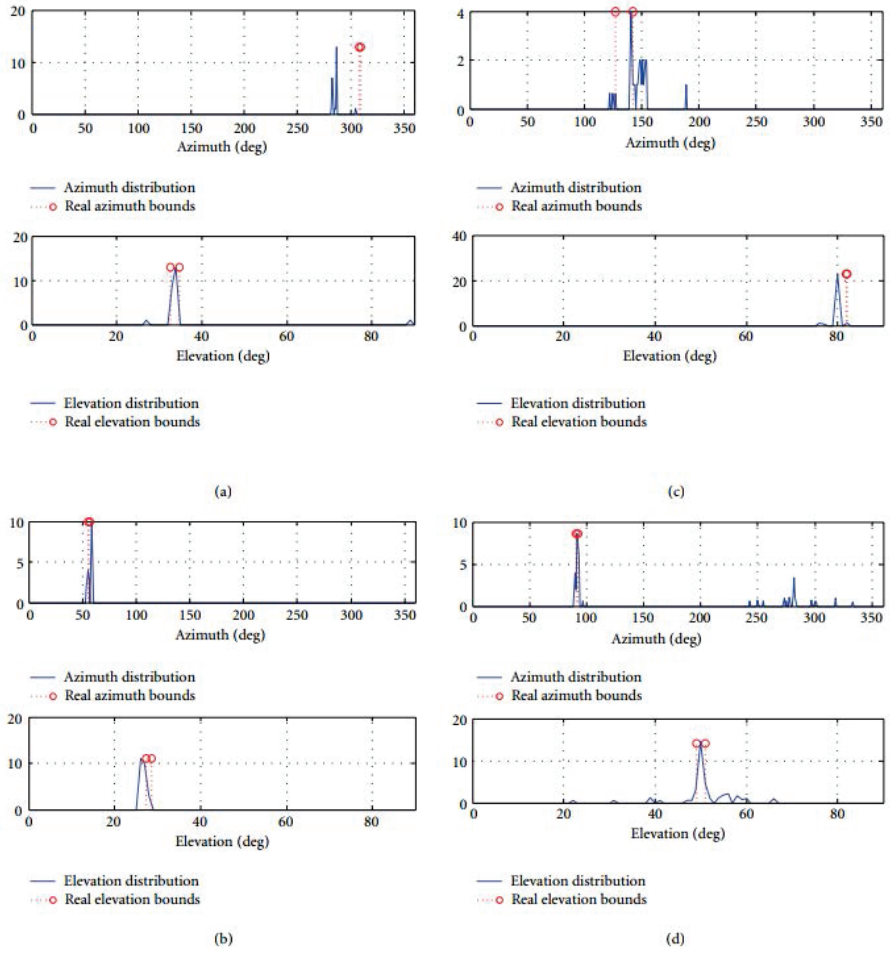


Figure 2.5: The distribution of azimuth and elevation angles for the signals of different satellites in urban environments

The Influence of Doppler Effect and Clock Bias on Code Phase

In contrast to wireless communication systems, GNSS signals experience a significant relative velocity between satellites and ground receivers, which results in a notable Doppler effect at the receiver end. This effect can be observed in two ways: First, there is a substantial DFOs in the received signal, and second, the code rate is also affected. By considering the relationship between the DFOs and the code rate [88], as well as the relationship between the clock deviation of the transmitter and receiver and the code rate, we can express this phenomenon mathematically

$$\frac{\delta_c + f_c}{f_c} = \frac{\delta_{chip} + f_{chip}}{f_{chip}} \tag{2.19}$$

where f_c and f_{chip} represents the central frequency and chip rate, respectively. The DFO variation can be defined as $\delta_c = {\delta_c}^{doppler} + {\delta_c}^{clock}$, which is the sum of the frequency offset caused by the Doppler effect and the DFO resulting from the clock bias of the transmitter and receiver. Similarly,

the chip rate variation can be defined as $\delta_{chip} = {\delta_{chip}}^{doppler} + {\delta_{chip}}^{clock}$, which is the sum of the chip rate variation caused by the Doppler effect and the chip rate variation resulting from the clock bias of the transmitter and receiver.

In ground-based wireless communication, the data length is typically short, measured in microseconds to milliseconds. Any effects caused by variations in chip rate can be ignored over such a short period. However, to improve the carrier-to-noise ratio, GNSS signals require longer accumulation time during tracking for coherent or non-coherent integration. It is essential to consider whether the code phase drift of the signal during receiver tracking can be ignored in some scenarios. For instance, the GPS C/A signal in the L1 frequency band has a DFO of 1 kHz, which causes a peak of the ACF to shift one code chip in 1540ms due to the code rate variation. In most GNSS signals, the typical range of DFOs lies between -5 kHz to 5 kHz, meaning that the fastest possible code chip shift would take 308 ms.

Several factors need to be evaluated when considering the impact of Doppler effects and clock bias on the code phase in GNSS signal processing. We must assess the effect of DFO on the GNSS signal received by a typical GNSS receiver based on specific scenarios to determine whether static GNSS channel models can reliably be used. For narrowband GNSS signals, subspace-based methods are often employed for multipath mitigation, but these methods require a longer signal accumulation time to establish their covariance matrix. To mitigate the impact of code phase drift, dynamic tracking loops can be combined with subspace-based methods [55]. Alternatively, SBL-based methods, which inherently require fewer snapshots for estimation, can reduce the sensitivity to code phase drift even in high Doppler scenarios. For example, the commonly used duration is only 10 ms. In the case of a 4 kHz DFO, the effect of code phase drift is approximately $0.026\,T_c$, which somewhat reduces the impact of code phase drift. This thesis mainly explores the improvement of multipath mitigation through joint multiple dimensions, and they are all constructed based on the premise of a stable tracking loop. In the case of meta-GNSS signals requiring precise estimation, they are extremely sensitive to code phase drift. Consequently, considering the fundamental principles of tracking loops, the practical processing of wideband GNSS signals must be approached.

The DFO Difference and Its Influence on Code Phase

The LOS signal and each of the multipath signals that have undergone reflection experience different propagation paths during the transmission. As a result, the DFO also varies between signals. In [89] and [83], the characteristics of GNSS channel at the physical layer, such as the DOAs of multipath signals, relative time delays, DFOs, and power distribution along different signals, were measured in urban scenarios. The figure below displays some of the test results.

From Figure 2.6, it is evident that during the process of mobile reception, multipath signals

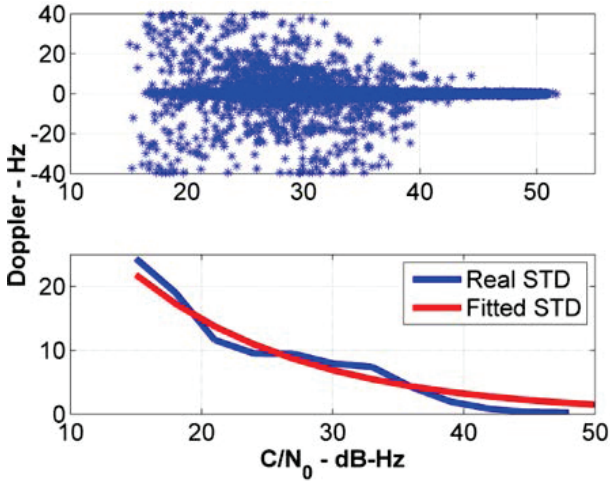


Figure 2.6: Changes in relative DFOs with power intensity for LOS and multipath signals

with power levels greater than 35 dB-Hz exhibit relative DFOs that are generally less than 10 Hz when compared to the LOS signal. This indicates that for the GPS's L1 frequency band C/A signal, the time delay variation between paths over a 100 ms period will not exceed $6.49 \times 10^{-4} T_c$. Thus, if only shorter data segments are considered, it can be assumed that the relative time delays between different reception signals during this period are approximately static. Given the code phase drift eliminated, the generalized joint spatial and temporal signal model established in this chapter can provide an approximate guarantee in multipath mitigation.

2.3.2 Analysis of Polarization Characteristics in Multipath Environments

Ideally, the RHCP antenna is designed to receive the RHCP component of combined the LOS and multipath signals, while the LHCP antenna receives the LHCP component of the mutlipath signals. However, a practical RHCP or LHCP antenna has finite amplitude attenuation to the signals with an opposite polarization state, thus, it receives both RHCP and LHCP signals [16]. This attenuation is known as polarization mismatch loss and is influenced by the Axial Ratios (ARs) of the antennas and signals, which define the polarization state of an electric field [38, 90, 91]. When the ARs of the signal and antenna differ, it results in polarization mismatch loss [90]. The AR of the antenna varies depending on the elevation and azimuth angles, while that of the LOS signal depends on the satellite antenna's AR, which is no worse than 1.8 dB [92], whereas the AR of the multipath signal primarily arises from reflection.

To measure and set the magnitude of the polarization coefficient vector $\boldsymbol{\lambda}$, we have employed a typical AR value for the signal and antenna. For instance, the AR for the LOS signal is set to 1.8 dB, while that of the antenna mapped to the azimuth and elevation angles of the LOS signal is set to 2 dB [90]. Based on these assumptions, and assuming the power of the LOS signal is normalized to $\lambda_{R,0}^2 = 0$ dB, the power leakage from the LOS signal to the LHCP signal depends on the tilt

angle between the polarization ellipse major axis of the signal and the receiving antenna, with $\lambda^2_{L,1}$ ranging from -39 dB to -13.3 dB. In general, since the AR of the LOS signal is less than 1.8 dB, the value of $\lambda^2_{L,1}$ can be further reduced. The feasibility of these values has been validated by [93].

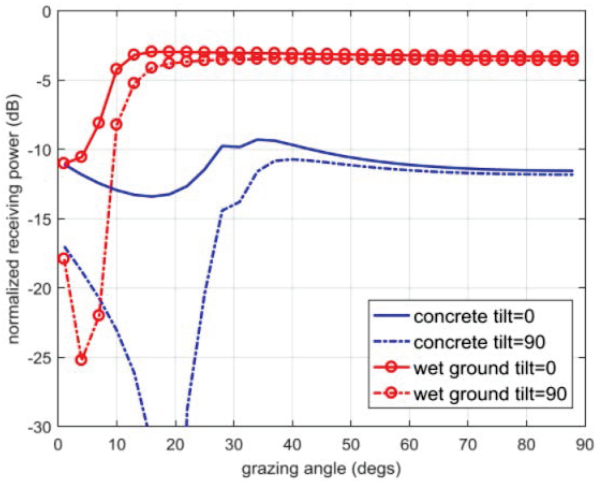


Figure 2.7: The power of multipath LHCP signals reflected by two typical reflective surfaces

In general, the powers of multipath signals reflected by objects near the receiver are lower than that of the LOS signal. According to measurements presented in [91], Figure 2.7 shows the powers of multipath LHCP signals via grazing angles, i.e., $\lambda^2_{L,2}$, reflected by surfaces such as concrete or wetlands under the aforementioned assumptions. If wetlands reflect the signal, the received multipath LHCP signal will not exceed -3 dB, while if it is reflected by concrete, the upper limit may only reach -9 dB. Based on these results from two different reflective surfaces, we can generally assume that the value range of $\lambda^2_{L,2}$ is between -40 dB and -3 dB. Similarly, when determining the value of $\lambda^2_{L,2}$, we can also infer that the value range of $\lambda^2_{R,2}$ lies between -40 dB and 0 dB.

We can provide the following guidelines in the preceding discussion of the polarization characteristics of various received signals. As the LOS signal is not reflected, its LHCP power is typically weak, usually below -15 dB. Hence, it is reasonable to assume that the LOS signal only comprises an RHCP component received by the RHCP antenna. Conversely, the powers of multipath signals vary substantially and cannot be determined based on one scenario. Therefore, it is crucial to define the concept of dual-polarization gain [38], as discussed extensively in Section 4. This notion represents the power ratio between the multipath LHCP and RHCP components, which can help inform us how to set different reflection powers for varying dual-polarization gains when modeling and simulating.

2.3.3 Analysis of Frequential Characteristics in Multipath Environments

This subsection aims to investigate the frequential characteristics of multipath GNSS signals by observing different frequency GNSS signals in multipath environments and understanding the impact of ionospheric propagation on the code phases. The findings will guide the utilization of meta-GNSS signals and assist in setting simulation parameters.

The Influence of Different Frequencies of Meta-Signal on Spatial Domain

In meta-GNSS signals, the two components are transmitted at different carrier frequencies. When using a multi-antenna GNSS receiver, the steering vectors corresponding to the left and right components differ in wavelength. Since the satellites are far from the ground, satisfying the far-field signal incident conditions [94], and the left and right components pass through the same transmission path reaching the receiver, their angles are basically the same.

In the discussion of different carrier frequencies influence on the spatial domain, we can provide the following guidance: the steering vectors corresponding to the left and right components of meta-GNSS signals are modeled differently. For typical meta-signals, such as the B1I and B1C signals in the Beidou system, which have a frequency separation of only 14 MHz, their steering vectors for different components can be assumed identical.

The Influence of Ionospheric Propagation Delay on Code Phase of Meta-Signals

Meta-signals' bandwidth is large, ranging from tens of megahertz to several hundred megahertz. Based on the fact that the ionosphere is dispersive, the different frequencies of components in the spectrum experience different time delays when passing through the upper atmosphere. Using the first-order ionospheric delay model [1], the group delay expressed in meters is given by:

$$\tau\left(f\right)=\frac{40.3\mathrm{TEC}}{f^{2}} \tag{2.20}$$

where TEC refers to the total electron content, and f is the transmission frequency. For traditional GNSS narrowband signals, such as the GPS C/A code signal in the L1 frequency band, which has a two-sided bandwidth of only 2 MHz. The delay carried by the signal is assumed to be represented by the ionospheric delay at the center frequency instead of the total group delay. As the bandwidth increases, the change in ionospheric delay across the entire band becomes more significant. This also applies to meta-signals, where the dispersion characteristics of the ionospheric medium result in different component signals experiencing varying delays, introducing some distortion compared to narrowband signals [95]. In contrast, wideband received signals are increasingly utilized in GNSS applications to achieve higher tracking accuracy and better multipath mitigation performance. Therefore, it is necessary to further discuss whether the delay model solely based on

the center frequency can meet the requirements of high-precision GNSS applications.

It is known that an ionosphere dispersion can cause the asymmetry ACF, which introduces bias in the estimation of peak delay, as shown in Figure 2.8 in reference [95].

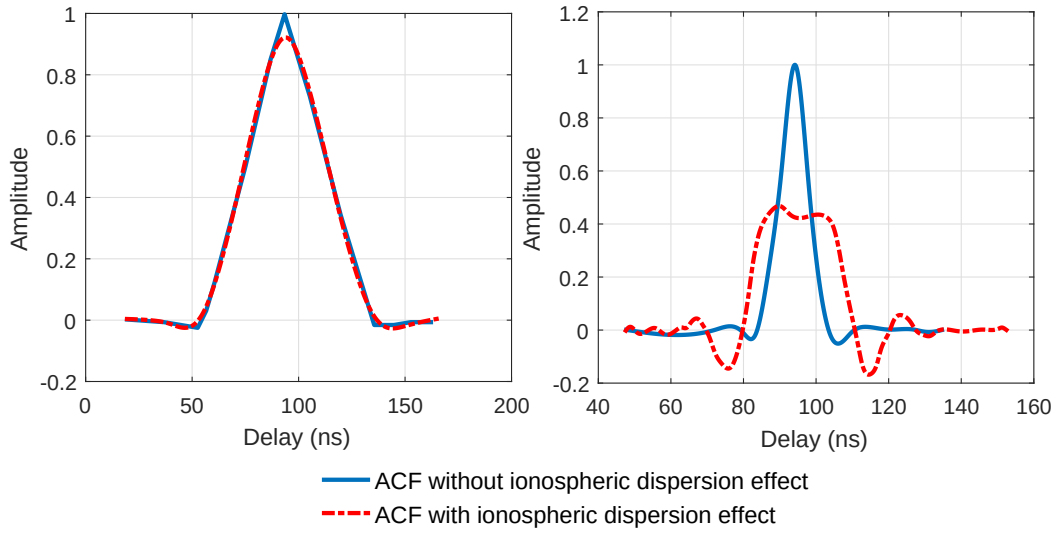


Figure 2.8: Effect of TEC=100 on the ACFs of a 50MHz bandwidth signal (left panel) and of a 100MHz bandwidth signal (right panel);

In addition, reference [95] points out that ionospheric dispersion can cause power loss due to a mismatch between the received signals and the local replica. Furthermore, ionospheric dispersion can also affect the constellation, resulting in distortion as illustrated in reference [96].

In the above discussion of the impact of ionospheric propagation on the code phase, we can provide the following guidelines. It is advisable to choose two adjacent signals from the same satellite, with the most commonly used pair being the B1I and B1C signals in the Beidou system, with a frequency separation of only 14 MHz that renders the effect of ionospheric propagation negligible. The relevant analysis and simulations in this thesis are based on this combination. However, if higher bandwidths are required, the impact of ionospheric propagation cannot be ignored. Many studies propose compensating for this delay before processing the baseband signal. For example, the all-pass filter proposed in [97] compensates for the delay at different frequencies to achieve a constant amplitude response across the entire bandwidth while non-linearly compensating for the phase.

2.4 Introduction to Classical Multipath Mitigation

2.4.1 Introduction to Maximization Likelihood Methods

The ML method is a widely used parameter estimation technique first proposed in the late 1980s [21, 98]. This method defines the likelihood function of the observed signal as the conditional prob-

ability density function (PDF) with unknown parameters. The goal is to select the optimal unknown parameters that maximize the likelihood function. In Equation (2.2), the conditional PDF is defined,

$$p\left(\boldsymbol{y}\left(t\right);\boldsymbol{\eta}\right)=\left(\pi\sigma^{2}\right)^{-M_{\theta}}\frac{\exp\left(-\left\|\boldsymbol{y}\left(t\right)-\boldsymbol{s}\left(t;\boldsymbol{\eta}\right)\right\|_{F}^{2}\right)}{\sigma^{2}} \tag{2.21}$$

where the parameter set is defined as $\boldsymbol{\eta}\doteq\left[\boldsymbol{\theta}^{T},\boldsymbol{\gamma}^{T},\boldsymbol{\tau}^{T}\right]^{T}$ and $\boldsymbol{s}\left(t;\eta\right)=\sum_{k=1}^{K}\boldsymbol{a}\left(\theta_{k}\right)\gamma_{k}c\left(t-\tau_{k}\right)$. To acquire the calculation convenience, the logarithm of Equation (2.21) is generally taken to obtain the cost function with ML,

$$\hat{\boldsymbol{\eta}}=\arg\max_{\eta}\left\{-\ln\left(p\left(\boldsymbol{y}\left(t\right);\boldsymbol{\eta}\right)\right)\right\} \tag{2.22}$$

The ML method maximizes the cost function by determining the parameter set $\boldsymbol{\eta}$. Usually, this involves solving for one parameter while considering the others as known values. While the ML method theoretically offers optimal performance, it presents challenges in high computational complexity when dealing with multiple parameters across multiple dimensions.

The SAGE algorithm [22] is based on the EM method, which facilitates optimizing ML-based cost functions that arise in statistical estimation problems, but with improvements regarding the trade-off between convergence rate and complexity. The first main step in SAGE is the Expectation-step, which constructs each path based on the estimated parameter except for that of the k th signal and estimates the hidden data space of the k th signal,

$$\hat{\boldsymbol{x}}_{k}\left(t\right)=\boldsymbol{y}\left(t\right)-\sum_{k'=1,k'\neq k}^{K}\boldsymbol{s}\left(t;\boldsymbol{\eta}_{k'}\right) \tag{2.23}$$

SAGE breaks down the multi-dimensional optimization problem into several smaller problems by conditioning sequentially on a subset of parameters. This step is called the Maximization-step.

$$\hat{\theta}_{k}=\arg\max_{\theta_{k}}\left\{\left|\boldsymbol{a}(\theta_{k})^{H}\hat{\boldsymbol{x}}_{k}\left(t\right)c(t-\hat{\tau}_{k})^{H}\right|^{2}\right\} \tag{2.24a}$$

$$\hat{\tau}_{k}=\arg\max_{\tau_{k}}\left\{\left|\boldsymbol{a}\left(\hat{\theta}_{k}\right)^{H}\hat{\boldsymbol{x}}_{k}\left(t\right)c(t-\tau_{k})^{H}\right|^{2}\right\} \tag{2.24b}$$

Using these two steps, SAGE completes one iteration. After several iterations, the results can approximate that of the ML estimator. Please refer to Chapter 3 and 5 for specific descriptions.

2.4.2 Introduction to Subspace-based Methods

The subspace-based methods include two most widely used algorithms: One is based on noise subspace, like MUSIC [26], and the other is based on signal subspace rotation invariance, such as

ESPRIT [27] and DOAMatrix [31].

MUSIC is based on the second-order statistics of the received signal. Extending the concept of geometry can obtain a reasonable approximate solution in the presence of noise. As long as the layout form of the antenna array is known, high-resolution estimates are obtained. Note that there is no strict requirement on the format of the array. Based on the model of Equation (2.2), the covariance matrix is calculated on the assumption that signal and noise are independent

$$\begin{aligned} \boldsymbol{R} &= E\left\{\boldsymbol{y}\left(t\right)\boldsymbol{y}^{H}\left(t\right)\right\} \\ &= \boldsymbol{A}\left(\boldsymbol{\theta}\right)\boldsymbol{R}_{s}\boldsymbol{A}^{H}\left(\boldsymbol{\theta}\right)+\sigma^{2}\boldsymbol{I} \end{aligned} \tag{2.25}$$

where $\boldsymbol{R}_s = E\left\{\begin{pmatrix} \gamma_1 c\left(t-\tau_1\right) \\ \vdots \\ \gamma_K c\left(t-\tau_K\right) \end{pmatrix}\begin{pmatrix} \gamma_1^* c^H\left(t-\tau_1\right) & \cdots & \gamma_K^* c^H\left(t-\tau_K\right) \end{pmatrix}\right\}$ represents the covariance matrix of received signal. The noise follows a Gaussian distribution with a mean of zero and a variance of σ^2. Conduct the eigen decomposition to $\boldsymbol{R}$ and we have

$$\boldsymbol{R} = \boldsymbol{U}_S\boldsymbol{\Sigma}_S\boldsymbol{U}_S^H + \sigma^2\boldsymbol{U}_N\boldsymbol{U}_N^H \tag{2.26}$$

$\boldsymbol{U}_S$ is the signal subspace, while $\boldsymbol{U}_N$ is the noise subspace. Ideally, the signal subspace and noise subspace in data space are mutually orthogonal [99], that is, the steering vector in signal subspace is also orthogonal to the noise subspace,

$$\boldsymbol{a}^H\left(\theta\right)\boldsymbol{U}_N = \boldsymbol{0} \tag{2.27}$$

Based on this fact, the spectrum of MUSIC is

$$\boldsymbol{P}_{MUSIC}\left(\theta\right) = \frac{1}{\boldsymbol{a}^H\left(\theta\right)\boldsymbol{U}_N\boldsymbol{U}_N^H\boldsymbol{a}\left(\theta\right)} \tag{2.28}$$

DOAMatrix, proposed by Prof. Yin et al., is a widely used method for DOA estimation that leverages the rotation invariance of ULA. It is a two-dimensional parameter estimation technique designed for parallel ULA, where the popular ESPRIT algorithm is a specific instance of DOAMatrix. This approach overcomes spectrum search and nonlinear optimization challenges, offering low computational requirements and automatic parameter matching. This thesis focuses on the ULA case, thus reducing DOAMatrix to a one-dimensional scenario.

Take first $M_\theta - 1$ elements in ULA denoting as $\boldsymbol{y}_x$, and take last $M_\theta - 1$ elements in ULA

denoting as $\boldsymbol{y}_y$. We, therefore, define the following covariance matrices

$$\begin{aligned}\boldsymbol{R}_{xx} &= E\left\{\boldsymbol{y}_x\left(t\right)\boldsymbol{y}_x^H\left(t\right)\right\} \\ &= \bar{\boldsymbol{A}}\left(\boldsymbol{\theta}\right)\boldsymbol{R}_s\bar{\boldsymbol{A}}^H\left(\boldsymbol{\theta}\right)+\sigma^2\boldsymbol{I}\end{aligned} \tag{2.29}$$

$$\begin{aligned}\boldsymbol{R}_{yx} &= E\left\{\boldsymbol{y}_y\left(t\right)\boldsymbol{y}_x^H\left(t\right)\right\} \\ &= \bar{\boldsymbol{A}}\left(\boldsymbol{\theta}\right)\boldsymbol{\Phi}_\theta\boldsymbol{R}_s\bar{\boldsymbol{A}}^H\left(\boldsymbol{\theta}\right)\end{aligned} \tag{2.30}$$

where $\boldsymbol{\Phi}_\theta = \text{diag}\left\{e^{j2\pi d\sin(\theta_1)/\lambda},\ldots,e^{j2\pi d\sin(\theta_K)/\lambda}\right\}$.

Define DOA matrix $\boldsymbol{R}$ as

$$\boldsymbol{R} = \boldsymbol{R}_{yx}\boldsymbol{R}_{xx0}^{-1} \tag{2.31}$$

with $\boldsymbol{R}_{xx0} = \boldsymbol{R}_{xx} - \sigma^2\boldsymbol{I}$.

If $\bar{\boldsymbol{A}}\left(\theta\right)$ and $\boldsymbol{R}_s$ are full rank, $\boldsymbol{\Phi}_\theta$ has no same diagonal elements, then the angles and steering vectors correspond to the non-zero eigenvalues and eigenvectors of DOA matrix $\boldsymbol{R}$

$$\boldsymbol{R}\bar{\boldsymbol{A}}\left(\boldsymbol{\theta}\right) = \bar{\boldsymbol{A}}\left(\boldsymbol{\theta}\right)\boldsymbol{\Phi}_\theta \tag{2.32}$$

As long as conducting the eigen decomposition of $\boldsymbol{R}$, $\bar{\boldsymbol{A}}\left(\boldsymbol{\theta}\right)$ and $\boldsymbol{\Phi}_\theta$ can be directly acquired.

2.4.3 Introduction to Sparse Representation Methods

Sparse representation is to use as few non-zero elements as possible to represent the signal simplifying the problem of signal processing. Based on the joint sparse spatial and temporal GNSS signal model (2.15), a sparse spatial expression is simplified (All subscripts b are omitted for the sake of convenience.)

$$\boldsymbol{y} = \boldsymbol{A}\boldsymbol{x} + \boldsymbol{n} \tag{2.33}$$

where $\boldsymbol{y}$ is the observable data, and $\boldsymbol{A} \in \mathbb{C}^{M_\theta \times N_\theta}$ is a spatial over-complete basis matrix composed of N_θ vectors. The Gaussian noise is denoted as $\boldsymbol{n}$. In the case of noise-free, the sparsest solution can be obtained through optimization,

$$\begin{cases}\hat{\boldsymbol{x}} = \arg\min\left\|\boldsymbol{x}\right\|_0 \\ \quad s.t.\boldsymbol{y} = \boldsymbol{A}\boldsymbol{x}\end{cases} \tag{2.34}$$

The solution to the above equation is a searching process to find the sparsest solution in the over-complete basis matrix. However, in the presence of noise, $\boldsymbol{y}$ cannot be accurately represented. The

relaxation optimization problem is adopted to obtain an approximate solution,

$$\boldsymbol{x}_0(\lambda) = \arg\min \|\boldsymbol{y} - \boldsymbol{A}\boldsymbol{x}\|_2^2 + \lambda\|\boldsymbol{x}\|_0 \tag{2.35}$$

This is a non-deterministic polynomial problem and is hard to solve. Moreover, the regularization parameter λ is challenging to choose and not guaranteed to be the best estimate of the global optimal solution $\boldsymbol{x}_{opt}$.

Via the Bayesian principle, Equation (2.35) can be rewritten by exponential transformation. Assume that the Gaussian likelihood function $p(\boldsymbol{y}|\boldsymbol{x})$ with variance λ is

$$p(\boldsymbol{y}|\boldsymbol{s}) \propto \exp\left[\frac{1}{\lambda}\|\boldsymbol{y} - \boldsymbol{A}\boldsymbol{x}\|_2^2\right] \tag{2.36}$$

The prior distribution $p_0(\boldsymbol{x})$ of complex amplitude vector $\boldsymbol{x}$ is

$$p_0(\boldsymbol{x}) \propto \exp\left[-\|\boldsymbol{x}\|_0\right] \tag{2.37}$$

Using the Bayesian principle, the maximization of the posterior probability of $\boldsymbol{x}$ is estimated as

$$\begin{aligned}\boldsymbol{x}_{MAP} &= \arg\max p_0(\boldsymbol{x}|\boldsymbol{y}) \\ &= \arg\max p(\boldsymbol{y}|\boldsymbol{x})\, p_0(\boldsymbol{x}) \\ &= \arg\min\left(-\ln\left(p(\boldsymbol{y}|\boldsymbol{x})\right) - \ln\left(p_0(\boldsymbol{x})\right)\right) \\ &= \boldsymbol{x}_0(\lambda)\end{aligned} \tag{2.38}$$

The aforementioned problem can be interpreted as a maximization of the posterior probability estimation. Two algorithms can be utilized to tackle this problem. The first approach involves employing a greedy algorithm, such as basis matching pursuit [66], which provides local optimal solutions. The second approach involves replacing the prior distribution $p_0(\boldsymbol{s})$ with a specific distribution, such as the FOCUSS algorithm [71]. Both algorithms seek posterior distributions under the assumption that the prior distributions remain fixed, albeit with notable drawbacks. Choosing a moderately sparse prior distribution simplifies the search process, but the result may not be sufficiently sparse to achieve an optimal solution. On the other hand, selecting an adequately sparse prior distribution increases the number of combinations of locally optimal solutions, thereby intensifying the search challenge.

A method based on automatic correlation determinism (ARD) solves the sparse representation problem in SBL. Suppose $p(\boldsymbol{y}|\boldsymbol{x})$ is Gaussian distributed, ARD for each component of the sparse vector exerted an independent Gaussian prior

$$p(x_n; \alpha_n) = \mathcal{CN}(0, \alpha_n) \tag{2.39}$$

with the prior distribution with respect to $\boldsymbol{X}$

$$p\left(\boldsymbol{x};\boldsymbol{\alpha}\right)=\prod_{n=1}^{N}p\left(s_n;\alpha_n\right) \tag{2.40}$$

which is controlled by hyperparameters $\boldsymbol{\alpha}=\left[\alpha_1,\ldots,\alpha_N\right]^T$. From the Bayesian principle, the posterior distribution of $\boldsymbol{x}$ is

$$p\left(\boldsymbol{x}\left|\boldsymbol{y}\right.;\boldsymbol{\alpha}\right)=\frac{p\left(\boldsymbol{y}\left|\boldsymbol{x}\right.;\boldsymbol{\alpha}\right)p\left(\boldsymbol{x};\boldsymbol{\alpha}\right)}{p\left(\boldsymbol{y}\right)} \tag{2.41}$$

Since both of the distributions are Gaussian, the posterior distribution of $\boldsymbol{x}$ is Gaussian as well

$$p\left(\boldsymbol{x}\left|\boldsymbol{y}\right.;\boldsymbol{\alpha}\right)=\mathcal{CN}\left(\boldsymbol{\mu},\boldsymbol{\Sigma}\right) \tag{2.42}$$

with the mean and variance

$$\boldsymbol{\mu}=E\left\{\boldsymbol{x}\left|\boldsymbol{y}\right.;\boldsymbol{\alpha}\right\}=\boldsymbol{\Gamma}\boldsymbol{A}^H\boldsymbol{\Sigma}_y^{-1}\boldsymbol{y} \tag{2.43}$$

$$\boldsymbol{\Sigma}=E\left\{\left(\boldsymbol{x}-\boldsymbol{\mu}\right)\left(\boldsymbol{x}-\boldsymbol{\mu}\right)^H\left|\boldsymbol{y};\boldsymbol{\alpha}\right.\right\}=\boldsymbol{\Gamma}-\boldsymbol{\Gamma}\boldsymbol{A}^H\Sigma_y^{-1}\boldsymbol{A}\boldsymbol{\Gamma} \tag{2.44}$$

respectively and with $\Gamma=\mathrm{diag}\left(\alpha\right)$, $\Sigma_y=\boldsymbol{A}^H\Gamma\boldsymbol{A}+\sigma^2\boldsymbol{I}$. The sparsity is achieved when the majority of α_n is zero. Therefore, the problem of obtaining the optimal solution is transformed to the estimation of hyperparameter $\boldsymbol{\alpha}$.

Under the observable data $\boldsymbol{y}$, each hyperparameter vector corresponds to the assumption of a prior distribution so that determining a suitable value for each hyperparameter $\boldsymbol{\alpha}$ is equivalent to a model selection. Generally, marginal processing is adopted, and the cost function based on ARD is

$$\begin{aligned}\ell\left(\boldsymbol{\alpha}\right)&=\log\int p\left(\boldsymbol{y}\left|\boldsymbol{x}\right.;\boldsymbol{\alpha}\right)p\left(\boldsymbol{x};\boldsymbol{\alpha}\right)d\boldsymbol{x}\\&=\log\left|\boldsymbol{\Sigma}_y\right|+\boldsymbol{y}^H\boldsymbol{\Sigma}_y^{-1}\boldsymbol{y}\end{aligned} \tag{2.45}$$

The sparse reconstruction method based on maximum a posterior utilizes a prior distribution that applies the same prior distribution to each element of the sparse vector, resulting in a discrepancy between the sparse and signal models. SBL addresses this issue by employing a set of independent hyperparameters $\boldsymbol{\alpha}$ that impose different prior distributions on each element of the complex amplitude vector. By optimizing these hyperparameters, SBL obtains a sparse $\boldsymbol{\alpha}$ estimate that leads to a posterior probability distribution function consistent with the real signal.

Table 2.1: Comparison of the merits and flaws of three methods

Methods	Merits	Flaws
ML (SAGE)	1. Performance approximates CRLB closely 2. No restrictions on estimable signals	1. Highly sensitive to initial values 2. Multipath mitigation decreases with high correlation 3. Complexity increases with the number of signals
Subspace (DOAMatrix)	Ideal trade-off between complexity and performance	1. Rank-deficient covariance matrix in multipath cases 2. Large snapshots required 3. Limited estimable signals
Sparse Representation (SBL)	1. Works with few snapshots 2. Process signals directly in the signal domain 3. Shares global convergence property with ℓ_0-norm	1. High complexity 2. Cause off-grid effects

2.4.4 Merits and Flaws

The above three methods, ML, subspace-based, and sparse representation, have strengths and weaknesses that can be analyzed. The ML method is built upon the principle of multi-dimensional maximum likelihood, representing different signals as linear superposition in each signal dimension. This approach offers natural performance advantages, closely approximates the CRLB, and is not limited by the number of elements in the antenna array.

However, the complexity of joint searching in multiple dimensions is exceedingly high. Even though SAGE can approximate the multi-dimensional ML performance through iterative single-dimensional searches, the complexity still increases significantly as the number of signals grows. Additionally, SAGE relies on reconstructed signals, making it highly sensitive to initial values and susceptible to convergence near local extrema rather than achieving global optimization. This phenomenon becomes evident in cases where the signals are highly correlated, leading to a decrease in SAGE to handle multipath in such situations.

Subspace-based methods strike a balance between complexity and performance, albeit with some deviation from the CRLB. However, subspace-based methods require computation of the covariance matrix, and an ideal recovery of the original covariance matrix requires more snapshots. This increase in the number of snapshots also raises the requirement for static channel characteristics. In the multipath scenario, where the covariance matrix is not full-rank, effective separation and identification of signal and noise subspaces through subspace decomposition is unfeasible. Instead, spatial smoothing must be used to construct a full-rank covariance matrix. Moreover,

subspace decomposition relies primarily on the number of antenna elements for multipath mitigation from different spatial directions, thus limiting the estimable radius to the number of array elements. For multipath environments, subspace decomposition necessitates large antenna arrays, which could be more practical.

Sparse representation process signals directly in the signal domain rather than estimating the signal's covariance matrix. This inherent property makes them less sensitive to the presence of multipath signals and enables them to work with fewer snapshots. The SBL algorithm shares the same global convergence property as the ℓ_0-norm and can achieve the most sparse minimum value among all extreme global values, making it practical for multipath mitigation. However, sparse representations have a large number of iterations, resulting in high complexity. The most significant drawback is the off-grid effect. While adding linear vectors to the complete basis matrix can improve the parameter estimation accuracy, an increased correlation between these basis vectors may lead to performance bottlenecks. Moreover, if the spacing between adjacent basis vectors is too large, a fixed error arises between the true value and the grid value, resulting in performance issues.

Each of these three methods offers unique advantages and limitations, and the choice of method depends on application requirements and trade-offs between accuracy, computational complexity, and real-time processing capability. Table 2.1 summarizes the typical methods' advantages and disadvantages.

2.5 Conclusions

This chapter begins by deriving an extended general joint spatial and temporal GNSS multipath signal model based on the existing characteristics of the GNSS spread spectrum and acquisition information, starting from the general expression of GNSS signals in multipath environments. This model serves as a unified mathematical matrix guide for joint analysis of various dimensions of information characteristics. Furthermore, this chapter forms specific models for subsequent joint spatial and temporal, joint spatial, polarization, and temporal, and joint spatial and frequential GNSS signals based on the generalized GNSS signal model. Additionally, to fulfill the requirement of sparse representation, we derive the off-grid joint spatial and temporal sparse model and off-grid joint spatial, polarization, and temporal sparse model, providing model possibilities for using sparse representation methods to address the problem of multipath mitigation. Subsequently, this chapter discusses the impact of various multipath input scenarios on GNSS measurements, exploring the effects of Doppler frequency differences between different signals and the spatial distribution of reception signals in urban environments. It also examines the measurement and distribution of reflected polarization in multipath environments and investigates the effect of ionospheric propagation delay on the multi-frequency GNSS signal code phase. These discussions

lay a foundation for proposing processing structures and relevant algorithms based on joint space and time, joint space, polarization and time, and joint space and frequency methods. Finally, this chapter introduces criteria and typical algorithms for ML-, subspace-, and sparse representation-based methods, comparing their advantages and disadvantages to provide a basis for subsequent algorithm selection for multipath-mitigating GNSS receivers.

Joint Spatial and Temporal GNSS Multipath Mitigation

3.1 Introduction

Multipath signals formed by signal reflection coming from objects in the vicinity of GNSS receivers result in a degradation of the tracking performance and an increase in the positioning error. In particular, the pseudo-range error produced by multipath can reach meters or even hundreds of meters in traditional GNSS receivers. Most GNSS receivers are equipped with a single-antenna and rely on typical multipath-mitigating techniques in the time or frequency domain. It is difficult to effectively identify cases of high correlation in the time domain (i.e. when the delay difference between the LOS and the multipath signals is less than half a chip). Even if the receiver has multiple antennas and uses cascaded spatial and temporal structure to suppress multipath signals, it may still be unable to deal with cases of high correlation in the spatial domain (i.e., when the angle difference between the LOS and the multipath signals is less than half the main lobe width of the antenna array). This chapter proposes a joint spatial and temporal GNSS receiving way that observes signals with a multipath environment from a two-dimensional perspective. The joint angle and time delay estimation based on subspace or MSBL is proposed based on different application requirements and advantages.

This chapter is structured as follows. First, the advantages and feasibility of joint spatial and temporal processing compared to cascaded approaches are analyzed based on channel characteristics discussed in Chapter 2. Second, we propose joint spatial and temporal subspace-based algorithms that ensure both multipath mitigation and complexity reduction. We also introduce a joint spatial and frequential smoothing subspace-based algorithm to address the rank-deficiency problem that may occur with highly correlated sources. Next, we extend MSBL to the joint spatial and temporal domains to account for sparsity in both domains. To overcome the limitations of sparse representation, two algorithms based on on-grid and off-grid estimators are proposed to

reduce complexity and improve resolution, making the proposed multipath mitigation applicable to various GNSS scenarios. We optimize angle and delay estimation using the SAGE algorithm, which yields a third algorithm with improved resolution. We provide complexity analyses for these methods and compare their performance in different multipath scenarios through LOS time delay estimation. Finally, we summarize our findings.

3.2 Feasibility Analysis of GNSS Joint Spatial and Temporal Multipath Mitigation

The methods for mitigating multipath in pure space are limited by the number of antenna elements, which determines the maximum number of multipath signals that can be resolved. While conventional multi-antenna GNSS receivers cannot carry a large volume of antennas due to their limited size, rendering pure space processing impractical for multipath mitigation. Existing multi-antenna GNSS receivers often employ a cascaded spatial and temporal processing structure as depicted in Figure 3.1 [100].

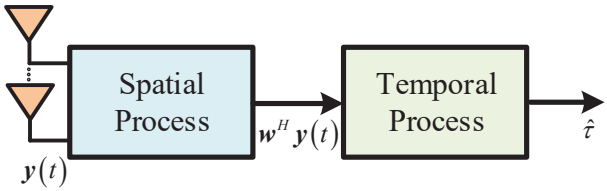


Figure 3.1: Cascaded Spatial and temporal structure of GNSS receiver

As mentioned in Figure 3.1, conventional multi-antenna GNSS receivers typically follow a cascaded structure of space processing followed by time processing. The received signals are first angles estimated and then subjected to beamforming operations. Since LOS signal and multipath signals arrive at different angles, even the simplest beamforming pointed to the LOS signal can partially suppress the multipath signals, as demonstrated in Figure 3.2.

Many spatial processing can be used for multipath mitigation based on these cascaded multi-antenna GNSS receivers, such as the RELAXation[101], SAGE[22] and other ML algorithms, MUSIC [26], ESPRIT[27] and other subspace-based algorithms, matching pursuit[33], IAA[102], MSBL[13] and other compressed sensing algorithms, as well as power inversion[103], MVDR[104] and spatial beamforming algorithms. After spatial beamforming, a conventional GNSS receiver applies temporal processing to suppress residual multipath signals further while capturing and tracking the satellite signals. Multipath mitigation commonly used in GNSS receivers, such as narrow-band early-late discriminators (nEMLs) [9], MEDLL [10], and other multipath-mitigating tracking loops can be directly employed in the temporal processing.

The advantage of the cascaded spatial and temporal GNSS receiver is that it does not require

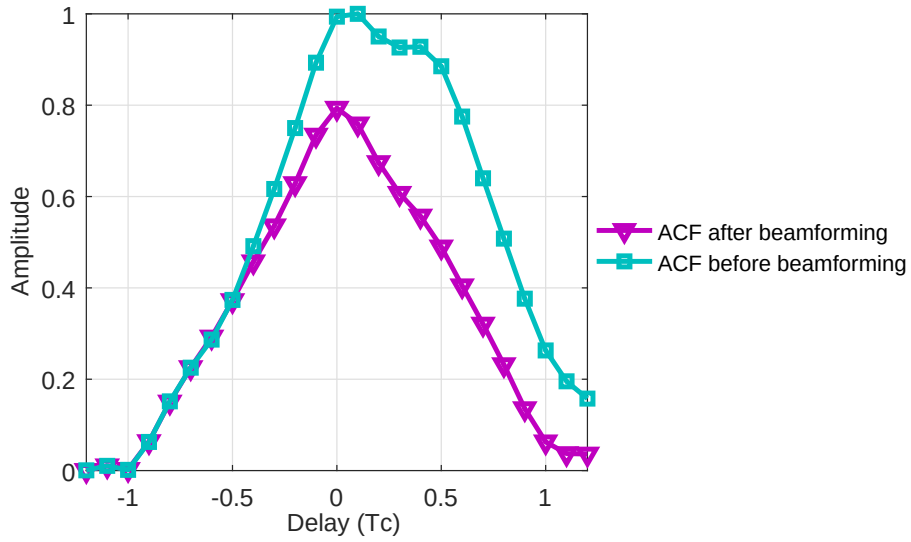


Figure 3.2: The effects of beamforming to multipath signals

changes to the internal structure of the receiver itself. Instead, it adds a multi-antenna array at the receiver's front end, which can apply the corresponding mature research results in signal processing. This makes it easier to develop and deploy GNSS receivers quickly. However, this cascaded spatial and temporal receiver is limited by the spatial degrees of freedom, as the number of multipath signals that can be distinguished must be smaller than the total number of antenna elements. Additionally, the cascaded spatial and temporal GNSS receiver processes signals separately in space and time, meaning that the spatial and temporal information of the received signals cannot be jointly utilized. As a result, there is a certain degree of inefficiency, and the performance may deteriorate significantly in multipath scenarios with high correlation in either time or space.

In the past decades, the idea of JADE, aiming at parameter estimation by the corporation of spatial and temporal information, was proposed. Subspace-based JADE processing has been applied in CDMA and other communication systems, and its effectiveness has been demonstrated with low complexity achieving good estimation performance [52]. JADE allows simultaneous observation of spatial and temporal information from two dimensions, which solves the problem of high correlation in either domain. This structure also expands the maximum number of signals estimated by the Kronecker product of temporal and spatial steering vectors. However, extended JADE subspace-based methods face challenges such as rank deficiency in the covariance matrix under the multipath environment with highly correlated sources. Moreover, subspace-based methods require a quasi-static signal model and many snapshots to form the covariance matrix decomposition for better performance. In sparse representation, the challenge is to estimate parameters with fewer snapshots while maintaining robustness to incomplete compensation of small fractional DFOs in multipath environments and overcoming computational complexity and off-grid effects.

3.3 Joint Spatial and Temporal Multipath Mitigation based on Subspace Method

Traditional subspace-based methods, such as the ESPRIT [27],[52] and DOAMatrix [31], both rely on steering vectors to construct subspace rotational invariance. They can obtain estimates through eigenvalue decomposition without the need for searching. The corresponding smoothing methods can achieve a perfect trade-off between performance and complexity in conventional multipath environments. In this section, we propose two fast spatial and temporal subspace-based multipath-mitigating algorithms, which can quickly estimate angles and delays through eigen decomposition.

3.3.1 Coherent Incidence Effects on Signal Subspace

Based on the joint spatial and temporal GNSS signal model (2.1), its auto-correlation matrix is denoted as

$$\begin{aligned}\boldsymbol{R}_{\boldsymbol{y}_b} &= E\left\{\boldsymbol{y}_b(n)\,\boldsymbol{y}_b^H(n)\right\} \\ &= \left(\boldsymbol{A}(\boldsymbol{\theta})\otimes\boldsymbol{R}(\bar{\boldsymbol{\tau}},\boldsymbol{\tau})\right)\boldsymbol{\gamma}_b\boldsymbol{\gamma}_b^H\left(\boldsymbol{A}(\boldsymbol{\theta})\otimes\boldsymbol{R}(\bar{\boldsymbol{\tau}},\boldsymbol{\tau})\right)^H+\sigma^2\boldsymbol{I} \\ &= \left(\boldsymbol{A}(\boldsymbol{\theta})\otimes\boldsymbol{R}(\bar{\boldsymbol{\tau}},\boldsymbol{\tau})\right)\boldsymbol{R}_s\left(\boldsymbol{A}(\boldsymbol{\theta})\otimes\boldsymbol{R}(\bar{\boldsymbol{\tau}},\boldsymbol{\tau})\right)^H+\sigma^2\boldsymbol{I}\end{aligned} \tag{3.1}$$

As Section 2.2 mentions, multiple GNSS signals typically have different DFOs. As a result, when the matrix $\boldsymbol{R}_s$ is full rank, the subspace formed by the K eigenvectors corresponding to the K largest eigenvalues is known as the signal subspace [105]. Additionally, the eigenvectors of $\boldsymbol{R}_{\boldsymbol{y}_b}$ in Equation (3.1) can be divided into two parts: the signal subspace and the noise subspace.

$$\boldsymbol{R}_{\boldsymbol{y}_b}=\begin{pmatrix}\boldsymbol{U}_s & \boldsymbol{U}_n\end{pmatrix}\begin{pmatrix}\boldsymbol{\Lambda}_s & 0\\ 0 & \boldsymbol{\Lambda}_n\end{pmatrix}\begin{pmatrix}\boldsymbol{U}_s^H\\ \boldsymbol{U}_n^H\end{pmatrix} \tag{3.2}$$

where $\boldsymbol{U}_s$ and $\boldsymbol{U}_n$ are basis vectors for the signal and noise subspaces, respectively, consisting of eigenvectors. $\boldsymbol{\Lambda}_s$ is a diagonal matrix composed of the K largest eigenvalues, while $\boldsymbol{\Lambda}_n$ is a diagonal matrix containing the remaining eigenvalues. It is worth noting that the GNSS signal is necessarily contained in the signal subspace. Therefore, the following relationship exists

$$\boldsymbol{A}(\boldsymbol{\theta})\otimes\boldsymbol{R}(\bar{\boldsymbol{\tau}},\boldsymbol{\tau})=\boldsymbol{U}_s\boldsymbol{T}_s \tag{3.3}$$

Assuming that the signals are uncorrelated, $\boldsymbol{T}_s\in\mathbb{C}^{K\times K}$ is a full rank matrix that represents the spatial and temporal steering vectors of each signal by a linear combination of column vectors in $\boldsymbol{U}_s$. By substituting Equation (3.3) into (3.1) and comparing it with (3.2), it can be observed that

the diagonal matrix $\boldsymbol{\Lambda}_s$ can also be expressed as

$$\boldsymbol{\Lambda}_s \approx \boldsymbol{T}_s \boldsymbol{R}_s \boldsymbol{T}_s^{-H} \tag{3.4}$$

However, one of the basic conditions for the derivation above is the full rank of $\boldsymbol{R}_s$, which may not be satisfied in the GNSS multipath environments. As mentioned earlier, the frequency separation between different signals received by the antenna from the same satellite is relatively small and can be approximately considered coherent in a static scenario. This may result in significant singularity, high condition number, or even rank deficiency of $\boldsymbol{R}_s$. This leads to an inaccurate estimation of the number of input signals and affects the selection of column vectors in $\boldsymbol{U}_s$.

Similar to the coherent source incident problem in spatial processing, when the correlation between various signals is high, it is impossible to directly apply the subspace-based method as in the case of incoherent sources. The high condition number and significantly different eigenvalue distribution of $\boldsymbol{R}_s$ also estimate the signal subspace very sensitive to noise perturbations, resulting in inaccurate spatial estimates, especially at low signal-to-noise ratio or with fewer snapshots. Therefore, to utilize the convenience of the subspace-based method for multipath mitigation, it is necessary first to address the problem of coherent source estimation.

3.3.2 Joint Spatial and Frequential Smoothing

To address the multipath-mitigating problem, traditional spatial processing usually employs spatial smoothing techniques [106]. By exploiting the repetitive nature of the spatial steering vectors produced by the received signals, spatial smoothing divides the receiving array into multiple subarrays with similar spatial features. Then, by combining the auto-correlation matrices of each subarray, it achieves coherent signal separation at the cost of reducing the array aperture in the spatial domain. Since this thesis focuses on multipath mitigation, which belongs to the case of coherent source incidence, the general subspace decomposition method cannot separate the two signals due to the rank deficiency of the auto-correlation matrix. Therefore, this method further constructs an extended matrix based on the idea of spatial smoothing[106], introducing some spatial degrees of freedom into the frequency domain and increasing the resolution of the multipath signals.

Based on the analysis of temporally filtered GNSS signal model, as shown in Equation (2.6), it can be inferred that the time domain matrix $\boldsymbol{R}^T(\bar{\boldsymbol{\tau}}, \boldsymbol{\tau})$ is selected based on the values of the signal's auto-correlation function around its peaks. By utilizing the time delay set $\bar{\boldsymbol{\tau}}$ close to the coarse delay, the signal's time domain waveform can be reconstructed, and pointwise amplitude distortion caused by the signal waveform can be removed in the frequency domain. This also creates rotation invariance with respect to the time delay in the frequency domain. The performance can be further improved by transforming Equation (2.6) into the frequency domain and equalization, as demonstrated in [65].

$$\dot{\boldsymbol{Y}}_f(n) = \boldsymbol{A}(\boldsymbol{\theta})\,\mathrm{diag}(\boldsymbol{\gamma})\,\boldsymbol{P}^T(\boldsymbol{\tau}) + \dot{\boldsymbol{N}}_f(n) \tag{3.5}$$

where the frequential matrix $\boldsymbol{P}^T(\boldsymbol{\tau})$ is defined as $\boldsymbol{P}(\boldsymbol{\tau}) \doteq [\boldsymbol{p}(\tau_1), \ldots, \boldsymbol{p}(\tau_K)]$ and $\boldsymbol{p}(\tau_k) \doteq \left[1, \ldots, e^{-j\frac{2\pi(M_\tau-1)\tau_k}{M_\tau}}\right]^T$.

To construct a spatial and frequential GNSS similar to the construction of the spatial and temporal GNSS signal in Equation (2.7), we have

$$\boldsymbol{y}_{fb}(n) = (\boldsymbol{A}(\boldsymbol{\theta}) \otimes \boldsymbol{P}(\boldsymbol{\tau}))\,\boldsymbol{\gamma}_{fb} + \boldsymbol{n}_{fb}(n) \tag{3.6}$$

combining the steering vector of ULA in (2.8) and the spatial and frequential vector $\boldsymbol{p}(\tau_k) \otimes \boldsymbol{a}(\theta_k)$ in (3.6), it can be seen that despite being extended by the frequency vector $\boldsymbol{p}(\tau_k)$, the spatial characteristics behave a Vandermonde structure. This means traditional spatial smoothing techniques can still be applied to this spatial and frequential vector.

Taking the first $M_{\theta_s} M_\tau$ rows of $\boldsymbol{A}(\boldsymbol{\theta}) \otimes \boldsymbol{P}(\boldsymbol{\tau})$ to form the submatrix $(\boldsymbol{\Psi}_\theta \boldsymbol{A}(\boldsymbol{\theta})) \otimes \boldsymbol{P}(\boldsymbol{\tau})$, the matrix $\boldsymbol{\Psi}_\theta$ can be defined by selecting elements from $(\boldsymbol{\Psi}_\theta \boldsymbol{A}(\boldsymbol{\theta})) \otimes \boldsymbol{P}(\boldsymbol{\tau})$. Let the selection matrix be $\boldsymbol{\Psi}_\theta \doteq \left[\boldsymbol{I}_{M_{\theta_s}}, \boldsymbol{0}_{M_{\theta_s} \times (M_\theta - M_{\theta_s})}\right] \in \mathbb{C}^{M_{\theta_s} \times M_\theta}$. There are $N_{\theta_s} = M_\theta - M_{\theta_s} + 1$ groups of spatial smoothing available, one of which can be expressed as follows

$$\boldsymbol{x}_s(n) = ((\boldsymbol{\Psi}_\theta \boldsymbol{A}(\boldsymbol{\theta})) \otimes (\boldsymbol{P}(\boldsymbol{\tau})))\,(\boldsymbol{\Phi}_\theta)^{n_{\theta_s}-1} \boldsymbol{\gamma}_{fb} + \boldsymbol{n}_s(n) \tag{3.7}$$

where $\boldsymbol{\Phi}_\theta$ is a diagonal matrix composed of phase shifts generated by the angles of each signal on adjacent array elements in spatial domain.

$$\boldsymbol{\Phi}_\theta = \mathrm{diag}\left\{e^{j2\pi d \sin(\theta_1)/\lambda}, \ldots, e^{j2\pi d \sin(\theta_K)/\lambda}\right\} \tag{3.8}$$

Taking the first $(M_{\theta_s} - 1) M_\tau$ rows as $\boldsymbol{x}_{sx}$ and the last $(M_{\theta_s} - 1) M_\tau$ rows as $\boldsymbol{y}_{sy}$, it can be observed that both $\boldsymbol{x}_{sx}$ and $\boldsymbol{y}_{sy}$ behave a rotated invariant structure. They are respectively represented as

$$\boldsymbol{x}_{sx}(n) = \left(\left(\boldsymbol{\Psi}_\theta \bar{\boldsymbol{A}}(\boldsymbol{\theta})\right) \otimes (\boldsymbol{P}(\boldsymbol{\tau}))\right)(\boldsymbol{\Phi}_\theta)^{n_{\theta_s}-1} \boldsymbol{\gamma}_{fb} + \boldsymbol{n}_{sx}(n) \tag{3.9a}$$

$$\boldsymbol{y}_{sy}(n) = \left(\left(\boldsymbol{\Psi}_\theta \bar{\boldsymbol{A}}(\boldsymbol{\theta})\right) \otimes (\boldsymbol{P}(\boldsymbol{\tau}))\right)(\boldsymbol{\Phi}_\theta)^{n_{\theta_s}} \boldsymbol{\gamma}_{fb} + \boldsymbol{n}_{sy}(n) \tag{3.9b}$$

Through Equation (3.6), we primarily utilize the rotation invariance in spatial domain to perform smoothing operation, which makes the inherently low-rank covariance matrix full rank. It can also be observed that the frequential domain matrix $\boldsymbol{P}(\boldsymbol{\tau})$ has rotational invariance due to equalization. By extending the smoothing operation from spatial to spatial and frequential domains, the subspace method's ability to resolve multipath is further enhanced through this kind of smoothing.

Use the spatial selection matrix $\boldsymbol{\Psi}_\theta \doteq \left[\boldsymbol{I}_{M_{\theta_s}}, \mathbf{0}_{M_{\theta_s}\times(M_\theta - M_{\theta_s})}\right] \in \mathbb{C}^{M_{\theta_s}\times M_\theta}$ and the frequential selection matrix $\boldsymbol{\Psi}_\tau \doteq \left[\boldsymbol{I}_{M_{\tau_s}}, \mathbf{0}_{M_{\tau_s}\times(M_\tau - M_{\tau_s})}\right] \in \mathbb{C}^{M_{\tau_s}\times M_\tau}$ to select the first M_{θ_s} rows from the spatial matrix $\boldsymbol{A}(\boldsymbol{\theta})$ and the first M_{τ_s} rows from the frequential matrix $\boldsymbol{P}(\boldsymbol{\tau})$, respectively, to form a new spatial and frequential submatrix $(\boldsymbol{\Psi}_\theta \boldsymbol{A}(\boldsymbol{\theta})) \otimes (\boldsymbol{\Psi}_\tau \boldsymbol{P}(\boldsymbol{\tau}))$ in Equation (3.7). It can be seen that there are $N_\theta N_\tau$ groups of smoothing techniques available in both the spatial and temporal domains, with $N_{\theta_s} = (M_\theta - M_{\theta_s} + 1)$ and $N_{\tau_s} = (M_\tau - M_{\tau_s} + 1)$. One of these can be expressed as follows

$$\boldsymbol{x}_s(n) = ((\boldsymbol{\Psi}_\theta \boldsymbol{A}(\boldsymbol{\theta})) \otimes (\boldsymbol{\Psi}_\tau \boldsymbol{P}(\boldsymbol{\tau})))(\boldsymbol{\Phi}_\theta)^{n_{\theta_s}-1}(\boldsymbol{\Phi}_\tau)^{n_{\tau_s}-1}\boldsymbol{\gamma}_{fb} + \boldsymbol{n}_m(n) \tag{3.10}$$

where $\boldsymbol{\Phi}_\tau$ is a diagonal matrix composed of phase shifts generated by the delays of each signal on adjacent array elements in the frequential domain.

$$\boldsymbol{\Phi}_\tau = \text{diag}\left\{e^{-j2\pi\tau_1/M_\tau}, \ldots, e^{-j2\pi\tau_K/M_\tau}\right\} \tag{3.11}$$

The spatial and frequential smoothing process and submatrix selection can be summarized in 3.3.

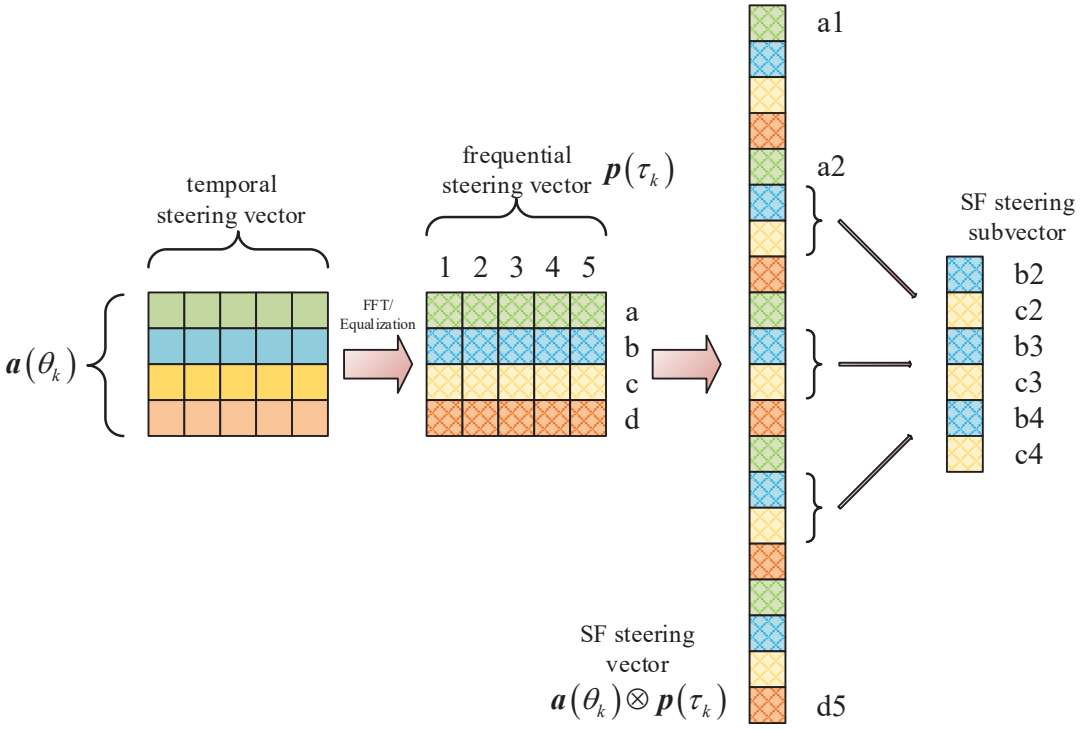


Figure 3.3: The spatial and frequential smoothing processing

Similarly, we have the subvectors $\boldsymbol{x}_{sx}$ and $\boldsymbol{y}_{ys}$

$$\boldsymbol{x}_{sx}(n) = \left(\left(\boldsymbol{\Psi}_\theta \bar{\boldsymbol{A}}(\boldsymbol{\theta})\right) \otimes \left(\boldsymbol{\Psi}_\tau \bar{\boldsymbol{P}}(\boldsymbol{\tau})\right)\right)(\boldsymbol{\Phi}_\theta)^{n_{\theta_s}-1}(\boldsymbol{\Phi}_\tau)^{n_{\tau_s}-1}\boldsymbol{\gamma}_{fb} + \boldsymbol{n}_{sx}(n) \tag{3.12a}$$

$$\boldsymbol{y}_{sy}(n) = \left(\left(\boldsymbol{\Psi}_{\theta}\bar{\boldsymbol{A}}(\boldsymbol{\theta})\right) \otimes \left(\boldsymbol{\Psi}_{\tau}\bar{\boldsymbol{P}}(\boldsymbol{\tau})\right)\right)(\boldsymbol{\Phi}_{\theta})^{n_{\theta_s}}(\boldsymbol{\Phi}_{\tau})^{n_{\tau_s}}\boldsymbol{\gamma}_{fb} + \boldsymbol{n}_{sy}(n) \tag{3.12b}$$

Under the condition of different angles for each signal, pure spatial processing can support coherent solutions for up to M_{θ_s} signals, which requires $M_{\theta_s} \geq K$. Unlike the spatial processing in [105], the spatial and frequential smoothing of the auto-correlation matrix benefits from the expansion of the frequency elements $\bar{\boldsymbol{P}}(\boldsymbol{\tau})$ in the spatial and frequential subarray steering vectors. This significantly reduces the requirement for the number of array elements during the smoothing, from $N_{\theta_s} \geq K$ to $N_{\tau_s}N_{\theta_s} \geq K$. Here, N_{τ_s} is the length of the frequential subvectors. Although $N_{\tau_s} \geq M_{\tau}$, the joint spatial and frequential processing method effectively treats the frequential subvectors as spatial elements, greatly increasing the estimated number of signals. Even for GNSS signals with BPSK modulation, the sampling rate is at least 4, and considering the need to fully reconstruct the whole signal by thoroughly sampling the main lobe, the value of M_{τ} is usually above 10. This makes the adequate number of elements in the spatial and frequential subvector $N_{\tau_s}N_{\theta_s}$ large enough such that only the smoothing factor M_{θ_s} needs to be considered during the spatial or spatial and frequential smoothing operations.

3.3.3 Joint Spatial and Temporal Estimation based on Subspace Method

According to the definitions of $\boldsymbol{x}_{sx}$ and $\boldsymbol{y}_{sy}$ in Equation (3.9) and (3.12), we know that the spatial-frequential subvectors output by these two adjacent submatrices have the same characteristic waveform matrix $\left(\left(\boldsymbol{\Psi}_{\theta}\bar{\boldsymbol{A}}(\boldsymbol{\theta})\right)\right) \otimes \left(\left(\boldsymbol{\Psi}_{\tau}\bar{\boldsymbol{P}}(\boldsymbol{\tau})\right)\right)$, the complex amplitude vector $\boldsymbol{\gamma}_{fb}$ are the same. The only difference is in the diagonal matrices $\boldsymbol{\Phi}_{\theta}$ and $\boldsymbol{\Phi}_{\tau}$, which correspond to the rotational invariance property of subspaces pointed out in ESPRIT [27]. Accordingly, an approach similar to DOA-Matrix [31] can be constructed by constructing a matrix, which can decompose the multipath signals into their respective angles and the joint spatial and temporal waveforms of the signals. This method can then be used to obtain the angles and delays of each signal. A simple derivation is provided below.

Firstly, compute the auto-correlation matrix within N code periods,

$$\boldsymbol{R}_{xx} = \frac{1}{N_{\tau_s}N_{\theta_s}} \sum_{n_{\tau_s}=1}^{N_{\tau_s}} \sum_{n_{\theta_s}=1}^{N_{\theta_s}} \boldsymbol{x}_{sx}(n)\, \boldsymbol{x}_{sx}^{H}(n) \tag{3.13}$$

The auto-covariance matrix of $\boldsymbol{R}_{xx}$ is recorded as

$$\boldsymbol{R}_{xx0} = \boldsymbol{R}_{xx} - \sigma^2\boldsymbol{I} \tag{3.14}$$

Meanwhile, compute the cross-correlation matrix

$$\boldsymbol{R}_{yx} = \frac{1}{N_{\tau_s} N_{\theta_s}} \sum_{n_{\tau_s}=1}^{N_{\tau_s}} \sum_{n_{\theta_s}=1}^{N_{\theta_s}} \boldsymbol{y}_{sy}(n)\, \boldsymbol{x}_{sx}^{H}(n) \tag{3.15}$$

An assumption has been made that each multipath signal's angle is different from others. Therefore, Equation (3.13) and (3.15) are full rank. According to (3.13) and (3.15), we have

$$\boldsymbol{R} = \boldsymbol{R}_{yx} \boldsymbol{R}_{xx} \tag{3.16}$$

then we have

$$\boldsymbol{R}\left(\left(\boldsymbol{\Psi}_{\theta} \bar{\boldsymbol{A}}(\boldsymbol{\theta})\right) \otimes \boldsymbol{P}(\boldsymbol{\tau})\right) = \left(\left(\boldsymbol{\Psi}_{\theta} \bar{\boldsymbol{A}}(\boldsymbol{\theta})\right) \otimes \boldsymbol{P}(\boldsymbol{\tau})\right) \boldsymbol{\Phi}_{\theta} \tag{3.17}$$

From Equation (3.16), the joint spatial and temporal subvector and angles can be obtained from the corresponding eigenvalue and eigenvector in eigen decomposition of $\boldsymbol{R}$. The Joint Angle and Delay Estimation with Spatial Smoothing DOAMatrix algorithm in (3.9) is abbreviated as JADE-SS-DOAMatrix, and the Joint Angle and Delay Estimation with Spatial and Frequential Smoothing DOAMatrix algorithm in (3.12) is short for JADE-SFS-DOAMatrix.

The JADE-SS-DOAMatrix and JADE-SFS-DOAMatrix algorithms can be summarized in the following Algorithm 1.

Algorithm 1 JADE-SS-DOAMatrix and JADE-SFS-DOAMatrix Algorithm

Input: The received signal $\dot{\boldsymbol{Y}}$ in N code periods and the number of signals K
Output: The estimated time delay set $\boldsymbol{\tau}$ and angle set $\boldsymbol{\theta}$

1: According to Equation (2.6), the vectorized signal $\dot{\boldsymbol{Y}}$ is conducted by temporal filter based on the acquisition information, and FFT processing is carried out to construct the spatial and temporal GNSS signal according to (3.5) and (3.6).
2: Apply spatial forward smoothing or space-frequency forward smoothing using Equations (3.7), (3.9), or (3.16), (3.17).
3: The spatial and temporal covariance matrix $\boldsymbol{R}_{xx}$ or $\boldsymbol{R}_{yx}$ is calculated based on the spatial and temporal vector after spatial smoothing or spatial and frequential smoothing and Equation (3.10) and (3.13).
4: Using the extended DOAMatrix method, and according to the formula (3.14) and (3.15), the angles and delays are obtained from the eigenvalues and eigenvectors, respectively.

3.4 Joint Spatial and Temporal Multipath Mitigation based on off-grid MSBL

Based on the robustness and effectiveness of MSBL in mitigating multipath signals [107], this section proposes three joint spatial-temporal multipath mitigation methods according to parameter estimation accuracy requirements for various GNSS applications. Firstly, we propose a joint angle

and delay estimation algorithm based on MSBL in a sparse spatial-temporal model that achieves simultaneous estimation of angle and delay, improves robustness against multipath, and adaptive capabilities in low signal-to-noise ratios and with few snapshots. Secondly, we combine on-grid and off-grid estimators with spatial-temporal domain processing to reduce computational complexity and improve parameter estimation accuracy. Thirdly, considering practical GNSS scenarios, three methods are proposed: JOADE-MSBL (joint on-grid angle and off-grid delay estimation based on MSBL) is proposed for cases where delay estimation requires more accuracy than angle estimation; JAODE-MSBL (joint off-grid angle and on-grid delay estimation based on MSBL) is proposed for reverse situations; Furthermore, the JOAODE-MSBL&SAGE (joint on-grid angle and on-grid delay estimation based on MSBL and SAGE) method, which uses SAGE to refine the estimation results of JOAODE-MSBL and obtain accurate angle and delay estimates.

JOADE-MSBL is described first, and the other two algorithms are outlined later.

3.4.1 Joint On-grid Angle and Off-grid Delay Estimation based on MSBL

The problem of joint on-grid angle and off-grid delay estimation consists in finding not only the set of nonzero indices of $\boldsymbol{X}$ but also the off-grid shifts $\boldsymbol{\beta}_\tau$ for the delays. A method based on the MSBL methodology is presented below.

Given that the additive noise $\boldsymbol{E}$ in (2.16) is assumed to be complex Gaussian with mean value zero and variance σ^2, the data likelihood for the sources $\boldsymbol{X}$ given the observation $\boldsymbol{Y}$ is complex Gaussian as

$$p\left(\boldsymbol{Y}\left|\boldsymbol{X},\lambda_n,\boldsymbol{\beta}_\tau\right.\right)=\prod_{n=1}^{N}\mathcal{CN}\left(\boldsymbol{y}_b\left(n\right)\left|\boldsymbol{\Phi}_{\boldsymbol{\beta}_\tau}\,\boldsymbol{x}_b\left(n\right)\right.,\lambda_n^{-1}\boldsymbol{I}_{M_\theta,M_\tau}\right) \tag{3.18}$$

A Gamma hyperprior (since it is a conjugate prior of the Gaussian distribution) is adopted for the unknown precision, $\lambda_n \doteq \sigma^{-2}$, and it can be expressed as

$$p\left(\lambda_n;a,b\right)=\mathcal{B}\left(\lambda_n\right|a,b) \tag{3.19}$$

with the hyperparameters a, b, and $\mathcal{B}\left(\lambda_n\right|a,b) \doteq [\Gamma\left(a\right)]^{-1}b^a\lambda_n^{a-1}e^{-b\lambda_n}$ being $\Gamma\left(a\right)\doteq\int_0^\infty x^{a-1}e^{-x}dx$ the Gamma function.

For the prior of $\boldsymbol{X}$, we assume that columns are uncorrelated between them and each one follows a zero-mean complex Gaussian distribution with angle-delay-dependent variance $\boldsymbol{\alpha} = [\alpha_1,\ldots,\alpha_{N_\theta N_\tau}]^T$ and $\boldsymbol{\Upsilon}=\operatorname{diag}\left(\boldsymbol{\alpha}\right)$,

$$p\left(\boldsymbol{X}\right|\boldsymbol{\alpha})=\prod_{n=1}^{N}\mathcal{CN}\left(\boldsymbol{x}_b\left[n\right]\right|0,\boldsymbol{\Upsilon}) \tag{3.20}$$

A two-stage hierarchical prior: $p\left(\boldsymbol{X};\rho\right)=\int p\left(\boldsymbol{X}\right|\boldsymbol{\alpha})p\left(\boldsymbol{\alpha};\rho\right)d\boldsymbol{\alpha}$ is adopted with hyperpa-

rameter $\rho > 0$

$$p(\boldsymbol{\alpha}, \rho) = \prod_{n_g=1}^{N_\theta N_\tau} \Gamma(\boldsymbol{\alpha}(n_g) | 1, \rho) \tag{3.21}$$

which promotes the row sparsity of $\boldsymbol{X}$, that is to say, it favors that most rows of $\boldsymbol{X}$ are zero.

For the off-grid parameter vector $\boldsymbol{\beta}_\tau$, a non-informative uniform prior is used

$$p(\boldsymbol{\beta}_\tau; r_\tau) = U\left(-\frac{1}{2}r_\tau, \frac{1}{2}r_\tau\right) \tag{3.22}$$

where we have

$$U([c,d]) = \begin{cases} \frac{1}{d-c}, & c \le x \le d \\ 0, & otherwise. \end{cases} \tag{3.23}$$

To estimate angle and delays, we can formulate the following problem to maximize the posterior probability given the received signal

$$\left\{\hat{\boldsymbol{X}}, \hat{\lambda}_n, \hat{\boldsymbol{\alpha}}, \hat{\boldsymbol{\beta}}_\tau\right\} = \arg \max_{\{\boldsymbol{X}, \alpha_n, \boldsymbol{\alpha}, \boldsymbol{\beta}_\tau\}} p(\boldsymbol{X}, \lambda_n, \boldsymbol{\alpha}, \boldsymbol{\beta}_\tau | \boldsymbol{Y}) \tag{3.24}$$

The problem of posterior probability above cannot be solved directly; hence, the EM method is applied to MSBL. By combining the stages of the hierarchical Bayesian model, the joint probability density function (PDF) is

$$p(\boldsymbol{X}, \boldsymbol{Y}, \lambda_n, \boldsymbol{\alpha}, \beta_\tau) = p(\boldsymbol{Y} | \boldsymbol{X}, \lambda_n, \boldsymbol{\beta}_\tau) p(\boldsymbol{X} | \boldsymbol{\alpha}) p(\boldsymbol{\alpha}) p(\lambda_n) p(\boldsymbol{\beta}_\tau) \tag{3.25}$$

with the distributions on the right-hand side as defined by (3.18), (3.20), (3.21), (3.19) and(3.22), respectively. To realize the proposed JOADE-MSBL, a graphical model is depicted in Figure 3.4 that the unknown parameters (written in circles) are determined by hyperparameters (written in rectangles).

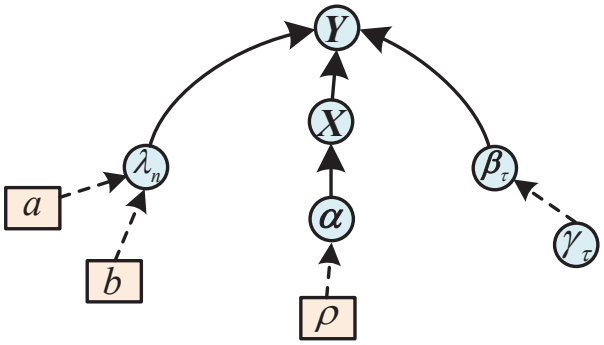


Figure 3.4: Graphical model of JOADE-MSBL

Given the likelihood of the array observations (3.18), and the priors (3.20) and (3.21), the posterior PDF for the source amplitudes $\boldsymbol{X}$ can be found using the Bayes rule conditioned on α_n

and $\boldsymbol{\alpha}$ as

$$p\left(\boldsymbol{X}\left|\boldsymbol{Y},\lambda_n,\boldsymbol{\alpha},\boldsymbol{\beta}_\tau\right.\right)\propto p\left(\boldsymbol{Y}\left|\boldsymbol{X},\lambda_n,\boldsymbol{\beta}_\tau\right.\right)p\left(\boldsymbol{X}|\boldsymbol{\alpha}\right) \tag{3.26}$$

It is easy to show that the posterior distribution of $\boldsymbol{X}$ is a complex Gaussian distribution, since both $p\left(\boldsymbol{Y}\left|\boldsymbol{X};\lambda_n,\boldsymbol{\beta}_\tau\right.\right)$ and $p\left(\boldsymbol{X};\rho\right)$ are Gaussian, with posterior mean $\boldsymbol{\mu}$ and covariance $\boldsymbol{\Sigma}$

$$\begin{aligned}\boldsymbol{\mu}\left(n\right)&=E\left\{\boldsymbol{x}_b\left(n\right)\left|\boldsymbol{Y},\lambda_n,\boldsymbol{\alpha},\boldsymbol{\beta}_\tau\right.\right\}\\&=\lambda_n\boldsymbol{\Sigma}\boldsymbol{\Phi}_{\beta_\tau}^H\boldsymbol{y}_b\left(n\right)\end{aligned} \tag{3.27}$$

$$\begin{aligned}\boldsymbol{\Sigma}&=E\left\{\left(\boldsymbol{x}_b\left(n\right)-\boldsymbol{\mu}\left(n\right)\right)\left(\boldsymbol{x}_b\left(n\right)-\boldsymbol{\mu}\left(n\right)\right)^H\left|\boldsymbol{Y},\lambda_n,\boldsymbol{\alpha},\boldsymbol{\beta}_\tau\right.\right\}\\&=\left(\lambda_n\boldsymbol{\Phi}_{\beta_\tau}^H\boldsymbol{\Phi}_{\beta_\tau}+\boldsymbol{\Upsilon}^{-1}\right)^{-1}\end{aligned} \tag{3.28}$$

where $n=1,\ldots,N$. The Woodbury matrix identity is applied to obtain $\boldsymbol{\Sigma}=\boldsymbol{\Upsilon}-\boldsymbol{\Upsilon}\boldsymbol{\Phi}_{\beta_\tau}^H\boldsymbol{\Sigma}_y^{-1}\boldsymbol{\Phi}_{\beta_\tau}\boldsymbol{\Upsilon}$, where the array data covariance $\boldsymbol{\Sigma}_y$ is

$$\begin{aligned}\boldsymbol{\Sigma}_y&=E\left\{\boldsymbol{y}_b\left(n\right)\boldsymbol{y}_b^H\left(n\right)\right\}\\&=\lambda_n^{-1}\boldsymbol{I}+\boldsymbol{\Phi}_{\beta_\tau}\boldsymbol{\Upsilon}\boldsymbol{\Phi}_{\beta_\tau}^H\end{aligned} \tag{3.29}$$

From the formulations mentioned above, hyperparameters λ_n, $\boldsymbol{\alpha}$, $\boldsymbol{\beta}_\tau$ are needed to be known to calculate $\boldsymbol{\mu}$ and $\boldsymbol{\Sigma}$. To address the estimation of hyperparameters, the EM algorithm is implemented. It treats $\boldsymbol{X}$ as a hidden variable and turns to maximizing $E\left\{\log p\left(\boldsymbol{X},\boldsymbol{Y},\lambda_n,\boldsymbol{\alpha},\boldsymbol{\beta}_\tau\right)\right\}$ with respect to each hyperparameter. Following a similar procedure as Tipping described [107], denoting $\boldsymbol{U}=\left[\boldsymbol{\mu}\left(1\right),\ldots,\boldsymbol{\mu}\left(N\right)\right]$, it is easy to obtain the following updates of λ_n and $\boldsymbol{\alpha}$ by maximizing $E\left\{\log p\left(\boldsymbol{X}\left|\boldsymbol{\alpha}\right.\right)p\left(\boldsymbol{\alpha}\right)\right\}$ and $E\left\{\log p\left(\boldsymbol{Y}\left|\boldsymbol{X},\lambda_n,\boldsymbol{\alpha},\boldsymbol{\beta}_\tau\right.\right)p\left(\lambda_n\right)\right\}$, respectively

$$\boldsymbol{\alpha}\left(n_g\right)=\frac{\sqrt{N^2+4\rho E\left\{\left\|\boldsymbol{X}\left(n_g,:\right)\right\|_2^2\right\}}-1}{2\rho} \tag{3.30}$$

$$\lambda_n=\frac{2M_\theta M_\tau\cdot N+a-1}{E\left\{\left\|\boldsymbol{Y}-\boldsymbol{\Phi}_{\boldsymbol{\beta}_\tau}\boldsymbol{X}\right\|_F^2\right\}\cdot N+b} \tag{3.31}$$

where $E\left\{\left\|\boldsymbol{X}\left(n_g,:\right)\right\|_2^2\right\}=\left\|\boldsymbol{U}\left(n_g,:\right)\right\|_2^2+\boldsymbol{\Sigma}\left(n_g,n_g\right)$, $E\left\{\left\|\boldsymbol{Y}-\boldsymbol{\Phi}_{\beta_\tau}\boldsymbol{X}\right\|_F^2\right\}=\left\|\boldsymbol{Y}-\boldsymbol{\Phi}_{\beta_\tau}\boldsymbol{U}\right\|_F^2+\boldsymbol{\alpha}\left(n_g\right)\sum_{n=1}^{N_\theta N_\tau}\varsigma\left(n_g\right)$, and $\boldsymbol{\varsigma}\left(n_g\right)=1-\boldsymbol{\alpha}^{-1}\left(n_g\right)\boldsymbol{\Sigma}\left(n_g,n_g\right)$ when $n_g=1,\ldots,2N_\theta N_\tau$.

As for the off-grid vector $\boldsymbol{\beta}_\tau$, we can obtain the following likelihood function by maximizing $E\left\{\log p\left(\boldsymbol{Y}\left|\boldsymbol{X},\lambda_n,\boldsymbol{\beta}_\tau\right.\right)p\left(\boldsymbol{\beta}_\theta\right)\right\}$, what results in the following expression after ignoring the terms

independent of $\boldsymbol{\beta}_\tau$

$$\begin{aligned} & E\left\{\tfrac{1}{N}\sum_{n=1}^{N}\left\|\boldsymbol{y}_b\left(n\right)-\boldsymbol{\Phi}_{\beta_\tau}\boldsymbol{x}_b\left(n\right)\right\|_2^2\right\} \\ &= \tfrac{1}{N}\sum_{n=1}^{N}\left\|\boldsymbol{y}_b\left(n\right)-\boldsymbol{\Phi}_{\beta_\tau}\boldsymbol{\mu}\left(n\right)\right\|_2^2+\mathrm{tr}\left\{\boldsymbol{\Phi}_{\beta_\tau}\boldsymbol{\Sigma}\boldsymbol{\Phi}_{\beta_\tau}^H\right\} \\ &= \boldsymbol{\beta}_\tau^T\boldsymbol{P}_\tau\boldsymbol{\beta}_\tau-2\boldsymbol{v}_\tau^T\boldsymbol{\beta}_\tau+C_1 \end{aligned} \tag{3.32}$$

where C_1 is a constant term independent of $\boldsymbol{\beta}_\tau$. $\boldsymbol{P}_\tau$ is a positive semi-definite matrix

$$\begin{aligned} \boldsymbol{P}_\tau = & \mathfrak{Re}\left\{\tfrac{1}{N}\sum_{n=1}^{N}\boldsymbol{\Xi}_\tau^H\boldsymbol{\Xi}_\tau\right\}+ \\ & \mathfrak{Re}\left\{\boldsymbol{J}_{N_\theta N_\tau\times N_\tau}^T\left(\boldsymbol{\Sigma}\odot\left(\boldsymbol{A}\otimes\boldsymbol{B}_\tau\right)^H\left(\boldsymbol{A}\otimes\boldsymbol{B}_\tau\right)\right)\boldsymbol{J}_{N_\theta N_\tau\times N_\tau}\right\} \end{aligned} \tag{3.33}$$

$$\begin{aligned} \boldsymbol{v}_\tau = & \mathfrak{Re}\left\{\tfrac{1}{N}\sum_{n=1}^{N}\left\{\left(\boldsymbol{y}_b\left(n\right)-\left(\boldsymbol{A}\otimes\boldsymbol{C}\right)\boldsymbol{\mu}\left(n\right)\right)^H\boldsymbol{\Xi}_\tau\right\}^T\right\} \\ & -\mathfrak{Re}\left\{\left\{\mathrm{diag}\left(\left(\boldsymbol{A}\otimes\boldsymbol{B}_\tau\right)^H\left(\boldsymbol{A}\otimes\boldsymbol{C}\right)\boldsymbol{\Sigma}\right)\right\}^T\boldsymbol{J}_{N_\theta N_\tau\times N_\tau}{}^T\right\} \end{aligned} \tag{3.34}$$

with $\boldsymbol{\Xi}_\tau = \left(\left(\boldsymbol{A}\cdot\mathrm{mat}\boldsymbol{\mu}^{\mathrm{T}}\left(\mathrm{n}\right)\right)\otimes\boldsymbol{I}_{M_\tau}\right)\left(\boldsymbol{I}_{N_\tau}\otimes\boldsymbol{B}_\tau\right)\boldsymbol{J}_{N_\tau^2\times N_\tau}$ and $\mathrm{mat}\boldsymbol{\mu}\left(n\right)\in\mathbb{C}^{2N_\theta\times N_\tau}$ being a reshaped matrix of $\boldsymbol{\mu}\left(n\right)$. $\boldsymbol{J}_{N_\theta N_\tau\times N_\tau}$ is defined by $\boldsymbol{J}_{N_\theta N_\tau\times N_\tau}\doteq\boldsymbol{1}_{N_\theta}\otimes\boldsymbol{I}_{N_\tau}$. $\boldsymbol{J}_{(N_\tau)^2\times N_\tau}$ is with the element of $\left(N_\tau\left(m_\tau-1\right)+m_\tau\right)$ th row m_τ th column being one, $m_\tau=1,\ldots,N_\tau$ and other elements being zero. Besides the detailed derivation of (3.32)-(3.34) is shown in Appendix 3.8.

For the purpose of estimating $\boldsymbol{\beta}_\tau$, we have

$$\hat{\boldsymbol{\Phi}}_\tau=\arg\min_{\boldsymbol{\beta}_\tau\in\left[-\frac{1}{2}r_\tau,\frac{1}{2}r_\tau\right]}\left\{\boldsymbol{\beta}_\tau^T\boldsymbol{P}_\tau\boldsymbol{\beta}_\tau-2\boldsymbol{v}_\tau^T\boldsymbol{\beta}_\tau\right\} \tag{3.35}$$

To simplify the above calculation, by (3.35) and $\frac{\partial}{\partial\boldsymbol{\beta}_\tau}\left\{\boldsymbol{\beta}_\tau^T\boldsymbol{P}_\tau\boldsymbol{\beta}_\tau-2\boldsymbol{v}_\tau^T\boldsymbol{\beta}_\tau\right\}=2\left(\boldsymbol{P}_\tau\boldsymbol{\beta}_\tau-\boldsymbol{v}_\tau\right)$ we have $\hat{\boldsymbol{\beta}}_\tau=\boldsymbol{P}_\tau^{-1}\boldsymbol{v}_\tau$ in case of $\boldsymbol{P}_\tau$ being invertible.

3.4.2 Joint Off-grid Angle and On-grid Delay Estimation based on MSBL

After describing in detail the derivation of JOADE-MSBL, we sketch how the other estimators are obtained since the derivation follows similar steps to the previous ones, so we highlight only the differences.

Following the sparse model (2.16) and (2.17) for JOADE-MSBL, the solutions of $\boldsymbol{\alpha}$ and λ_n can be obtained by adopting the same steps of (3.30) and (3.31). We can compute the off-grid angle estimate vector $\boldsymbol{\beta}_\theta$ following the same procedure described in (3.32)-(3.35) with the corresponding

changes in the expressions:

$$\begin{aligned} & E\left\{\frac{1}{N}\sum_{n=1}^{N}\left\|\boldsymbol{y}_b\left(n\right)-\boldsymbol{\Phi}_{\beta_\theta}\boldsymbol{x}_b\left(n\right)\right\|_2^2\right\} \\ &= \frac{1}{N}\sum_{n=1}^{N}\left\|\boldsymbol{y}_b\left(n\right)-\boldsymbol{\Phi}_{\beta_\theta}\boldsymbol{\mu}\left(n\right)\right\|_2^2+\mathrm{tr}\left\{\boldsymbol{\Phi}_{\beta_\theta}\boldsymbol{\Sigma}\boldsymbol{\Phi}_{\beta_\theta}^H\right\} \\ &= \boldsymbol{\beta}_\theta^T\boldsymbol{P}_\theta\boldsymbol{\beta}_\theta-2\boldsymbol{v}_\theta^T\boldsymbol{\beta}_\theta+C_2 \end{aligned} \tag{3.36}$$

with the matrix $\boldsymbol{P}_\theta$ and the vector $\boldsymbol{v}_\theta$ given by

$$\begin{aligned} \boldsymbol{P}_\theta = & \mathfrak{Re}\left\{\frac{1}{N}\sum_{n=1}^{N}\boldsymbol{\Xi}_\theta^H\boldsymbol{\Xi}_\theta\right\}+ \\ & \mathfrak{Re}\left\{\boldsymbol{J}_{N_\theta N_\tau\times N_\theta}^T\left(\boldsymbol{\Sigma}\odot\left(\boldsymbol{B}_\theta\otimes\boldsymbol{C}\right)^H\left(\boldsymbol{B}_\theta\otimes\boldsymbol{C}\right)\right)\boldsymbol{J}_{N_\theta N_\tau\times N_\theta}\right\} \end{aligned} \tag{3.37}$$

$$\begin{aligned} \boldsymbol{v}_\theta = & \mathfrak{Re}\left\{\frac{1}{N}\sum_{n=1}^{N}\left\{\left(\boldsymbol{y}_b\left(n\right)-\left(\boldsymbol{A}\otimes\boldsymbol{C}\right)\boldsymbol{\mu}\left(n\right)\right)^H\boldsymbol{\Xi}_\theta\right\}\right\} \\ & -\mathfrak{Re}\left\{\left\{\mathrm{diag}\left(\left(\boldsymbol{B}_\theta\otimes\boldsymbol{C}\right)^H\left(\boldsymbol{A}\otimes\boldsymbol{C}\right)\boldsymbol{\Sigma}\right)\right\}^T\boldsymbol{J}_{N_\theta N_\tau\times N_\tau}\right\} \end{aligned} \tag{3.38}$$

In the above equations, $\boldsymbol{\Xi}_\theta = \left(\boldsymbol{B}_\theta\otimes\boldsymbol{I}_{M_\tau}\right)\left(\boldsymbol{I}_{N_\theta}\otimes\left(\boldsymbol{C}\cdot mat\boldsymbol{\mu}\left(n\right)\right)\right)\boldsymbol{J}_{N_\theta^2\times N_\theta}$. $\boldsymbol{J}_{N_\theta N_\tau\times N_\tau}$ is defined by $\boldsymbol{J}_{N_\theta N_\tau\times N_\theta}\doteq\left[\boldsymbol{O}_{N_\tau\times N_\theta}\left(1\right),\ldots,\boldsymbol{O}_{N_\tau\times N_\theta}\left(N_\theta\right)\right]^T$, and the n_θ th matrix $\boldsymbol{O}_{N_\tau\times N_\theta}\left(n_\theta\right)$ is with the n_θ th column being one and the other entries being zeros. $\boldsymbol{J}_{N_\theta^2\times N_\theta}$ is with the element of $\left(N_\theta\left(m_\theta-1\right)+m_\theta\right)$ th row and m_θ th column being one where $m_\theta=1,\ldots,N_\theta$ and other entries being zeros. The JOADE-MSBL and JAODE-MSBL are summarized in Algorithm 2.

Algorithm 2 JOADE-MSBL and JAODE-MSBL algorithms

Require: $\boldsymbol{Y}$, $\boldsymbol{A}$ and $\boldsymbol{C}$, $\boldsymbol{B}_\theta$ or $\boldsymbol{B}_\tau$ and the number of signals K
Ensure: $\boldsymbol{\alpha}$, $\boldsymbol{\beta}_\tau$ and $\boldsymbol{\beta}_\theta$
1: $\lambda_n=100/var\left\{\boldsymbol{Y}\right\}$, $\boldsymbol{\beta}_\theta=\boldsymbol{0}$, or $\boldsymbol{\beta}_\tau=\boldsymbol{0}$.
2: The hyperparameters are defined as $a=b=1\times10^{-4}$ and $\rho=0.01$.
3: **while** it meets $\varepsilon\leq10^{-3}$ or exceeds the maximum iteration ≤ 500 **do**
4: Calculate $\boldsymbol{\mu}$, $\boldsymbol{\Sigma}$ and $\boldsymbol{\Phi}_{\beta_\tau}$ or $\boldsymbol{\Phi}_{\beta_\theta}$ using the current values of the hyperparameters according to (3.26), (3.27), (3.28), and (2.17) or (2.18), respectively.
5: Update $\boldsymbol{\alpha}$ and λ_n according to (3.30) and (3.31) with the sparse model $\boldsymbol{\Phi}_{\beta_\tau}$ or $\boldsymbol{\Phi}_{\beta_\theta}$.
6: Find $K+1$ largest peaks in $\boldsymbol{\alpha}$ and calculate the corresponding angles and delays grid numbers, respectively.
7: Update $\boldsymbol{\beta}_\theta$ or $\boldsymbol{\beta}_\tau$ according to (3.32), (3.33), (3.34) or (3.36), (3.37), (3.38).
8: Calculate the error $\varepsilon=\left\|\boldsymbol{\alpha}^{new}-\boldsymbol{\alpha}^{old}\right\|_2/\left\|\boldsymbol{\alpha}^{old}\right\|_2$.
9: **end while**

3.4.3 Joint Angle and Delay Estimation based on MSBL and SAGE

Thanks to the robustness against correlated multipath, JOADE-MSBL and JAODE-MSBL are powerful methods to obtain either accurate delay or angle estimates. However, high resolution in both angle and delay may be needed in specific GNSS use cases. The SAGE algorithm [22, 23] provides a

way to achieve super-resolution and unbiased estimates, but it has the drawback that it only guarantees local optimality, which makes it extremely sensitive to initial values. Therefore, a combination of SAGE and JOAODE-MSBL is proposed whereby JOAODE-MSBL provides with SAGE the precise initialization values; meanwhile, SAGE returns the finer estimates.

The graphical model of JOAODE-MSBL is depicted in Figure 3.5 that the unknown parameters (written in circles) are determined by hyperparameters (written in rectangles).

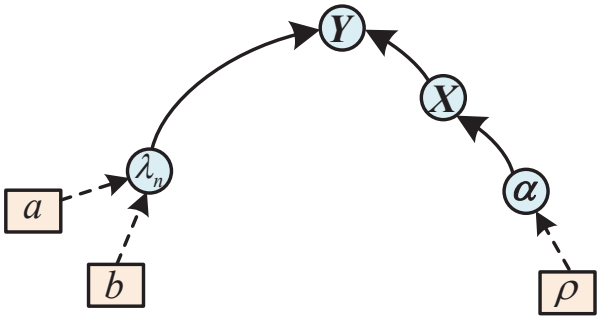


Figure 3.5: Graphical model of JOAODE-MSBL

As Fleury [22] described, the basic concepts of SAGE are the hidden data space breaking down the multi-dimensional optimization problem into several smaller ones, and the parameter estimation for each path by sequentially conditioning on a subset of parameters while keeping the parameters of the complement subset fixed.

According to model (2.2), we introduce a definition of $\boldsymbol{s}_k(t) \doteq \gamma_k \boldsymbol{a}(\theta_k)\, c(t-\tau_k)$. After collecting N code periods and we get

$$\boldsymbol{Y}_N = [\boldsymbol{y}(1), \ldots, \boldsymbol{y}(L), \ldots, \boldsymbol{y}((N-1)L+1), \ldots, \boldsymbol{y}((N-1)L+L)] \in \mathbb{C}^{M_\theta \times LN} \tag{3.39}$$

and $\boldsymbol{S}_{N,k} \in \mathbb{C}^{M_\theta \times LN}$, $\boldsymbol{E}_{N,k} \in \mathbb{C}^{M_\theta \times LN}$, $\boldsymbol{c}_N(\tau_k) \in \mathbb{C}^{1 \times LN}$. The stochastic mapping of the hidden data space to the observed signal is $\boldsymbol{Y}_N = \boldsymbol{X}_{N,k} + \sum_{k'=1,k' \neq k}^{K} \left(\boldsymbol{S}_{N,k'} + \boldsymbol{E}_{N,k'}\right)$ where $\boldsymbol{X}_{N,k} \doteq \boldsymbol{S}_{N,k} + \boldsymbol{E}_{N,k}$. After estimating the hidden data space in the so-called expectation step with

$$\hat{\boldsymbol{X}}_{N,k} = \boldsymbol{Y}_N - \sum_{k'=1,k' \neq k}^{K} \hat{\boldsymbol{S}}_{N,k'} \tag{3.40}$$

where $\boldsymbol{S}_{N,k} = \boldsymbol{a}(\theta_k)\, \gamma_k \boldsymbol{c}_N(\tau_k)$. The maximization step is used to estimate in each hidden data space

$$z(\theta_k, \tau_k, v_k) = \boldsymbol{a}^H(\theta_k)\, \hat{\boldsymbol{X}}_{N,k} \boldsymbol{c}_N^H(\tau_k) \tag{3.41a}$$

$$\hat{\theta_k} = \arg\max_{\theta_k} \left\{ |z(\theta_k, \hat{\tau}_k, \hat{v}_k)|^2 \right\} \tag{3.41b}$$

$$\hat{\tau_k} = \arg\max_{\tau_k} \left\{ \left| z\left(\hat{\theta}_k, \tau_k, \hat{v}_k\right) \right|^2 \right\} \tag{3.41c}$$

$$\hat{\gamma}_k = \frac{z\left(\hat{\theta}_k, \hat{\tau}_k, \hat{v}_k\right)}{M_\theta LN} \tag{3.41d}$$

which are performed. Obviously, the estimated hidden data space in (3.40) is the vulnerable step that requires precise estimates to ensure the correct path elimination, and these estimates can be the on-grid estimated angles and delays obtained with JOAODE-MSBL. The JOAODE-MSBL&SAGE algorithm is outlined in Algorithm 3.

Algorithm 3 JOAODE-MSBL&SAGE algorithm

Input: $\boldsymbol{Y}$, $\boldsymbol{A}$ and $\boldsymbol{C}$ and the number of signals K
Output: The estimated time delay set $\boldsymbol{\tau}$ and angle set $\boldsymbol{\theta}$
1: $\lambda_n = 100/var\{\boldsymbol{Y}\}$.
2: The hyperparameters are defined as $a = b = 1 \times 10^{-4}$ and $\rho = 0.01$.
3: **while** it meets $\varepsilon \leq 10^{-3}$ or exceeds the maximum iteration ≤ 500 **do**
4: Calculate $\boldsymbol{\mu}$, $\boldsymbol{\Sigma}$ and $\boldsymbol{\Phi}$ using the current values of the hyperparameters according to (3.26), (3.27), (3.28) and (2.14) respectively.
5: Update $\boldsymbol{\alpha}$ and λ_n according to (3.29) and (3.30) with the sparse model $\boldsymbol{\Phi}$.
6: Find the $K+1$ largest peaks in $\boldsymbol{\alpha}$ and calculate the corresponding angles and delays grid numbers, respectively.
7: Calculate the error $\varepsilon = \left\|\boldsymbol{\alpha}^{new} - \boldsymbol{\alpha}^{old}\right\|_2 / \left\|\boldsymbol{\alpha}^{old}\right\|_2$.
8: **end while**

3.5 Complexity and Convergence Analysis

3.5.1 Complexity Analysis

In Section 3.3, the two subspace-based methods differ only in the type of smoothing applied, either in the spatial or joint spatial and frequential domains. Therefore, their computational complexities are approximately similar and mainly involve one FFT, one matrix decomposition, and one matrix inversion. For instance, the computational complexity of a complex multiplication for one FFT should be $O\left(LN \cdot \log_2\left(L\right)\right)$. Due to the acquisition information, the GNSS signal is filtered to the time domain, and a segment near the peak value of the ACF is extracted. As a result, the complexity is reduced to almost $O\left(M_\tau N \cdot \log_2\left(M_\tau\right)\right)$. The assumption is that $M_\tau \ll L$ significantly reduces the computational complexity compared to performing an FFT directly on the original signal. Both matrix decomposition and inversion are equally complex as they are performed on a joint spatial and temporal matrix and consume resources up to $O\left(\left(M_\theta M_\tau\right)^3\right)$.

The computational complexity of the SAGE mainly depends on the resource consumption of each dimension's search. In this section, we used 2D-SAGE, so the complexity of SAGE can be expressed as $O\left(2K \cdot LN \cdot N_n \cdot I_S\right)$, where N_n represents the number of search points per dimension (assuming that the number of search points is the same for all dimensions), and I_S denotes the number of iterations. The number of search points in SAGE changes with search precision, and

generally, the iteration count of SAGE should be at least 10 times with over 200 search points.

For the JADE-MSBL, the computational complexity of the three proposed MSBL algorithms is almost the same. The most complex operation in each iteration is the inversion of the spatial and temporal matrix, which has a complexity of $O\left(\left(N_\theta N_\tau\right)^3\right)$. After multiple iterations, the overall complexity can reach $O\left(I_L \cdot \left(N_\theta N_\tau\right)^3\right)$, where I_L denotes the number of iterations required. Generally, the JADE-MSBL algorithms should have at least 30 iterations.

The above three methods can be summarized as Table 3.1.

Table 3.1: Complexity Analysis

Methods	FFT	Decomposition	Matrix Inversion	Searching
JADE-DOAMatrix	$O\left(M_\tau N \log_2\left(M_\tau\right)\right)$	$O\left(\left(M_\theta M_\tau\right)^3\right)$	$O\left(\left(M_\theta M_\tau\right)^3\right)$	/
JOAODE-MSBL	/	/	$O\left(I_L (N_\theta N_\tau)^3\right)$	/
SAGE	/	/	/	$O\left(2KLNN_nI_S\right)$

The joint spatial and temporal subspace-based multipath mitigation has a clear advantage in terms of computational complexity compared to SAGE or the joint spatial and temporal MSBL-based multipath mitigation methods. Although the SAGE algorithm has fewer iterations, its complexity increases significantly with the number of search points and multipath signals. On the other hand, the MSBL-based method is not affected by the number of multipath signals, but due to more iterations and an increase or decrease in the spatial and temporal dimensions caused by grid division, its complexity is relatively high.

3.5.2 Convergence Analysis

The hyperparameters $\boldsymbol{\alpha}$, λ_n are estimated by a type-III ML, i.e., by maximizing the evidence that was treated as constant in (3.26), and the cost function can be expressed as

$$\begin{aligned} \ell\left(\boldsymbol{\alpha}, \lambda_n\right) &= \log p\left(\boldsymbol{Y} \mid \lambda_n, \alpha, \beta_\tau\right) \\ &= \int p\left(\boldsymbol{Y} \mid \boldsymbol{X}, \lambda_n, \alpha, \beta_\tau\right) p\left(\boldsymbol{X} \mid \alpha\right) d\boldsymbol{X} \\ &\propto -\operatorname{tr}\left(\boldsymbol{Y}^H \boldsymbol{\Sigma}_y^{-1} \boldsymbol{Y}\right) - N \log\left|\boldsymbol{\Sigma}_y\right| \end{aligned} \tag{3.42}$$

where the EM method is adopted to minimize (3.42). The hyperparameters updating rules are derived from the cost function $\ell\left(\boldsymbol{\alpha}, \lambda_n\right)$ with respect to $\boldsymbol{\alpha}$ and λ_n, denoting as

$$\boldsymbol{\alpha}^{new}\left(n_g\right) = \frac{\left(\boldsymbol{\alpha}^{old}\left(n_g\right)\right)^2}{N} \left\|\boldsymbol{Y}^H \boldsymbol{\Sigma}_y^{-1} \boldsymbol{\Phi}_{\beta_\tau}\left(:, n_g\right)\right\|_2^2 + \boldsymbol{\Sigma}\left(n_g, n_g\right) \tag{3.43}$$

The sequence of parameter estimates in the EM iteration converges [108]. However, conver-

gence is guaranteed toward a local optimum of the marginal log-likelihood $\log p\left(\boldsymbol{Y}, \lambda_n, \boldsymbol{\beta}_\tau\right)$ [35]. Guarantees for convergence can be given provided $\left|\partial \boldsymbol{\alpha}^{new}\left(n_g\right) / \partial \boldsymbol{\alpha}^{old}\left(n_g\right)\right| < 1$ but is hard to prove analytically [13, 35], while we can observe the convergence of the proposed methods through simulations.

To demonstrate the convergence performance of the proposed methods, the simulations in terms of spatial and temporal spectra, convergence rate, the estimated variance of noise, and RMSEs via increased iterations are shown in the following subsections. The three proposed methods based on MSBL have similar convergence performance, and here we only take JOADE-MSBL as an example. The simulation is conducted with a carrier-to-noise ratio of $C/N_0 = 45$ dB-Hz. In the simulation, we define the highly spatial correlation as the angle difference between the LOS signal and the multipath signal less than half of the main lobe of beamwidth. Similarly, highly temporal correlation is defined as the time delay difference between the LOS signal and the multipath signal is less than half of the chip T_c [25, 75]. These definitions will be used consistently throughout the rest of the thesis. Two simulation scenarios are set in this section. One is temporally correlated, where the time delays of the LOS signal and the multipath signal are $0.03\,T_c$ and $0.38\,T_c$, respectively, and the angles are $0.3°$ and $30.8°$, respectively. The other scenario is both highly spatially and temporally correlated, where the time delays of the LOS signal and the multipath signal are $0.03\,T_c$ and $0.38\,T_c$, respectively, and the angles are $0.3°$ and $6.8°$, respectively. All channel and name settings are consistent with Subsection 3.6.1.

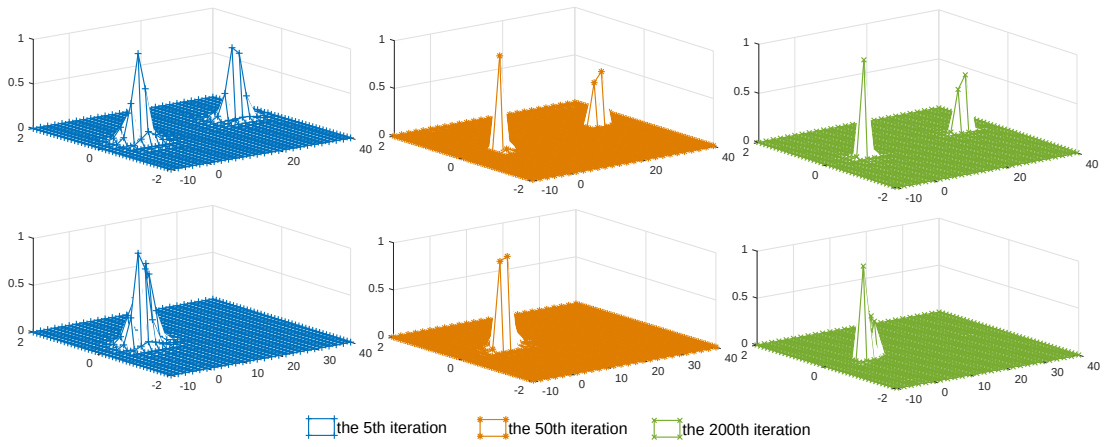


Figure 3.6: The spatial and temporal spectra of JOADE-MSBL with temporally correlated signals (1st row) and spatially and temporally correlated signals (2nd row)

The spatial and temporal spectra of JOADE-MSBL under two different correlated situations and varied iterations are displayed in Figure 3.6. As the number of iterations increases, the mitigation results of the LOS signal and the multipath signal become better, from having a clear main peak at the beginning to finally removing the multipath interference completely.

The convergence rate $\varepsilon = \left\|\boldsymbol{\alpha}^{new} - \boldsymbol{\alpha}^{old}\right\|_2 / \left\|\boldsymbol{\alpha}^{old}\right\|_2$ of JOADE-MSBL in different correlated

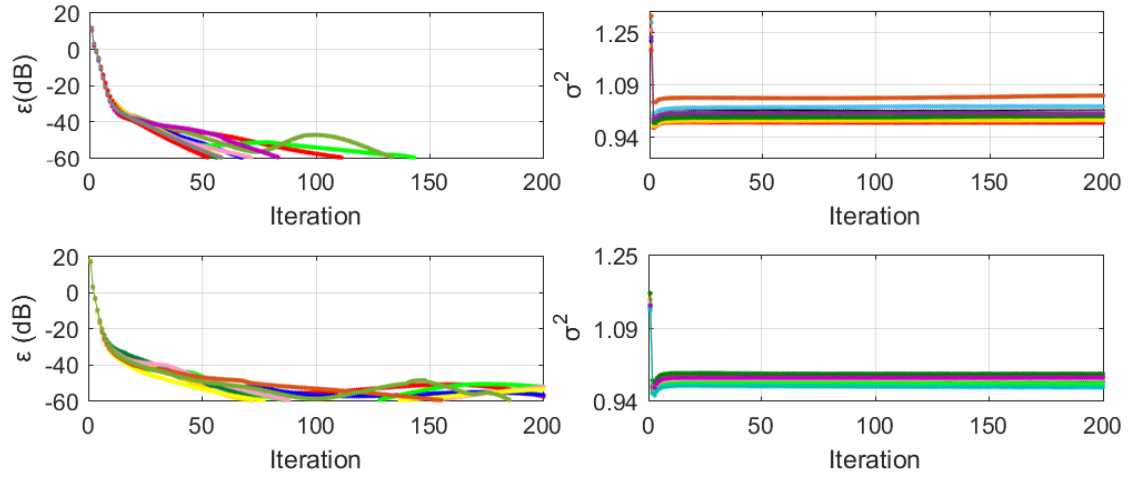


Figure 3.7: Convergence rate ε and noise variance σ^2 of JOADE-MSBL for 10 monte carlo simulations with temporally correlated signals (1st row) and spatially and temporally correlated signals (2nd row)

scenarios are demonstrated in Figure 3.7. JOADE-MSBL exhibits good convergence (with $\varepsilon_{\min} = -60$ dB defined) and the convergence rate is faster in purely temporal correlated scenario than in the spatial and temporal correlated scenario. At the same time, as the number of iterations increases, the noise variance can converge quickly to a fixed value.

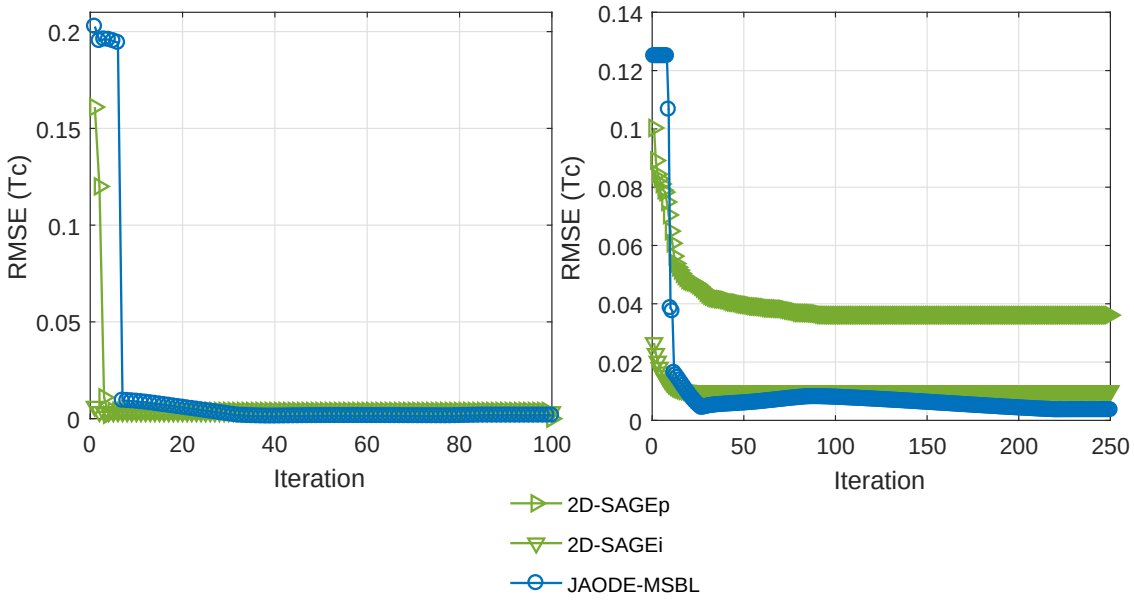


Figure 3.8: The RMSEs via increased iterations with temporally correlated signals (left panel) and spatially and temporally correlated signals (right panel)

To observe the relationship between the number of iterations and the multipath mitigation performance, the RMSE of JOADE-MSBL and SAGE are compared. In the case of temporally cor-

related signals, as shown in Figure 3.8, it can be seen that 2D-SAGE, whether ideal or practical initialization, has a faster convergence rate than JAODE-MSBL. 2D-SAGE only converges a few iterations, while JAODE-MSBL requires twice as many iterations to achieve nearly the same performance. In particular, on the correlation between signals, a relatively low number of iterations for JOADE-MSBL between 10 and 25 suffices.

3.6 Simulation Results and Performance Analysis

In this section, we evaluate the root mean square error (RMSE) performance of the subspace-based and off-grid MSBL-based methods to mitigate multipath effects in simulation. We assess their performance under varying carrier-to-noise ratio (C/N_0) and varying angle and time delay differences between LOS signals and multipath signals. The simulations use GPS L1 C/A code signals as the target signal to validate the effectiveness of the proposed methods.

3.6.1 RMSEs as a Function of C/N_0

The RMSEs of the subspace-based and off-grid MSBL methods as a function of C/N_0 are displayed. In the following two subsections, we assume the use of an 8-element uniform linear array (ULA) with half-wavelength spacing between elements. The simulations assume the presence of a LOS signal and a multipath signal, and the signal-to-multipath ratio (SMR) is defined as 3 dB.

RMSEs of JADE-DOAMatrix as a Function of C/N_0

We observe a 100 ms signal, corresponding to using $N = 100$ C/A code periods. The RMSEs of JADE-SS-DOAMatrix, JADE-SFS-DOAMatrix, and their CRLB as a function of C/N_0 are shown under two multipath scenarios. One multipath scenario is with only temporal correlation conditions, and the other one is with spatial and temporal correlation conditions. The LOS and multipath signals have time delays of $0\,T_c$ and $0.6\,T_c$, respectively, but are incident from different angles in the spatial domain. In the temporal-only correlated scenario, they are from 0° and 60°, respectively. In spatial and temporally correlated scenarios, they are from 0° and 10°, respectively.

Figure 3.9 compares the two joint spatial and temporal subspace-based algorithms. In the case of separable space (left panel), the performance of JADE-SS-DOAMatrix and JADE-SFS-DOAMatrix algorithms are close to CRLB. However, in the right panel, JADE-SS-DOAMatrix, which only relies on spatial smoothing to solve the rank deficit problem of the covariance matrix, cannot effectively distinguish multipath signals in highly spatially correlated cases. By contrast, JADE-SFS-DOAMatrix adopts both spatial smoothing and frequential smoothing, which ensures the full rank requirement of the covariance matrix. Therefore, it can distinguish multipath more effectively than JADE-SS-DOAMatrix when the C/N_0 is over 39 dB-Hz.

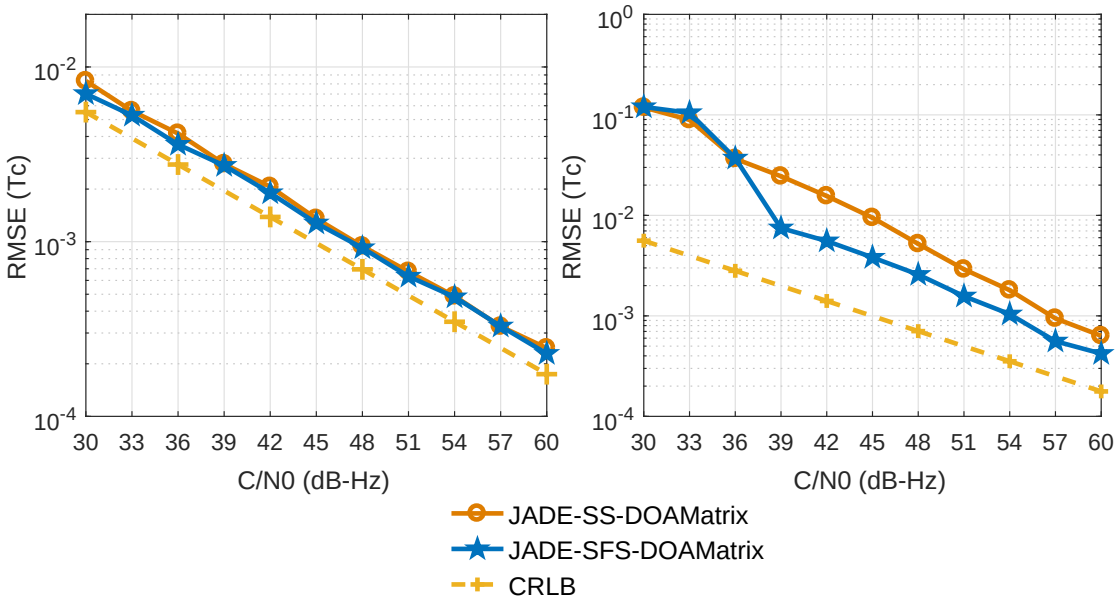


Figure 3.9: RMSEs of LOS signal time delay via C/N_0 in case of temporally correlated signals (left panel) and spatially and temporally correlated signals (right panel)

RMSEs of JADE-MSBL as a Function of C/N_0

This section investigates JOADE-MSBL, JAODE-MSBL, JOAODE-MSBL&SAGE, SAGE, and JADE-SS-MUSIC for various GNSS multipath cases.

For all the proposed approaches based on sparse representation, the scanning angle grid is uniformly distributed in the range from $-90°$ to $90°$ with the angle interval of $r_\theta = 2°$ between adjacent grid points. Likewise, we use a uniform scanning delay grid range from $-T_c$ to T_c, with delay interval $r_\tau = 0.1\,T_c$. As for the initialization, we set $\rho = 0.01$ and $a = b = 1 \times 10^{-4}$. In addition, λ_n and $\boldsymbol{\alpha}$ are initialized as $\lambda_n = \frac{100}{var\{\boldsymbol{Y}\}}$ with $var\{\boldsymbol{Y}\}$ denoting as the element-wise variance of $\boldsymbol{Y}$ and $\boldsymbol{\alpha} = \frac{1}{M_\theta M_\tau N} \sum_{n=1}^{N} \left|\boldsymbol{\Phi}^H \boldsymbol{y}_b(n)\right| var\{\boldsymbol{Y}\}$. Off-grid vectors are set as $\boldsymbol{\beta}_\tau = \mathbf{0}$ or $\boldsymbol{\beta}_\theta = \mathbf{0}$. The convergence condition is satisfied with $\varepsilon_{\text{min}} = -30\,\text{dB}$ or the number of iterations exceeding 500.

Unless noted otherwise, SAGE is implemented by two different initializations: the ideal one (SAGEi) and the practical one (SAGEp). The former is that both angles and delays are initialized in a uniformly random way within a very range around the true value of the parameters. The ranges for angle and delay are $\left(-\frac{3}{4}r_\theta, \frac{3}{4}r_\theta\right)$ and $\left(-\frac{3}{4}r_\tau, \frac{3}{4}r_\tau\right)$, respectively. To account for a more realistic environment, in SAGEp, the initial angles are unknown and the initial delays are constrained to be in a $[-T_c, T_c]$ range centered on the true delay, since in practice a rough estimation of the delay is available thanks to the acquisition step. For comparison purposes, two-dimensional (2D) SAGE for angle and delay is applied to all cases, and the 3D-SAGE for angle, delay and FFO is used in cases C and D, as described below.

JADE-MUSIC subspace method is implemented as described in [65]. Spatial smoothing with 6 sliding elements and forward averaging are adopted to facilitate the decorrelation of the LOS and multipath signals.

Case A: RMSEs as a Function of C/N_0 with Temporally Correlated Signals In this case, we consider the LOS and multipath signals to be separable in the spatial domain. These two correlated rays impinge from angles equal to $-0.7°$ and $30.2°$, and the corresponding delays are $0.03\,T_c$ and $0.38\,T_c$. The FFOs of both the LOS signal and multipath signal are assumed zero.

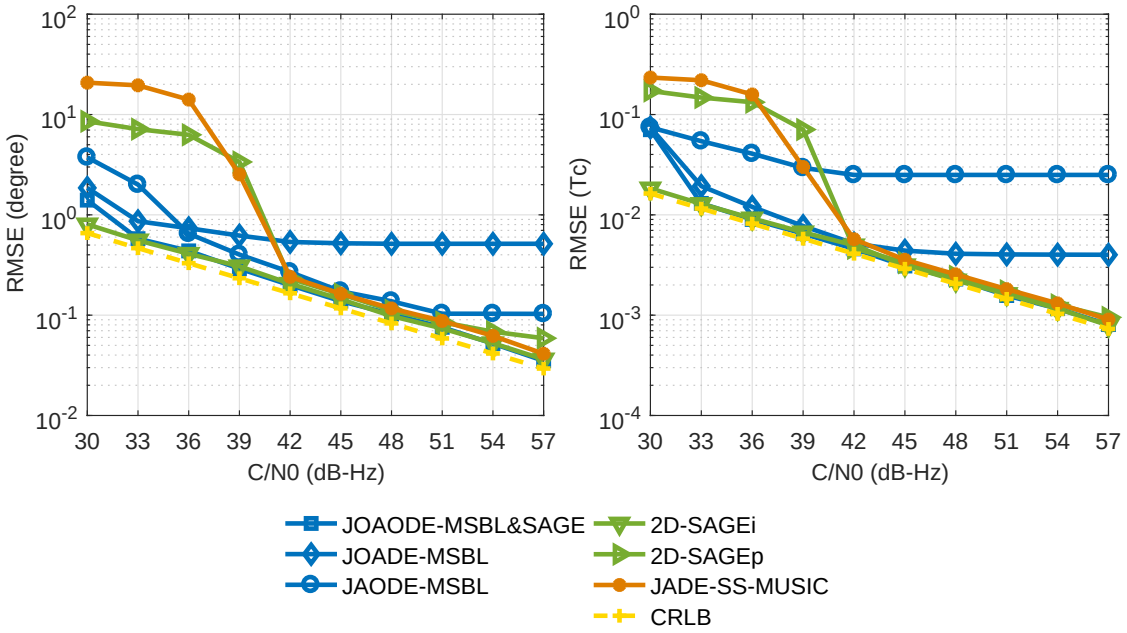


Figure 3.10: RMSEs of the angles (left panel) and the delays (right panel) via C/N_0 for case A

Figure 3.10 compares the RMSEs of the three proposed algorithms, 2D-SAGE, SS-JADE-MUSIC and the CRLB as a function of the C/N_0 under the separable angles case. As expected, 2D-SAGEi performs well thanks to the help of the exact initialization. In addition, both of 2D-SAGEp and SS-JADE-MUSIC are strongly degraded at moderate and low C/N_0 values.

For the proposed algorithms, the low and inaccurate C/N_0 region is narrowed down to only 3 dB-Hz wide from 30 dB-Hz to 33 dB-Hz. Then, two estimations of on-grid one and off-grid one begin to show a difference. For the angle of JOADE-MSBL and the delay of JAODE-MSBL, the off-grid effects become evident when C/N_0 is greater than 42 dB-Hz which means that even if C/N_0 increases, the residual biases are determined by the granularity of the grid, namely $1/2r_\theta$ or $1/2r_\tau$. In contrast, the JAODE-MSBL angle and the JOADE-MSBL delay adopting off-grid estimation outperform 2D-SAGEp and JADE-SS-MUSIC. Nevertheless, the performance of off-grid estimation reaches an error floor in high C/N_0 because of the first-order Taylor series expansions. Since JOAODE-MSBL provides accurate on-grid estimations and SAGE further refines the results,

JOAODE-MSBL&SAGE has more precision than the other proposed algorithms at the price of increased complexity. In general, these simulation results show that our proposed methods are more appropriate than the existing ones in the range of typical C/N_0 values for the GNSS signals, that is from 35 dB-Hz to 50 dB-Hz.

Case B: RMSEs as a Function of C/N_0 with Both Spatially and Temporally Correlated Signals In order to gain deeper insight into the performance of the proposed algorithms in both spatially and temporally correlated case, the angles of the LOS signal and the multipath signal are set to $0.3°$ and $6.8°$, while the delays remain $0.03\,T_c$ and $0.38\,T_c$, respectively. This means that the angular difference between the two signals is less than half of the first beamwidth of the antenna array, and the delay difference is less than half a chip. The FFOs are the same as in case A.

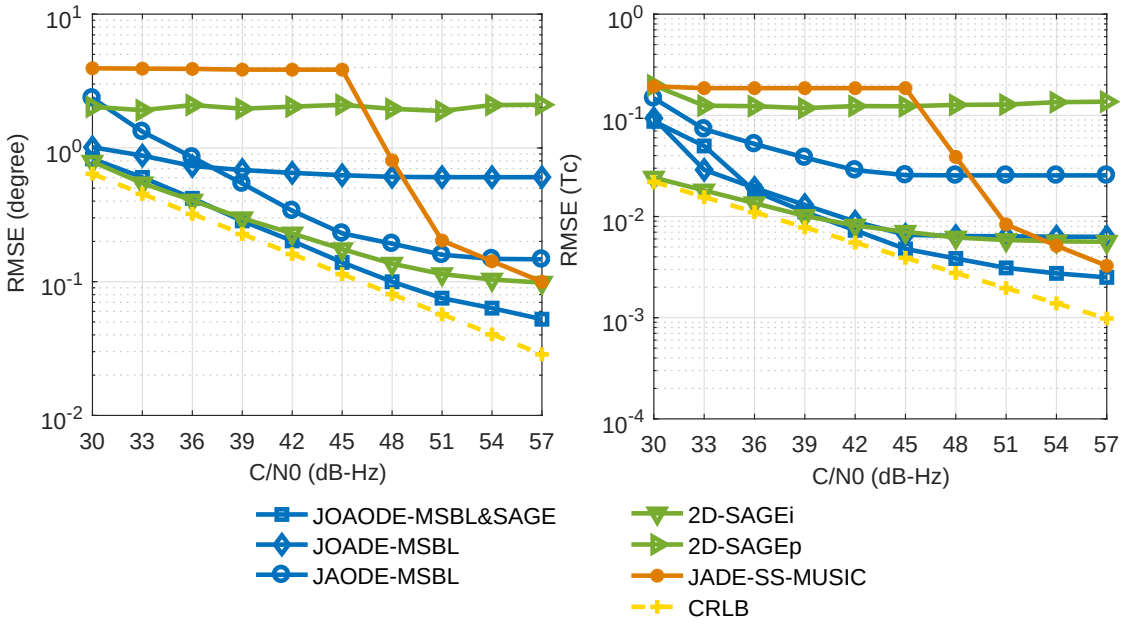


Figure 3.11: RMSEs of the angles (left panel) and the delays (right panel) via C/N_0 for case B

Figure 3.11 results confirm that it is difficult to resolve the two signals if the angle and delay difference are both close enough unless the C/N_0 is high enough. Worse still, 2D-SAGEp can hardly distinguish the signals in any case. 2D-SAGEi always behaves good, but the RMSE reaches a floor level at high C/N_0.

JOAODE-MSBL-based algorithms show strong robustness to multipath. In spite of the fact that JOADE-MSBL and JAODE-MSBL also experience an error floor in the angle and delay RMSEs, respectively, both of them vehave well, especially from 30 dB-Hz to 48 dB-Hz. In particular, as far as the delay estimate is concerned, JOADE-MSBL performs as good as 2D-SAGEi, even reaching the $10^{-2}\,T_c$ level, which corresponds to a decimeter error level in the pseudo-range at 42 dB-Hz. Moreover, JOAODE-MSBL&SAGE provides more reliable estimates, what means that

the on-grid initial estimates obtained with JOAODE-MSBL are more accurate than the idealistic initialization values assumed in 2D-SAGEi.

Case C: RMSEs as a Function of C/N_0 with Both Spatially and Temporally Correlated Signals and FFOs Under the situation of DFOs completely compensated, the proposed algorithms indeed perform well no matter how spatially and temporally correlated the signals are. However, in practice, DFOs of each path are neither identical nor completely compensated, and hence, some FFOs remain to be estimated. In Case C, we consider FFOs within ± 500 Hz, and we analyze the performance and the robustness against FFOs.

First, we use the same settings as in case B, but adding to each signal an FFO of 400 Hz and -300 Hz, respectively.

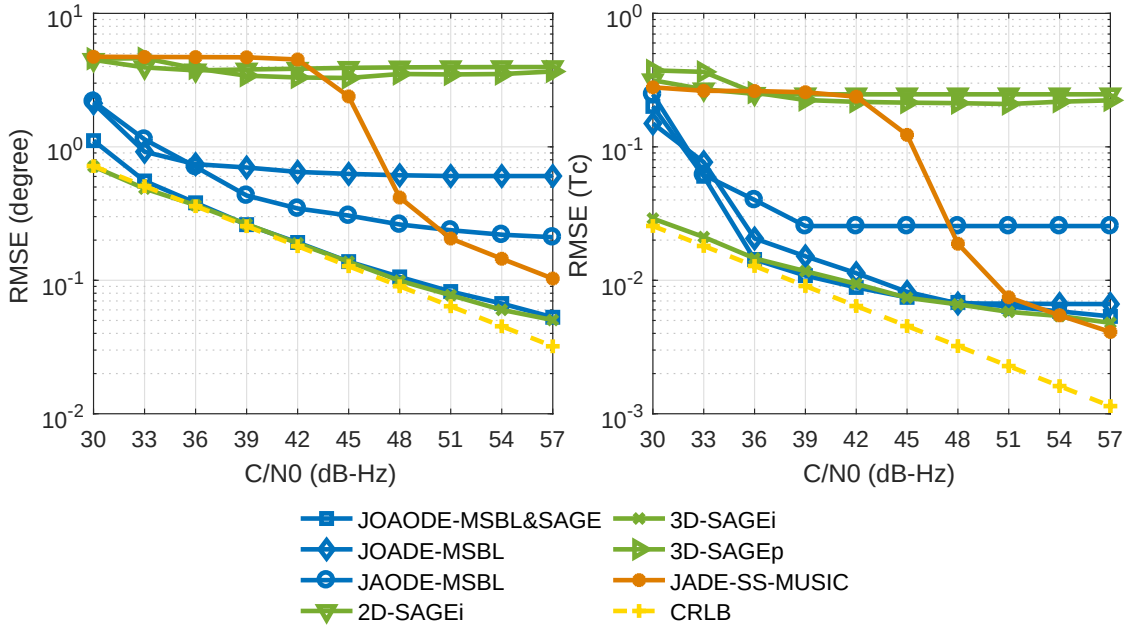


Figure 3.12: RMSEs of the angles (left panel) and the delays (right panel) via C/N_0 for case C

As can be seen in Figure 3.12, 3D-SAGEi losses its resolvable ability due to the lack of FFO estimation step. This phenomenon also happens in 3D-SAGEp, but the reason is inaccurate initialization. On the other hand, 3D-SAGEi performs very well and the initial FFOs values are very accurate and different among them. Besides, as the large FFO difference between the LOS signal and the multipath signal improves the resolution, JADE-SS-MUSIC performs better than that in case B butstill suffers a clear degradation at low C/N_0. On the contrary, although JAODE-MSBL and JOADE-MSBL only perform a 2D estimation, both of them have almost the same performance as that in case B, which stands out for their robustness to FFOs. Moreover, unlike in case B, JOAODE-MSBL&SAGE no longer tends flat to be flat at high C/N_0, but it is close to CRLB since the large FFO difference decreases the similarity of two signals.

3.6.2 RMSEs as a Function of Angle Difference or Delay Difference

All the cases above consider fixed angles and delays. In this case, we study the performances as a function of the delay or the angle differences.

In this subsection, the angles are set to $0.2°$ and $10.2°$. This means that the angle difference is smaller than the first beamwidth of array. The delay difference $\Delta\tau$ is denoted as the difference between the LOS signal and the multipath signal, ranging from 0 to 1 T_c, and the $C/N_0 = 45$ dB-Hz.

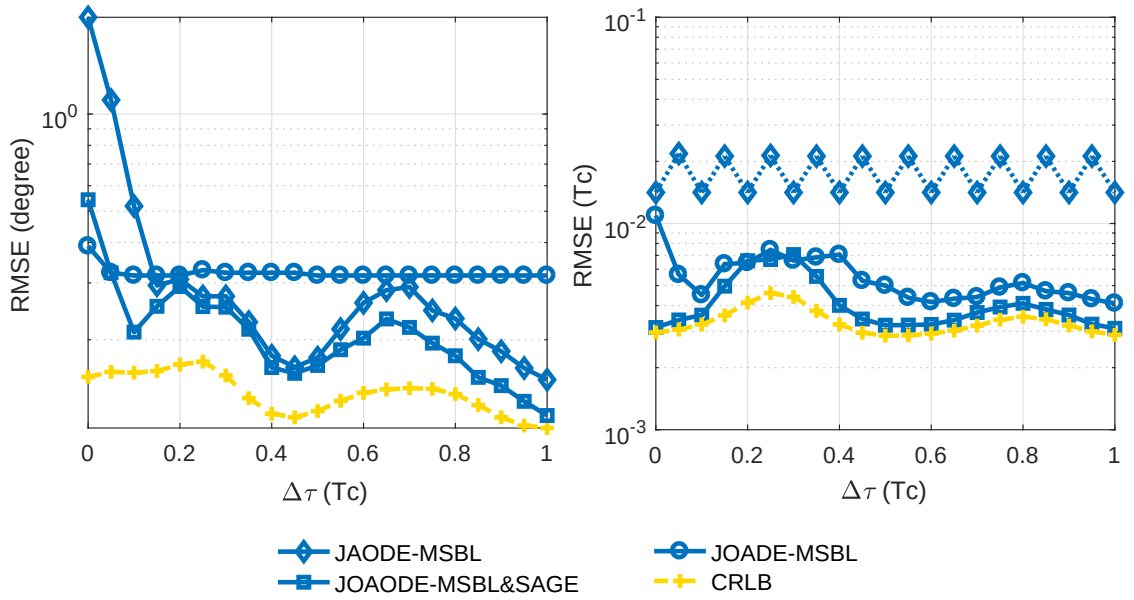


Figure 3.13: RMSEs of the angles (left panel) and the delays (right panel) for case D as a function of $\Delta\tau$

Case D: RMSEs as a Function of Delay Difference with Spatially Correlated Signals Figure 3.13 illustrates the RMSEs of angles and delays as a function of the relative delay. All the proposed algorithms follow the trend of CRLBs except, as expected, the JOADE-MSBL for DOA and JAODE-MSBL for a delay due to the on-grid estimation. The irregular behaviors of the CRLB are due to the very small angle difference between the signals. It is worth noting that, in general, JOAODE-MSBL&SAGE is much closer to the CRLB than JOADE-MSBL does in delay and JAODE-MSBL does in angle. Only for some points of $\Delta\tau$ around $0.25\,T_c$ the RMSE of JOAODE-MSBL&SAGE is slightly above JOADE-MSBL. This occurs because SAGE suffer sometimes from poor separation capability of highly correlated signals.

Case E: RMSEs as a Function of Angle Difference with Temporally Correlated Signals Next, we consider another case with two temporally correlated signals with a delay difference of $0.25\,T_c$

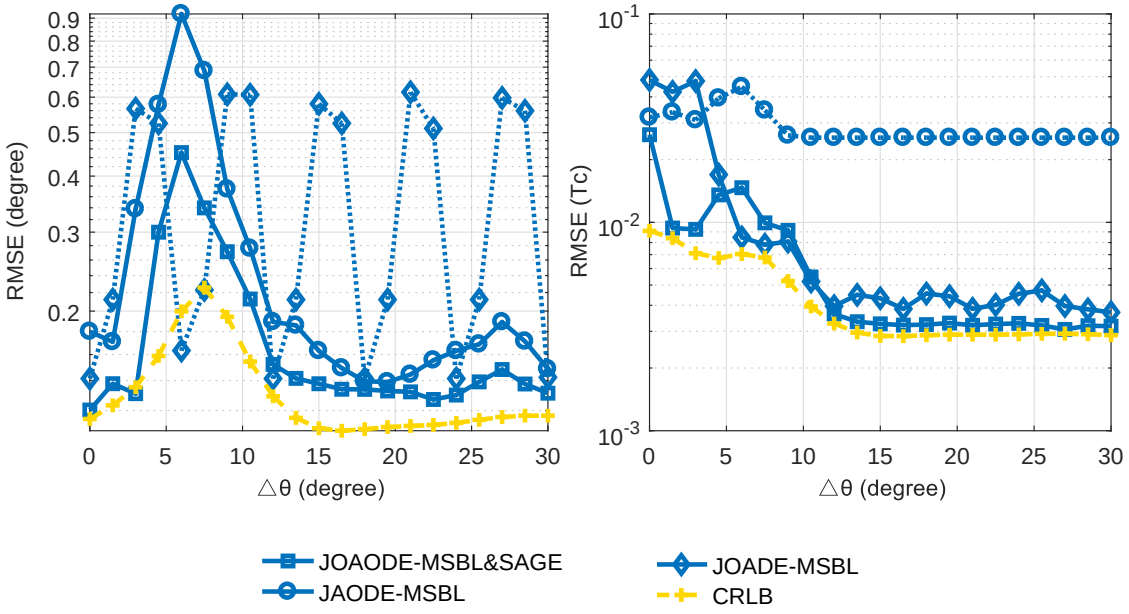


Figure 3.14: RMSEs of the angles (left panel) and the delays (right panel) for case E as a function of $\Delta\theta$

while the angle difference $\Delta\theta$ varies from 0° to 30° and the $C/N_0 = 45$ dB-Hz.

Figure 3.14 presents the RMSEs of angle and delay as a function of the relative angle. As expected, in general, the error decreases as the relative angle increases. In Figure 3.14, the RMSEs of JOADE-MSBL and JOAODE-MSBL&SAGE become very close to the CRLB when the two angles are non-spatially separable. The delay RMSE of JAODEMSBL remains constant because of the grid granularity. In contrast, the angle RMSE of both JAODE-MSBL and JOAODE-MSBL&SAGE follows the CRLB, while JOADEMSBL has some specific errors in the very particular cases when the true values of DOA coincide with the grid points.

3.7 Conclusions

This chapter proposes two types of multipath mitigation methods based on the joint spatial and temporal structure: the subspace-based and MSBL-based spatial and temporal algorithms. The subspace-based algorithm balances complexity and multipath mitigation performance, achieving a perfect trade-off, while the MSBL-based algorithms further improve the ability of multipath mitigation and achieve better performance. We compare the complexities of two types of algorithms and provide convergence analysis for space-time algorithms based on MSBL. Finally, through simulations in multipath environments with different spatial and temporal correlations, we demonstrate the performance of proposed algorithms in low signal-to-noise ratios, with fewer snapshots and small fractional DFOs, validating the advantages of joint spatial and temporal processing.

3.8 Derivation of (3.32)

To obtain the off-grid angle vector $\boldsymbol{\beta}_\theta$ and off-grid delay vector $\boldsymbol{\beta}_\tau$, the maximum likelihood functions can be derived by maximizing the $\boldsymbol{\beta}_\theta$ dependent part $E\left\{\log p\left(\boldsymbol{Y}\left|\boldsymbol{X},\lambda_n,\boldsymbol{\alpha},\boldsymbol{\beta}_\tau,\boldsymbol{\beta}_\theta\right.\right)p\left(\boldsymbol{\beta}_\theta\right)\right\}$ and the $\boldsymbol{\beta}_\tau$ dependent part $E\left\{\log p\left(\boldsymbol{Y}\left|\boldsymbol{X},\lambda_n,\boldsymbol{\alpha},\boldsymbol{\beta}_\tau,\boldsymbol{\beta}_\theta\right.\right)p\left(\boldsymbol{\beta}_\tau\right)\right\}$ in (3.32), respectively (the sampling point is omitted for short)

$$\begin{aligned}
&E\left\{\tfrac{1}{N}\sum_{n=1}^{N}\left\|\boldsymbol{y}_s\left(n\right)-\left(\hat{\boldsymbol{\Phi}}_{\beta_\theta}\otimes\boldsymbol{\Phi}_{\beta_\tau}\right)\boldsymbol{x}_s\left(n\right)\right\|_2^2\right\}\\
&=\tfrac{1}{N}\sum_{n=1}^{N}\left\|\boldsymbol{y}_s\left(n\right)-\left(\hat{\boldsymbol{\Phi}}_{\beta_\theta}\otimes\boldsymbol{\Phi}_{\beta_\tau}\right)\boldsymbol{\mu}\left(n\right)\right\|_2^2+\mathrm{tr}\left(\hat{\boldsymbol{\Phi}}_{\beta_\theta}\otimes\boldsymbol{\Phi}_{\beta_\tau}\right)\boldsymbol{\Sigma}\left(\hat{\boldsymbol{\Phi}}_{\beta_\theta}\otimes\boldsymbol{\Phi}_{\beta_\tau}\right)^H\\
&=\boldsymbol{\beta}_\tau^T\boldsymbol{P}_\tau\boldsymbol{\beta}_\tau-2\boldsymbol{v}_\tau^T\boldsymbol{\beta}_\tau+C_1
\end{aligned}\tag{3.44a}$$

$$\begin{aligned}
&E\left\{\tfrac{1}{N}\sum_{n=1}^{N}\left\|\boldsymbol{y}_s\left(n\right)-\left(\boldsymbol{\Phi}_{\beta_\theta}\otimes\hat{\boldsymbol{\Phi}}_{\beta_\tau}\right)\boldsymbol{x}_s\left(n\right)\right\|_2^2\right\}\\
&=\tfrac{1}{N}\sum_{n=1}^{N}\left\|\boldsymbol{y}_s\left(n\right)-\left(\boldsymbol{\Phi}_{\beta_\theta}\otimes\hat{\boldsymbol{\Phi}}_{\beta_\tau}\right)\boldsymbol{\mu}\left(n\right)\right\|_2^2+\mathrm{tr}\left(\boldsymbol{\Phi}_{\beta_\theta}\otimes\hat{\boldsymbol{\Phi}}_{\beta_\tau}\right)\boldsymbol{\Sigma}\left(\boldsymbol{\Phi}_{\beta_\theta}\otimes\hat{\boldsymbol{\Phi}}_{\beta_\tau}\right)^H\\
&=\boldsymbol{\beta}_\theta^T\boldsymbol{P}_\theta\boldsymbol{\beta}_\theta-2\boldsymbol{v}_\theta^T\boldsymbol{\beta}_\theta+C_2
\end{aligned}\tag{3.44b}$$

where C_1 and C_2 are constant terms independent of $\boldsymbol{\beta}_\theta$ and $\boldsymbol{\beta}_\tau$, respectively.

Similar to the derivation deduced in [75], we respectively calculate (3.44a) and (3.44b) through the following two groups of equalities (since the estimation with respect to off-grid time delay vector $\boldsymbol{\beta}_\tau$ is similar to that of $\boldsymbol{\beta}_\theta$, we hereafter put a short derivation of $\boldsymbol{\beta}_\tau$ for simplicity)

$$\begin{aligned}
&\left\|\boldsymbol{y}_s-\boldsymbol{\Phi}_{\beta_\tau}\boldsymbol{\mu}\right\|_2^2\\
&=\left\|\boldsymbol{y}_s-\left(\boldsymbol{A}\otimes\boldsymbol{C}\right)\boldsymbol{\mu}-vec\left(\left(\boldsymbol{B}_\tau\mathrm{diag}\left(\boldsymbol{\beta}_\tau\right)\right)\mathrm{mat}\boldsymbol{\mu}^T\cdot\boldsymbol{A}^T\right)\right\|_2^2\\
&=\left\|\boldsymbol{y}_s-\left(\boldsymbol{A}\otimes\boldsymbol{C}\right)\boldsymbol{\mu}-\left(\left(\boldsymbol{A}\cdot\mathrm{mat}\boldsymbol{\mu}^T\right)\otimes\boldsymbol{I}_{M_\tau}\right)\left(\boldsymbol{I}_{N_\tau}\otimes\boldsymbol{B}_\tau\right)\boldsymbol{J}_{N_\tau^2\times N_\tau}\boldsymbol{\beta}_\tau\right\|_2^2\\
&=\boldsymbol{\beta}_\tau^T\boldsymbol{\Xi}_\tau^H\boldsymbol{\Xi}_\tau\boldsymbol{\beta}_\tau-2\mathfrak{Re}\left\{\left(\boldsymbol{y}_s-\left(\boldsymbol{A}\otimes\boldsymbol{C}\right)\boldsymbol{\mu}\right)^H\boldsymbol{\Xi}_\tau\right\}\boldsymbol{\beta}_\tau+C_1
\end{aligned}\tag{3.45}$$

and

$$\begin{aligned}
&\mathrm{tr}\left\{\boldsymbol{\Phi}_{\beta_\tau}\boldsymbol{\Sigma}\boldsymbol{\Phi}_{\beta_\tau}^H\right\}\\
&=\mathrm{tr}\left\{\left(\boldsymbol{A}\otimes\boldsymbol{C}\right)\boldsymbol{\Sigma}\left(\boldsymbol{A}\otimes\boldsymbol{C}\right)^H\right\}+\mathrm{tr}\left\{\left(\boldsymbol{A}\otimes\boldsymbol{C}\right)\boldsymbol{\Sigma}\left(\boldsymbol{A}\otimes\left(\boldsymbol{B}_\tau\mathrm{diag}\left(\boldsymbol{\beta}_\tau\right)\right)\right)^H\right\}\\
&\quad+\mathrm{tr}\left\{\left(\boldsymbol{A}\otimes\left(\boldsymbol{B}_\tau\mathrm{diag}\left(\boldsymbol{\beta}_\tau\right)\right)\right)\boldsymbol{\Sigma}\left(\boldsymbol{A}\otimes\boldsymbol{C}\right)^H\right\}\\
&\quad+\mathrm{tr}\left\{\left(\boldsymbol{A}\otimes\left(\boldsymbol{B}_\tau\mathrm{diag}\left(\boldsymbol{\beta}_\tau\right)\right)\right)\boldsymbol{\Sigma}\left(\boldsymbol{A}\otimes\left(\boldsymbol{B}_\tau\mathrm{diag}\left(\boldsymbol{\beta}_\tau\right)\right)\right)^H\right\}\\
&=2\mathfrak{Re}\left\{\left\{\mathrm{tr}\left\{\left(\boldsymbol{A}\otimes\boldsymbol{C}\right)\boldsymbol{\Sigma}\left(\boldsymbol{A}\otimes\left(\boldsymbol{B}_\tau\mathrm{diag}\left(\boldsymbol{\beta}_\tau\right)\right)\right)^H\right\}\right\}\right\}\\
&\quad+\mathrm{tr}\left\{\left(\boldsymbol{A}\otimes\left(\boldsymbol{B}_\tau\mathrm{diag}\left(\boldsymbol{\beta}_\tau\right)\right)\right)\boldsymbol{\Sigma}\left(\boldsymbol{A}\otimes\left(\boldsymbol{B}_\tau\mathrm{diag}\left(\boldsymbol{\beta}_\tau\right)\right)\right)^H\right\}+C_2
\end{aligned}\tag{3.46}$$

where C_1 and C_2 are constant terms independent of $\boldsymbol{\beta}_\theta$ and $\boldsymbol{\beta}_\tau$, respectively. Equation (3.46) can

be obtained by the following two group of parts:

$$\begin{aligned}
&\mathfrak{Re}\left\{\text{tr}(\boldsymbol{A}\otimes\boldsymbol{C})\,\boldsymbol{\Sigma}(\boldsymbol{A}\otimes(\boldsymbol{B}_\tau\text{diag}\,(\boldsymbol{\beta}_\tau)))^H\right\}\\
&=\mathfrak{Re}\left\{\text{tr}(\boldsymbol{A}\otimes\boldsymbol{C})\,\boldsymbol{\Sigma}\left[\text{diag}\,(\boldsymbol{J}_{N_\theta N_\tau\times N_\tau}\boldsymbol{\beta}_\tau)\left(\boldsymbol{A}^H\otimes\boldsymbol{B}_\tau^H\right)\right]\right\}\\
&=\mathfrak{Re}\left\{\text{diag}\left(\left(\boldsymbol{A}^H\boldsymbol{A}\otimes\boldsymbol{B}_\tau^H\boldsymbol{C}\right)\boldsymbol{\Sigma}\right)^T\right\}(\boldsymbol{J}_{N_\theta N_\tau\times N_\tau}\boldsymbol{\beta}_\tau)
\end{aligned}\tag{3.47}$$

$$\begin{aligned}
&\text{tr}\left\{(\boldsymbol{A}\otimes(\boldsymbol{B}_\tau\text{diag}\,(\boldsymbol{\beta}_\tau)))\,\boldsymbol{\Sigma}(\boldsymbol{A}\otimes(\boldsymbol{B}_\tau\text{diag}\,(\boldsymbol{\beta}_\tau)))^H\right\}\\
&=\text{tr}\left\{((\boldsymbol{A}\otimes\boldsymbol{B}_\tau)\,\text{diag}\,(\boldsymbol{J}_{N_\theta N_\tau\times N_\tau}\boldsymbol{\beta}_\tau))\,\boldsymbol{\Sigma}\left(\text{diag}\,(\boldsymbol{J}_{N_\theta N_\tau\times N_\tau}\boldsymbol{\beta}_\tau)\left(\boldsymbol{A}^H\otimes\boldsymbol{B}_\tau^H\right)\right)\right\}\\
&=\boldsymbol{\beta}_\tau^T\boldsymbol{J}_{N_\theta N_\tau\times N_\tau}^T\left(\boldsymbol{\Sigma}\odot(\boldsymbol{A}\otimes\boldsymbol{B}_\tau)^H(\boldsymbol{A}\otimes\boldsymbol{B}_\tau)\right)\boldsymbol{J}_{N_\theta N_\tau\times N_\tau}\boldsymbol{\beta}_\tau
\end{aligned}\tag{3.48}$$

Note that $\boldsymbol{\beta}_\tau^T\boldsymbol{Q}\boldsymbol{\beta}_\tau$ belongs to real domain under the circumstance of a positive semi-definite matrix $\boldsymbol{Q}$ and thus leads to a result $\boldsymbol{\beta}_\tau^T\boldsymbol{Q}\boldsymbol{\beta}_\tau=\mathfrak{Re}\left\{\boldsymbol{\beta}_\tau^T\boldsymbol{Q}\boldsymbol{\beta}_\tau\right\}=\boldsymbol{\beta}_\tau^T\mathfrak{Re}\left\{\boldsymbol{Q}\right\}\boldsymbol{\beta}_\tau$ due to the real-valued $\boldsymbol{\beta}_\tau$. Then we have the positive semi-definite matrix $\boldsymbol{P}_\tau$. Regarding the solutions to Equation (3.36) in Chapter 3, and Equation (4.16a) and (4.16b) in Chapter 4, they can all be referred to this derivation.

Joint Spatial, Polarization, and Temporal GNSS Multipath Mitigation

4.1 Introduction

The polarization domain possesses a unique property in which a portion of RHCP signals transforms into LHCP ones after reflection. This has attracted significant research interest in the field of multipath mitigation. By deploying DPAs and utilizing polarization diversity, it becomes possible to resolve the LOS and multipath signals in the polarization domain. This chapter investigates the use of joint spatial, polarization, and time structures to improve the multipath mitigation capability under high correlation conditions. We take advantage of the spatial freedom and temporal waveform characteristics of these structures and deeply explore sparse representation as a method for mitigating multipath effects, comparing it to traditional methods such as subspace and ML. Sparse representation is effective in recasting received signals into a sparse linear problem, offering improved performance in solving multipath mitigation problems. Among various sparse representation-based algorithms, MSBL stands out as one that follows Bayesian principles while implementing the EM method, with sparser global minima and fewer local minima. As such, MSBL is highly effective in solving multipath mitigation problems [68].

Inspired by the robustness and effectiveness of joint processing in the spatial, polarization, and temporal domains, as well as the sparse representation approach, this chapter proposes a MSBL for joint estimation of angle, polarization information, and time delay to improve the ability of multipath resolution, especially in scenarios where there is high correlation between the LOS signal and multipath signals in the space or time. The organization of this chapter is as follows. We begin with an analysis of polarized characteristics in Chapter 2, followed by a proposal of joint processing in the spatial, polarization, and temporal domains to improve multipath mitigation. We first introduce the feasibility of joint space, polarization, and time for multipath mitigation enhancement. Next, we propose a joint space, polarization, and time method based on off-grid MSBL, which

addresses multipath mitigation within highly spatially and temporally correlated signals. Furthermore, we derive a closed-form expression for the CRLB of time delay under the DPA. Then, using simulation experiments, we demonstrate the advantages of the proposed algorithm compared to other algorithms such as joint spatial and temporal processing, and spatial processing. Finally, we provide a conclusion in this chapter.

4.2 Feasibility Analysis of GNSS Joint Spatial, Polarization, and Temporal Multipath Mitigation

Chapter 3 provides a comparison of the advantages and disadvantages of cascaded space and time and space-time GNSS receivers for multipath mitigation. Joint spatial and temporal processing offers the multipath-mitigating ability by utilizing two-dimensional information in both the space and time domains, which extends the subspace-based method and SBL to achieve joint angle and time delay estimation in multipath environments. These algorithms offer benefits such as low complexity and robustness in low carrier-to-noise ratio or fewer snapshots. Additionally, method headways are proposed for different application purposes, including space-time beamforming, fine time delay estimation, or fine joint angle and time delay estimation, leading to improved time delay accuracy under high correlation in space or time domains. However, when the differences in angle or time delay between LOS and multipath signals are small, relying solely on joint spatial and temporal processing for multipath mitigation is limited, especially in rich urban multipath environment [84], low elevation angle with ground reflections or high elevation angle with reflections from tall buildings in urban areas, where there is a high correlation in the spatial domain.

In the scenarios above, polarization diversity is particularly valuable as it provides additional assistance in multipath mitigation. Currently, most GNSS receivers adopt RHCP antennas. When the reflection angle exceeds the Brewster angle, the polarization flips, becoming LHCP signals [15]. In such cases, we can naturally utilize RHCP receiving antennas to suppress multipath interference [36]. However, due to differences in reflection coefficients, not all RHCP signals change their polarization characteristics after reflection, and typically, a portion of RHCP signals co-exist with LHCP signals. Many studies have focused on the joint processing of spatial and polarization domains. Various beamforming techniques [59–61] based on estimating multipath signal angles and polarization information can effectively mitigate the effects of multipath interference. However, these joint processing only estimate the signals received by two polarization antennas separately and only partially utilize the information received by the polarization antenna, which cannot wholly describe the characteristics of the polarization domain. Moreover, the joint spatial and polarization processing needs to consider that temporal information may also have some identifying ability. Therefore, accurate time delay estimation cannot be achieved by solely considering the spatial and polarization domains. Additionally, the isolation between DPAs cannot be completely free from

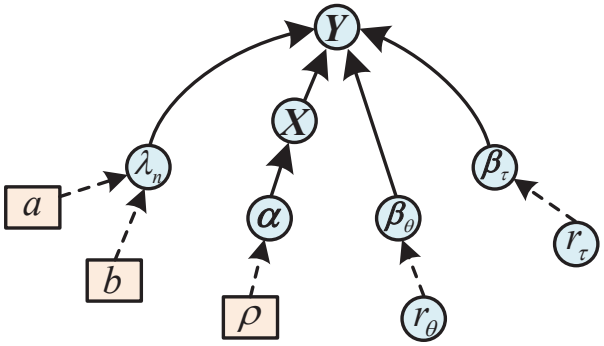


Figure 4.1: Graphical model of JAPDE-MSBL

cross-talk. Using the aforementioned joint spatial and polarization processing will affect the estimation of LOS and multipath angles, as well as polarization information.

Furthermore, considering the limitation of GNSS receiver antenna size, various joint processing methods in the spatial and polarization domains suffer from significant degradation in rich multipath environments. Therefore, we have chosen to consider joint spatial, polarization, and temporal processing in this chapter. This way, observations of multipath can be made simultaneously from three dimensions: spatial domain, polarization domain, and time domain, providing a comprehensive joint analysis of all information to mitigate multipath. As a result, the joint space-polarization-time structure constructed can benefit from gains in spatial, polarization, and temporal diversities, enhancing the robustness of methods built on this structure. Thus, regardless of whether multipath has a high correlation in the spatial, polarization, or temporal dimensions, joint angle, polarization information, and time delay estimation method can effectively mitigate the multipath signals.

4.3 Joint Spatial, Polarization, and Temporal Multipath Mitigation based on MSBL

This section proposes a Bayesian-based algorithm for jointly estimating multipath signals from spatial, polarization, and temporal domains. The main challenge is determining the on-grid points closest to the true values of angle and time delay. The second challenge is obtaining the deviation between the corresponding on-grid value and the true parameters. Finally, we form a joint spatial, polarization, and temporal spectrum to estimate.

4.3.1 Joint On-grid Angle, Polarization and Delay Estimation based on MSBL

To realize the proposed joint off-grid angle, polarization, and time delay estimation based on MSBL (JAPDE-MSBL), a graphical model is depicted in Figure 4.1 that the unknown parameters (written in circles) are determined by hyperparameters (written in rectangles).

Assuming elements in the white noise vector are independent and each of them has a Gaussian distribution, we have

$$p\left(\boldsymbol{E}\left|\sigma_n^2\right.\right)=\prod_{n=1}^{N}\mathcal{CN}\left(\boldsymbol{e}_s\left(n\right)\left|\mathbf{0}_{2M_\theta M_\tau,1},\sigma_n^2\boldsymbol{I}_{2M_\theta M_\tau}\right.\right) \tag{4.1}$$

To simplify the following analysis, we define the precision $\lambda_n \doteq \sigma_n^{-2}$, a Gamma distribution is used to describe the inverse of noise variance

$$p\left(\lambda_n;a,b\right)=\mathcal{B}\left(\lambda_n\right|a,b) \tag{4.2}$$

where $\mathcal{B}\left(\lambda_n\right|a,b)\doteq[\Gamma\left(a\right)]^{-1}b^a\lambda_n^{a-1}e^{-b\lambda_n}$ with the Gamma function $\Gamma\left(a\right)\doteq\int_0^\infty x^{a-1}e^{-x}dx$. The parameters a and b refer to the hyperparameters for λ_n.

Then, the data likelihood for the complex sourse amplitudes matrix $\boldsymbol{X}$ given the observation $\boldsymbol{Y}$ is complex Gaussian

$$p\left(\boldsymbol{Y}\left|\boldsymbol{X},\lambda_n,\boldsymbol{\beta}_\tau,\boldsymbol{\beta}_\theta\right.\right)=\prod_{n=1}^{N}\mathcal{CN}\left(\boldsymbol{y}_s\left(n\right)\left|\boldsymbol{\Phi}_\beta\,\boldsymbol{x}_s\left(n\right)\right.,\lambda_n^{-1}\boldsymbol{I}_{2M_\theta,M_\tau}\right) \tag{4.3}$$

As all the columns of $\boldsymbol{X}$ are independent among snapshots and share the same prior, the prior of $\boldsymbol{X}$ is given by

$$p\left(\boldsymbol{X}\right|\boldsymbol{\alpha})=\prod_{n=1}^{N}\mathcal{CN}\left(\boldsymbol{x}_s\left[n\right]\right|0,\boldsymbol{\Upsilon}) \tag{4.4}$$

where the spatial-polarization-temporal dependent variance $\boldsymbol{\alpha}=[\alpha_1,\ldots,\alpha_{2N_\theta N_\tau}]^T$ is a hyperparameter vector controlling the row sparsity of $\boldsymbol{X}$ and $\boldsymbol{\Upsilon}=\mathrm{diag}\left(\boldsymbol{\alpha}\right)$. A two-stage hierarchical prior is adopted here, which favors most rows of $\boldsymbol{X}$ being zeros

$$p\left(\boldsymbol{\alpha},\rho\right)=\prod_{n_g=1}^{N_\theta N_\tau}\Gamma\left(\boldsymbol{\alpha}\left(n_g\right)\right|1,\rho) \tag{4.5}$$

with $p\left(X,\rho\right)=\int p\left(X\left|\alpha\right.\right)p\left(\alpha,\rho\right)d\alpha$ and the hyperparameter for $\boldsymbol{\alpha}$ being $\rho>0$.

For the off-grid spatial-polarization vector $\boldsymbol{\beta}_\theta$ and temporal parameter vector $\boldsymbol{\beta}_\tau$, we use non-informative uniform prior

$$p\left(\boldsymbol{\beta}_\tau,r_\tau\right)=U\left(-\frac{1}{2}r_\tau,\frac{1}{2}r_\tau\right) \tag{4.6a}$$

$$p\left(\boldsymbol{\beta}_\theta,r_\theta\right)=U\left(-\frac{1}{2}r_\theta,\frac{1}{2}r_\theta\right) \tag{4.6b}$$

where we have

$$U\left([c,d]\right)=\begin{cases}\frac{1}{d-c}, & c\leq x\leq d\\ 0, & otherwise.\end{cases} \tag{4.7}$$

To find the estimates of angle, polarization, and time delay, we combine the stages of the hierarchical Bayesian model, thus the joint distribution of $\boldsymbol{X}$ for all parameters is obtained

$$p\left(\boldsymbol{X},\boldsymbol{Y},\lambda_n,\boldsymbol{\alpha},\boldsymbol{\beta}_\tau,\boldsymbol{\beta}_\theta\right)=p\left(\boldsymbol{Y}\left|\boldsymbol{X},\lambda_n,\boldsymbol{\alpha},\boldsymbol{\beta}_\tau,\boldsymbol{\beta}_\theta\right.\right)p\left(\boldsymbol{X}\right|\boldsymbol{\alpha}\left.\right)p\left(\boldsymbol{\alpha}\right)p\left(\lambda_n\right)p\left(\boldsymbol{\beta}_\tau\right)p\left(\boldsymbol{\beta}_\theta\right) \quad (4.8)$$

where the distributions $p\left(\boldsymbol{Y}\left|\boldsymbol{X},\lambda_n,\boldsymbol{\alpha},\boldsymbol{\beta}_\tau,\boldsymbol{\beta}_\theta\right.\right)$, $p\left(\boldsymbol{X}\right|\boldsymbol{\alpha}\left.\right)$, $p\left(\boldsymbol{\alpha}\right)$, $p\left(\boldsymbol{\beta}_\tau\right)$, and $p\left(\boldsymbol{\beta}_\theta\right)$ defined by (4.3), (4.4), (4.5), (4.6a), and (4.6b), respectively.

Using the Bayes rule, we obtain the posterior for $\boldsymbol{X}$

$$\begin{aligned}p\left(\boldsymbol{X}\right|\boldsymbol{Y},\lambda_n,\boldsymbol{\alpha},\boldsymbol{\beta}_\theta,\boldsymbol{\beta}_\tau\left.\right)&=\frac{p(\boldsymbol{Y},\boldsymbol{X},\lambda_n,\boldsymbol{\alpha},\boldsymbol{\beta}_\tau,\boldsymbol{\beta}_\theta)}{p(\boldsymbol{Y},\lambda_n,\boldsymbol{\alpha},\boldsymbol{\beta}_\tau,\boldsymbol{\beta}_\theta)}\\&=\frac{p(\boldsymbol{Y}|\boldsymbol{X},\lambda_n,\boldsymbol{\alpha},\boldsymbol{\beta}_\theta,\boldsymbol{\beta}_\tau)p(\boldsymbol{X}|\boldsymbol{\alpha})}{p(\boldsymbol{Y}|\lambda_n,\boldsymbol{\alpha},\boldsymbol{\beta}_\theta,\boldsymbol{\beta}_\tau)}\end{aligned} \quad (4.9)$$

As $p\left(\boldsymbol{Y}\right|\boldsymbol{X},\lambda_n,\boldsymbol{\alpha},\boldsymbol{\beta}_\theta,\boldsymbol{\beta}_\tau\left.\right)$ is irrelevant to $\boldsymbol{X}$, the posterior distribution of $\boldsymbol{X}$ can be simplified as

$$p\left(\boldsymbol{X}\right|\boldsymbol{Y},\lambda_n,\boldsymbol{\alpha},\boldsymbol{\beta}_\theta,\boldsymbol{\beta}_\tau\left.\right)\propto p\left(\boldsymbol{Y}\right|\boldsymbol{X},\lambda_n,\boldsymbol{\alpha},\boldsymbol{\beta}_\theta,\boldsymbol{\beta}_\tau\left.\right)p\left(\boldsymbol{X}\right|\boldsymbol{\alpha}\left.\right) \quad (4.10)$$

where $p\left(\boldsymbol{Y}\right|\boldsymbol{X},\lambda_n,\boldsymbol{\alpha},\boldsymbol{\beta}_\theta,\boldsymbol{\beta}_\tau\left.\right)$ and $p\left(\boldsymbol{X}\right|\boldsymbol{\alpha}\left.\right)$ can be calculated in (4.3) and (4.4), respectively, and they are both Gaussian distributions. Therefore, the posterior distribution of $\boldsymbol{X}$ follows the Gaussian function

$$p\left(\boldsymbol{X}\left|\boldsymbol{Y},\lambda_n,\boldsymbol{\alpha},\boldsymbol{\beta}_\theta,\boldsymbol{\beta}_\tau\right.\right)=\mathcal{CN}\left(\boldsymbol{\mu},\boldsymbol{\Sigma}\right) \quad (4.11)$$

with the mean value

$$\boldsymbol{\mu}\left(n\right)=\lambda_n\boldsymbol{\Sigma}_x\boldsymbol{\Phi}_\beta^H\boldsymbol{y}_s\left(n\right) \quad (4.12)$$

and the covariance matrix

$$\boldsymbol{\Sigma}=\left(\lambda_n\boldsymbol{\Phi}_\beta^H\boldsymbol{\Phi}_{\boldsymbol{\beta}}+\boldsymbol{\Upsilon}^{-1}\right)^{-1} \quad (4.13)$$

where $n=1,\ldots,N$.

When calculating $\boldsymbol{\mu}$ and $\boldsymbol{\Sigma}$, we need to estimate the noise variance λ_n, the spatial-polarization-temporal dependent variance $\boldsymbol{\alpha}$, the off-grid angle vector $\boldsymbol{\beta}_\theta$, and the off-grid delay vector $\boldsymbol{\beta}_\tau$. To address the estimates of these hyperparameters, we employ the EM method [108] to implement JAPDE-MSBL, treating $\boldsymbol{X}$ as a hidden variable, and maximizing the expectation with respect to the joint distribution $E\left\{\log p\left(\boldsymbol{X},\boldsymbol{Y},\lambda_n,\boldsymbol{\alpha},\boldsymbol{\beta}_\theta,\boldsymbol{\beta}_\tau\right)\right\}$. Following a similar procedure as in [107] by denoting $\boldsymbol{U}=\left[\boldsymbol{u}\left(1\right),\ldots,\boldsymbol{u}\left(N\right)\right]$, it is easy to obtain the following updates of $\boldsymbol{\alpha}$ and λ_n by maximizing $E\left\{\log p\left(\boldsymbol{X}\left|\boldsymbol{\alpha}\right.\right)p\left(\boldsymbol{\alpha}\right)\right\}$ and $E\left\{\log p\left(\boldsymbol{Y}\left|\boldsymbol{X},\lambda_n,\boldsymbol{\alpha},\boldsymbol{\beta}_\theta,\boldsymbol{\beta}_\tau\right.\right)p\left(\lambda_n\right)\right\}$

$$\boldsymbol{\alpha}\left(n_g\right)=\frac{\sqrt{N^2+4\rho E\left\{\left\|\boldsymbol{X}\left(n_g,:\right)\right\|_2^2\right\}}-1}{2\rho} \quad (4.14)$$

$$\lambda_n = \frac{2M_\theta M_\tau \cdot N + a - 1}{E\left\{\left\|\boldsymbol{Y} - \boldsymbol{\Phi}\left(\boldsymbol{\beta}_\tau\right)\boldsymbol{X}\right\|_F^2\right\} \cdot N + b} \tag{4.15}$$

where $E\left\{\left\|\boldsymbol{X}\left(n_g,:\right)\right\|_2^2\right\}$ and $E\left\{\left\|\boldsymbol{Y}-\boldsymbol{\Phi}\boldsymbol{X}\right\|_F^2\right\}$ are defined $E\left\{\left\|\boldsymbol{X}\left(n_g,:\right)\right\|_2^2\right\} = \left\|\boldsymbol{U}\left(n_g,:\right)\right\|_2^2 + \boldsymbol{\Sigma}\left(n_g,n_g\right)$ and $E\left\{\left\|\boldsymbol{Y}-\boldsymbol{\Phi}\boldsymbol{X}\right\|_F^2\right\} = \left\|\boldsymbol{Y}-\boldsymbol{\Phi}\boldsymbol{U}\right\|_F^2 + \boldsymbol{\alpha}\left(n_g\right)\sum_{n=1}^{2N_\theta N_\tau}\boldsymbol{\varsigma}\left(n_g\right)$, respectively, with $\boldsymbol{\varsigma}\left(n_g\right) = 1 - \boldsymbol{\alpha}^{-1}\left(n_g\right)\boldsymbol{\Sigma}\left(n_g,n_g\right)$ and $n_g = 1,\ldots,2N_\theta N_\tau$.

4.3.2 Joint Off-grid Angle and Delay Estimation based on MSBL

Referring to the estimation of off-grid vectors $\boldsymbol{\beta}_\theta$ and $\boldsymbol{\beta}_\tau$, we respectively maximize two parts in (4.8) $E\left\{\log p\left(\boldsymbol{Y}\left|\boldsymbol{X},\lambda_n,\boldsymbol{\beta}_\theta,\boldsymbol{\beta}_\tau\right.\right)p\left(\boldsymbol{\beta}_\theta\right)\right\}$ and $E\left\{\log p\left(\boldsymbol{Y}\left|\boldsymbol{X},\lambda_n,\boldsymbol{\beta}_\theta,\boldsymbol{\beta}_\tau\right.\right)p\left(\boldsymbol{\beta}_\tau\right)\right\}$. After lengthy but straightforward calculations similar in Appendix 3.8, we have

$$\hat{\boldsymbol{\beta}}_\theta = \arg\min_{\boldsymbol{\beta}_\theta \in \left[-\frac{1}{2}r_\theta,\frac{1}{2}r_\theta\right]}\left\{\boldsymbol{\beta}_\theta^T\boldsymbol{P}_\theta\boldsymbol{\beta}_\theta - 2\boldsymbol{v}_\theta^T\boldsymbol{\beta}_\theta\right\} \tag{4.16a}$$

$$\hat{\boldsymbol{\beta}}_\tau = \arg\min_{\boldsymbol{\beta}_\tau \in \left[-\frac{1}{2}r_\tau,\frac{1}{2}r_\tau\right]}\left\{\boldsymbol{\beta}_\tau^T\boldsymbol{P}_\tau\boldsymbol{\beta}_\tau - 2\boldsymbol{v}_\tau^T\boldsymbol{\beta}_\tau\right\} \tag{4.16b}$$

where $\boldsymbol{P}_\theta$ and $\boldsymbol{P}_\tau$ are positive semi-definite matrices

$$\begin{aligned}\boldsymbol{P}_\theta = {} & \mathfrak{Re}\left\{\tfrac{1}{N}\sum_{n=1}^{N}\boldsymbol{\Xi}_\theta^H\boldsymbol{\Xi}_\theta\right\} + \\ & \mathfrak{Re}\left\{\boldsymbol{J}_{2N_\theta N_\tau \times 2N_\theta}^T\left(\boldsymbol{\Sigma}\odot\left(\boldsymbol{B}_\theta\otimes\hat{\boldsymbol{\Phi}}_{\beta_\tau}\right)^H\left(\boldsymbol{B}_\theta\otimes\hat{\boldsymbol{\Phi}}_{\beta_\tau}\right)\right)\boldsymbol{J}_{2N_\theta N_\tau,2N_\theta}\right\}\end{aligned} \tag{4.17a}$$

$$\begin{aligned}\boldsymbol{v}_\theta = {} & \mathfrak{Re}\left\{\tfrac{1}{N}\sum_{n=1}^{N}\left\{\left(\boldsymbol{y}_s\left(n\right) - \left(\boldsymbol{A}\otimes\hat{\boldsymbol{\Phi}}_{\beta_\tau}\right)\boldsymbol{\mu}\left(n\right)\right)^H\boldsymbol{\Xi}_\theta\right\}\right\} - \\ & \mathfrak{Re}\left\{\left\{\mathrm{diag}\left(\left(\boldsymbol{B}_\theta\otimes\hat{\boldsymbol{\Phi}}_{\beta_\tau}\right)^H\left(\boldsymbol{A}\otimes\hat{\boldsymbol{\Phi}}_{\beta_\tau}\right)\boldsymbol{\Sigma}\right)\right\}^T\boldsymbol{J}_{2N_\theta N_\tau,N_\tau}\right\}\end{aligned} \tag{4.17b}$$

$$\begin{aligned}\boldsymbol{P}_\tau = {} & \mathfrak{Re}\left\{\tfrac{1}{N}\sum_{n=1}^{N}\boldsymbol{\Xi}_\tau^H\boldsymbol{\Xi}_\tau\right\} + \\ & \mathfrak{Re}\left\{\boldsymbol{J}_{2N_\theta N_\tau \times N_\tau}^T\left(\boldsymbol{\Sigma}\odot\left(\hat{\boldsymbol{\Phi}}_{\beta_\theta}\otimes\boldsymbol{B}_\tau\right)^H\left(\hat{\boldsymbol{\Phi}}_{\beta_\theta}\otimes\boldsymbol{B}_\tau\right)\right)\boldsymbol{J}_{2N_\theta N_\tau,N_\tau}\right\}\end{aligned} \tag{4.18a}$$

$$\begin{aligned}\boldsymbol{v}_\tau = {} & \mathfrak{Re}\left\{\tfrac{1}{N}\sum_{n=1}^{N}\left\{\left(\boldsymbol{y}_s\left(n\right) - \left(\hat{\boldsymbol{\Phi}}_{\beta_\theta}\otimes C\right)\boldsymbol{\mu}\left(n\right)\right)^H\boldsymbol{\Xi}_\tau\right\}^T\right\} - \\ & \mathfrak{Re}\left\{\left\{\mathrm{diag}\left(\left(\hat{\boldsymbol{\Phi}}_{\beta_\theta}\otimes\boldsymbol{B}_\tau\right)^H\left(\hat{\boldsymbol{\Phi}}_{\beta_\theta}\otimes\boldsymbol{C}\right)\boldsymbol{\Sigma}\right)\right\}^T\boldsymbol{J}_{2N_\theta N_\tau,N_\tau}^{\quad T}\right\}\end{aligned} \tag{4.18b}$$

with the definitions of

$$\boldsymbol{\Xi}_\theta = \left(\boldsymbol{B}_\theta\otimes\boldsymbol{I}_{M_\tau}\right)\left(\boldsymbol{I}_{2N_\theta}\otimes\left(\hat{\boldsymbol{\Phi}}_{\beta_\tau}\cdot\mu_M\left(n\right)\right)\right)\boldsymbol{J}_{(2N_\theta)^2,2N_\theta} \tag{4.19a}$$

$$\boldsymbol{\Xi}_{\tau}=\left(\left(\hat{\boldsymbol{\Phi}}_{\beta_{\theta}}\cdot\mu_{M}\left(n\right)\right)\otimes\boldsymbol{I}_{M_{\tau}}\right)\left(\boldsymbol{I}_{N_{\tau}}\otimes\boldsymbol{B}_{\tau}\right)\boldsymbol{J}_{N_{\tau}^{2},N_{\tau}} \tag{4.19b}$$

where $\mu_{M}\left(n\right)\in\mathbb{C}^{2N_{\theta}\times N_{\tau}}$ is a reshaped matrix of $\boldsymbol{\mu}\left(n\right)$. The specific definitions are listed below: $\boldsymbol{J}_{2N_{\theta}N_{\tau},2N_{\theta}}\doteq\mathbf{1}_{N_{\tau},1}\otimes\boldsymbol{I}_{2N_{\theta}}$, $\boldsymbol{J}_{2N_{\theta}N_{\tau},2N_{\tau}}\doteq\mathbf{1}_{2N_{\theta},1}\otimes\boldsymbol{I}_{2N_{\tau}}$, $\boldsymbol{J}_{(2N_{\theta})^{2},2N_{\theta}}\doteq\boldsymbol{I}_{N_{\theta}}\diamondsuit\boldsymbol{I}_{N_{\theta}}$, and $\boldsymbol{J}_{(N_{\tau})^{2},N_{\tau}}\doteq\boldsymbol{I}_{N_{\tau}}\diamondsuit\boldsymbol{I}_{N_{\tau}}$.

In summary, JAPDE-MSBL is concluded as follows.

Algorithm 4 JAPDE-MSBL algorithm for DPA

Input: $\boldsymbol{Y}$, $\boldsymbol{A}$ and $\boldsymbol{C}$ and the number of signals K

Output: $\boldsymbol{\alpha}$, $\boldsymbol{\beta}_{\tau}$ and $\boldsymbol{\beta}_{\theta}$ (The estimated time delay of LOS signal is obtained from the position of peak value in $\boldsymbol{\alpha}$ and the corresponding position in $\boldsymbol{\beta}_{\tau}$)

1: $\lambda_{n}=100/var\left\{\boldsymbol{Y}\right\}$.
2: The hyperparameters are defined as $a=b=1\times10^{-4}$ and $\rho=0.01$.
3: **while** it meets ε_{min} or maximum iteration **do**
4: Calculate $\boldsymbol{\Sigma}$, $\boldsymbol{\mu}$ and $\boldsymbol{\Phi}_{\beta}$ using the current values of the hyperparameters according to (4.13), (4.12) and (2.15), respectively.
5: Update $\boldsymbol{\alpha}$ and λ_{n} according to (4.15) and (4.16).
6: Find $K+1$ largest peaks in amplitudes $\boldsymbol{\alpha}$, and calculate the corresponding angle-polarization and delay on-grid numbers, respectively.
7: Update $\boldsymbol{\beta}_{\theta}$, $\boldsymbol{\beta}_{\tau}$ according to (2.15), (4.16a), (4.17a), (4.18a) and (4.16b), (4.17b), (4.18b), respectively.
8: Calculate the error $\varepsilon=\left\|\boldsymbol{\alpha}^{new}-\boldsymbol{\alpha}^{old}\right\|_{2}/\left\|\boldsymbol{\alpha}^{old}\right\|_{2}$.
9: **end while**

4.4 CRLB Derivation and Convergence Analysis

4.4.1 Derivation of CRLB with Dual-polarization Antenna

To facilitate comparison, we derive the CRLB under the circumstance of DPA in this subsection employing the Bangs-Slepian's formula [109], [110] as a theoretical reference. The CRLB for the time delay is

$$\begin{aligned}\mathrm{CRLB}^{-1}\left(\boldsymbol{\tau}\right)&=\mathfrak{Re}\left\{\boldsymbol{W}_{4}\right\}-\mathfrak{Re}\left\{\boldsymbol{W}_{5}^{H}\boldsymbol{W}_{1}^{-1}\boldsymbol{W}_{5}\right\}\\&+\left(\mathfrak{Re}\left\{\boldsymbol{W}_{6}{}^{T}\right\}\boldsymbol{\Omega}-\mathfrak{Re}\left\{\boldsymbol{W}_{5}^{H}\boldsymbol{W}_{1}^{-1}\boldsymbol{W}_{3}\right\}\right)\left(\mathfrak{Re}\left\{\boldsymbol{W}_{3}^{H}\boldsymbol{W}_{1}^{-1}\boldsymbol{W}_{5}\right\}-\mathfrak{Re}\left\{\boldsymbol{W}_{6}\right\}\right)\end{aligned} \tag{4.20}$$

where the definitions of $\boldsymbol{W}_{1}$, $\boldsymbol{W}_{3}$, $\boldsymbol{W}_{4}$, $\boldsymbol{W}_{5}$, $\boldsymbol{W}_{6}$, $\boldsymbol{\Omega}$, and the detailed derivations can be found in Appendix 4.7.

4.4.2 Convergence Analysis

JAPDE-MSBL, like other MSBL-based algorithms, uses the EM algorithm to update $\boldsymbol{\alpha}$ and λ_{n}. While it is challenging to provide rigorous analytical proof of convergence, it is conjectured that JAPDE-MSBL converges based on the fact that the EM algorithm is guaranteed to converge during

iterations [111]. To verify the convergence property of JAPDE-MSBL, subsequent simulations were conducted.

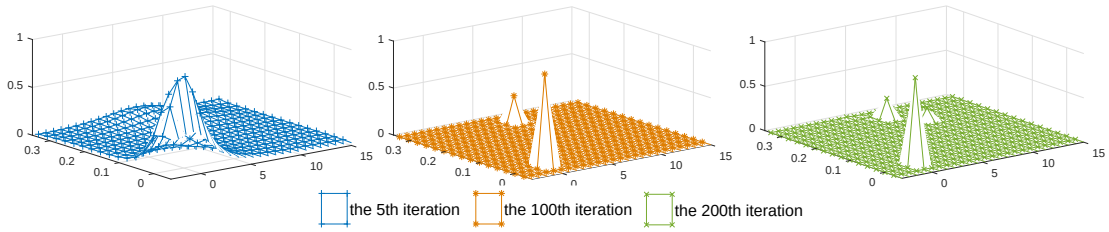


Figure 4.2: JAPDE-MSBL spatial, right polarization, and temporal spectrum at different iterations

The convergence performance of JAPDE-MSBL will be demonstrated through simulations of the spatial, right polarization, and temporal spectrum at different iterations, convergence rates, noise variances, and RMSE with increasing iterations. The simulations were conducted using carrier-to-noise ratio of $C/N_0 = 45$ dB-Hz. Since JAPDE-MSBL is an extension of JADE-MSBL presented in Chapter 3, their convergence properties are expected to be similar. In this section, an extreme scenario is observed where one LOS signal with two multipath signals, correlated in both space and time, are present at angles of $0°$, $9°$, and $6°$, respectively. The DPG value is set to 2, while all other settings were consistent with those described in Section 4.5.

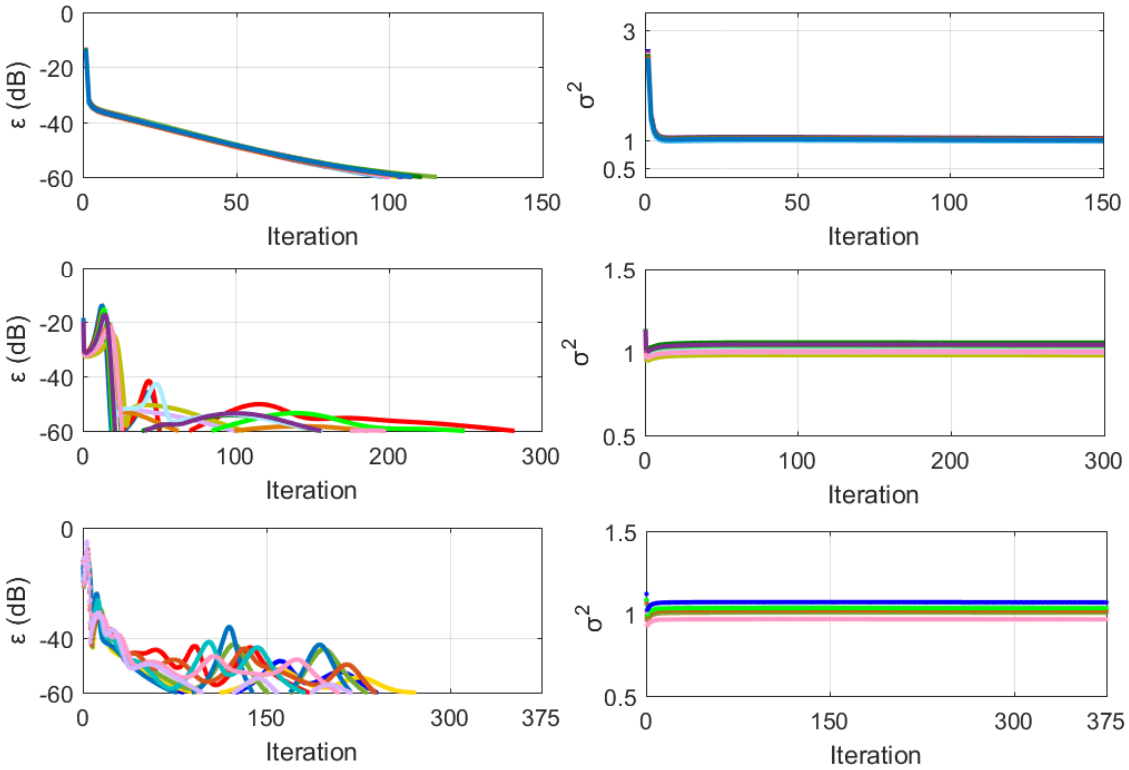


Figure 4.3: Convergence of MSBL (1st row), JADE-MSBL (2nd row), and JAPDE-MSBL (3rd row) for monte carlo simulations

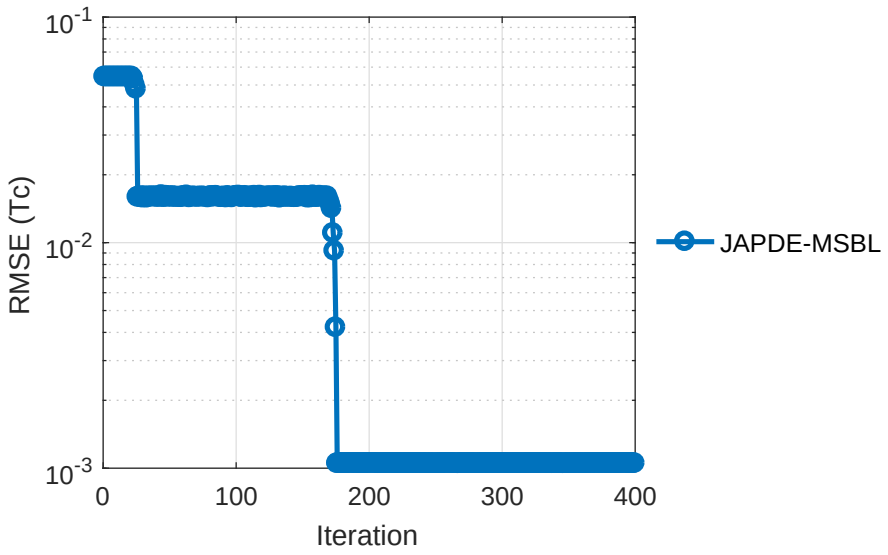


Figure 4.4: The RMSE of JAPDE-MSBL via iterations

For demonstration, the RHCP part of the estimated spatial, polarization, and temporal spectra is used to construct the spatial and temporal spectra. Figure 4.2 shows the JAPDE-MSBL spatial and temporal spectra at different iterations under spatially and temporally correlated condition. Comparing with the convergence analysis of JADE-MSBL in Chapter 3, it can be observed that JAPDE-MSBL operates not only in the spatial domain but also incorporates the polarization domain, resulting in slower convergence but the more pronounced main peak for multipath signals as the iteration increases.

Simulation results in Figure 4.3 demonstrate that all update rules (MSBL with 2M-SPA, JADE-MSBL with 2M-SPA, and JAPDE-MSBL) converge. JAPDE-MSBL exhibits slower convergence than JADE-MSBL and MSBL to $\varepsilon_{\text{min}} = -60$ dB where the methods stop, see Figure 4.3. Considering the setting of ε_{min} is -30 dB in the rest cases, a relatively low number of iterations no more than 50 suffices.

Under spatially correlated conditions, the RMSE of JAPDE-MSBL as a function of iterations exhibits three distinct stages, as shown in Figure 4.4. These stages correspond to the resolution of multipath signals in the spatial, polarization, and temporal spectrum at different iterations in Figure 4.2. In the first stage, the LOS signal time delay estimation is inaccurate with relatively few iterations. In the second stage, the ACF peaks of the two multipath signals are estimated. Still, the independent main peaks of two multipath signals are not yet identified separately, resulting in decreased estimation resolution. However, as the iteration increases, the ACF peaks of both multipath signals become clear, leading to improved estimation accuracy.

4.5 Simulation Results and Performance Analysis

This section focuses on evaluating the performance of several methods, including the proposed JAPDE-MSBL with M_θ-element dual-polarization antenna (M-DPA), JADE-MSBL [75] with M_θ-element single-polarization antenna (M-SPA) and $2M_\theta$-element SPA (2M-SPA), and MSBL [102] with 2M-SPA. In addition to these methods, we also compare the spectra of the spatial smoothing MUSIC (SS-MUSIC) [106] with 2M-SPA. It is noteworthy that "M-DPA" refers to the M_θ-element RHCP antenna combined with M_θ-element LHCP antenna, and "M-SPA" refers to M_θ-element RHCP antenna. We assume a uniform linear array with the half-wavelength spacing antenna array and $M_\theta = 4$ for both SPA and DPA. The SPA has the same information on angles and polarization information as the DPA but uses only the RHCP channels for calculation.

One LOS signal and two multipath signals utmost are assumed in the simulations. These signals are in phase $\arg(\gamma_k) = 0$, $k = 0, 1, 2$, and the direct-to-multipath ratio is $|\gamma_0|/|\gamma_k| = 3\,\text{dB}$, $k = 1, 2$. All the simulations use $C/N_0 = 45\,\text{dB-Hz}$. For the known waveform $c(t)$, we consider the GPS C/A code with code period $T = 1\,\text{ms}$, 1023 chips per code period each with a chip duration $T_c = 977.52\,\text{ns}$ and $N = 20\,\text{ms}$ code periods in total. We assume the set of uniformly distributed delays $\bar{\boldsymbol{\tau}}$ that ranges from $-0.5\,T_c$ to $0.8\,T_c$ with delay interval $0.1\,T_c$, i.e., $M_\tau = 14$. Unless noted, we consider three highly spatially and temporally correlated signals with time delays $\boldsymbol{\tau} = [0, 0.25, 0.3]\ T_c$ from directions specified by the angles $\boldsymbol{\theta} = [0, 9, 6]^\circ$ in most following cases.

Various materials of the reflecting objects are known to affect the multipath reflection coefficients. For the sake of convenience, we define the Dual-Polarization Gain (DPG) [38] of the k th multipath signal as $\text{DPG}_k \doteq \frac{\lambda_{R,k}^2+\lambda_{L,k}^2}{\lambda_{R,k}^2}$, $k = 1, 2$, which is one plus the ratio between the power of the LHCP component of one reflection and the power of the RHCP component. We assume each multipath signal has the same DPG value, i.e., $\text{DPG}_\text{k} = 2$, $k = 1, 2$. As for the reflection coefficients, we assume the phases $\arg(\lambda_{R,k}) = 0$, $k = 1, 2$ and $\arg(\lambda_{L,k}) = 0.5\pi$, $k = 1, 2$ for multipath signals, and these reflection coefficients satisfying $\lambda_{R,k}^2 + \lambda_{L,k}^2 = 1$. Considering mutual coupling effects of DPA, we model this effect as $\boldsymbol{a}_{Rc}(\theta_k) = \boldsymbol{a}_{Lc}(\theta_k) = \boldsymbol{a}(\theta_k)$, $\boldsymbol{a}_{Rx}(\theta_k) = \kappa_R \boldsymbol{a}(\theta_k)$, and $\boldsymbol{a}_{Lx}(\theta_k) = \kappa_L \boldsymbol{a}(\theta_k)$ where $\boldsymbol{a}(\theta_k)$ is the steering vector of a uniformly distributed antenna. The cross-talk parameters $\kappa_R = \kappa_L = -10\,\text{dB}$ are chosen for each signal.

For the sparse methods, the scanning angle grid is uniformly distributed in the range from -90° to 90° with angle interval of $r_\theta = 2^\circ$ between adjacent grid points. Likewise, we adopt a uniform scanning delay grid range covering the $\bar{\boldsymbol{\tau}}$, with delay interval $r_\tau = 0.05\,T_c$. In addition, the hyperparameters $\rho = 0.01$ and $a = b = 1e^{-4}$ are set. Off-grid vectors are set as $\beta_\theta = 0$ and $\beta_\tau = 0$. The convergence condition is satisfied with $\varepsilon_{min} = -30\,\text{dB}$ or the iterative number exceeding 1000.

4.5.1 Multi-dimensional Spectra

In this subsection, the spatial spectra and joint spatial and temporal spectra are shown. Specifically, we display the RHCP part of JAPDE-MSBL's joint spatial, polarization, and temporal spectrum to illustrate the joint spatial-polarization-temporal spectrum. We then compare this RHCP part with other methods within the joint spatial and temporal spectrum.

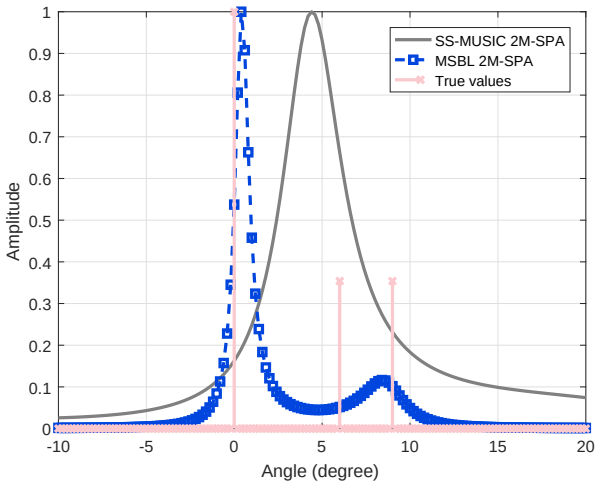


Figure 4.5: Spatial spectra of spatial processing

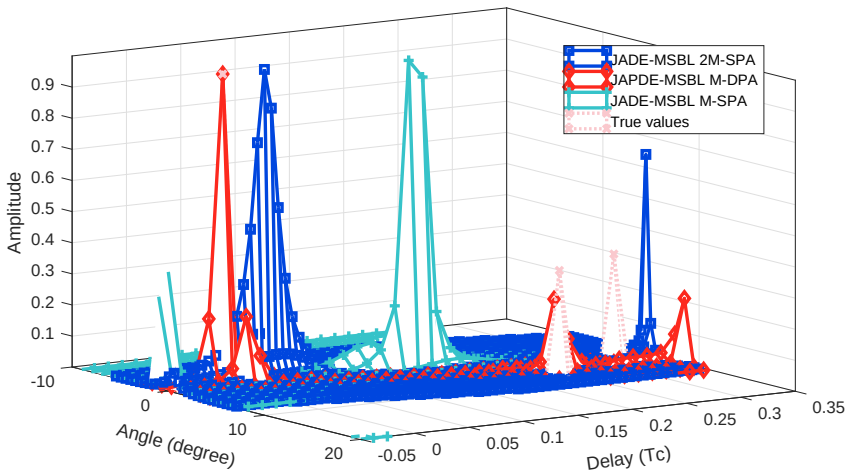


Figure 4.6: Spatial and temporal spectra of multi-dimensional processing

The spectra of two multipath mitigation methods in the spatial domain are depicted in Figure 4.5. SS-MUSIC fails to identify the signals due to a lack of sufficient spatial degrees of freedom, while MSBL only provides an approximate outline, deviating from the true values. These results demonstrate that more than relying solely on spatial processing is needed for distinguishment between correlated signals.

In Figure 4.6, we compare the spectrum of the proposed JAPDE-MSBL with those of JADE-MSBL with M_θ and $2M_\theta$ antennas. The JADE-MSBL spectrum using 2M-SPA is notably sharper, whereas with M-SPA, it becomes difficult to separate the signals. However, JAPDE-MSBL exhibits peaks that are much closer to the true values, confirming the effectiveness of joint spatial, polarization, and temporal domain processing for highly correlated signals.

4.5.2 RMSEs as a Function of Angle Difference

In this section, we examine the RMSEs of LOSS time delay as a function of the angle difference between the LOSS and the first multipath signal. We present two cases: Case A with one LOS signal and one multipath signal; Case B with one LOS signal and two multipath signals.

Case A: RMSEs as a Function of Angle Difference with Two Signals

To comprehensively demonstrate the performance as a function of angle difference, low temporally correlated signals and highly temporally correlated signals are assumed. We set the time delays of the LOS and multipath signal as $[0, 0.1]\ T_c$ and $[0, 0.5]\ T_c$, respectively, for the two scenarios mentioned above.

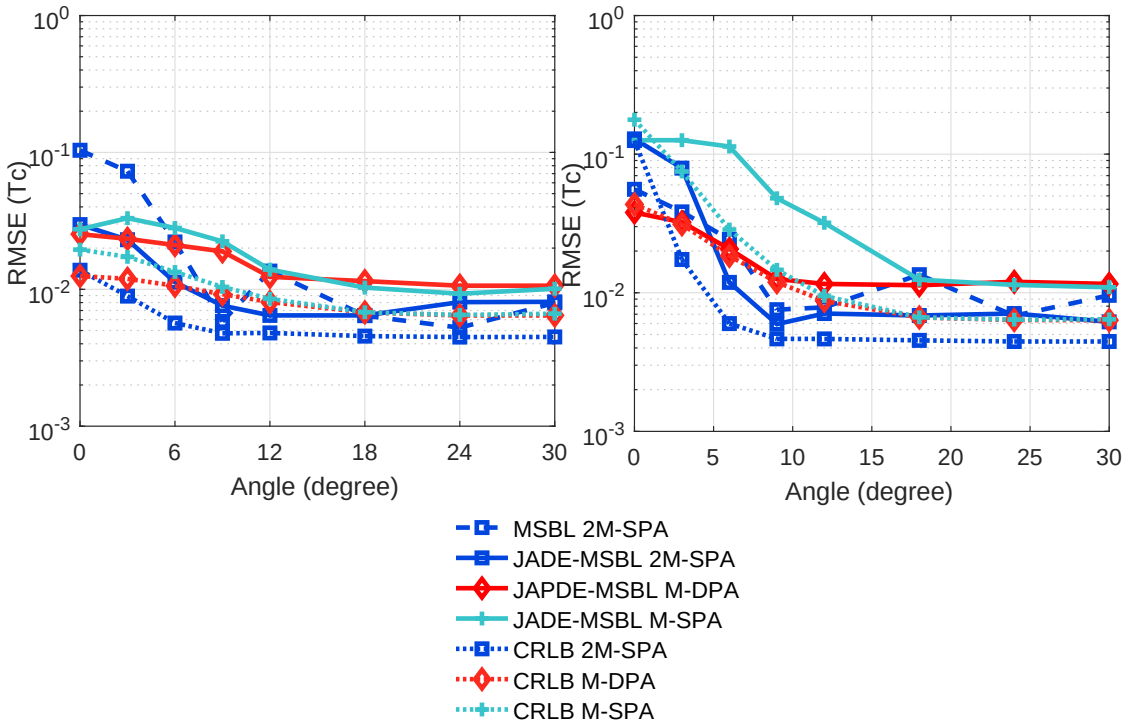


Figure 4.7: RMSEs of LOS time delay as a function of angle difference in case of low temporally correlated signals (left panel) and highly temporally correlated signals (right panel)

The RMSE of MSBL with 2M-SPA, as detailed in Figure 4.7, is generally consistent with that of JADE-MSBL with 2M-SPA across most angle differences, while it occurs a noticeable decrease

in small angle differences. JAPDE-MSBL with M-DPA, in the case of low temporally correlated signals, tends to align with JADE-MSBL with M-SPA. In the case of highly temporally correlated signals, JAPDE-MSBL with M-DPA substantially outperforms the other methods from $0°$ to $5°$. This improvement is attributed to the utilization of polarization information.

Case B: RMSEs as a Function of Angle Difference with Three Signals

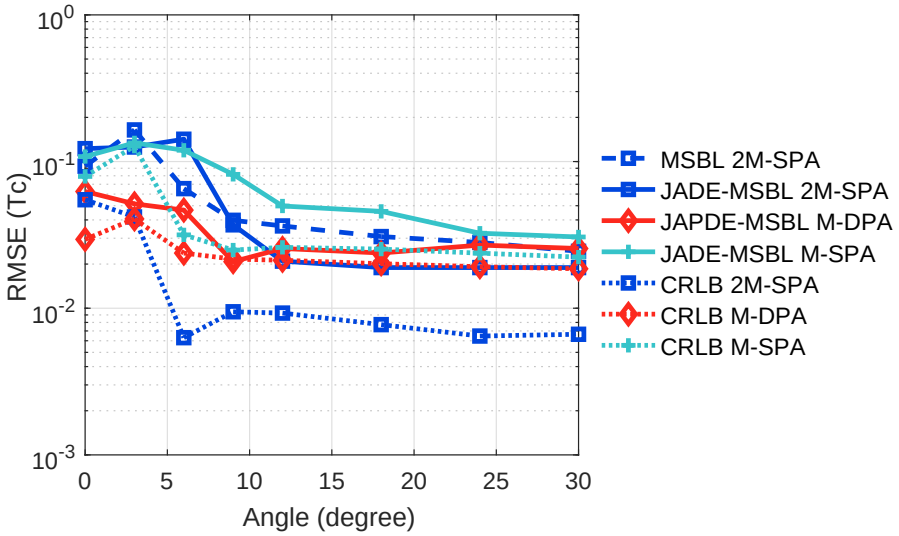


Figure 4.8: RMSEs of LOS time delay as a function of angle difference

In the scenario where three signals exhibit high correlations in space and time, JADE-MSBL with M-SPA results in limited improvement, observable only for large angle differences (see in Figure 4.8). Similarly, using 2M-SPA leads to unsatisfactory resolution for multipath between $0°$ to $12°$ for both MSBL and JADE-MSBL. However, joint space, time, and polarization processing demonstrates superior performance. Specifically, JAPDE-MSBL significantly improves under highly correlated scenarios and yields results closer to the CRLB.

4.5.3 RMSEs as a Function of Delay Difference

This subsection describes in detail RMSEs varying from delay difference between the LOS signal and the first multipath signal. Two cases are further presented: Case C with one LOS signal and one multipath signal; Case D with one LOS signal and two multipath signals.

Case C: RMSEs as a Function of Delay Difference with Two Signals

Similarly, highly spatially correlated and low spatially correlated signals are conducted to investigate different scenarios. We set the LOS and multipath signal time delays for the above two scenarios as $[0, 30]^\circ$ and $[0, 3]^\circ$, respectively.

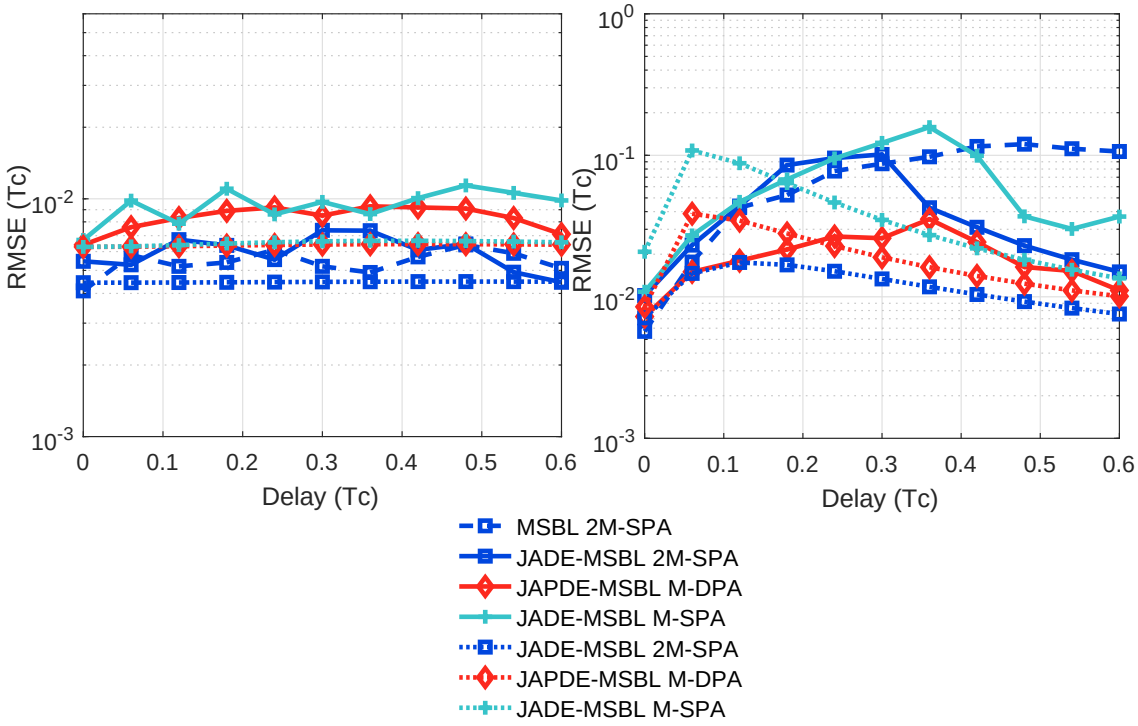


Figure 4.9: RMSEs of LOS time delay as a function of delay difference in case of low spatially correlated signals (left panel) and highly spatially correlated signals (right panel)

Consistent with the analysis in Case 4.5.2, the spatial beamforming MSBL shows a distinct sensitivity to angle differences. When the angle difference is small, MSBL is unable to resolve two spatially correlated signals, as seen in the right panel of Figure 4.9. On the contrary, JAPDE-MSBL facilitates multipath mitigation from additional characteristics in the polarization domain. Its performance in region $[0, 0.3]$ T_c is even better than that of both MSBL and JADE-MSBL using 2M-SPA.

Case D: RMSEs as a Function of Delay Difference with Three Signals

As shown in Figure 4.10, it is evident that three signals have strong spatial and temporal correlations within the region $[0.23, 0.48]$ T_c. The use of MSBL, JADE-MSBL with 2M-SPA, and JADE-MSBL with M-SPA does not appear to effectively address the issue of multipath in this region. Conversely, the proposed JAPDE-MSBL method performs remarkably well, as demonstrated by the results.

4.5.4 RMSEs as a Function of the Number of Antenna Elements

Figure 4.11 illustrates the performance of LOS time delay estimation with respect to the number of antenna elements. Increased size of the antenna array offers more spatial degrees of freedom,

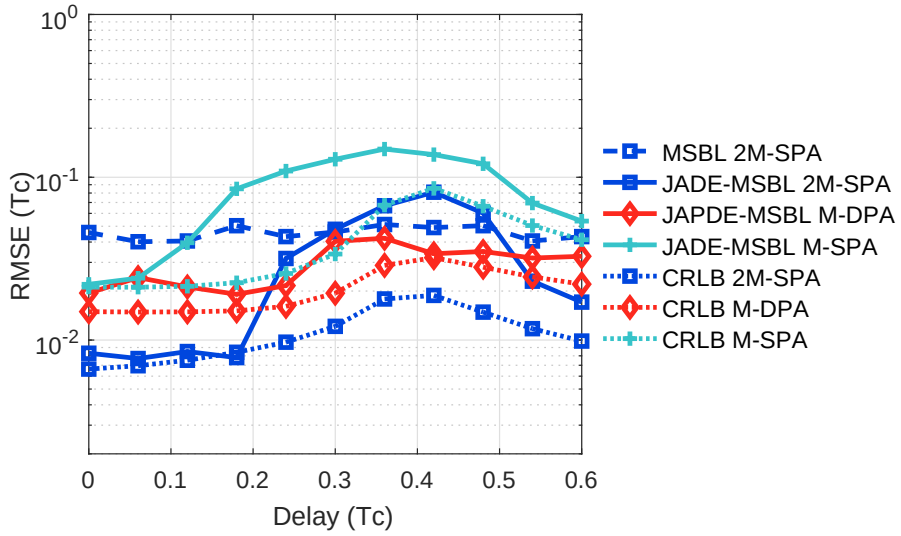


Figure 4.10: RMSEs of LOS time delay as a function of delay difference

resulting in better mitigation of multipath effects for both DPA and SPA. In general, CRLB with 2M-SPA outperforms CRLB with M-DPA (e.g., see the RMSE of M-SPA at $M_\theta = 8$ and the RMSE of M-DPA at $M_\theta = 4$). Thus, it is theoretically better to use 'twice' the number of SPA elements than the same number of DPA, . However, in such a highly correlated signals scenario, JAPDE-MSBL with M-DPA shows comparable or even superior performance to JADE-MSBL with 2M-SPA.

4.5.5 RMSEs as a function of DPG

Figure 4.12 displays the RMSEs of LOSS time delay estimation for various DPG values. In particular, we focus on DPG_1 of the first multipath signal, which ranges from 1.125 to 3, gradually transitioning from a weak LHCP to a strong LHCP multipath signal. For small DPG values where a strong RHCP component dominates the multipath signal, all methods experience performance degradation except for JAPDE-MSBL. JAPDE-MSBL, on the other hand, accounts for both RHCP and LHCP components. Incorporating the LHCP component can aid JAPDE-MSBL in effectively mitigating multipath signals, leading to a favorable effect on LOSS estimation.

4.6 Conclusions

The multipath mitigation problem in the presence of highly spatially and temporally correlated signals has been addressed in this chapter. We propose a joint angle, polarization, and time delay estimation based on the MSBL method by systematically exploiting the sparsity in spatial and temporal domains and characteristics in the polarization domain. The off-grid angle and time delay

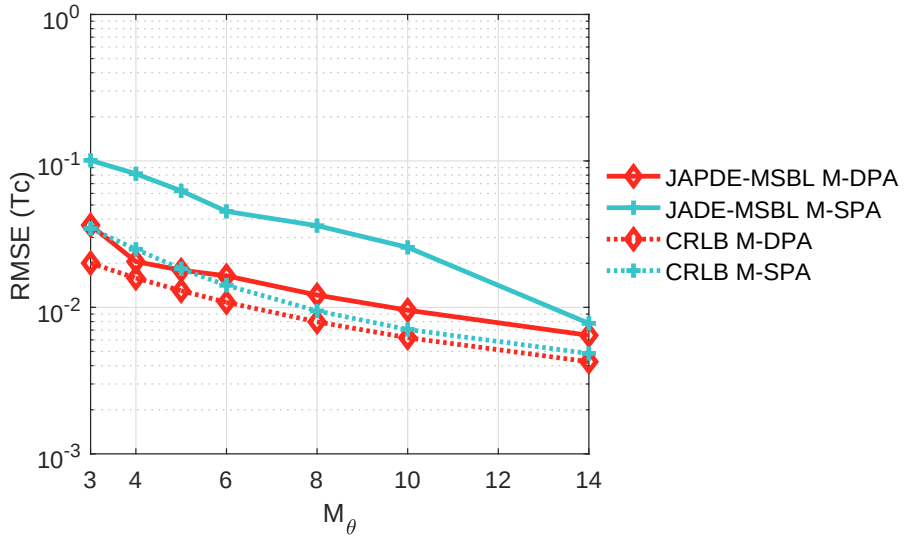


Figure 4.11: RMSEs of LOSS time delay as a function of M_θ

estimation have also been considered concurrently, aiming at accuracy enhancement. The improvement in terms of estimation performance of the LOSS and the ability to distinguish multipath signals are thoroughly verified by simulations showing the estimated spatial spectra and the time delay RMSEs as a function of the varied time delay difference, angle difference, number of antenna elements, and the gain of the LHCP component. Numerical results show that the proposed method JAPDE-MSBL with M-DPA has superiority concerning multipath mitigation in high spatial and temporal correlations between the LOS and the multipath signals, as compared with the existing JADE-MSBL with 2M-SPA and M-SPA, MSBL with 2M-SPA.

4.7 Derivation of CRLB with Dual-polarization Antenna

This appendix provides a closed-form CRLB based on unknown polarization information. In this derivation process, we use Bangs-Slepian's formula [109, 110]. For convenience purposes, we redefine the dual-polarization signal model (2.5) and (2.11),

$$\boldsymbol{Y}_b(n) = \boldsymbol{A}_b(\theta)\,\boldsymbol{V}\boldsymbol{C}_b(\tau) + \boldsymbol{E}_b(n) \tag{4.21}$$

where $\boldsymbol{V} \in \mathbb{C}^{2(K+1)\times(K+1)}$, defined as $\boldsymbol{V} \doteq \mathrm{diag}(\boldsymbol{\lambda})\,\boldsymbol{I}_b\mathrm{diag}(\boldsymbol{\gamma})$, including the complex amplitudes, the reflection coefficient vector $\boldsymbol{v} \doteq [v_{R,0}, v_{L,0}, \ldots, v_{R,K}, v_{L,K}]^T$, $v_{R,k} \doteq \gamma_k\lambda_{R,k}$ and $v_{L,k} \doteq \gamma_k\lambda_{L,k}$. Form the signal parameters into a set,

$$\boldsymbol{\eta} = \left[\mathfrak{Re}\left\{(\boldsymbol{v})^T\right\}, \mathfrak{Im}\left\{(\boldsymbol{v})^T\right\}, \boldsymbol{\theta}^T, \boldsymbol{\tau}^T\right]^T \tag{4.22}$$

According to the Bangs-Slepian's formula, the i,jth element of the Fisher Information Matrix

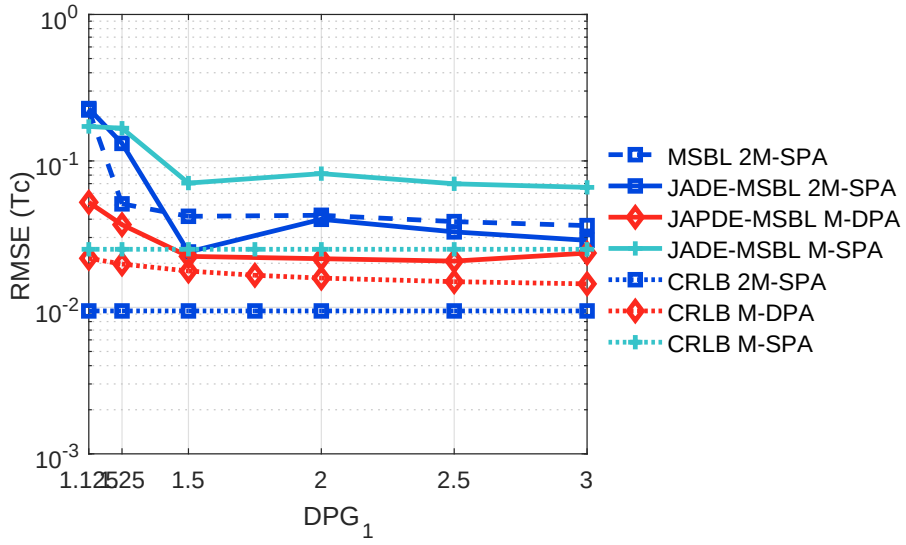


Figure 4.12: RMSEs of LOSS time delay as a function of DPG value

(FIM), which is the inverse of the CRLB matrix, is

$$[\text{FIM}\,(\boldsymbol{\eta})]_{i,j} = -E\left\{\frac{\partial^2 \ln p\,(\boldsymbol{Y}_b, \boldsymbol{\eta})}{\partial \eta_i \partial \eta_j}\right\} \tag{4.23}$$

Therefore, the CRLB for the signal parameters is the inverse of the corresponding block of the FIM, which is partitioned as follows

$$\text{FIM}\,(\boldsymbol{\eta}) = \begin{bmatrix} \Re\mathfrak{e}\,\{\boldsymbol{W}_1\} & -\Im\mathfrak{m}\,\{\boldsymbol{W}_1\} & \Re\mathfrak{e}\,\{\boldsymbol{W}_3\} & \Re\mathfrak{e}\,\{\boldsymbol{W}_5\} \\ \Im\mathfrak{m}\,\{\boldsymbol{W}_1\} & \Re\mathfrak{e}\,\{\boldsymbol{W}_1\} & \Im\mathfrak{m}\,\{\boldsymbol{W}_3\} & \Im\mathfrak{m}\,\{\boldsymbol{W}_5\} \\ \Re\mathfrak{e}\,\{\boldsymbol{W}_3{}^T\} & \Im\mathfrak{m}\,\{\boldsymbol{W}_3{}^T\} & \Re\mathfrak{e}\,\{\boldsymbol{W}_2\} & \Re\mathfrak{e}\,\{\boldsymbol{W}_6\} \\ \Re\mathfrak{e}\,\{\boldsymbol{W}_5{}^T\} & \Im\mathfrak{m}\,\{\boldsymbol{W}_5{}^T\} & \Re\mathfrak{e}\,\{\boldsymbol{W}_6{}^T\} & \Re\mathfrak{e}\,\{\boldsymbol{W}_4\} \end{bmatrix} \in \mathbb{C}^{4(K+1)\times 4(K+1)} \tag{4.24}$$

After straightforward but lengthy calculations, similar to the derivations in [112], we get

$$\boldsymbol{W}_1 = \frac{2}{\sigma_n^2}\left[\left(\boldsymbol{A}_b^H \boldsymbol{A}_b\right) \odot \left(\left(\boldsymbol{C}_b^* \boldsymbol{C}_b^T\right) \otimes [\boldsymbol{e}, \boldsymbol{e}]\right)\right] \in \mathbb{C}^{2(K+1)\times 2(K+1)} \tag{4.25a}$$

$$\boldsymbol{W}_2 = \frac{2}{\sigma_n^2}\left[\left(\boldsymbol{C}_b^* \boldsymbol{C}_b^T\right) \odot \left(\left(\boldsymbol{D}_\theta \boldsymbol{V}\right)^H \left(\boldsymbol{D}_\theta \boldsymbol{V}\right)\right)\right] \in \mathbb{C}^{(K+1)\times(K+1)} \tag{4.25b}$$

$$\boldsymbol{W}_3 = \frac{2}{\sigma_n^2}\left\{\left(\boldsymbol{A}_b^H \boldsymbol{D}_\theta \boldsymbol{V}\right) \odot \left(\left(\boldsymbol{C}_b^* \boldsymbol{C}_b^T\right) \otimes \boldsymbol{e}\right)\right\} \in \mathbb{C}^{2(K+1)\times(K+1)} \tag{4.25c}$$

$$\boldsymbol{W}_4 = \frac{2}{\sigma_n^2}\left\{\left(\boldsymbol{V}^H \boldsymbol{A}_b^H \boldsymbol{A}_b \boldsymbol{V}\right) \odot \left(\boldsymbol{D}_\tau \boldsymbol{D}_\tau^H\right)^T\right\} \in \mathbb{C}^{(K+1)\times(K+1)} \tag{4.25d}$$

$$\boldsymbol{W}_5 = \frac{2}{\sigma_n^2}\left\{\left(\boldsymbol{A}_b^H \boldsymbol{A}_b \boldsymbol{V}\right) \odot \left(\left(\boldsymbol{C}_b^* \boldsymbol{D}_\tau^T\right) \otimes \boldsymbol{e}\right)\right\} \in \mathbb{C}^{2(K+1)\times(K+1)} \tag{4.25e}$$

$$\boldsymbol{W}_6 = \frac{2}{\sigma_n^2}\left\{\left(\boldsymbol{V}^H \boldsymbol{D}_\theta^H \boldsymbol{A}_b \boldsymbol{V}\right) \odot \left(\boldsymbol{C}_b^* \boldsymbol{C}_b^T\right)\right\} \in \mathbb{C}^{(K+1)\times(K+1)} \tag{4.25f}$$

where $e = [1,1]^T$. We also have $\boldsymbol{D}_\theta = \left[\frac{\partial \boldsymbol{a}_{R,0}(\theta_0)}{\partial \theta_0}, \frac{\partial \boldsymbol{a}_{L,0}(\theta_0)}{\partial \theta_0}, \ldots, \frac{\partial \boldsymbol{a}_{R,K}(\theta_K)}{\partial \theta_K}, \frac{\partial \boldsymbol{a}_{L,K}(\theta_K)}{\partial \theta_K}\right] \in \mathbb{C}^{2M_\theta \times 2(K+1)}$ and $\boldsymbol{D}_\tau = \left[\frac{\partial \boldsymbol{c}(\tau_0)}{\partial \tau_0}, \ldots, \frac{\partial \boldsymbol{c}(\tau_K)}{\partial \tau_K}\right]^T \in \mathbb{C}^{(K+1)\times L}$.

Based on the properties valid for non-singular matrices, the CRLB for the time delays is the trailing block of the inverse of FIM ($\boldsymbol{\eta}$). Via the formula of the inverse of a partitioned matrix, this CRLB can be expressed as

$$\mathrm{CRB}^{-1}(\boldsymbol{\tau}) = \Re\{\boldsymbol{W}_4\} - \begin{bmatrix} \Re\left\{\{\boldsymbol{W}_5\}^T\right\} & \Im\left\{\{\boldsymbol{W}_5\}^T\right\} & \Re\left\{\{W_6\}^T\right\} \end{bmatrix} \boldsymbol{\Pi} \begin{bmatrix} \Re\{\boldsymbol{W}_5\} \\ \Im\{\boldsymbol{W}_5\} \\ \Re\{\boldsymbol{W}_6\} \end{bmatrix} \tag{4.26}$$

and $\boldsymbol{\Pi}$ can be simplified using the formula of the partitioned matrix inverse again,

$$\begin{aligned} \boldsymbol{\Pi} &= \begin{bmatrix} \Re\{\boldsymbol{W}_1\} & -\Im\{\boldsymbol{W}_1\} & \Re\{W_3\} \\ \Im\{\boldsymbol{W}_1\} & \Re\{\boldsymbol{W}_1\} & \Im\{\boldsymbol{W}_3\} \\ \Re\left\{\boldsymbol{W}_3{}^T\right\} & \Im\left\{\boldsymbol{W}_3{}^T\right\} & \Re\{\boldsymbol{W}_2\} \end{bmatrix}^{-1} \\ &= \begin{bmatrix} \boldsymbol{\Omega}_1 + \boldsymbol{\Omega}_2 & -\begin{bmatrix} \Re\left\{\boldsymbol{W}_1^{-1}\boldsymbol{W}_3\right\} \\ \Im\left\{\boldsymbol{W}_1^{-1}\boldsymbol{W}_3\right\} \end{bmatrix} \boldsymbol{\Omega} \\ -\boldsymbol{\Omega}\begin{bmatrix} \Re\left\{\boldsymbol{W}_3^T\left(\boldsymbol{W}_1^{-1}\right)^*\right\} & \Im\left\{\boldsymbol{W}_3^T\left(\boldsymbol{W}_1^{-1}\right)^*\right\} \end{bmatrix} & \boldsymbol{\Omega} \end{bmatrix} \end{aligned} \tag{4.27}$$

with $\boldsymbol{\Omega}_1 = \begin{bmatrix} \Re\left\{\boldsymbol{W}_1^{-1}\right\} & -\Im\left\{\boldsymbol{W}_1^{-1}\right\} \\ \Im\left\{\boldsymbol{W}_1^{-1}\right\} & \Re\left\{\boldsymbol{W}_1^{-1}\right\} \end{bmatrix}$, $\boldsymbol{\Omega} = \left\{\Re\{\boldsymbol{W}_2\} - \Re\left\{\boldsymbol{W}_3^H \boldsymbol{W}_1^{-1} \boldsymbol{W}_3\right\}\right\}^{-1}$ and $\boldsymbol{\Omega}_2 = \begin{bmatrix} \Re\left\{\boldsymbol{W}_1^{-1}\boldsymbol{W}_3\right\} \\ \Im\left\{\boldsymbol{W}_1^{-1}\boldsymbol{W}_3\right\} \end{bmatrix} \boldsymbol{\Omega} \begin{bmatrix} \Re\left\{\boldsymbol{W}_3^T\left(\boldsymbol{W}_1^{-1}\right)^*\right\} & \Im\left\{\boldsymbol{W}_3^T\left(\boldsymbol{W}_1^{-1}\right)^*\right\} \end{bmatrix}$.

Substituting (4.27) into (4.26), we further simplify the $\mathrm{CRB}^{-1}(\tau)$,

$$\begin{aligned} \mathrm{CRB}^{-1}(\boldsymbol{\tau}) = &\Re\{\boldsymbol{W}_4\} - \Re\left\{\boldsymbol{W}_5^H \boldsymbol{W}_1^{-1} \boldsymbol{W}_5\right\} \\ &+ \left(\Re\left\{\boldsymbol{W}_6{}^T\right\}\boldsymbol{\Omega} - \Re\left\{\boldsymbol{W}_5^H \boldsymbol{W}_1^{-1} \boldsymbol{W}_3\right\}\right)\left(\Re\left\{\boldsymbol{W}_3^H \boldsymbol{W}_1^{-1} \boldsymbol{W}_5\right\} - \Re\{\boldsymbol{W}_6\}\right) \end{aligned} \tag{4.28}$$

Joint Spatial and Frequential GNSS Multipath Mitigation

5.1 Introduction

As discussed in Chapter 3 and 4, many representative multipath mitigation methods have been proposed for GNSS signals in the past decades. For the single-antenna GNSS receiver, nEML [9] and MEDLL [10, 113] are the most popular ones. Thanks to the major leap forward in multi-antenna technology, joint spatial and temporal multipath mitigation methods exploit both spatial and temporal domains, which can improve the robustness of multipath resolution. These methods are basically classified into three categories, joint spatial and temporal GNSS multipath mitigation based on subspace methods [27, 54], joint spatial and temporal GNSS multipath mitigation based on ML methods [112], and joint spatial and temporal GNSS multipath mitigation based on compressed sensing methods [68, 75]. Among these methods, SAGE can perform closely to the Cramer-Rao lower bound and reach the balance between convergence and complexity. It can be regarded as an appropriate alternative in the direction of GNSS multipath mitigation.

The signal processing techniques currently used for GNSS signals are primarily designed to handle narrowband signals. However, in scenarios where the signals are highly temporally correlated, these techniques may not be effective due to limited temporal resolution, leading to sub-optimal meter-level ranging accuracy. To overcome this issue, it is necessary to break the bandwidth limitation and use meta-signals, which combine two GNSS signals transmitted on different carrier frequencies, to achieve bandwidths of tens or hundreds of megahertz. This approach fundamentally supports higher tracking accuracy and better multipath mitigation [39]. Most current meta-signal processing methods adopt a ”divide and conquer” approach, where each of the two signals is processed separately before being coherently combined to process the entire wideband signal. For example, pioneering work [20] and double loop-based techniques [47–49] are presented. Unfortunately, although meta-signals are suitable for multipath mitigation, the shape of ACF will

be distorted in the multipath environment.

Based on the superiority of spatial processing brought by multi-antenna technology, this chapter utilizes the synergistic effect of spatial characteristics and meta-signal temporal characteristics to process jointly and design the SAGE-based locked loop. To sum up, this chapter is arranged as follows: Firstly, the temporal characteristics of meta-signal are firstly introduced, especially the characteristics and performance in the case of multipath signals, and the feasibility of spatial and frequential processing for multipath mitigation is analyzed. Secondly, a double side-band processing tracking loop design based on multi-dimensional processing was proposed to maintain the time delay estimation accuracy of decimeter- or even centimeter-level in multipath environment. Thirdly, this chapter demonstrates the proposed scheme's effectiveness in extremely highly correlated signals compared with typical multipath mitigation methods.

5.2 Feasibility Analysis of Joint Spatial and Frequential GNSS Multipath Mitigation

This section first presents the definition of meta-signal and the characteristics of three representative meta-signals from the perspective of power spectrum density (PSD) and ACF. Then, the multipath-induced ACFs of the meta-signals are examined. A spatial-temporal spectrum of the meta-signal is also provided and discussed as an improved solution to multipath mitigation.

5.2.1 Brief Introduction to Meta-signal

Meta-signal is defined as an ensemble of two different frequency band GNSS signals, and hence has a wider bandwidth compared to standard GNSS signals. This wide-bandwidth property allows the meta-signal to obtain a better time resolution, therefore more precise ranging accuracy. Any pair of synchronized signals could be in principle chosen, however the signals from the same satellite and modulated on adjacent frequencies are more appropriate than others [20] that they enjoy the same propagation path and similar time delay between the two components in meta-signal. Among a couple of discussed examples, this section will examine the three combinations in detail: the GPS L1 and L2C signals transmitted on L-band, the Galileo E5a and E6 signals transmitted on E-band, and the Beidou B1I and B1C signals transmitted on B-band. The characteristics of the meta-signal are given in terms of PSD and ACF, as follows.

The PSD of the meta-signal is approximated by the sum of the PSDs of the left and right side-band components [45]. As the bandwidth of the meta-signal is normally spaced by greater than several megahertz, the vast majority of the spectrum of each component of the meta-signal does not overlap, which allows for negligible interaction between the two components of the spectrum. The PSDs of typical meta-signals are shown in Figure 5.1.

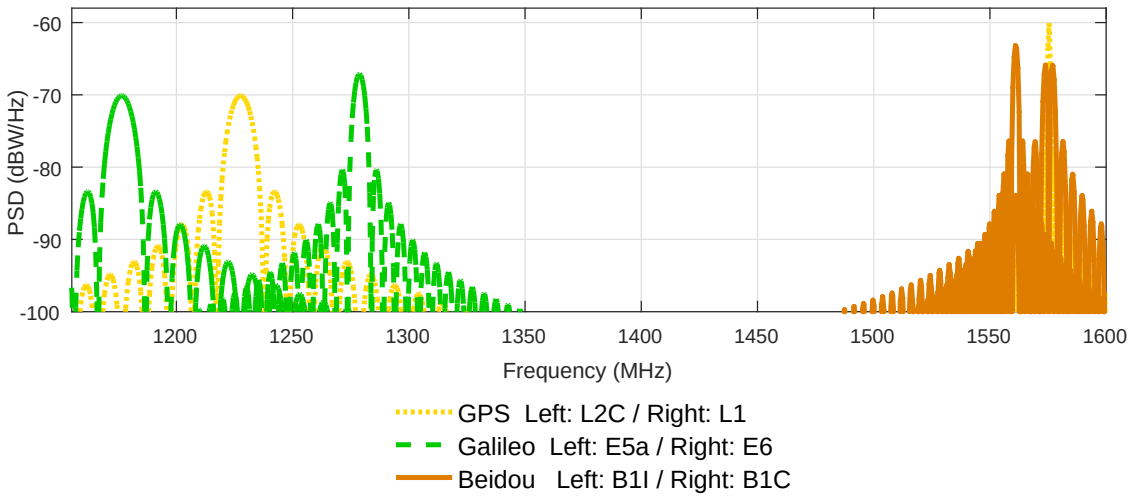


Figure 5.1: PSDs of typical meta-signals

To display the potential of the meta-signal more intuitively, we next discuss the ACF of the meta-signal [20], which can be derived as follows,

$$\begin{aligned} R(\Delta\tau) &= R^{L}(\Delta\tau) + R^{R}(\Delta\tau) \\ &= R_{c^{L}}(\Delta\tau)\, e^{j2\pi f_s \Delta\tau} + R_{c^{R}}(\Delta\tau)\, e^{-j2\pi f_s \Delta\tau} \end{aligned} \tag{5.1}$$

where $R_{c^{L}}(\Delta\tau)$ and $R_{c^{R}}(\Delta\tau)$ denote the ACFs of the left and right side-band component, respectively. The corresponding ACFs of three typical meta-signals are depicted in Figure 5.2.

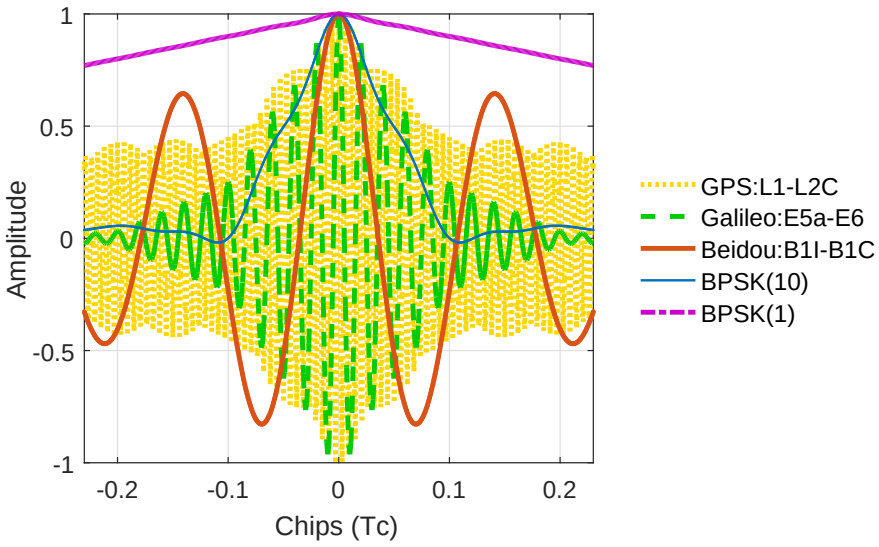


Figure 5.2: ACFs of different satellite signals and meta-signals

In the two figures above, we show the PSDs of typical meta-signals and compare the main ACF peaks, where as expected, a wider PSD implies a narrower ACF and hence a higher time resolution.

In particular, the ACF main peaks of typical meta-signals are evidently narrower compared to the ACF peaks of standard GNSS signals. The main peak of the B-band meta-signal of Beidou B1I and B1C signals, for example, is just about one-fourteenth as large as that of GPS L1 of the C/A signal. The above performance indicates that such a high-resolution meta-signal is a compelling feature for multipath mitigation. A detailed description of the different GNSS meta-signals' main characteristics is given in Table 5.1.

Table 5.1: Meta-signals main characteristics

Signals		Modulation	Frequency (MHz)	Bandwidth (MHz)	Main Peak
GPS	L2C	BPSK(10)	1227.6	347.82	$0.00288\,T_c$
	L1	BPSK(1)	1575.42		
Galileo	E5a	BPSK(10)	1176.45	102.3	$0.00977\,T_c$
	E6	BPSK(5)	1278.75		
Beidou	B1I	BPSK(2)	1561.098	14.322	$0.0698\,T_c$
	B1C data	BOC(1,1)	1575.42		

5.2.2 Characteristic Analysis of Meta-signal in Multipath Case

The main peak of ACF has a sharp, almost triangular shape, which facilitates multipath mitigation theoretically, as shown in Figure 5.2. However, the ACF will be seriously deformed in practical multipath environments. To verify the multipath effect on the meta-signal, we consider two signals: one LOS signal with one multipath signal, and the time delay of the LOS signal is assumed as $0\,T_c$. The SMR is supposed to be 6 dB and we take the Beidou B1I-B1C signals as the meta-signal example. When the time delay difference between the LOS signal and the multipath signal is large, i.e., on the order of magnitude or larger than the width of the main peak (the time delay of the multipath signal is assumed to be $0.2\,T_c$), the amplitudes of the peaks change and a side peak can become higher than the central one, as depicted in the red curve of Figure 5.3. When the time delay difference between the LOS signal and the multipath signal is small, i.e., restricted in the main peak (the time delay of the multipath signal here is assumed to be $0.03\,T_c$), then the shape of the main peak is distorted, as demonstrated in the blue curve of Figure 5.3. The ACFs in the above two cases are distorted and may lead to inaccurate estimation of LOS signal.

5.2.3 Feasibility Analysis of Spatial and Frequential Multipath Mitigation

To tackle multipath mitigation, especially in the presence of highly temporally correlated signals, the multi-antenna technology can be efficiently exploited, as it provides extra spatial degrees of freedom. With the help of the spatial domain, we can observe the LOS and multipath signals from multiple characteristics, such as angle and time delay. Figure 5.4 illustrates the spatial and

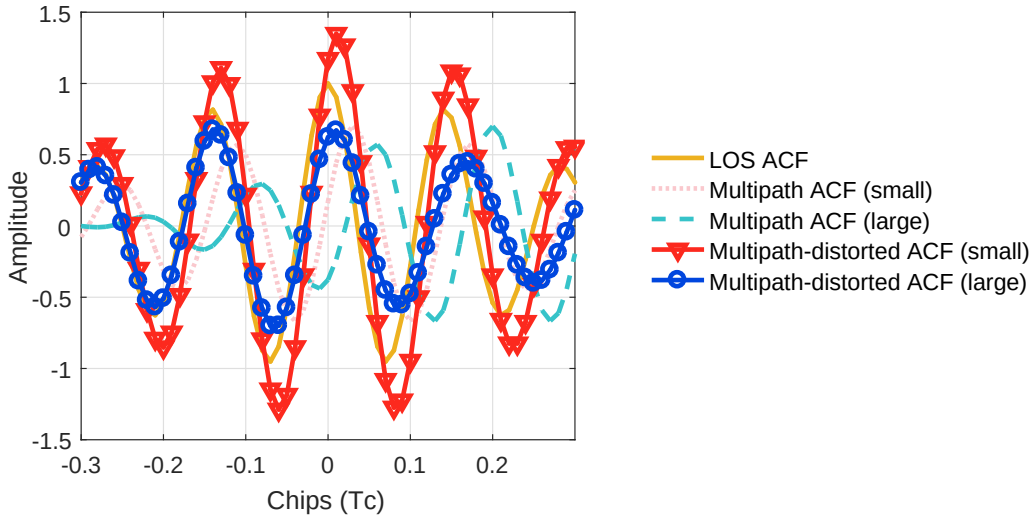


Figure 5.3: Spatial-temporal spectrum of the meta-signal in multipath situation

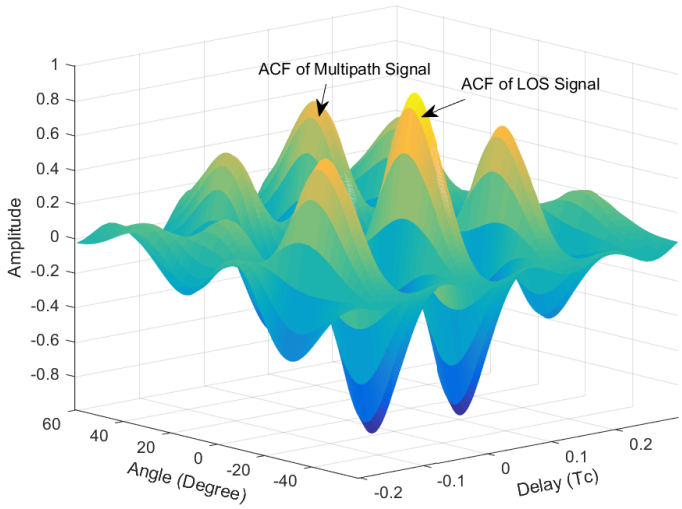


Figure 5.4: Spatial-temporal spectrum of the meta-signal in multipath situation

temporal spectrum of Beidou B-band meta-signal received by the multi-antenna array within the same settings in Figure 5.3. Note that this spectrum is directly acquired by the two-dimensional ML method in spatial and temporal domains.

Figure 5.4 shows that the LOS signal and the multipath signal are undoubtedly discriminated thanks to the joint use of spatial and temporal domains, and two perfect triangle-shaped ACFs are observed. Besides, the sharp main peak of each separated ACF indicates excellent time delay estimation accuracy. Inspired by this spatial and temporal meta-signal spectrum, such a combination of multi-dimensional processing and meta-signal is expected to further improve multipath mitigation.

5.3 GNSS Meta-signal SAGE-based Multipath-Mitigating Loop Design

Based on the above analyses, we next investigate the specific processing structure dedicated to meta-signal. In particular, several techniques are available: The SAGE iteratively deals with multipath mitigation from multi-dimensions and provides precise descriptions for each signal. The broadband advantage of the meta-signal contributes to high-accuracy estimates and the improvement of multipath mitigation in the temporal domain. Numerous types of loops: Angle Locked Loops (ALLs), DLLs, and PLLs, can be extended to filter and predict each signal. Our major concern is how to incorporate the above techniques into a multipath-mitigating loop design and achieving multipath mitigation (even in highly correlated signals). In the upcoming section, we first discuss the basic concept of the SAGE algorithm and then introduce the proposed SAGELL design from its structure to the whole scheme.

5.3.1 SAGE-based Estimator for Side-band Component

The derivation of SAGE relies on two key notions: complete (unobservable) and incomplete (observable) data. In the problem of estimating superimposed single side-band meta-signals, referring to Equation (2.12), the individually observable signal* $\boldsymbol{s}_k^L(t)$ is expressed as

$$\begin{aligned}\boldsymbol{s}_k^L(t) &\doteq \boldsymbol{s}_k^L\left(t;\boldsymbol{\xi}_k^L,\alpha_k^L\right)\\ &= \alpha_k^L \boldsymbol{a}^L(\theta_k)\, c^L(t-\tau_k)\, e^{-j2\pi f_s(t-\tau_k)} e^{j\left(2\pi f_{d,k}t+\phi_k\right)}\end{aligned} \tag{5.2}$$

based on previous parameter estimate vector $\boldsymbol{\xi}_k \doteq [\theta_k, \tau_k, f_{d,k}, \phi_k]$ of the k th signal for the left side-band component. Corrupted by a part of the additive noise, the equation

$$\boldsymbol{x}_k^L(t) \doteq \boldsymbol{s}_k^L(t) + \boldsymbol{n}_k^L(t) \tag{5.3}$$

constitutes the natural set of complete data [22]. The received side-band component $\boldsymbol{y}_k^L(t)$ is identified with incomplete data. It is related to the received signal according to $\boldsymbol{y}^L(t) = \sum_{k=1}^K \boldsymbol{x}_k^L(t)$.

Since $\boldsymbol{x}_k^L(t)$ is not observable, one can try to estimate it based on the observation $\boldsymbol{y}^L(t)$ of the incomplete data and previous estimates. A natural estimate of $\boldsymbol{x}_k^L(t)$ is its conditional expectation (Expectation-step) which is given by

$$\hat{\boldsymbol{x}}_k^L(t) = \boldsymbol{y}^L(t) - \sum_{k'=1,k'\neq k}^{K} \boldsymbol{s}_{k'}^L(t) \tag{5.4}$$

*To avoid repetition, the left side-band component of the meta-signal is taken as an example. The SAGE algorithm of the right side-band component can be processed in a similar way.

To get parameters estimated, including angles, time delays, DFOs, amplitudes, and carrier phase offsets for each signal, the Maximization-step is presented,

$$z\left(\theta_k,\tau_k,f_{d,k}\right) \doteq \left(\boldsymbol{a}^L\left(\theta_k\right)\right)^H \hat{\boldsymbol{x}}_k^L\left(t\right)\left(c^L(t-\tau_k)\, e^{-j2\pi f_s(t-\tau_k)} e^{j2\pi f_{d,k}t}\right)^H \tag{5.5a}$$

$$\hat{\theta}_k = \arg\max_{\theta}\left\{\left|z\left(\theta_k,\hat{\tau}_k,\hat{f}_{d,k}\right)\right|^2\right\} \tag{5.5b}$$

$$\hat{\tau}_k = \arg\max_{\tau}\left\{\left|z\left(\hat{\theta}_k,\tau_k,\hat{f}_{d,k}\right)\right|^2\right\} \tag{5.5c}$$

$$\hat{f}_{d,k} = \arg\max_{f_d}\left\{\left|z\left(\hat{\theta}_k,\hat{\tau}_k,f_{d,k}\right)\right|^2\right\} \tag{5.5d}$$

$$\hat{\alpha}_k = \left|z\left(\hat{\theta}_k,\hat{\tau}_k,\hat{f}_{d,k}\right)\right| \Big/ M_\theta \tag{5.5e}$$

$$\hat{\phi}_k = \text{angle}\left(z\left(\hat{\theta}_k,\hat{\tau}_k,\hat{f}_{d,k}\right)\right) \tag{5.5f}$$

where the multi-dimensional procedure is turned into single-dimensional ones. It should be noted that although SAGE ensures the multipath mitigation while reducing the complexity, it tends to fall into local optimality due to its sensitivity against initialization in a multipath environment. Any initialization algorithms that provide practical spatial and temporal initial values can be arbitrarily selected, for example, [102], [25]. To initial the SAGELL, we use a joint spatial and temporal sparse representation algorithm to estimate the coarse time delays and angles for all signals of the meta-signal via DSB processing. Please refer to the reference [75] for more details.

5.3.2 SAGELL for Meta-signal

The multi-dimensional estimator SAGE and the meta-signal are a good combination to attain a centimeter-level ranging accuracy in a multipath case. Moreover, with the help of various ALLs, DLLs, and PLLs, the design of SAGELL for meta-signal can resolve and track each signal. As shown in Figure 5.5, the SAGELL design for meta-signal is generally divided into two distinct sections: the SAGE-based discriminator (the purple, yellow, and green parts) and the combinational tracking loops (the blue part). The SAGE-based discriminator contributes to multipath mitigation by means of iterative SAGE and meta-signal. The two SAGE-based estimators are based on the left and right component of the meta-signal and the meta-signal processing unit is responsible for coherent or noncoherent combinations of all the estimates. The whole procedure of discriminator tends to follow the dotted lines. To keep a low resource consumption, we take the divide-and-conquer processing into account that the SAGE-based discriminator consists of two SAGE-based estimators and one meta-signal processing unit.

More specifically, we could expand the SAGELL to analyze the signal processing, as the specific description of SAGELL structure demonstrated in Figure 5.6 (The parts of the same color in

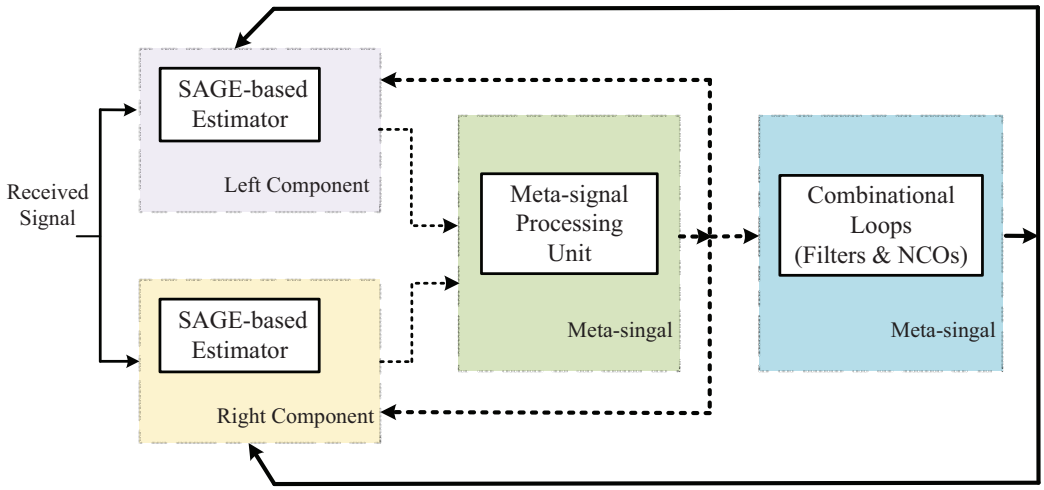


Figure 5.5: SAGELL Overview

the two figures 5.5 and 5.6 have the same function.)

SAGE-based estimator for side-band component (the purple and yellow parts): We here carry out two SAGE-based estimators to sequentially separate each signal of the left and right side-band component. The black dotted lines show the process in each side-band estimator. Firstly, the observable side-band signals $\left\{\boldsymbol{s}_k^L(t), \boldsymbol{s}_k^R(t)\right\}$ are reconstructed based on the updated variables $\left\{\Delta\hat{\alpha}_k^L, \Delta\hat{\alpha}_k^R, \Delta\hat{\boldsymbol{\xi}}_k\right\}$ obtained by the SAGE-based discriminator and the results $\hat{\boldsymbol{\xi}}_k$ predicted in the last loop period. Secondly, the unobservable side-band signals $\left\{\boldsymbol{x}_k^L(t), \boldsymbol{x}_k^R(t)\right\}$ are achieved through the Expectation-step. Thirdly, with the help of the Maximization-step, we acquire the estimated spatial ACFs $\left\{\hat{R}_{\theta,k}^L\left(\Delta\theta_k^L\right), \hat{R}_{\theta,k}^R\left(\Delta\theta_k^R\right)\right\}$, temporal ACFs $\left\{\hat{R}_{\tau,k}^L\left(\Delta\tau_k^L\right), \hat{R}_{\tau,k}^R\left(\Delta\tau_k^R\right)\right\}$, and the prompt correlators $\left\{\hat{P}_{\phi,k}^L\left(\Delta\phi_k^L\right), \hat{P}_{\phi,k}^R\left(\Delta\phi_k^R\right)\right\}$ for each side-band component.

Meta-signal processing (the green part): In order to obtain high accuracy of time delay estimation, we take advantage of the meta-signal characteristics, such as wide-bandwidth and strong coherence between the two components. The estimated ACFs and prompt correlators of each SAGE-based estimator are sent to the angle, code phase, and carrier phase units to coherently or incoherently form the global parameters, namely, angle $\Delta\hat{\theta}_k$, time delay $\Delta\hat{\tau}_k$, and carrier phase $\Delta\hat{\phi}_k$. These variables, along with the amplitudes $\left\{\Delta\hat{\alpha}_k^L, \Delta\hat{\alpha}_k^R\right\}$ for each signal are further updated through iterations going inside the whole SAGE-based discriminator. It is reminded that the process of the entire meta-signal shall be observed through the colored dotted lines.

Regarding the tracking loops (the blue part) where the process flow goes after the solid lines, the parameters (angles, time delays, and carrier phases) for each signal merged by the meta-signal processing unit are sent into the corresponding ALLs, DLLs and PLLs for filtering and predicting. These functions can be realized by common filters and Numerically-Controlled Oscillators (NCOs) in GNSS locked loops [114]. The precise prediction results $\hat{\boldsymbol{\xi}}_k$ are fed back to the next tracking period for initialization of SAGE-based discriminator.

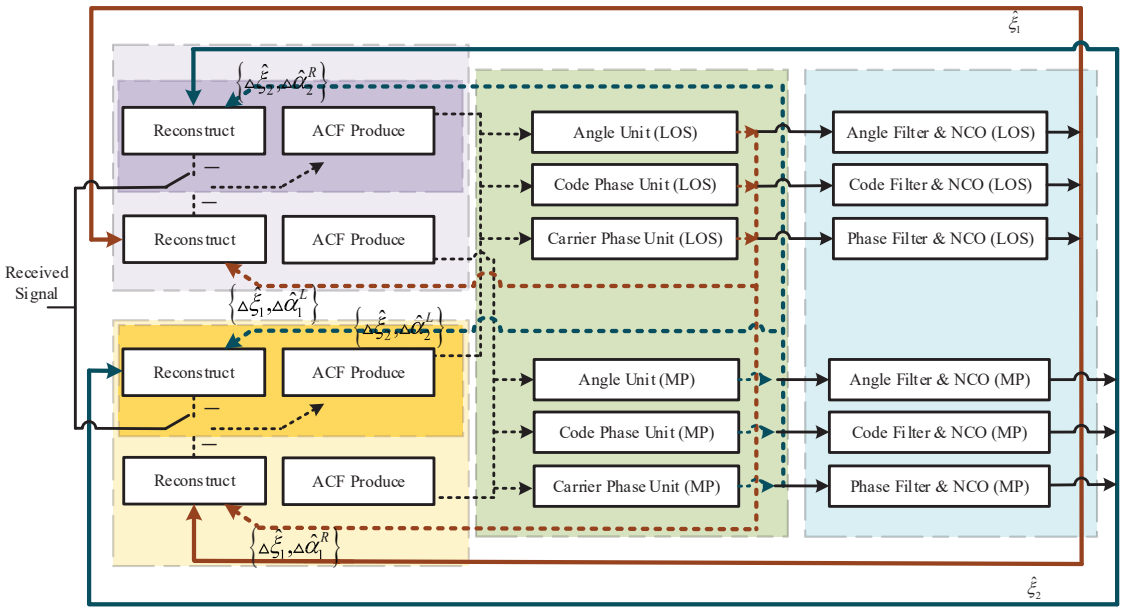


Figure 5.6: SAGELL Structure

SAGE-based estimator for side-band component

Now we take a more detailed look at the SAGE-based discriminator, including the purple, yellow, and green parts, considering the particular case of the SAGE-based estimator that there is one LOS signal and one multipath signal of each side-band component. The further specification referring to the SAGE-based discriminator for meta-signal is displayed in Figure 5.7.

Based on the prediction results in SAGELL, the estimated parameter vectors $\hat{\boldsymbol{\xi}}_1$ and $\hat{\boldsymbol{\xi}}_2$, and the estimated amplitudes $\left\{\Delta\hat{\alpha}_1^L, \Delta\hat{\alpha}_2^L, \Delta\hat{\alpha}_1^R, \Delta\hat{\alpha}_2^R\right\}$, the reconstructed multipath signal $\boldsymbol{s}_2^L(t)$ can be expressed as

$$\begin{aligned}\boldsymbol{s}_2^L(t) &\doteq \boldsymbol{s}_2^L\left(t;\hat{\boldsymbol{\xi}}_2,\Delta\hat{\alpha}_2^L\right)\\ &= \Delta\hat{\alpha}_2^L\boldsymbol{a}^L\left(\hat{\theta}_2\right)c^L\left(t-\hat{\tau}_1\right)e^{-j2\pi f_s(t-\hat{\tau}_2)}e^{j\left(2\pi\hat{f}_{d,2}t+\hat{\phi}_2\right)}\end{aligned} \tag{5.6}$$

The residual part is defined as the estimated LOS signal $\hat{\boldsymbol{x}}_0^L(t)$, i.e., an unobservable one,

$$\hat{\boldsymbol{x}}_1^L(t) = \boldsymbol{y}^L(t) - \sum_{k'=1,k'\neq k}^{K}\boldsymbol{s}_{k'}^L(t) \tag{5.7}$$

Thus, the variables for the LOS signal of left side-band component, such as the spatial ACF $\hat{R}_{\theta,1}^L\left(\Delta\theta_1^L\right)$, the temporal ACF $\hat{R}_{\tau,1}^L\left(\Delta\tau_1^L\right)$, the prompt correlator $\hat{P}_{\phi,1}^L\left(\Delta\phi_1^L\right)$, and its amplitude $\Delta\hat{\alpha}_1^L$ are estimated successively. They can be approximately denoted as the equations

$$\hat{R}_{\theta,1}^L\left(\Delta\theta_1^L\right) = \frac{1}{T}\int_0^T\left(\boldsymbol{a}^L\left(\hat{\theta}_1+\Delta\theta_1^L\right)\right)^H\hat{\boldsymbol{x}}_1^L(t)\left(c^L(t-\hat{\tau}_1)\,e^{-j2\pi f_s(t-\hat{\tau}1)}e^{j\left(2\pi\hat{f}_{d,1}t+\hat{\phi}_1\right)}\right)^H dt \tag{5.8a}$$

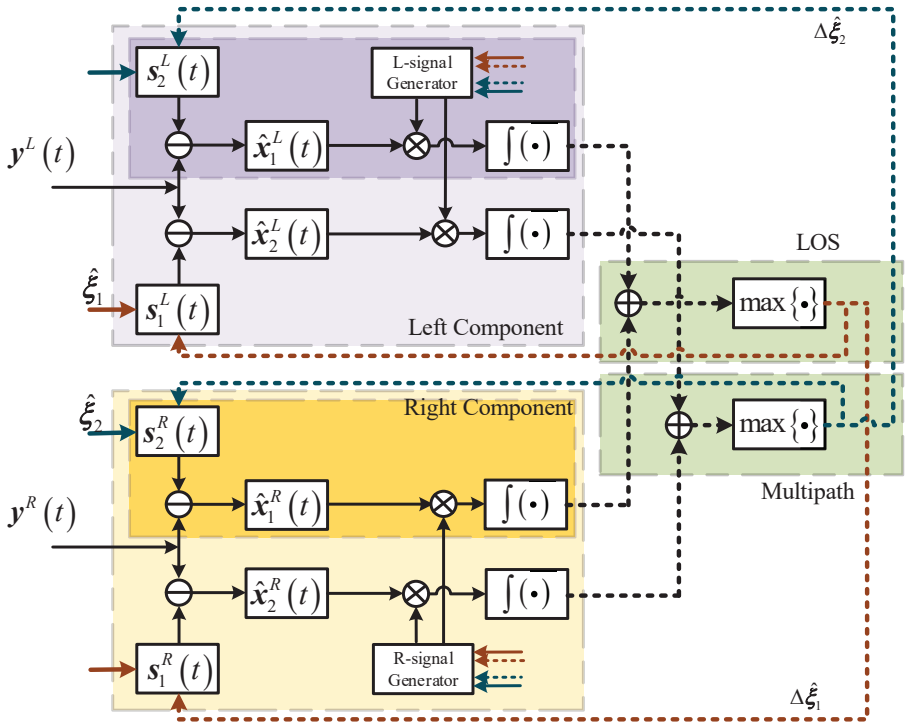


Figure 5.7: The Proposed SAGE-based Discriminator for Meta-signal

$$\hat{R}^L_{\tau,1}(\Delta\tau^L_1)=\frac{1}{T}\int_0^T\left(\boldsymbol{a}^L\left(\hat{\theta}_1\right)\right)^H\hat{\boldsymbol{x}}^L_1(t)\left(c^L\left(t-\hat{\tau}_1+\Delta\tau^L_1\right)e^{-j2\pi f_s\left(t-\left(\hat{\tau}_1+\Delta\tau^L_1\right)\right)}e^{j\left(2\pi\hat{f}_{d,1}t+\hat{\phi}_1\right)}\right)^H dt \tag{5.8b}$$

$$\hat{P}^L_{\phi,1}(\Delta\phi^L_1)=\frac{1}{T}\int_0^T\left(\boldsymbol{a}^L\left(\hat{\theta}_1\right)\right)^H\hat{\boldsymbol{x}}^L_1(t)\left(c^L(t-\hat{\tau}_1)\,e^{-j2\pi f_s(t-\hat{\tau}_1)}e^{j\left(2\pi\hat{f}_{d,1}t+\left(\hat{\phi}_1+\Delta\phi^L_1\right)\right)}\right)^H dt \tag{5.8c}$$

$$\Delta\hat{\alpha}^L_1=\left|\frac{1}{T}\int_0^T\left(\boldsymbol{a}^L\left(\hat{\theta}_1\right)\right)^H\hat{\boldsymbol{x}}^L_1(t)\left(c^L\left(t-\hat{\tau}_0\right)e^{-j2\pi f_s(t-\hat{\tau}_1)}e^{j\left(2\pi\hat{f}_{d,1}t+\hat{\phi}_0\right)}\right)^H dt\right|\Big/M_\theta \tag{5.8d}$$

where the Doppler frequency $\hat{f}_{d,1}$ and carrier phase offsets $\hat{\phi}_1$ for the LOS signal of the meta-signal are acquired by standard PLLs, and $\Delta\hat{\phi}_1$ for the LOS signal of the left side-band component is estimated by the left side-band prompt correlator.

It is worth noting that no significant DFO difference (generally within a few Hertz) was found between the LOS and multipath signals, as verified in several practical measurements [83, 84, 89]. Without loss of generality, we can reasonably assume that the LOS and multipath signals have similar DFOs, and most of the DFOs will be compensated in the acquisition stage [85]. Starting with the fundamental fact that the residual DFOs are very similar for all signals, we cannot profit much from the frequency offsets for multipath mitigation. To reduce the complexity, the signals are mainly resolved from the spatial and temporal ACF correlators. Meanwhile, we set up PLLs to complete the carrier tracking as well. Thanks to these PLLs, the architecture of SAGELL incorporates frequency discrimination of the signals if the frequency separation of signals is larger than the bandwidth of PLLs.

Similarly, the expressions $\left\{\hat{R}^L_{\theta,2}\left(\Delta\theta^L_2\right),\hat{R}^L_{\tau,2}\left(\Delta\tau^L_2\right),\hat{P}^L_{\phi,2}\left(\Delta\phi^L_2\right),\Delta\hat{\alpha}^L_2\right\}$ for the multipath signal of left component, the expressions $\left\{\hat{R}^R_{\theta,1}\left(\Delta\theta^R_1\right),\hat{R}^R_{\tau,1}\left(\Delta\tau^R_1\right),\hat{P}^R_{\phi,1}\left(\Delta\phi^R_1\right),\Delta\hat{\alpha}^R_1\right\}$ for the LOS signal, and the expressions $\left\{\hat{R}^R_{\theta,2}\left(\Delta\theta^R_2\right),\hat{R}^R_{\tau,2}\left(\Delta\tau^R_2\right),\hat{P}^R_{\phi,2}\left(\Delta\phi^R_2\right),\Delta\hat{\alpha}^R_2\right\}$ for the multipath signal of right component of the meta-signal will not be detailed displayed anymore. Moreover, the amplitudes $\Delta\hat{\alpha}^L_k$ and $\Delta\hat{\alpha}^R_k$ for each signal of component are kept to the next iteration.

Meta-signal Processing Unit

To improve accuracy, a coherent combination referring to ACFs of meta-signal (5.1), including the spatial ACFs $\left\{\hat{R}^L_{\theta,k}\left(\Delta\theta^L_k\right),\hat{R}^R_{\theta,k}\left(\Delta\theta^R_k\right)\right\}$, the temporal ACFs $\left\{\hat{R}^L_{\theta,k}\left(\Delta\theta^L_k\right),\hat{R}^R_{\theta,k}\left(\Delta\theta^R_k\right)\right\}$, are conducted to acquire the angles $\Delta\hat{\theta}_k$ and time delays $\Delta\hat{\tau}_k$ estimates of the meta-signal,

$$\Delta\hat{\theta}_k = \arg\max_{\Delta\theta}\left|\gamma\hat{R}^L_{\theta,k}\left(\Delta\theta^L_k\right)+\hat{R}^R_{\theta,k}\left(\Delta\theta^R_k\right)\right| \tag{5.9}$$

$$\Delta\hat{\tau}_k = \arg\max_{\Delta\tau}\left|\gamma\hat{R}^L_{\tau,k}\left(\Delta\tau^L_k\right)+\hat{R}^R_{\tau,k}\left(\Delta\tau^R_k\right)\right| \tag{5.10}$$

with the compensation γ for unequal powers of two components, which is necessary to know the amplitude ratio between two signals [48]. This coherent combination of the LOS signal and the multipath signal of the meta-signal is mentioned in Figure 5.7 as well.

Moreover, the prompt correlators $\left\{\hat{P}^L_{\phi,k}\left(\Delta\phi^L_k\right),\hat{P}^R_{\phi,k}\left(\Delta\phi^R_k\right)\right\}$ for each signal of each component are sent to incoherently estimate the carrier phases of the meta-signals,

$$\Delta\hat{\phi}_k = \frac{1}{2}\left(\text{angle}\left(\hat{P}^L_{\phi,k}\left(\Delta\phi^L_k\right)\right)+\text{angle}\left(\hat{P}^R_{\phi,k}\left(\Delta\phi^R_k\right)\right)\right) \tag{5.11}$$

The meta-signal parameters obtained above, the amplitudes for each signal of each component, together with the prediction results tracked through the last loop, are sent back to the SAGE-based discriminator for initialization. Inside the SAGE-based discriminator, the first two kinds of variables are updated until the convergence criteria get satisfied. Afterwards, they are filtered and predicted through various loops to get more accurate estimates and fed back to initialize the SAGE-based discriminator eventually.

5.4 Simulation Results and Performance Analysis

In this section, we provide two kinds of simulation experiments to evaluate the performance of three methods. Firstly, the maximum error envelopes (MEEs) experiments are arranged to indicate the ultimate time delay bias. Secondly, the simulations of time delay RMSE via C/N_0 in different multipath cases are shown. The typical combination of Beidou B1I and B1C signals is considered for the targeted meta-signal. The subcarrier frequency offset f_s locates at 7.161 MHz.

Three DSB methods are adopted in the simulation experiments: the MEDLL [10], the Double Estimator Technique (DET) based technique [47, 48] and the proposed SAGELL. In the MEDLL for meta-signal, we first iteratively acquire the temporal ACF and the prompt correlator for the LOS signal and the multipath signal of each side-band component according to Equation (5.8b) and (5.8c), then coherently and incoherently combine the time delay estimates and carrier phases according to Equation (5.10) and (5.11), respectively. Finally, the DLLs with Early-Late discriminator and PLLs are utilized to track each signal of the meta-signal. A 4-element ULA with a half-wavelength antenna spacing is assumed. To make a relatively fair comparison, we make beamforming to the LOS direction before conducting the conventional MEDLL and DET, and the detailed ACF distortion before and after beamforming are described in reference [54]. Generally, the multipath distortion after beamforming can be further relieved by the temporal multipath-mitigating methods. Furthermore, we utilize narrowband GPS C/A code signals as our target and apply the simplified SAGELL method to estimate the LOS time delay. To compare the advantages of meta-GNSS signals over single-frequency GNSS signals in mitigating multipath signals, the C/A code signal in GPS is also adopted using the SAGELL tracking loop.

Under the assumption of two signals (one LOS signal and one multipath signal), we suppose four multipath scenarios that are differentiated by the angles and the time delays. For angles, we consider two cases: one is with large angle difference that the angle of LOS signal is from 0° and the multipath signal is from 40°, and the other one is with small angle difference that the angle of LOS signal is from 0° and the multipath signal is from 10°. Likewise, we consider two cases in time delays: One is with large delay difference that the time delay of LOS signal is $0\,T_c$ and the multipath signal is $0.08\,T_c$, and the other one is with small delay difference that the time delay of LOS signal is $0\,T_c$ and the multipath signal is $0.007\,T_c$. The denotation T_c refers to the time duration $T_c = 977.52$ ns of two adjacent chips per C/A code period. The SMR is set to be 6 dB. The pre-detection integration time T is 20 ms. The noise bandwidth parameters of angle, delay, and carrier tracking lock loops are 5 Hz, 5 Hz, and 10 Hz, respectively. All the lock loops' orders are second order. The early-late spacing in the DLL of DET are $0.5\,T_c$ and $0.33\,T_c$ for B1I and B1C signals, respectively. And that of MEDLL is set to be $0.034\,T_c$.

5.4.1 MEEs via Multipath Delay

In this subsection, the MEEs of the LOS signal with large angle difference and small angle difference between the LOS signal and multipath signal are demonstrated.

It is apparent from Figure 5.8 that the MEEs with large angle difference generally behave about twice as large as that with small angle difference. In situations with large angle differences, single-frequency GNSS signal (referring to C/A code) demonstrates excellent resolution. However, in scenarios with small angle differences, mitigating the multipath signal from the LOS signal re-

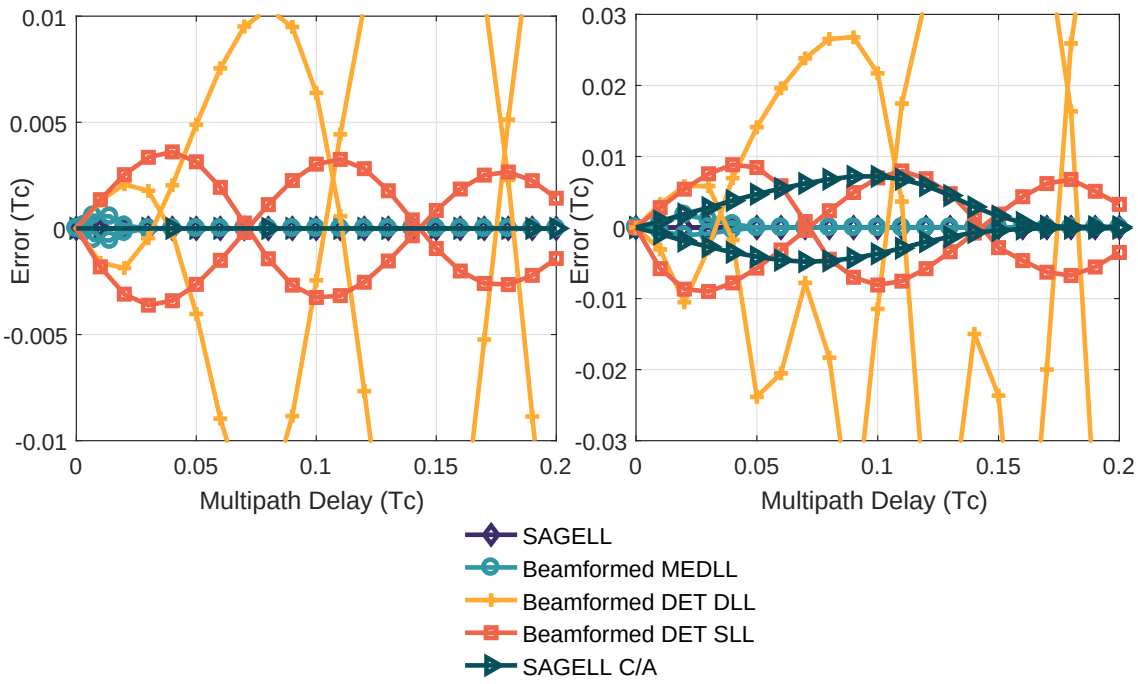


Figure 5.8: MEEs of LOS signal with large angle difference (left panel) or small angle difference (right panel)

quires a multipath delay that is greater than $0.15\,T_c$. Among these three comparisons for meta-signal, the beamformed DET reveals comparatively poor multipath mitigation with a small angle difference and a large one. A possible explanation is that the beamforming cannot thoroughly mitigate the multipath signal. Thus, the residual multipath still causes quite a considerable influence on subcarrier phase tracking of the LOS signal.

The error of beamformed MEDLL, by contrast, maintains a competitive advantage out of the range $[0\,T_c, 0.02\,T_c]$ irrespective of the similarity in spatial domain. However, the curves of the beamformed MEDLL in the range $[0\,T_c, 0.02\,T_c]$ rise and fall drastically, and they peak at nearly $0.007\,T_c$ reaching 0.6 m. By only time domain characteristics, MEDLL cannot eliminate the multipath under the condition of two highly temporally correlated signals. Besides, beamforming contributes to multipath mitigation when the low spatially correlated signals exist, but it offers poor attenuation in highly spatially correlated situations. A direct consequence of combining multiple dimensions is that SAGELL observes and differentiates the multipath from both spatial and temporal domains, so it exhibits reasonably good performance.

5.4.2 RMSEs via C/N_0

Five specific simulated scenarios are set to evaluate and compare the thermal noise performance, and the RMSEs of the LOS signal are exploited in this section. These five scenarios conclude single signal, large angle difference within small delay difference and large delay difference, together with

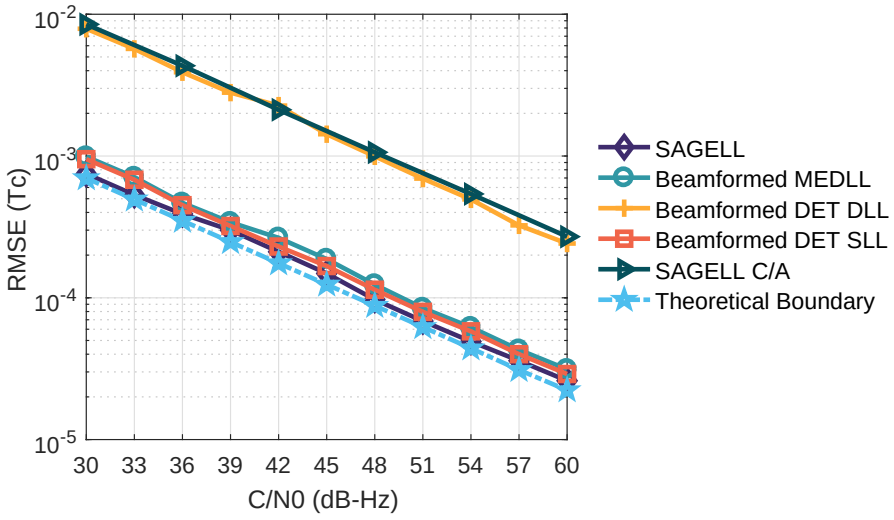


Figure 5.9: Delay RMSEs comparison of single signal

small angle difference within small delay difference and large delay difference. The other settings are the same as those in the previous section.

In Figure 5.9, the comparisons of the LOS time delay RMSEs among three methods in a single signal (i.e., LOS only) scenario and the theoretical boundary of the meta-signal are shown. Since the single is set, the beamforming in this scenario plays a crucial role in the signal gain increase instead of multipath mitigation. The theoretical boundary with a single antenna can be plotted according to [115, 116], and the theoretical boundary with a four-element antenna could be derived easily. The curves show that these methods yielded the best values, especially the SAGELL and the SLL of DET, almost reaching the theoretical boundary. Given that SAGELL adopts an iterative multiple correlators discriminator in multi-dimensions, whereas the DET and MEDLL use prompt or Early-Late discriminators in the temporal domain, the complexity of SAGELL slightly exceeds that of the MEDLL.

Next, the RMSEs of the LOS time delay in four multipath scenarios are presented. The trend of beamformed MEDLL corresponds to the fact that it can differentiate the multipath in large time delay difference in the previous analysis of MEE, which are shown in the left-hand side plots in Figure 5.10 and Figure 5.11. However, this fact is in contrast with the behaviors of the beamformed MEDLL in a small delay difference scenario. The beamformed MEDLL suffers from limitations of only resolving multipath via time delays, especially in the presence of highly spatially and temporally correlated signals, as displayed by the right panel in Figure 5.11.

Unlike other methods carried out in this case, SAGELL is found to perform exceptionally well with high C/N_0, benefiting from spatial, and temporal domains. Despite the appearance of the meta-signal ambiguity in the low C/N_0 range [42], the SAGELL has basically reached a centimeter-level ranging performance at 39 dB-Hz.

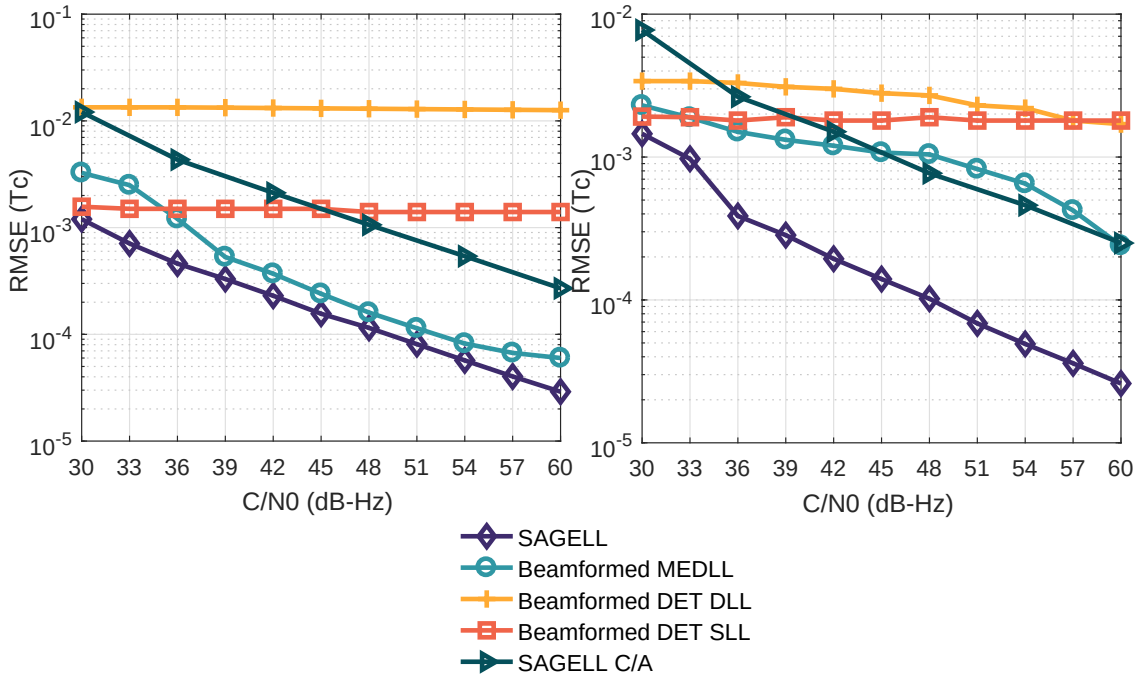


Figure 5.10: Delay RMSEs of LOS signal comparison when LOS and multipath signals are separate from $0°$ and $40°$, respectively, with large delay difference $0.08\,T_c$ (left panel) and small delay difference $0.007\,T_c$ (right panel)

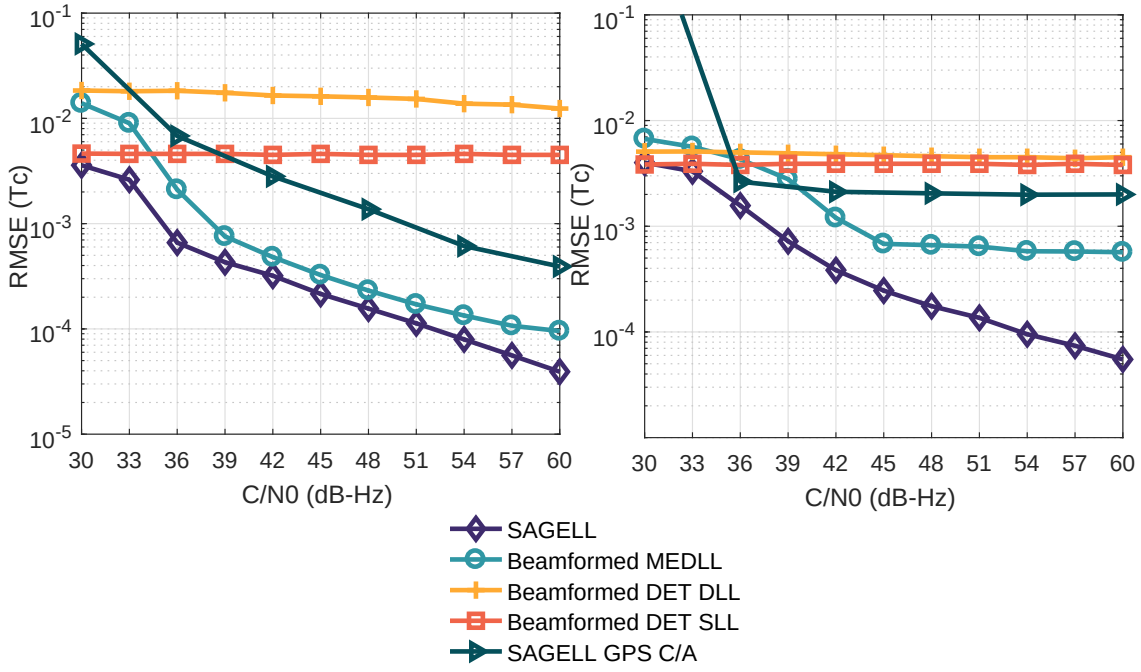


Figure 5.11: Delay RMSEs of LOS signal comparison when LOS and multipath are similar from $0°$ and $10°$, respectively, with large delay difference $0.08\,T_c$ (left panel) and small delay difference $0.007\,T_c$ (right panel)

5.5 Conclusions

In this chapter, a series of researches are carried out for the purpose of providing decimeter- or even centimeter-level ranging accuracy in multipath environments. Meta-GNSS signals can be highly precise with the bandwidth of tens of megahertz or even hundreds of megahertz. Meanwhile, multi-antenna technology can improve signal gain and provide spatial freedom for multipath mitigation. The combination of the multi-antenna technology and meta-signals can easily reach the decimeter-level ranging accuracy and effectively distinguish multipath, especially in highly correlated signals.

This chapter addresses the challenges of achieving accurate ranging in multipath environments by studying the characteristics of meta-signals and analyzing their ACFs. The study highlights that the ACFs of meta-signals exhibit distortions in the presence of multipath, rendering temporal domain analysis inadequate for distinguishing highly correlated signals. To overcome this limitation, the chapter proposes the SAGELL design, which leverages the robustness of SAGE against multipath signals and the excellent temporal resolution of meta-signals. Using the basic principles of SAGE, the SAGE-based discriminator combats multipath signals from both spatial and temporal domains to provide coherently precise estimates of the meta-signal. To maintain high accuracy in multipath mitigation, various loops, including ALLs, DLLs, and PLLs, are employed to track and predict the signals for SAGELL. The study shows that combining multi-dimensional processing with wide bandwidth provides optimal time delay estimation in severe multipath propagation. Simulation results demonstrate that the proposed SAGELL design reaches the theoretical bound in an environment with no multipath signals and performs remarkably well in mitigating multipath, particularly when dealing with small time delay differences and angle differences between the LOS signal and the multipath signal.

Multi-antenna GNSS Signal Collection Platform and Verification

6.1 Introduction

In this chapter, we build a multi-antenna GNSS signal collection platform to collect GNSS signals and validate the feasibility of the joint spatial and temporal multipath mitigation algorithms proposed in Section 3. Additionally, the data collected from this platform is publicly shared for experimental purposes, addressing the gap in existing public data sources that only provide single-antenna measured data. This valuable datasets can support further research and development in the field of GNSS signal processing.

This chapter discusses the requirements for indicators and the real measurement environment of the multi-antenna GNSS signal collection platform. Subsequently, we also present the calibration method. Building upon these foundations, we provide and demonstrate functional verification results for the primary methods presented in this thesis. Finally, we conclude this chapter.

6.2 Introduction to Multi-antenna GNSS Signal Collection Platform

The multi-antenna GNSS signal collection platform mainly comprises two parts, including an outside radio frequency front-end (RFFE) part and an inside data collection part. The specific module is illustrated in Figure 6.1.

The GNSS signal is first received by an outdoor multi-antenna consisting of 4-element ULA, as shown in Figure 6.2. The spacing between each element is $10\,\text{cm}$, and the gain of each element is approximately $5\,\text{dBi}$. The antenna includes a low noise amplifier that provides a gain of 28-30 dB with a noise figure below $2\,\text{dB}$. The signal is then connected to the power division network and correcting network, constructed by a Mini-Circuits ZN2PD2-63-S+ broadband power splitter. This network performs amplitude and phase calibration between channels for the single-frequency

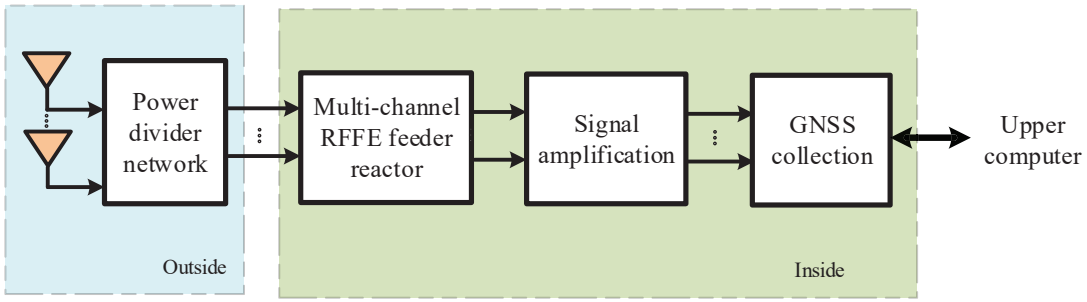


Figure 6.1: Structure of multi-antenna GNSS signal collection platform

signal sent prior.

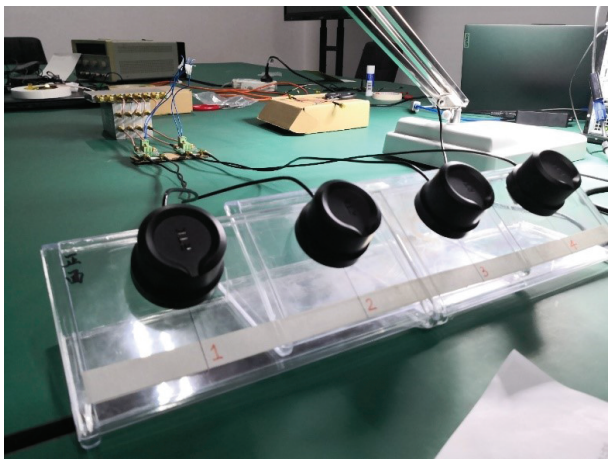


Figure 6.2: 4-element ULA

After passing through the power division network for calibration, the GNSS signal is transmitted through RF coaxial cables to the indoor section. The indoor section consists of three parts. Firstly, the multi-channel RFFE feeder reactor powers the low noise amplifier in the antenna. It provides power to the RF coaxial cable connected to the antenna using an onboard high cut-off filter and uses a series capacitor on the RF channels for direct current (DC) potential isolation between stages, as shown in Figure 6.3. Secondly, considering the long-distance transmission loss of GNSS signals, the signal power at the receiver is usually below the noise level. Its spread spectrum modulation can recover gain ranging from 30 dB by despreading. Therefore, we only consider the noise level for the gain design of the receiving link. An indoor signal amplifier module with a gain of approximately 50 dB was designed based on the INA-02186 wideband high-gain module on the ADRV9009 multi-channel agile transceiver. The module is encased in a shielded enclosure to prevent channel self-excitation, coupling, and cross-talk, as shown in Figure 6.4. Finally, the amplified signal undergoes down-conversion, sampling, and uploading in the multi-antenna GNSS collection platform. The GNSS collection unit is implemented on the ADRV9009 multi-channel agile transceiver processing board, which supports up to 8 channels, as shown in Figure 6.5. Ac-

cording to the requirements of this chapter, the local oscillator signal of the core processing board is set to 1575 MHz to receive the C/A code of the GPS in the L1 frequency band (1575.42 MHz). The 420 KHz frequency residual is compensated for in the down-conversion. The sampling rate of the entire core board is set to 10.24 MSPS, with 4-bit quantization data for both the I and Q channels. These data are uploaded to the host computer via a user datagram protocol (UDP) network interface.

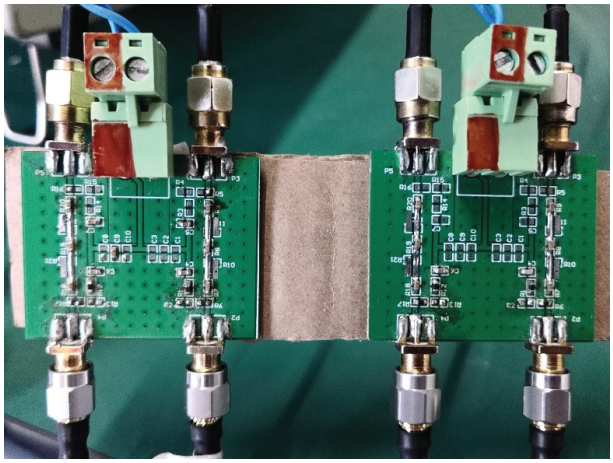


Figure 6.3: Indoor multi-channel RFFE feeder reactor



Figure 6.4: Indoor instrument amplifier

This platform can fulfill the design requirements. Specific requirements are as follows: The platform should have a 4-element ULA, compatible with typical GNSS frequency bands to enable the comprehensive collection; Each channel should provide a gain of over 40 dB to address the attenuation problem of the satellite-ground link. Considering the amplitude and phase inconsistencies between channels, the calibration unit should be designed to maintain consistent amplitude and phase among all channels; Since the bandwidth of GNSS signals varies, the analog-to-digital converter (ADC) of this platform should meet the typical bandwidth requirements of GNSS signals,



Figure 6.5: Indoor multi-channel data collection

achieving a maximum sampling rate of 30 MHz for single-frequency signals; Finally, to ensure secure and efficient transmission, the platform should communicate with the host computer via a UDP interface using gigabit Ethernet.

6.3 Introduction to GNSS Signal Collecting Environment

GNSS signals experience significant path loss when transmitting from high altitude to the ground. Signals with higher elevation angles are more easily received by antennas. Considering the need for isolation between indoor amplifier conditioning and antenna, we have placed the multi-antenna on the roof of Hongli building in Xi'an Jiaotong University. Each element of the antenna is oriented towards satellites with high elevation angles, as demonstrated in Figure 6.6. The remaining components of the collection platform are located indoors and linked to the antenna through the 10 m RF coaxial cables for signal transmission and antenna power supply.

The antenna is deployed along the direction of the stairs, with the array orientation roughly aligned with the stairs, as displayed in Figure 6.7. It should be noted that the stairs of Hongli building in Xi'an Jiaotong University are located approximately 30° west of true north.

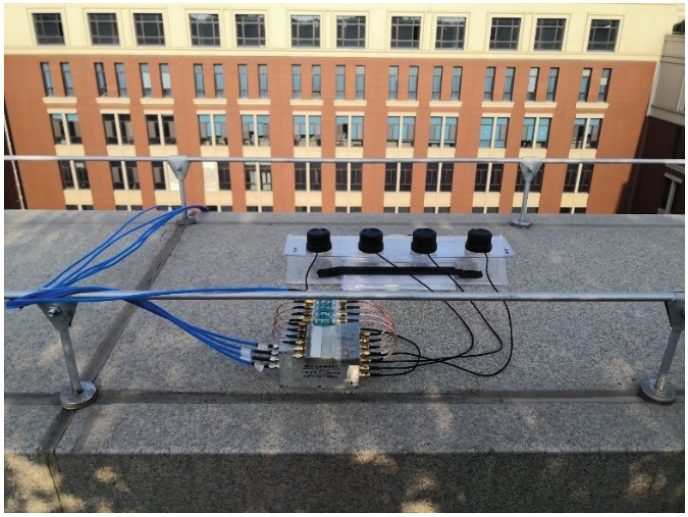


Figure 6.6: Placement of multi-antenna GNSS collection platform



Figure 6.7: Related azimuth information of multi-antenna GNSS collection platform

6.4 Channel Calibration and Attitude Estimation

Although the multi-antenna GNSS collection platform has completed collecting, sampling, and uploading GNSS signals, the data received by each antenna may need to be consistent and urgently need calibration. In addition, the platform can recognize the DOAs of GNSS signals. Therefore, an estimation of attitude is required to verify the functionality of the methods proposed. This section presents the amplitude and phase calibration method for the channels of the platform, as well as the relevant thinking for attitude estimation.

6.4.1 Amplitude and Phase Calibration

This subsection describes the selection of the single-frequency calibration method for various channels of the multi-antenna GNSS data collection platform. Specifically, an offline calibration method is adopted. To avoid the impact of local oscillator leakage, a single-tone signal $s(t)$ with the frequency of 1575 MHz and power of -50 dBm was emitted indoors. After calculation and measurement, the signal was amplified to approximately -17 dBm before reaching the ADRV9009, resulting in a power increase of around 33 dB, much higher than the noise of the antennas. Based on this fact, we can conclude that the received signal primarily consists of calibrated signals, which can be utilized for channel calibration.

Through the sampling and transmission of the indoor data collection unit, the single-tone signal is received as $s_R(t)$ in the upper computer. By utilizing the known signal and the conjugate result of the received signal within time T, the complex amplitude estimation of each receiving channel can be obtained

$$\hat{\boldsymbol{w}} = \frac{1}{T}\int_0^T \boldsymbol{s}_R(t)\, s^*(t)\, dt \tag{6.1}$$

where the estimated complex amplitude for each channel is $\hat{\boldsymbol{w}} = [\hat{w}_1, \ldots, \hat{w}_{M_\theta}]^T$.

Define the m_θ th element of $\hat{\boldsymbol{w}}$ as $\hat{w}_{m_\theta}$, where $m_\theta = 1, \ldots, M_\theta$. Take the first receiving channel as a reference, the correction coefficient of the m_θ th receiving channel is

$$\bar{w}_{m_\theta} \doteq \frac{\hat{w}_1}{\hat{w}_{m_\theta}} \tag{6.2}$$

6.4.2 Attitude Estimation for Array

The GNSS signal collection platform collected 10 s GNSS signal. The amplitude and phase of each channel were corrected using the correction coefficients provided in Equation (6.2), resulting in the corrected data $\bar{\boldsymbol{s}}_R(t)$. Following the collecting stage, the local waveform was conjugated and correlated with the corrected waveform to estimate the spatial steering vector of the multi-antenna.

$$\hat{\boldsymbol{a}}_p = \frac{\int_0^T \bar{\boldsymbol{s}}_R(t)\, c^*(t)\, dt}{\int_0^T \bar{s}_{R1}(t)\, c^*(t)\, dt} \tag{6.3}$$

where $\bar{s}_{R1}(t)$ denotes the calibrated data from the first receiving channel. Since we use a ULA structure, $\boldsymbol{a}$ in (2.8) behaves the Vandermonde structure.

The website `www.gnssplanningonline.com` provides satellite information for various systems, including azimuth information between satellites relative to a ground observation point. As shown in Figure 6.8, the data collected by our platform was around 10:15 pm on October 28th, 2021. During this period, GPS signals above Xi'an could be acquired from satellites with PRN numbers 04, 07, 08, 09, 16, 21, and 27, and the corresponding elevation angles of these satellites are shown

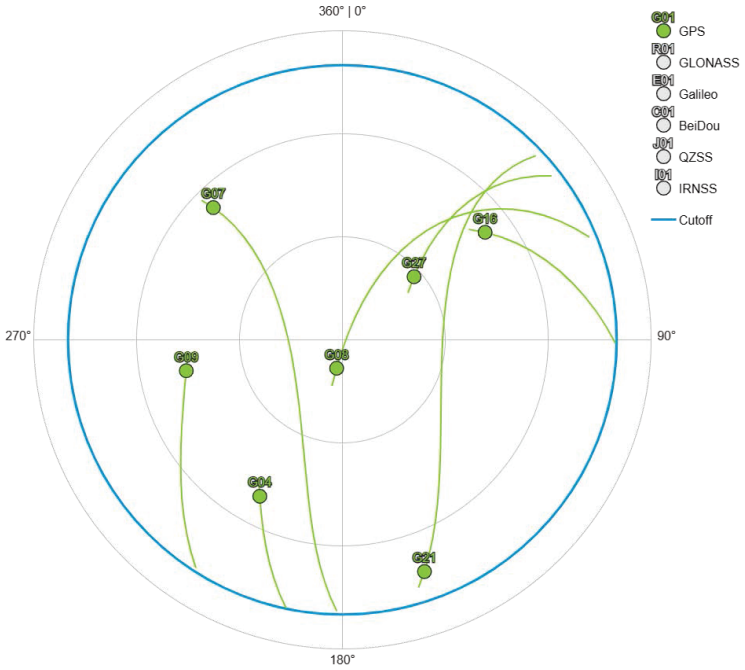


Figure 6.8: The azimuth information of GNSS provided by Trimble

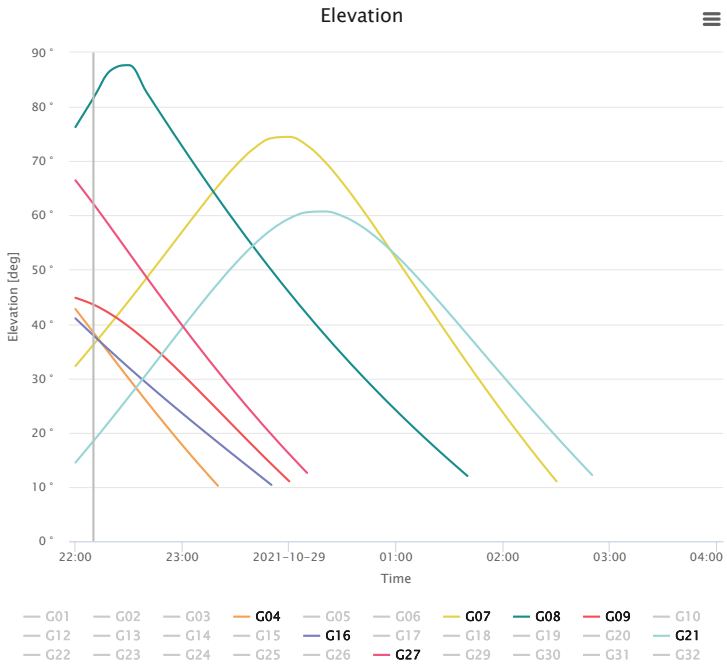


Figure 6.9: The elevation information of GNSS provided by Trimble

in Figure 6.9. The elevation angle in Figure 6.9 represents the satellite's elevation angle, while the angle relative to the center point in Figure 6.8 represents the satellite's azimuth angle. Based on these information, we can obtain the azimuth and elevation information of each GPS satellite relative to the geocentric coordinate system. In this case, the y-axis represents the north direction.

Table 6.1: The direction information of GPS relative to the local spherical coordinate system

PRN	22:10		22:20		22:15	
	Azimuth	**Elevation**	**Azimuth**	**Elevation**	**Azimuth**	**Elevation**
04	-117.9	38.63	-114.5	34.32	-116.2	36.475
07	134	36.72	133.8	40.28	133.9	38.5
08	-100.3	81.67	-90	86.82	-95.15	84.245
09	-169	43.83	-167.6	42.02	-168.3	42.925
16	36.7	37.72	33.5	34.69	35.1	36.205
21	-70.5	18.39	-68	22.43	-69.25	20.41
27	41	61.96	45	52.92	43	57.44

The azimuth and elevation angles of each satellite at different time intervals are presented in Table 6.1.

The antenna of platform was placed roughly 30° west of north and horizontally on the rooftop. Thus, the elevation angle of the array steering vector can be approximated as zero. Consequently, the steering vector of the antenna can be modeled using the following equations:

$$\boldsymbol{a}_p = \left[1, e^{-j\frac{2\pi d}{\lambda_{ant}}\boldsymbol{h}_p^T\boldsymbol{h}_l}, \ldots, e^{-j\frac{2\pi d}{\lambda_{ant}}(M_\theta-1)\boldsymbol{h}_p^T\boldsymbol{h}_l}\right]^T \tag{6.4}$$

The DOA of the signal, which is the angle between the signal steering vector $\boldsymbol{h}_g$ and the array steering vector $\boldsymbol{h}_l$, is defined as

$$\boldsymbol{h}_p = [\cos\theta_p \cos\varphi_p, \sin\theta_p \cos\varphi_p, \sin\varphi_p]^T \tag{6.5}$$

$$\boldsymbol{h}_l = [\cos\theta_0, \sin\theta_0, 0]^T \tag{6.6}$$

where θ_p is the azimuth angle of the steering vector of the p th satellite, φ_p is the pitch angle relative to the ground, and θ_0 is the azimuth angle of the array steering vector.

To determine the direction of the array steering vector $\hat{\boldsymbol{h}}_l$, we can perform inter-satellite differencing between the steering vectors, yielding $\hat{\boldsymbol{a}}_p \odot \hat{\boldsymbol{a}}_m^*$ (where subscripts p and m indicate the two satellites used for inter-satellite differencing). The differential signal obtained from the difference between signals received by the first $M_\theta - 1$ and last $M_\theta - 1$ elements is then used to solve the phase $(\boldsymbol{h}_p - \boldsymbol{h}_m)^T\hat{\boldsymbol{h}}_l$, which can be expressed as

$$(\boldsymbol{h}_p - \boldsymbol{h}_m)^T\hat{\boldsymbol{h}}_l = \begin{pmatrix} \cos\theta_p\cos\varphi_p - \cos\theta_m\cos\varphi_m \\ \sin\theta_p\cos\varphi_p - \sin\theta_m\cos\varphi_m \\ \sin\theta_p - \sin\varphi_m \end{pmatrix}^T \begin{pmatrix} \cos\theta_0 \\ \sin\theta_0 \\ 0 \end{pmatrix} \tag{6.7}$$

The steering vector estimation of array can be obtained by using more than or equal to four different satellites

$$\hat{\boldsymbol{h}}_l = \begin{pmatrix} \boldsymbol{h}_2 - \boldsymbol{h}_1 & \boldsymbol{h}_3 - \boldsymbol{h}_1 & \boldsymbol{h}_4 - \boldsymbol{h}_1 \end{pmatrix}^{-1} \begin{pmatrix} (\boldsymbol{h}_2 - \boldsymbol{h}_1)^T \hat{\boldsymbol{h}}_l \\ (\boldsymbol{h}_3 - \boldsymbol{h}_1)^T \hat{\boldsymbol{h}}_l \\ (\boldsymbol{h}_4 - \boldsymbol{h}_1)^T \hat{\boldsymbol{h}}_l \end{pmatrix} \tag{6.8}$$

Based on the information provided in Table 6.1, the azimuth angle θ_0 can be estimated as $120.3°$, which is consistent with the approximate direction of the steering vector. This result provides a reliable theoretical basis for comparing the angle estimation results obtained in subsequent analyses.

6.5 Verifications

This section validates the functional performance of two GNSS joint spatial and temporal multipath mitigation methods in Chapter 3 using data collected by the platform. Both methods were integrated into the classical loop of a traditional GNSS receiver to ensure good tracking capability. The signal for validation is the L1 frequency C/A code of GPS. The sampling rate is 10.24 MHz, and the data was collected for approximately 10 s above Xi'an on the evening of October 28 th, 2021. A 4-element ULA is utilized with an element spacing of 10 cm.

6.5.1 Short Period Estimation Verification

In the validation, we will verify the performance of JADE-SFS-DOAMatrix and JAODE-MSBL discussed in Section 3. In this scenario, we consider these two algorithms standalone discriminators and estimate the time delay and angle based on the acquisition information. The duration of short period is set to 20 ms.

Based on the GPS information during the collecting period, the measurements of satellites with PRNs 04, 07, 08, 09, 16, 21, and 27 were processed using joint spatial and temporal multipath mitigation algorithms. The real DOAs of each satellite were then computed using Equation (6.8) and are presented in Table 6.2.

Figure 6.10 illustrates the spatial and temporal spectrum of GPS signals for PRN 04 and 16 while comparing two discriminators, namely the joint spatial and temporal ML-based algorithm and the JAODE-MSBL algorithm. The figure suggests that the JAODE-MSBL algorithm has a sharper peak than the ML-based algorithm, while it may suffer from the issue of reduced accuracy or long computed time due to over-sparse or over-dense grid division. In such cases, conducting a small-range ML search around the estimated parameters can mitigate the off-grid effect.

Table 6.2: Real DOA calculation and angle estimation of two algorithms in Chapter 3

PRN	Real DOA	Estimated DOA JAODE-MSBL	Estimated DOA JADE-SFS-DOAMatrix	Note
04	116.2731°	115.81°	115.4499°	
07	40.4489°	38.46°	37.7815°	Blocked by tower
08	94.6796°	93.6°	93.4976°	
09	76.4221°	78.14°	78.7086°	Blocked by trees
16	86.209°	86.82°	87.0345°	
21	157.512°	146.1°	142.0029°	Blocked by tower
27	83.2579°	83.36°	83.4546°	

6.5.2 Tracking Performance Verification

The two joint spatial and temporal multipath mitigation algorithms were treated as discriminators in the tracking loop and validated during a short period. The estimated results of these discriminators under short-term static channel conditions were provided. To ensure the tracking performance of the GNSS receiver and address the Doppler phase drifting, we embedded the discriminators into a typical tracking loop, forming an improved joint spatial and temporal GNSS tracking loop. Figure 6.11 shows a schematic diagram.

The upper part constitutes a new joint spatial and temporal DLL, while the lower part uses the classical PLL. This way, the joint spatial and temporal discriminator can be used mainly for joint spatial and temporal multipath mitigation and parameter estimation. In contrast, PLL and DLL are primarily used for signal filtering and tracking.

We name the two proposed loops the JADE-SFS-DOAmatrix tracking loop and JAODE-MSBL tracking loop, respectively. The accuracy of code phase tracking is compared with that of a typical single-antenna tracking loop. The relevant parameters are listed as follows: GPS signals corresponding to PRN 04 and 16 are used as the measured data. A typical single-antenna tracking loop uses an early-late-prompt discriminator with a spacing of 0.5 T_c, DLL bandwidth of 10 Hz, PLL bandwidth of 15 Hz, and 10 ms data for each discrimination. It should be noted that the true code phase cannot be obtained here, making it impossible to calculate the estimation error of the code phase precisely. Therefore, linear regression is performed using the tracking loop to obtain the reference value, and the tracking error is calculated based on the fitted value.

Figure 6.12 compares the code phase tracking error of the three tracking loops using 2 s of stable tracking data as a reference. The analysis shows that the two proposed spatial and temporal tracking

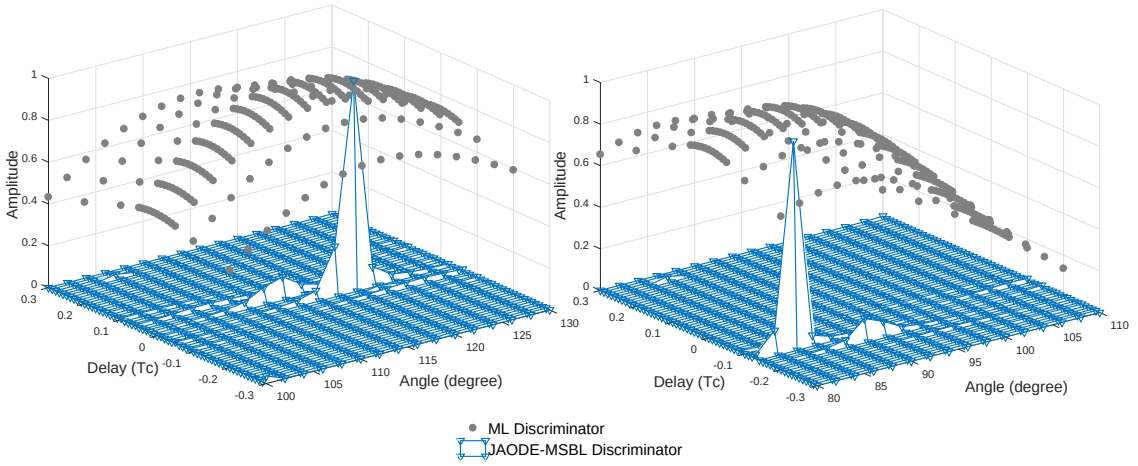


Figure 6.10: Spatial and temporal spectrum of the discriminator for PRN 04 (left panel) and PRN 16 (right panel)

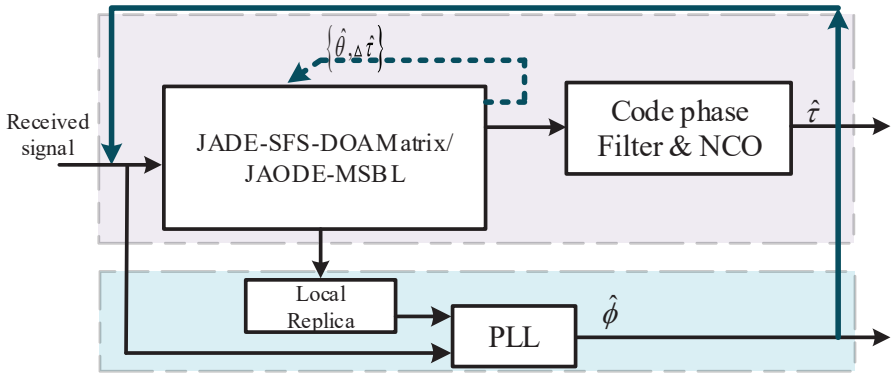


Figure 6.11: Schematic diagram of the improved joint spatial and temporal processing GNSS tracking loop

loops outperform the typical single-antenna tracking loop regarding code phase error. This is partly due to the spatial gain provided by multi-antenna and the advantage of having more correlation points in the discriminator. However, since the acquired data only contains clear LOS signal and lacks obvious multipath signals, the mitigation capability of the multipath cannot be evaluated accurately. As a result, the difference between the JADE-SFS-DOAMatrix tracking loop and the JAODE-MSBL tracking loop is not very apparent.

Table 6.3 presents the RMSEs of the code phase for the three tracking loops. The table shows that the performance of the three tracking loops is consistent with the theoretical analysis, thereby verifying the functionality and effectiveness of the proposed methods. It is worth noting that the performance of JADE-SFS-DOAMatrix tracking loop and JAODE-MSBL tracking loop are almost identical. This is because only one LOS signal is present, and no multipath interference exists in this scenario.

Due to the limitations of the platform and time constraints, we are currently unable to use this

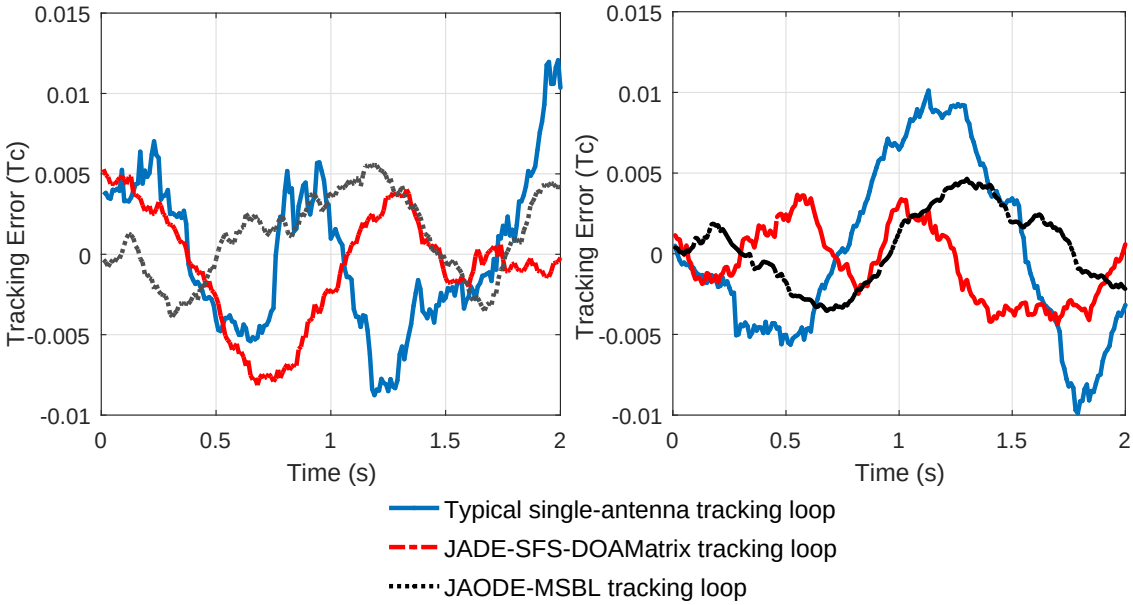


Figure 6.12: Tracking error of the proposed tracking loops of PRN 04 (left panel) and PRN 16 (right panel)

Table 6.3: RMSEs of code phase for three tracking loops

PRN	Single-antenna	JADE-SFS-DOAMatrix	JAODE-MSBL
04	$0.0044\,T_c$	$0.0028\,T_c$	$0.0026\,T_c$
16	$0.0035\,T_c$	$0.0023\,T_c$	$0.002\,T_c$

platform to create a multipath environment and thus verify the performance. Additionally, the feasibility and performance of the joint space, polarization and time method in Chapter 4 and the joint space and frequency method in Chapter 5 cannot be validated at this time. In future research, we will make efforts to improve the platform and its integration as soon as possible in order to complete the functionality and performance verification of the proposed methods. The relevant results will be published in GNSS-related conferences or journals.

6.6 Conclusions

This chapter introduces a GNSS data collection platform with multiple antennas, utilizing existing equipment. It explores the calibration of antenna phase errors and estimation of array attitude. Specifically, the platform receives GPS L1 frequency C/A signals through a 4-element ULA, aiming to validate the functionality and effectiveness of the JADE-SFS-DOAMatrix and JAODE-MSBL algorithms proposed in Chapter 3. To assess these algorithms, a comprehensive analysis is

conducted: Firstly, the joint spatial and temporal spectrum is carefully examined as a discriminator in short periods; Next, the tracking performance of the integrated GNSS tracking loop with the two algorithms is compared to the error performance of the spatial and temporal cascaded tracking loop; Finally, this comparison evaluates the practical implementation and effectiveness of the proposed algorithms.

Summary and Topics for Future Research

7.1 Summary

This thesis focuses on the study of multi-dimensional GNSS receivers in positioning services, aiming to solve the multipath mitigation problem in urban environments. By analyzing the characteristics of GNSS channels and typical GNSS signals, the thesis proposes a joint multi-dimensional processing structure that includes spatial, temporal, polarization, and frequency domains to identify and mitigate multipath signals. Some of the proposed structures and corresponding algorithms are verified through practical observed data using a multi-antenna GNSS data collection platform.

The content of this thesis can be summarized into several categories based on different multipath processing objectives: Considering general multipath environment and receiver complexity, the thesis first proposes a joint spatial and frequential smoothing subspace-based algorithm; Further exploring the sparsity of GNSS multipath signals in space and time domains, the thesis presents a series of sparse off-grid joint spatial and temporal MSBL-based algorithms; To meet the demand for multipath mitigation of high correlation signals in space and time, the thesis proposes a sparse off-grid joint spatial, polarization, and temporal MSBL algorithm; For high-precision GNSS applications, the thesis breaks through the limitation of GNSS signal's time resolution and combines the wideband characteristic of meta-GNSS signals with their spatial domain to design a meta-signal multipath-mitigating tracking loop based on SAGE; Finally, the proposed joint angle and time delay estimation algorithms are validated using GNSS signals collected from a multi-antenna GNSS data collection platform. Specifically, the main contents of this thesis can be summarized as follows:

1. At the system model level of GNSS joint multi-dimensional receivers, this thesis departs from the traditional cascaded space-time processing in GNSS receivers. Instead, it fully utilizes the spatial, temporal, polarization, and frequential dimensions of GNSS multipath signals and proposes a generalized joint multi-dimensional GNSS multipath-mitigating receiver and reception model. Additionally, the thesis explores the sparsity in spatial and temporal domains to-

gether with the characteristics in polarization domain, establishing corresponding joint multi-dimensional sparse models for applying sparse representation algorithms. This architecture effectively combines the characteristics of GNSS multipath signals in various dimensions to enhance the capability of multipath identification and mitigation.

2. Based on the temporal and spatial characteristics of GNSS signals, this thesis explores the advantages of a joint spatial and temporal architecture over the traditional spatial-temporal cascaded one. It proposes two categories of joint spatial and temporal processing to cater to different GNSS receiver requirements: subspace-based and off-grid MSBL-based methods. In order to address parameter estimation in general multipath environments where spatial and temporal correlation behaves low, a subspace-based joint spatial and temporal multipath mitigation algorithm is introduced. This algorithm leverages spatial smoothing and offers the advantage of low complexity, making it suitable for general multipath scenarios. Moreover, in high spatial correlation environments, the proposed algorithm takes advantage of the rotation-invariant property of GNSS multipath signals in the frequency domain to tackle the issue of rank-deficient covariance matrices. It presents a subspace-based algorithm performing joint angle and time delay estimation with spatial and frequency smoothing. To handle scenarios with high spatial or temporal correlation, the thesis explores joint spatial and temporal sparsity of GNSS multipath signals. It introduces an off-grid MSBL-based approach that capitalizes on the ability of MSBL to select sparser global points from extremal points. This algorithm applies both on-grid and off-grid estimation techniques for angle and delay estimation, depending on the specific requirements of the GNSS application. This reduces the complexity resulting from the joint spatial and temporal MSBL and enhances the resolution of off-grid estimation parameters. The proposed algorithms demonstrate improved multipath mitigation performance in scenarios with low carrier-to-noise ratios and few snapshots. They also achieve accurate ranging in scenarios with spatial and temporal correlations in GNSS signals.

3. GNSS tracking performance can be hampered in a severe multipath environment, leading to meter-level pseudo-range errors. This thesis proposes a method for parameter estimation (angle, polarization, and time delay) in the presence of high spatial and temporal correlation between the LOS and multipath signals. The method uses MSBL and multi-dimensional processing to enhance multipath mitigation. A jointly spatial, polarization, and temporal GNSS signal model is established to exploit sparsity in the spatial and temporal domains and characteristics in the polarized domain. An MSBL-based joint solution of angle, polarization, and time delay estimator is derived for each multipath signal. An off-grid estimator for angles and time delays is also extended to reduce complexity and improve resolution. Simulation results demonstrate that the proposed method is promising with strong robustness and effectiveness in combating multipath. It performs close to the CRLB and outperforms other methods in highly spatially or

temporally correlated signals and multiple multipath signal scenarios.

4. Recent findings indicate that the integration of wide bandwidth signals and multi-antenna technology is crucial for improving GNSS multipath mitigation. This has led to the emergence of meta-GNSS signals and multi-dimensional processing. To estimate the time delay of the LOS signal in a multipath environment, we propose a locked loop design called SAGELL, which leverages the high resolution of meta-signals and incorporates spatial and temporal domain characteristics. The SAGELL design consists of two main components: the SAGE-based discriminator and combinational loops. By utilizing multi-dimensional processing and the bandwidth of meta-signals, the SAGE-based discriminator first estimates the LOS signal and multipath signals in single side-band components, achieving coherent global estimates of the dual side-band components. To accurately track each signal of the meta-signal, we employ angle, code phase, and carrier phase-locked loops in the SAGELL, which filter and predict the estimates. The proposed GNSS meta-signal multipath-mitigating loop design enables high-precision mitigation and tracking in multipath scenarios, even when dealing with highly correlated signals.

5. We constructed a GNSS data collection platform with a 4-antenna array. Two multipath mitigation algorithms, subspace-based and MSBL-based joint spatial-temporal approaches, were integrated into traditional GNSS loops. Validation using the acquired data showed that both methods achieved superior time delay estimation accuracy compared to traditional GNSS loops, confirming their effectiveness. Additionally, the collected data demonstrated the feasibility of online uploading and sharing multi-antenna GNSS sampling data for scientific research purposes.

7.2 Topics for Future Research

This thesis addresses the growing demand for effective multipath mitigation techniques in complex multipath environments, with a specific focus on achieving high-precision positioning. To tackle this challenge, the multi-dimensional processing structure is proposed for multi-antenna GNSS receivers. The structure incorporates multiple dimensions and signal features, including joint space and time, joint space, time, and polarization, and joint space, time, and frequency. Various algorithms, such as subspace, MSBL, and SAGE, are employed to mitigate multipath. The results demonstrate significant improvements in multipath mitigation and estimation accuracy. Nevertheless, there are still challenges to address, and future research can explore mitigating the impact of multipath signals, enhancing robustness, and integrating with other estimation algorithms.

1. Research on off-grid effects in sparse representation. Current off-grid estimation methods, relying on first-order Taylor expansion, have limitations in achieving high precision. As the carrier-to-noise ratio increases, off-grid effects become more pronounced, impacting accurate

estimation. Two approaches can be pursued to address this issue. The first approach involves developing a dynamic off-grid estimation model that adjusts the grid in time and space during each iteration. However, challenges arise in establishing a dynamic grid model that reduces bias from fixed grids and minimizes off-grid effects caused by the Taylor expansion. The second approach explores gridless reconstruction that eliminates off-grid effects by avoiding grid selection. However, this approach faces challenges in applying gridless methods in extreme multipath environments where the covariance matrix's Toeplitz property may not hold. Practical techniques for dynamic off-grid estimation and gridless reconstruction need further investigation to achieve accurate estimation, even in complex multipath environments.

2. Enhancing high-precision and high-dynamic positioning through the bandwidth and sparse properties of meta-GNSS signals. Achieving high-precision and high-dynamic positioning using meta-GNSS signals presents a significant challenge due to the difficulty of establishing signal models in high-dynamic scenarios. This can limit our ability to accurately estimate over long-term data accumulation periods or track signals effectively. To address this challenge, one potential solution is to utilize sparse representation, which can operate effectively with few snapshots. By combining meta-GNSS signals with sparse representation, it may be possible to achieve high-precision positioning even in high-dynamic scenarios. Specifically, sparse representation can exploit the sparsity and structure of meta-signals to enable accurate and efficient estimation. Nevertheless, further research is needed to explore effective ways to combine meta-GNSS signals and sparse representation methods in high-dynamic scenarios. It is necessary to develop methods that provide quick and effective high-precision estimation while resisting the Doppler effects caused by high dynamics. Addressing these challenges could pave the way for achieving simultaneous high-precision and high-dynamic positioning using meta-signals and sparse representation.

3. Receiver-based spoofing detection and mitigation. Intelligently resisting receiver-based spoofing is a challenging problem in GNSS anti-spoofing studies, particularly in military applications. Receiver-based spoofing resembles true GNSS signals, with identical spreading codes and navigation messages differing only in time delay and slightly stronger signal power, similar to multipath signals. Establishing an analysis and identification method for different features of receiver-based spoofing using multi-antenna GNSS receivers is a promising area for future research. However, this thesis mainly focuses on multi-dimensional mitigation, a promising approach for achieving accurate GNSS positioning in challenging environments. Extending this approach to receiver-based spoofing detection and mitigation could be a breakthrough in solving the current challenges posed by receiver-based spoofing. By analyzing the various features of spoofing from multiple dimensions, it may be possible to establish a more comprehensive approach for detecting and suppressing this type of interference.

4. GNSS channel modeling and algorithm extension based on multiple GNSS data sets. To accurately study multipath-mitigating algorithms for GNSS signals, measuring and modeling their feature distributions in various real-world scenarios using multi-antenna and multi-frequency GNSS collection platform is necessary. This is particularly important given the limited understanding of statistical channel distribution corresponding to various parameters, especially for GNSS signals in complex electromagnetic environments. Thus, this thesis proposes to use multiple real-world data sets to inform GNSS channel modeling and algorithm extension, with a focus on modeling and setting spatial and temporal parameters for GNSS signals in multipath environments.

References

[1] P. Misra, P. Enge, Global Positioning System: Signals, Measurements, and Performance, 2nd Edition, Ganga-Jamuna Press, Lincoln, MA, 2004.

[2] R. D. J. van Nee, Multipath effects on GPS code phase measurements, Navigation 39 (2) (1992) 177–190.

[3] T. Kos, I. Markezic, J. Pokrajcic, Effects of multipath reception on GPS positioning performance, in: Proceedings ELMAR-2010, IEEE, Zadar, Croatia, 2010, pp. 399–402.

[4] M. Braasch, GPS multipath model validation, in: Proceedings of Position, Location and Navigation Symposium - PLANS '96, IEEE, Atlanta, GA, USA, 1996, pp. 672–678.

[5] S. K. Kalyanaraman, M. S. Braasch, J. M. Kelly, Code tracking architecture influence on GPS carrier multipath, IEEE Transactions on Aerospace and Electronic Systems 42 (2) (2006) 548–561.

[6] F. Scire-Scappuzzo, S. N. Makarov, A low-multipath wideband GPS antenna with cutoff or non-cutoff corrugated ground plane, IEEE Transactions on Antennas and Propagation 57 (1) (2009) 33–46.

[7] S. Daneshmand, A. Jafarnia-Jahromi, A. Broumandan, G. Lachapelle, A GNSS structural interference mitigation technique using antenna array processing, in: 2014 IEEE 8th Sensor Array and Multichannel Signal Processing Workshop (SAM), IEEE, A Coruna, Spain, 2014, pp. 109–112.

[8] A. R. Lopez, GPS landing system reference antenna, IEEE Antennas and Propagation Magazine 52 (1) (2010) 104–113.

[9] A. J. V. Dierendonck, P. Fenton, T. Ford, Theory and performance of narrow correlator spacing in a GPS receiver, Navigation 39 (3) (1992) 265–283.

[10] R. van Nee, The multipath estimating delay lock loop, in: IEEE Second International Symposium on Spread Spectrum Techniques and Applications, IEEE, New York, USA.

[11] K. Chen, Research on theory and methodology of GNSS multipath estimation, Ph.D. thesis, Zhengzhou (2012).

[12] J. Capon, High-resolution frequency-wavenumber spectrum analysis, Proceedings of the IEEE 57 (8) (1969) 1408–1418.

[13] D. P. Wipf, B. D. Rao, An empirical Bayesian strategy for solving the simultaneous sparse approximation problem, IEEE Transactions on Signal Processing 55 (7) (2007) 3704–3716.

[14] T. Yardibi, J. Li, P. Stoica, M. Xue, A. B. Baggeroer, Source localization and sensing: A nonparametric iterative adaptive approach based on weighted least squares, IEEE Transactions on Aerospace and Electronic Systems 46 (1) (2010) 425–443.

[15] F. G. Nievinski, K. M. Larson, Forward modeling of GPS multipath for near-surface reflectometry and positioning applications, Gps Solutions 18 (2) (2014) 309–322.

[16] A. Izadpanah, Parameterization of GPS L1 mulitpath using a dual polarized RHCP/LHCP antenna (2009).

[17] D. N. Aloi, F. V. Graas, Ground-multipath mitigation via polarization ssteering of GPS signal, IEEE Transactions on Aerospace and Electronic Systems 40 (2) (2004) 536–552.

[18] J.-L. Issler, M. Paonni, B. Eissfeller, Toward centimetric positioning thanks to L- and S-band GNSS and to meta-GNSS signals, in: 2010 5th ESA Workshop on Satellite Navigation Technologies and European Workshop on GNSS Signals and Signal Processing (NAVITEC), IEEE, Noordwijk, Netherlands, 2010, pp. 1–8.

[19] J.-A. Avila-Rodriguez, S. Wallner, G. W.Hein, B. Eissfeller, M. Irsigler, J.-L. Issler, A vision on new frequencies, signals and concepts for future GNSS systems, in: Proceedings of the 20th International Technical Meeting of the Satellite Division of The Institute of Navigation (ION GNSS 2007), Institute of Navigation, Fort Worth, TX, 2007, pp. 517–534.

[20] M. Paonni, J. Curran, M. Bavaro, J. Fortuny-Guasch, GNSS meta signals: Coherently composite processing of multiple GNSS signals, in: Proceedings of the 27th International Technical Meeting of the Satellite Division of The Institute of Navigation (ION GNSS+ 2014), Institute of Navigation, Tampa, Florida, 2014, pp. 2592–2601.

[21] A. Jaffer, Maximum likelihood direction finding of stochastic sources: a separable solution, in: ICASSP-88., International Conference on Acoustics, Speech, and Signal Processing, IEEE Computer Society, New York, USA, 1988, pp. 2893–2896 vol.5.

[22] B. Fleury, M. Tschudin, R. Heddergott, D. Dahlhaus, K. I. Pedersen, Channel parameter estimation in mobile radio environments using the SAGE algorithm, IEEE Journal on Selected Areas in Communications 17 (3) (1999) 434–450.

[23] F. Antreich, J. Nossek, W. Utschick, Maximum likelihood delay estimation in a navigation receiver for aeronautical applications, Aerospace Science and Technology 12 (3) (2008) 256–267.

[24] Q. Jia, R. Wu, W. Wang, D. Lu, L. Wang, J. Li, Multipath interference mitigation in GNSS via WRELAX, GPS Solutions 21 (2) (2017) 487–498.

[25] F. Antreich, J. A. Nossek, G. Seco-Granados, A. L. Swindlehurst, The extended invariance principle for signal parameter estimation in an unknown spatial field, IEEE Transactions on Signal Processing 59 (7) (2011) 3213–3225.

[26] R. Schmidt, Multiple emitter location and signal parameter estimation, IEEE Transactions on Antennas and Propagation 34 (3) (1986) 276–280.

[27] T. Kailath, ESPRIT–estimation of signal parameters via rotational invariance techniques, Optical Engineering 29 (4) (1990) 296.

[28] D. G. Manolakis, V. K. Ingle, S. M. Kogon, Statistical and Adaptive Signal Processing, Artech House, Inc., Norwood, 2005.

[29] P. Stoica, J. Li, X. Tan, On spatial power spectrum and signal estimation using the pisarenko framework, IEEE Transactions on Signal Processing 56 (10) (2008) 5109–5119.

[30] H. Van Trees, Optimum Array Processing: Part IV of Detection, Estimation, and Modulation Theory, Wiley, USA, 2022.

[31] Q. Yin, L. Zou, R. W. Newcomb, A high resolution approach to 2-D signal parameter estimation-DOA matrix method, Journal of China Institute of Communications 12 (4) (1991) 8.

[32] S. Pillai, B. Kwon, Forward/backward spatial smoothing techniques for coherent signal identification, IEEE Transactions on Acoustics, Speech, and Signal Processing 37 (1) (1989) 8–15.

[33] S. S. Chen, D. L. Donoho, M. A. Saunders, Atomic decomposition by basis pursuit, SIAM Journal on Scientific Computing 20 (1) (1998) 33–61.

[34] D. Malioutov, M. Cetin, A. S. Willsky, A sparse signal reconstruction perspective for source localization with sensor arrays, IEEE Transactions on Signal Processing 53 (8) (2005) 3010–3022.

[35] P. Gerstoft, C. F. Mecklenbräuker, A. Xenaki, S. Nannuru, Multisnapshot sparse bayesian learning for DOA, IEEE Signal Processing Letters 23 (10) (2016) 1469–1473.

[36] L. Sccot, GNSS solutions: Signal acquisition and search and antenna polarization, Inside GNSS 2 (2) (2007).

[37] P. D. Groves, Z. Jiang, B. Skelton, P. A. Cross, Novel multipath mitigation methods using a dual-polarization antenna, in: ION GNSS 2010, Institute of Navigation, Portland, OR, 2010.

[38] L. Xie, X. Cui, S. Zhao, M. Lu, Mitigating multipath bias using a dual-polarization antenna: Theoretical performance, algorithm design, and simulation, Sensors 17 (2) (2017) 359.

[39] J. Garcia-Molina, M. Navarro-Gallardo, G. Lopez-Risueño, M. Crisci, Unambiguous tracking of high-order BOC signals in urban environments: Channel considerations, in: 2014 7th ESA Workshop on Satellite Navigation Technologies and European Workshop on GNSS Signals and Signal Processing (NAVITEC), IEEE, Noordwijk, Netherlands, 2014, pp. 1–6.

[40] Z. Liu, B. Li, X. Zhu, L. Li, G. Sun, Band-pass sampling in high-order BOC signal acquisition, Applied Sciences 8 (11) (2018) 2226.

[41] R. Weiler, P. Blunt, M. Unwin, S. Hodgart, A direct-conversion receiver for wide-band GNSS signals, in: GNSS Signals & Signal Processing Workshop, Toulouse, France, IEEE, Toulous,France, 2008.

[42] P. Das, L. Ortega, J. Vilà-Valls, F. Vincent, E. Chaumette, L. Davain, Performance limits of GNSS code-based precise positioning: GPS, Galileo & meta-signals, Sensors 20 (8) (2020) 2196.

[43] L. Ortega, D. Medina, J. Vilà-Valls, F. Vincent, E. Chaumette, Positioning performance limits of GNSS meta-signals and HO-BOC signals, Sensors 20 (12) (2020) 3586.

[44] D. M. Akos, A. Ene, J. Thor, A prototyping platform for multi-frequency GNSS receivers, in: Proceedings of the 16th International Technical Meeting of the Satellite Division of The Institute of Navigation (ION GPS/GNSS 2003), Institute of Navigation, Portland, OR, 2003, pp. 117–128.

[45] M. S. Hodgart, P. D. Blunt, M. Unwin, Double estimator—a new receiver principle for tracking BOC signals, Inside GNSS 3 (3) (2008) 26–36.

[46] Y. Zhu, X. Cui, M. Lu, Dual binary phase-shift keying tracking method for Galileo E5 AltBOC(15,10) signal and its thermal noise performance., IET Radar (2015).

[47] D. Borio, Double phase estimator: new unambiguous binary offset carrier tracking algorithm, IET Radar, Sonar & Navigation 8 (7) (2014) 729–741.

[48] C. Wang, X. Cui, T. Ma, S. Zhao, M. Lu, Asymmetric dual-band tracking technique for optimal joint processing of BDS B1I and B1C signals, Sensors 17 (10) (2017) 2360.

[49] Y. Gao, Z. Yao, M. Lu, High-precision unambiguous tracking technique for BDS B1 wideband composite signal, NAVIGATION 67 (3) (2020) 633–650.

[50] M. Vanderveen, C. Papadias, A. Paulraj, Joint angle and delay estimation (JADE) for multipath signals arriving at an antenna array, IEEE Communications Letters 1 (1) (1997) 12–14.

[51] A.-J. van der Veen, M. Vanderveen, A. Paulraj, Joint angle and delay estimation using shift-invariance properties, IEEE Signal Processing Letters 4 (5) (1997) 142–145.

[52] B. Jiang, W. Wang, Q. Yin, Joint two dimensional angle and delay estimation method suitable for general arrays, Acta Electronica Sinica 28 (012) (2000) 1–4.

[53] W. Wang, Space-Time processing for wideband CDMA systems, Ph.D. thesis, Xi'an (2001).

[54] X. Hong, W. Wang, N. Chang, Q. Yin, A subspace-based code tracking loop design for GPS multi-antenna receiver in multipath environment, GPS Solutions 24 (4) (2020).

[55] X. Hong, Research on spatial and temporal subspace-based anti-multipath tracking methods in GNSS receiver, Ph.D. thesis, Xi'an (2021).

[56] M. Brenneman, J. Morton, C. Yang, F. V. Graas, Mitigation of GPS multipath using polarization and spatial diversities, proceedings of international technical meeting of the satellite division of the institute of navigation (2007).

[57] Caroline, Paulus, Jérme, I., Mars, Vector-sensor array processing for polarization parameters and DOA estimation, EURASIP Journal on Advances in Signal Processing 2010 (1) (2010).

[58] E. Jr, T. M. Parks, Direction finding with an array of antennas having diverse polarizations, IEEE Transactions on Antennas and Propagation 31 (2) (1983) 231–236.

[59] J. Li, R. Compton, Angle and polarization estimation in a coherent signal environment, IEEE Transactions on Aerospace and Electronic Systems 29 (3) (1993) 706–716.

[60] F. Fohlmeister, A. Iliopoulos, M. Sgammini, F. Antreich, J. Nossek, Dual polarization beamforming algorithm for multipath mitigation in GNSS, Signal Processing 138 (2017) 86–97.

[61] M. Costa, V. Koivunen, Application of manifold separation to polarimetric capon beamformer and source tracking, IEEE Transactions on Signal Processing 62 (4) (2014) 813–827.

[62] J. A. García-Molina, J. A. Fernández-Rubio, Array processing and unambiguous positioning of signals with multi-peak correlations, in: Proceedings of the 32nd International Technical Meeting of the Satellite Division of The Institute of Navigation (ION GNSS+ 2019), Institute of Navigation, Miami, Florida, 2019, pp. 3754–3758.

[63] G. Seco-Granados, J. Fernandez-Rubio, C. Fernandez-Prades, ML estimator and hybrid beamformer for multipath and interference mitigation in GNSS receivers, IEEE Transactions on Signal Processing 53 (3) (2005) 1194–1208.

[64] P. Stoica, A. Nehorai, MUSIC, maximum likelihood, and cramer-rao bound, IEEE Transactions on Acoustics, Speech, and Signal Processing 37 (5) (1989) 720–741.

[65] N. Chang, X. Hong, W. Wang, Z. Wang, Subspace based joint delay and direction of arrival estimation for GNSS multipath signals, in: China Satellite Navigation Conference (CSNC) 2018 Proceedings, Springer, Singapore, 2018, pp. 189–199.

[66] Y. Pati, R. Rezaiifar, P. Krishnaprasad, Orthogonal matching pursuit: recursive function approximation with applications to wavelet decomposition, in: Proceedings of 27th Asilomar Conference on Signals, Systems and Computers, IEEE, Pacific Grove, CA, USA, 1993.

[67] I. F. Gorodnitsky, B. D. Rao, Sparse signal reconstruction from limited data using FOCUSS: a re-weighted minimum norm algorithm, IEEE Transactions on Signal Processing 45 (3) (2002) 600–616.

[68] Z. Zhang, B. D. Rao, Sparse signal recovery with temporally correlated source vectors using sparse bayesian learning, IEEE Journal of Selected Topics in Signal Processing 5 (5) (2011) 912–926.

[69] D. Wipf, B. Rao, Sparse Bayesian learning for basis selection, IEEE Transactions on Signal Processing 52 (8) (2004) 2153–2164.

[70] E. Candès, M. B. Wakin, S. P. Boyd, Enhancing sparsity by reweighted l1 minimization, Journal of Fourier Analysis and Applications 14 (5) (2008).

[71] S. Cotter, B. Rao, K. Engan, K. Kreutz-Delgado, Sparse solutions to linear inverse problems with multiple measurement vectors, IEEE Transactions on Signal Processing 53 (7) (2005) 2477–2488.

[72] Y. C.Eldar, G. Kutyniok, Compressed Sensing: Theory and Applications, Cambridge University Press, Cambridge, UK, 2018.

[73] S. Fortunati, R. Grasso, F. Gini, M. S. Greco, K. LePage, Single-snapshot DOA estimation by using compressed sensing, EURASIP Journal on Advances in Signal Processing 2014 (1) (2014) 120.

[74] Z. Yang, L. Xie, C. Zhang, Off-grid direction of arrival estimation using sparse bayesian inference, IEEE Transactions on Signal Processing 61 (1) (2013) 38–43.

[75] N. Chang, W. Wang, X. Hong, J. A. López-Salcedo, G. Seco-Granados, Joint angle and delay estimation for GNSS multipath signals based on multiple sparse bayesian learning, GPS Solutions 25 (2) (2021) 1–14.

[76] N. Chang, X. Hong, W. Wang, Z. Wang, Joint delay and angle estimation for GNSS multipath signals based on spatial and frequential smoothing, in: 2018 14th IEEE International Conference on Signal Processing (ICSP), 2018, pp. 203–207.

[77] N. Chang, W. Wang, X. Hong, J. A. Lopez-Salcedo, G. Seco-Granados, Sparse spatial and temporal estimation for multipath mitigation in GNSS, in: 2020 IEEE/ION Position, Location and Navigation Symposium (PLANS), 2020, pp. 1267–1272.

[78] N. Chang, X. Hong, W. Wang, G. Seco-Granados, A GNSS meta-signal sage-based multipath-mitigating loop design, Digital Signal Processing 131 (2022) 103759.

[79] H. Akaike, A new look at the statistical model identification, IEEE Transactions on Automatic Control 19 (6) (1974) 716–723.

[80] Wax, M., Kailath, T., Detection of signals by information theoretic criteria, Acoustics, Speech and Signal Processing, IEEE Transactions on (1985).

[81] S. Kritchman, B. Nadler, Non-parametric detection of the number of signals: Hypothesis testing and random matrix theory, IEEE Transactions on Signal Processing 57 (10) (2009) 3930–3941.

[82] M. Zhang, S. Zhu, X. Chen, A. Zhang, Fast detection of the number of signals based on ritz values: A noise-power-aided approach, IEEE Transactions on Aerospace and Electronic Systems 58 (1) (2022) 651–662.

[83] P. Xie, M. G. Petovello, Measuring GNSS multipath distributions in urban canyon environments, IEEE Transactions on Instrumentation and Measurement 64 (2) (2015) 366–377.

[84] H. Keshvadi, A. Broumandan, G. Lachapelle, Spatial characterization of GNSS multipath channels, International Journal of Antennas and Propagation 2012 (2012) 1–15.

[85] A. J. O'Brien, Adaptive antenna arrays for precision GNSS receivers, Ph.D. thesis, The Ohio State University (2010).

[86] D. J. R. Van Nee, A. Coenen, New fast GPS code-acquisition technique using FFT, Electronics Letters 27 (2) (1991) 158–160.

[87] H. Zhu, G. Leus, G. B. Giannakis, Sparsity-cognizant total least-squares for perturbed compressive sampling, IEEE Transactions on Signal Processing 59 (5) (2011) 2002–2016.

[88] W. L. Mao, A. B. Chen, New code delay compensation algorithm for weak gps signal acquisition, International Journal of Electronics and Communications 63 (8) (2009) 665–677.

[89] M. Irsigler, Characterization of multipath phase rates in different multipath environments, GPS Solutions 14 (4) (2010) 305–317.

[90] B. Rao, Introduction of GNSS Antenna Performance Parameters, Artech House, Norwood, MA, USA, 2013.

[91] B. Hannah, Modelling and simulation of GPS multipath propagation, Ph.D. thesis, Brisbane, Australia (2001).

[92] U. A. F. G. J. P. Office, Global positioning system directorate systems engineering & intergration interface specification (2016).

[93] K. Palamartchouk, P. Clarke, S. Edwards, Dual-polarization GNSS observations for multipath mitigation and better high precision, in: Proceedings of the 28th International Technical Meeting of the Satellite Division of The Institute of Navigation (ION GNSS+ 2015), Institute of Navigation, Tampa, Florida, 2015, pp. 2772–2779.

[94] S. Zhong, Antenna Theory and Techniques, Publishing House of Electronics Industry, Beijing, 2015.

[95] G. Gao, S. Datta-Barua, T. Walter, P. Enge, Ionosphere effects for wideband GNSS signals, in: 63rd Annual Meeting of the Institute of Navigation 2007, Proceedings of the Annual Meeting - Institute of Navigation, Institute of Navigation, Cambridge, MA, 2007, pp. 147–155.

[96] U. Hörmann, S. Thoelert, M. Sgammini, C. Enneking, J. Furthner, M. Meurer, F. Antreich, Ionospheric deformation of broadband GNSS signals and its analysis with a high gain antenna, GPS Solutions 22 (4) (2018) 94.

[97] N. Guo, Y. Kou, Y. Zhao, Z. Yu, Y. Chen, An all-pass filter for compensation of ionospheric dispersion effects on wideband GNSS signals, GPS Solutions 18 (4) (2014) 625–637.

[98] P. Stoica, K. Sharman, Maximum likelihood methods for direction-of-arrival estimation, IEEE Transactions on Acoustics, Speech, and Signal Processing 38 (7) (1990) 1132–1143.

[99] Y. Wang, Theory and Algorithm of Spatial Spectral Estimation, Tsinghua University Press, Beijing, 2004.

[100] R. Wu, W. Wang, D. Lu, L. Wang, Q. Jia, Multipath Interference Suppression, Springer Singapore, Singapore, 2018, pp. 201–233.

[101] J. Li, D. Zheng, P. Stoica, Angle and waveform estimation via RELAX, IEEE Transactions on Aerospace Electronic Systems 33 (3) (1997) 1077–1087.

[102] L. Du, T. Yardibi, J. Li, P. Stoica, Review of user parameter-free robust adaptive beamforming algorithms, Digital Signal Processing 19 (4) (2009) 567–582.

[103] M. Zoltowski, A. Gecan, Advanced adaptive null steering concepts for GPS, in: Proceedings of MILCOM '95, Vol. 3, IEEE, San Diego, CA, USA, 1995, pp. 1214–1218 vol.3.

[104] D. Swingler, A low-complexity MVDR beamformer for use with short observation times, IEEE Transactions on Signal Processing 47 (4) (1999) 1154–1160.

[105] T. J. Shan, M. Wax, T. Kailath, On spatial smoothing for direction-of-arrival estimation of coherent signals, Acoustics, Speech and Signal Processing, IEEE Transactions on 33 (4) (1985) 806–811.

[106] J. Thompson, P. Grant, B. Mulgrew, Performance of spatial smoothing algorithms for correlated sources, IEEE Transactions on Signal Processing 44 (4) (1996) 1040–1046.

[107] M. E. Tipping, Sparse Bayesian learning and the relevance vector machine, Journal of Machine Learning Research 1 (2001) 211–244.

[108] A. P. Dempster, N. M. Laird, D. B. Rubin, Maximum likelihood from incomplete data via the EM algorithm, Journal of the Royal Statistical Society 39 (1) (1977) 1–22.

[109] W. J. Bangs, Array processing with generalized beamformers (1971).

[110] S. M. Kay, Fundamentals of statistical signal processing, PTR Prentice hall (1993).

[111] A. P. Dempster, N. M. Laird, D. B. Rubin, Maximum Likelihood from Incomplete Data Via the EM Algorithm, Journal of the Royal Statistical Society: Series B (Methodological) 39 (1) (2018) 1–22.

[112] G. Seco-Granados, Antenna arrays for multipath and interference mitigation in GNSS receivers, Ph.D. thesis (2000).

[113] B. R. Townsend, P. C. Fenton, K. J. V. Dierendonck, D. J. R. van Nee, Performance evaluation of the multipath estimating delay lock loop, Navigation 42 (3) (1995) 502–514.

[114] E. D. Kaplan, C. J. Hegarty, Understanding GPS: principles and applications, 3rd edn, Artech House (2017).

[115] J. W. Betz, K. R. Kolodziejski, Generalized theory of code tracking with an early-late discriminator part I: Lower bound and coherent processing, IEEE Transactions on Aerospace and Electronic Systems 45 (4) (2009) 1538–1556.

[116] J. W. Betz, K. R. Kolodziejski, Generalized theory of code tracking with an early-late discriminator part II: Noncoherent processing and numerical results, IEEE Transactions on Aerospace and Electronic Systems 45 (4) (2009) 1557–1564.